X-ray Resonators and other Applications of Bragg Backscattering

Yuri Shvyd'ko

Institut für Experimentalphysik
Universität Hamburg

Habilitationsschrift
November 2001

Yuri Shvyd'ko

Institut für Experimentalphysik, Universität Hamburg,
Luruper Chaussee 149, D-22761 Hamburg
yuri.shvydko@desy.de

Abstract

Fabry-Pérot resonators are indispensable in modern optical science and metrology. Such instruments are used to perform high-precision wavelength measurements in atomic spectroscopy, light scattering, laser physics, astrophysics, and other physical sciences.

High resolution instruments of this kind would be extremely useful for measurements in the x-ray range. X-ray Fabry-Pérot resonators would be able to achieve μeV spectral resolution. They could be applied in metrology to bridge the gap between optical and x-ray wavelengths. They could be used as interference filters of very high spectral resolution for studying the dynamics of solids, liquids, and macroscopic biological molecules. X-ray resonators present an exciting and challenging problem.

In this report the results of experimental and theoretical studies are presented detailing solutions aimed at developing x-ray Fabry-Pérot resonators. In particular, *exact* Bragg backscattering of x rays is studied. Sapphire crystals are investigated for use as normal incidence x-ray mirrors. Selected applications of Bragg backscattering are presented including up to $\simeq 0.2$ ppm precise measurements of x-ray wavelengths and crystal lattice parameters. A new easily reproducible and precise wavelength standard is introduced for nanometrology - the Mössbauer wavelength standard. The theory of perfect and imperfect x-ray Fabry-Pérot resonators is propounded and provides insight into the technical challenges that have to be overcome to implement such devices. A test sapphire x-ray resonator for hard x-rays ($\simeq 14.3$ keV) with independently adjustable crystal mirrors has been designed, fabricated and investigated. The measured time response of the test device agrees well with the theoretical predictions and indicates excitation of $\simeq 0.73$ μeV broad x-ray resonances.

Acknowledgments

Without active engagement, valuable help, and support of my colleagues and friends this work would be impossible. I would like to express my sincere gratitude:

To Erich Gerdau for drawing my attention to the problem of x-ray Fabry-Pérot interferometers, also for his long-standing active support, stimulated interest, encouragement, enthusiasm, openness and friendship during many years of working together.

To Hans Dierk Rüter for generously sharing his experience and knowledge, for cooperativeness during many years of working together, for support in solving small and big everyday problems, and for friendship.

To Ercan Alp (APS) for stimulated interest, and for many years of fruitful cooperation. Many exciting projects have been carried out together, not to forget about the first backscattering through the APS undulator.

To Alfred Baron (SPring-8) for sharing his experience with APDs, for loan of the fast and effective Hamamatsu APD, which was essential for experiments at HASYLAB, and for stimulated discussions.

To Peter Becker (PTB) for cooperation in many projects, for providing reference silicon crystals, and for sharing his experience in nano-positioning and precise measurements.

To Margaret Draht who has helped us a lot with technical drawings of the first x-ray resonator.

To Karl Geske for building APD x-ray detectors, and relevant electronics, which have played a crucial role in our experiments.

To Ditter Giesenberg for technical design of the precision furnace, cryostat, and many other important devices used in the backscattering experiments.

To Hermann Franz (HASYLAB) for support during our experiments at the PETRA beamline.

To Benno Frensche for technical design of the x-ray resonator parts.

To Joachim Jäschke (now at Materna GmbH) for active engagement in our first backscattering experiments.

To Robert Johnson for stimulated interest to our projects and for valuable discussions.

To Ruben Khachatryan (APS) for fabrication of sapphire mirrors for the x-ray resonators.

To Victor Kohn (Kurchatov Institute) for fruitful cooperation in understanding difficult question in the theory of x-ray Fabry-Pérot resonators.

To Ulrich Kuetgens (PTB) for sharing his experience in nano-positioning.

To Michael Lerche for his active engagement in many projects, including the γ-ray wavelength standard, x-ray topography studies of sapphire crystals, and x-ray resonators.

To Olaf Leupold (now at ESRF) for assistance during our first backscattering experiments at BW4, and for cooperativeness during many years of working together.

To Barbara Lohl for everyday assistance in solving all possible problems during many years of working together. The five o'clock tea discussions have played a significant role in the activity of our group.

To Martin Lucht who has devised the temperature control software, which accompanied us in our experiments on backscattering and x-ray resonators.

To Patrick McNally and Weimin Chen (Dublin University) for sharing their

experience and secrets in the white beam x-ray topography, and for x-ray topography studies of many sapphire crystals.

To Wolfgang Sturhahn (APS) for fruitful cooperation and discussions of many interesting physical problems, including x-ray resonators.

To John Sutter (APS/HASYLAB) for assistance in our experiments at APS and discussions of multiple beam Bragg diffraction.

To Thomas Toellner (APS) for assistance in our experiments at APS and many interesting discussions concerning high energy resolution x-ray optics.

To Hans-Christian Wille for active participation in experiments on backscattering and x-ray resonators.

To Jürgen Roemmert, Jürgen Weber, Arnis Levitz, Thomas Marckmann and many others at the Feinemechanischewerkstatt des Instituts für Experimentalphysik for manufacturing the equipment for our experiments including the x-ray resonator.

To the current and former staff members of BW4, HASYLAB: Sabine Cunis, Rainer Gehrke, and Gebhard von Krosigk for assistance during experiments at BW4.

To the staff members of Sector 3, SRI CAT at APS for assistance during experiments at APS: Ahmet Alatas, Michael Hu, Caroline L'abbe, Harald Sinn, Jiyang Zhao, and Sandy Zygmuntowicz.

I am greatly indebted to Erich Gerdau, Robert Johnson, Patrick McNally, and Hans Dierk Rüter for many helpful remarks and discussions while reading the manuscript.

Finally, I wish to thank my dearest wife Natasha for her love, encouragement, patience and understanding during all these years.

This project was funded by the Bundesministerium für Bildung, Forschung und Technologie under Contract No. 05 SK8GU1 6. Use of HASYLAB (DESY, Hamburg) and APS (Argonne National Laboratory) facilities is highly appreciated.

Contents

Abstract **iii**

Acknowledgments **v**

Contents **xi**

1 Preface **1**

2 Exact Bragg backscattering **5**
2.1 Historical background and an overview of the field 5
2.2 Dynamical theory of Bragg backscattering 8
2.2.1 General equations 8
2.2.2 Wave fields in a crystal and in vacuum. 15
2.2.3 Reflectivity of thick crystals 18
2.2.4 Asymptotic solutions for parallel-sided crystals 29
2.2.5 Time dependence 32
2.3 Backscattering experimental techniques 37
2.4 Experiments on exact Bragg backscattering 44
2.4.1 Temperature and angular dependence 44
2.4.2 Energy and thickness dependence 50
2.4.3 Multiple-beam effects in Bragg backscattering 53

3 Normal incidence x-ray mirrors **59**
3.1 Why not perfect Si? 59
3.2 Non-cubic α-Al_2O_3. 61
3.3 α-Al_2O_3 as a universal meV-monochromator 67
3.4 Quality assessment of α-Al_2O_3 crystals 71
3.4.1 Preparation of samples 71
3.4.2 White beam x-ray topography technique 72
3.4.3 Bragg reflectivity vs. dislocation density 77

4 Selected applications of backscattering **81**
4.1 Introduction . . . 81
4.2 Why do we need a new wavelength standard? . . . 83
4.3 Measuring lattice constants and wavelengths . . . 86
4.4 γ-ray wavelength standard for atomic scales . . . 89
4.4.1 Setup . . . 89
4.4.2 Experimental details and discussion . . . 91
4.5 α-Al_2O_3 lattice constants . . . 95
4.5.1 Experimental details . . . 95
4.5.2 Data evaluation . . . 97
4.5.3 Discussion and conclusions . . . 100
4.6 Wavelengths of the ^{151}Eu, ^{119}Sn, and ^{161}Dy Mössbauer photons . 102
4.6.1 Experimental details . . . 102
4.6.2 Wavelengths of the ^{151}Eu, ^{119}Sn, and ^{161}Dy Mössbauer radiation . . . 104
4.6.3 Discussion and conclusions . . . 105
4.7 Powder Bragg backscattering spectroscopy . . . 107
4.7.1 Experimental details . . . 108
4.7.2 Results and discussion . . . 109
4.8 Nuclear Resonant Scattering from ^{161}Dy . . . 112
4.8.1 Overview of the field . . . 112
4.8.2 Experimental setup . . . 113
4.8.3 NIS energy spectra of Dy_2O_3 . . . 116
4.8.4 NFS time spectra of metallic Dy . . . 117
4.8.5 Conclusions . . . 121

5 Theory of x-ray Fabry-Pérot resonators **123**
5.1 Introduction . . . 123
5.2 Multiple-beam interference in optics . . . 126
5.2.1 Plane resonators . . . 126
5.2.2 Wedge resonators . . . 132
5.3 Perfect x-ray Fabry-Pérot resonator . . . 134
5.3.1 General equations . . . 134
5.3.2 Comparison with optical resonators . . . 139
5.3.3 Enhanced phase sensitivity . . . 140
5.3.4 Influence of the gap width . . . 142
5.3.5 Spectral dependence . . . 144
5.3.6 Time dependence . . . 153
5.3.7 Angular dependence . . . 157

5.3.8 Temperature dependence 163
5.3.9 Finite number of multiple reflections 164
5.3.10 A practical expression for the Airy phase 166
5.4 Imperfect x-ray Fabry-Pérot resonator 167
5.4.1 Roughness of internal surfaces 167
5.4.2 Inhomogeneous mirror thickness 168
5.4.3 Non-parallel mirrors 168
5.4.4 Temperature gradients 169
5.5 Exemplary applications 171
5.5.1 X-ray to visible light wavelength ratios 171
5.5.2 μeV energy resolution interference filters 173
5.5.3 Instruments for inelastic x-ray scattering 175
5.5.4 Phase contrast imaging 179

6 Towards achieving x-ray resonators **181**
6.1 Concept of the test device 181
6.2 Instrumentation 184
6.2.1 Manufacturing sapphire mirrors 184
6.2.2 Two-axis monolithic nanoradian stage 186
6.2.3 Temperature control 190
6.2.4 Fast detectors 191
6.2.5 Experimental setup 191
6.3 Experiments on x-ray resonators 194
6.3.1 Time response 194
6.3.2 Effects of angular and temperature mismatch 197
6.3.3 Transmission spectrum in different time windows 198
6.3.4 Repeated transmission through x-ray cavity 202

Concluding remarks **205**

Bibliography **209**

Chapter 1

Preface

The use of x rays has moved in the forefront of science and technology in the second half of the 20th century. This progress has been greatly stimulated by the advent of synchrotron x-ray sources. The dedicated undulator-based synchrotron radiation sources which have appeared during the last five years gave a new impetus to such development. The brilliance of the x-ray sources has increased by 12 orders of magnitude in the last 40 years and this trend does not show any signs of stagnation. The future x-ray sources based on free electron lasers driven by linacs which are planned in the coming 5-10 years will provide sub-picosecond radiation pulses with by many orders of magnitude higher brilliance and full transverse coherence (LCLS 1998, Materlik and Tschentscher 2001). The x-ray sources of the newest generation allow one to realize more than ever before the great potential of x-ray optics and, as a consequence, to elaborate new sophisticated instrumentation with unprecedented resolution and eventually to move in new directions of research in fundamental physics, materials science, life sciences, x-ray technology, etc.

These new sources offer the potential to solve challenging problems in x-ray optics. X-ray resonators, highly desirable for high-resolution spectroscopy and interferometry, are among these problems.

Fabry-Pérot resonators (or interferometers) are standard instruments in visible-light optics[1]. Invented by Fabry and Pérot (1899), they have been used as narrow-bandpass filters for more than a hundred years, as instruments for measuring very precisely spectral linewidths and wavelength, as indispensable elements of lasers, etc. (Born and Wolf 1980, Vaughan 1989). The main components of a simplest Fabry-Pérot resonator are two highly reflecting high

[1] According to the established nomenclature in optics, Fabry-Pérot interferometers with a fixed gap are called Fabry-Pérot étalons. As the formation of resonance modes is the main and general feature we shall use the word "resonator" as a generic name for such devices.

quality plane mirrors with a fixed separation. The system becomes transparent despite of the high reflectivity of each mirror when the gap $d_{\rm g}$ between the mirrors is an integer multiple of half of the radiation wavelength so that the resonance condition for standing wave formation in the gap is fulfilled. The free spectral range $E_{\rm f}$, i.e., the separation between two successive transmission peaks on the energy scale is a constant independent of the photon energy: $E_{\rm f} = hc/2d_{\rm g}$. For a gap of 1 cm $E_{\rm f} = 62$ μeV. The spectral width Γ of the transmission resonances is smaller the higher the reflectivity $\mathcal{R}$ of each mirror: $\Gamma = E_{\rm f}(1-\mathcal{R})/\pi\sqrt{\mathcal{R}}$. With a reflectivity of $\mathcal{R} = 0.99$ the spectral width of the transmission peaks is in the range of sub-microelectronvolts.

Instruments with such a high resolution power would also be highly desirable for interferometry and spectroscopy in the x-ray spectral region. However, optical mirrors are inefficient for x rays. Unlike the visible spectral region where backscattering mirrors are easy to produce, this is a central problem for hard x rays.

To minimize the effect of the finite beam divergence on the resolution of Fabry-Pérot resonators backscattering geometry is essential. Producing normal incidence x-ray mirrors of high reflectivity is one of the main technical challenges in the realization of x-ray resonators.

Steyerl and Steinhauser (1979) have proposed a *Fabry-Perot-type interference filter for x rays* with a purpose of monochromatization of hard x rays to a bandwidth of less than 1 meV. Basically, they have proposed replacing the back reflection of optical mirrors by the Bragg back reflection from parallel-sided silicon single crystals. Steyerl and Steinhauser (1979) also have addressed the problem of parasitic (multiple beam) reflections occurring in silicon crystals at exact normal incidence to reflecting atomic planes. They have warned that these parasitic reflections would reduce drastically the mirror reflectivity and deteriorate the performance of the proposed device.

Steyerl and Steinhauser (1979) have not only pioneered the idea of a Fabry-Pérot-type interference filter for x rays, they have also performed the first theoretical analysis, although restricted to *exact* normal incidence. Caticha and Caticha-Ellis (1990b) and Caticha et al. (1996) have extended the theoretical treatment to an arbitrary angle of incidence.

Barbee and Underwood (1983), and Lepetre et al. (1984) have demonstrated a kind of soft x-ray Fabry-Pérot étalon. Tungsten-carbon multilayer mirrors *at grazing* incidence have been used. Because of low mirror reflectivity the observed resonances were not sharp. The performance of such devices has been analyzed by Guichet and Rasigni (1997).

An attempt to build a resonator for hard x rays by using Bragg backscat-

tering from silicon single crystals has been reported recently by Liss et al. (2000). Though multiple Bragg reflections from the crystal mirrors have been observed, the intensity of the reflected beams was, however, low, because of the low reflectivity of silicon crystals in backscattering arising from parasitic Bragg reflections (Shvyd'ko and Gerdau 1999, Sutter et al. 2001). It has not been also possible to improve the situation by increasing the mirror thickness.

When we started this project in 1997, our first goals were: i) to study *exact* Bragg backscattering and to elaborate techniques for its observation; ii) to find and to test a single crystal material which could be used for construction of x-ray backscattering mirrors of high reflectivity in a wide spectral range, iii) to develop further the theory of x-ray Fabry-Pérot resonators, to extend it to practical cases, and to understand all the technical challenges of realization of x-ray resonators; iv) to built and study a test device. In the present report the results of the experimental and theoretical studies are summarized as well as those detailing technical solutions aimed at developing x-ray Fabry-Pérot resonators.

Bragg backscattering is essential for the realization of x-ray Fabry-Pérot resonators. However, it is not the only reason why it will be encountered so often in this report. Bragg backscattering has a unique feature of selecting x rays with a narrow spectral bandwidth. This property underlies many high precision techniques in x-ray physics. New applications of Bragg backscattering to monochromatization of x rays, to high precision measurements of radiation wavelengths and crystal lattice constants, to studies of hyperfine interactions, and applications to phonon spectroscopy will be presented in this report as important byproducts en route to the main goal - an x-ray Fabry-Pérot resonator.

The organization of the report is as follows. In Chapter 2 the dynamical theory of x-ray Bragg backscattering and the results of experimental studies of *exact* Bragg backscattering are presented. In Chapter 3 we address practical issues of selecting materials for elements of normal-incidence Bragg reflection optics. Sapphire (α-Al_2O_3) crystals are presumed to play an important part in the role of normal-incidence mirrors for x-ray resonators, as well as for x-ray monochromators and analyzers with meV and μeV resolution. Selected applications of Bragg backscattering are presented in Chapter 4. In Chapter 5 the theory of perfect and imperfect x-ray Fabry-Pérot resonators is propounded, and the technical challenges of their realization are discussed. An account of first experiments on x-ray resonators is presented in Chapter 6.

Chapter 2

Exact Bragg backscattering

2.1 Historical background and an overview of the field

Bragg backscattering from the viewpoint of the dynamical theory of diffraction in perfect crystals was first considered in the paper of Kohra and Matsushita (1972). Already in this publication two outstanding features of backscattering were pointed out: approaching the Bragg angle of $\pi/2$ the reflection width reaches its smallest value on the energy scale and its largest value on the angular scale. Backscattering thus promised to found a basis for x-ray optics with enhanced luminosity and high energy resolution. These predictions have stimulated further theoretical (Brümmer et al. 1979, Caticha and Caticha-Ellis 1982, Graeff and Materlik 1982, Caticha and Caticha-Ellis 1990a) and experimental (Graeff and Materlik 1982, Kushnir and Suvorov 1986, 1990) studies of backscattering, as well as its application in different schemes of high energy resolution monochromators and analyzers for hard x rays (Faigel et al. 1987, Burkel 1991, Ishikawa et al. 1992, Mooney et al. 1994, Chumakov et al. 1996b, Verbeni et al. 1996, Toellner et al. 1997, Toellner 2000, Toellner et al. 2001, Baron et al. 2001a, Yabashi et al. 2001). Though restricted to angles of incidence deviating from normal incidence to the reflecting atomic planes by $\delta\theta \geq 2$ mrad the experiments of Graeff and Materlik (1982) and of Kushnir and Suvorov (1986) have confirmed the two outstanding features of backscattering.

Cusatis et al. (1996) were the first to observe x rays reflected exactly backwards from a Si(111) plate at an energy of 1.9 keV. The angular profiles in reflection and transmission were studied. Soon afterwards Shvyd'ko et al. (1998) reported the observation of exact backscattering and comprehensive studies of its energy and angular dependence in sapphire (α-Al_2O_3) single crystals

with well collimated and ideally monochromatic 14.4 keV Mössbauer radiation. High reflectivity at exact backscattering close to the theoretical value was observed. A detailed comparison with the predictions of the dynamical theory of x ray diffraction was made.

A new feature in Bragg backscattering has been observed by Kikuta et al. (1998), when studying the angular dependence of transmissivity and reflectivity at a Bragg angle near $\pi/2$ in thin Si(991) crystal plates. It has been ascertained that, upon approaching exact backscattering, the reflectivity goes down. This is a general property of *exact* Bragg back diffraction in crystals with cubic symmetry. The reduction of the reflectivity happens because of the transition from two-beam Bragg diffraction to multiple-beam diffraction while approaching normal incidence. Shvyd'ko and Gerdau (1999), Sutter (2000) and Sutter et al. (2001) have studied the effects of multiple-beam diffraction on the angular and energy dependence of the reflectivity at near normal incidence to the atomic planes (12 4 0) in Si crystals. Kohn et al. (1999) and Sutter (2000) have investigated this problem theoretically. The multiple beam diffraction effects may completely suppress the reflectivity in the back reflection channel (Sutter et al. 2001). Crystals with lower crystal symmetry allows one to avoid this problem (Shvyd'ko and Gerdau 1999). For instance, sapphire, a crystal with rhombohedral lattice, allows exact Bragg backscattering with high reflectivity for x rays over a broad spectral range.

In the present report the experimental and theoretical studies of exact backscattering together with prospects of its applications in γ- and x-ray optics, are discussed, in detail. The organization of the present chapter is as follows.

Elements of the dynamical theory of diffraction of x rays in perfect crystals with emphasis on the points crucial to the backscattering geometry are discussed in sec. 2.2. Equations for the crystal reflectivity in backscattering geometry as a function of angle, energy, time and temperature are derived and used for the reflectivity and transmissivity of x-ray Fabry-Pérot resonators.

The experimental techniques for the observation of exact backscattering are described in sec. 2.3.

The results of experimental studies of exact Bragg backscattering is presented in sec. 2.4. Studies of the angular and energy profiles of exact backscattering in the two-beam diffraction case by using sapphire crystals is given in sec. 2.4.1. The dependence of the peak reflectivity and energy width of the reflection curves on the crystal thickness is studied in sec. 2.4.2. The experimental reflectivities are compared with the predictions of the dynamical theory of diffraction.

The results of the experimental studies of exact backscattering in silicon

single crystals are given in sec. 2.4.3 using the example of the (12 4 0) Bragg reflection. The main purpose was to demonstrate that perfect crystals of cubic symmetry like Si are not adequate for applications in normal-incidence Bragg reflection optics. The arguments are supported by the measurements of the energy and angular dependence of the reflectivity in silicon at normal incidence to the (12 4 0) atomic planes.

2.2 Dynamical theory of Bragg backscattering

The dynamical theory of x-ray diffraction in perfect crystals is considered with an emphasis on the points crucial to the backscattering geometry. The dynamical theory of two-beam diffraction in the backscattering geometry was discussed by Kohra and Matsushita (1972), Brümmer et al. (1979), Caticha and Caticha-Ellis (1982), and Graeff and Materlik (1982). Particular cases of Bragg backscattering influenced by multiple-beam diffraction effects were addressed by Kohn et al. (1999) and Sutter (2000).

In the subsequent discussion the two-beam diffraction case is considered. The expressions are derived, which are used further to evaluate the angular, energy, time and temperature dependence of the crystal reflectivity as well as for the evaluation of the reflectivity and transmissivity of x-ray Fabry-Pérot resonators. The derivation is based on the concept that the basic equations of dynamical diffraction theory as derived by von Laue (1931), see also (Zachariasen 1945, Batterman and Cole 1964, Azaroff et al. 1974, Pinsker 1978), are also valid in backscattering geometry. However, the parameter of deviation from Bragg's condition, denoted as α, is defined differently. Caticha and Caticha-Ellis (1982) have derived a new expression for α valid in backscattering geometry. A more general expression for α valid for any angle of incidence was given in (Shvyd'ko et al. 1998) and derived by Shvyd'ko and Gerdau (1999). This expression allows us to formulate the results of the dynamical theory (e.g., the dynamical Bragg law) in a generalized form valid for the whole range of glancing angles without division into "standard" and "backscattering" regimes.

2.2.1 General equations

We consider scattering from a perfect crystal of the plane monochromatic electromagnetic wave

$$\boldsymbol{\mathcal{E}}(\boldsymbol{r},t) \;=\; \boldsymbol{\mathcal{E}}_0^{(\boldsymbol{in})} \exp[\mathrm{i}(\boldsymbol{K}_0\boldsymbol{r} - Et/\hbar)] \tag{2.1}$$

with the energy E and wave vector $\boldsymbol{K}_0$ ($|\boldsymbol{K}_0| = K = E/\hbar c = 2\pi/\lambda$). The wave is regarded to be linearly polarized. The crystal is a plate of thickness d. The incident wave excites inside the crystal a radiation field with electric vector $\boldsymbol{\mathcal{D}}(\boldsymbol{r},t) = \exp(-\mathrm{i}Et/\hbar)\boldsymbol{\mathcal{D}}(\boldsymbol{r})$. The spatial part $\boldsymbol{\mathcal{D}}(\boldsymbol{r})$ is obtained as a solution of the wave equation

$$[-\nabla^2 - K^2]\boldsymbol{\mathcal{D}}(\boldsymbol{r}) = K^2\chi(\boldsymbol{r})\boldsymbol{\mathcal{D}}(\boldsymbol{r}), \tag{2.2}$$

which is derived from Maxwell's equations for a medium with electric susceptibility $\chi(\boldsymbol{r})/4\pi$. In the derivation of (2.2) it is assumed that the electric field

inside the crystal remains practically transverse[1]. $\chi(\boldsymbol{r})$ is a continuous periodic function in space having the symmetry of the crystal lattice. It can be represented in the form of Fourier series:

$$\chi(\boldsymbol{r}) = \sum_{H} \chi_{H} \, \mathrm{e}^{\mathrm{i}\boldsymbol{H}\boldsymbol{r}}. \tag{2.3}$$

Here $\boldsymbol{H}$ are the reciprocal lattice vectors of the crystal. The Fourier components of the susceptibility χ_0, χ_H, etc, are given by

$$\chi_{H} = -\, r_{\mathrm{e}} \frac{\lambda^2}{\pi V} F_{H} \tag{2.4}$$

with

$$F_{H} = \sum_{\mathrm{n}} f_{\mathrm{n}}(\boldsymbol{H}) \, \mathrm{e}^{\mathrm{i}\boldsymbol{H}\boldsymbol{r}_{\mathrm{n}}} \mathrm{e}^{-W_{\mathrm{n}}(\boldsymbol{H})} \tag{2.5}$$

as the structure factor of the crystal unit cell. Here

$$f_{\mathrm{n}}(\boldsymbol{H}) = f_{\mathrm{n}}^{(0)}(\boldsymbol{H}) + f_{\mathrm{n}}'(\lambda) + \mathrm{i} f_{\mathrm{n}}''(\lambda) \tag{2.6}$$

is the atomic scattering amplitude, which is the sum of the atomic form factor $f_{\mathrm{n}}^{(0)}$ and the anomalous scattering corrections $f'(\lambda)$ and $f''(\lambda)$ of an atom located in the unit cell at a point with radius vector $\boldsymbol{r}_{\mathrm{n}}$. The corrections are energy (wavelength) dependent. Their values can be obtained, e.g., from the library of anomalous scattering factors computed using relativistic Hartree-Fock-Slater wavefunctions (Kissel and Pratt 1990, Kissel et al. 1995).

The value $\exp(-W_{\mathrm{n}})$ in eq. (2.5) is known as the square root of the Debye-Waller factor, cf., Ziman (1969). The Debye-Waller factor measures thermal vibrations of the atoms. It is defined as

$$f_{\mathrm{DW_n}}(\boldsymbol{H}) = \exp\left[-2W_{\mathrm{n}}(\boldsymbol{H})\right]$$

$$W_{\mathrm{n}} = \frac{B_{\mathrm{n}}(\boldsymbol{H})}{4\, d_{H}^2}, \quad B_{\mathrm{n}}(\boldsymbol{H}) = 8\pi^2 \langle u_{H}^2 \rangle_{\mathrm{n}}, \tag{2.7}$$

where $\langle u_{H}^2 \rangle_{\mathrm{n}}$ is the mean square displacement of the atom from the equilibrium position in the unit cell projected on the direction of the scattering vector $\boldsymbol{H}$.

[1] In many texts, discussing the dynamical theory, the *electric displacement* field is calculated inside the crystal and not the *electric* field. This choice is dictated by the purely transverse character of the electric displacement field inside the crystal. However, as long as the electric field inside the crystal is practically transverse, which is justified by the smallness of χ, the distinction between the electric field and the electric displacement field representation inside the crystal is not essential. In the following the electric field inside the crystal is denoted by $\mathcal{D}$, while the electric field in vacuum is denoted by $\mathcal{E}$.

The variable V in eq. (2.4) is the unit cell volume and $r_{\rm e}$ is the classical electron radius. For hard x rays ($\lambda = 1 - 0.1$ Å) the coefficients $\chi_{_H}$ are negative with values typically 10^{-5} and less.

The classical derivation of eqs. (2.4)-(2.5) is given, e.g., by Zachariasen (1945), James (1950), Batterman and Cole (1964), Azaroff et al. (1974), Pinsker (1978), and others. The quantum mechanical derivation with a very thorough account of the role of lattice vibrations is given by Afanas'ev and Kagan (1967).

The Fourier components of the susceptibility are complex values. In the following the real parts are denoted with primes as $\chi_0', \chi_{_H}'$, etc, and the imaginary parts - with double primes as $\chi_0'', \chi_{_H}''$, etc. The same rule is valid for other complex values.

The reciprocal lattice vectors of a crystal are defined as $\boldsymbol{H} = h\boldsymbol{b}_1 + k\boldsymbol{b}_2 + l\boldsymbol{b}_3$, where h, k, and l are integer variables, termed Miller indices, and $\boldsymbol{b}_1$, $\boldsymbol{b}_2$, and $\boldsymbol{b}_3$ is a set of three mutually non-coplanar vectors, called the reciprocal lattice unit vectors. Atomic planes perpendicular to $\boldsymbol{H}$ are denoted as (hkl). The interplanar spacing between the atomic planes (hkl) is

$$d_{_H} = 2\pi/H. \tag{2.8}$$

Since $\chi(\boldsymbol{r})$ is periodic, the solution of equation (2.2) is a Bloch wave (Ziman 1969)

$$\boldsymbol{\mathcal{D}}(\boldsymbol{r}) = {\rm e}^{{\rm i}\boldsymbol{k}_0\boldsymbol{r}} \sum_{_H} \boldsymbol{\mathcal{D}}_{_H}\, {\rm e}^{{\rm i}\boldsymbol{H}\boldsymbol{r}} = \sum_{_H} \boldsymbol{\mathcal{D}}_{_H}\, {\rm e}^{{\rm i}\boldsymbol{k}_{_H}\boldsymbol{r}}, \tag{2.9}$$

where

$$\boldsymbol{k}_{_H} = \boldsymbol{k}_0 + \boldsymbol{H}. \tag{2.10}$$

Thus the radiation field inside the crystal is a set of plane waves with wave vectors $\boldsymbol{k}_{_H}$. Substituting (2.9) into (2.2) one obtains after transformations a system of linear algebraic equations for the vector amplitudes $\boldsymbol{\mathcal{D}}_{_H}$ of the plane waves:

$$\frac{\boldsymbol{k}_{_H}^2 - K^2}{K^2}\, \boldsymbol{\mathcal{D}}_{_H} = \sum_{_G} \chi_{_{H-G}}\, \boldsymbol{\mathcal{D}}_{_G}. \tag{2.11}$$

The reciprocal vectors $\boldsymbol{H}$ and $\boldsymbol{G}$ in (2.11) take all possible discrete values including zero. By virtue of eq. (2.11), one can also interpret the coefficients $\chi_{_{H-G}}$ as be proportional to the probability amplitude of scattering the plane wave with wave vector $\boldsymbol{k}_G$ into the plane wave with wave vector $\boldsymbol{k}_{_H}$ with a momentum transfer $\boldsymbol{H} - \boldsymbol{G}$. Scattering with momentum transfer equal to a reciprocal lattice vector is called Bragg scattering. Thus (2.11) is a system of dynamical equations for the plane wave amplitudes $\boldsymbol{\mathcal{D}}_{_H}$ mutually coupled by Bragg scattering in the crystal.

The system has generally speaking a very large number of equations. However, as long as the coefficients χ_{H-G} are very small only those components $\boldsymbol{\mathcal{D}}_H$ are significant for which $|\boldsymbol{k}_H^2 - K^2|$ are also small, i.e., for which $|\boldsymbol{k}_H| \simeq K$. The latter is often referred to as the resonance condition.

Single-beam case

If the resonance condition is fulfilled for only one wave vector, the system reduces to a single linear equation for the component. To be specific it is denoted with index 0. It follows immediately from eq. (2.11) that the magnitude of the crystal wave vector $k_0 = K(1 + \chi_0/2)$. The value

$$1 + \chi_0/2 \equiv n(\lambda) = 1 + \delta(\lambda) + \mathrm{i}\beta(\lambda) \tag{2.12}$$

is the complex index of refraction. Since χ_0' is small and negative, the real part of the index of refraction is less than unity. Due to this fact the crystal wave vector k_0 is smaller than the vacuum wave vector K. The crystal wavelength is respectively larger than the wavelength in vacuum λ and equals

$$\lambda_{\mathrm{crystal}} = \lambda/(1 + \chi_0'/2) \simeq \lambda \left(1 + r_{\mathrm{e}} \frac{\lambda^2}{2\pi V} F_0'\right). \tag{2.13}$$

Two-beam case

In the subsequent discussion, it is assumed that the resonance condition is fulfilled for two particular vectors, denoted by $\boldsymbol{k}_0$ and $\boldsymbol{k}_H$. Here one has to understand H as a specific rather than a running index. The system composed of a large number of equations then reduces to a system of two linear equations for two vector field amplitudes $\boldsymbol{\mathcal{D}}_0$ and $\boldsymbol{\mathcal{D}}_H$:

$$\frac{\boldsymbol{k}_0^2 - K^2}{K^2} \boldsymbol{\mathcal{D}}_0 = \chi_0 \boldsymbol{\mathcal{D}}_0 + \chi_{\bar{H}} \boldsymbol{\mathcal{D}}_H \tag{2.14}$$

$$\frac{\boldsymbol{k}_H^2 - K^2}{K^2} \boldsymbol{\mathcal{D}}_H = \chi_H \boldsymbol{\mathcal{D}}_0 + \chi_0 \boldsymbol{\mathcal{D}}_H. \tag{2.15}$$

This is commonly referred to as a two-beam approximation.

The in-crystal wave vector $\boldsymbol{k}_0$ is associated in the following with the vacuum wave vector $\boldsymbol{K}_0$ of the incident wave, while the in-crystal wave vector $\boldsymbol{k}_H$ is associated with the vacuum wave vector $\boldsymbol{K}_H$ of the diffracted (scattered) wave. Diffraction takes place on the atomic planes of the crystal which are perpendicular to the reciprocal lattice vector $\boldsymbol{H}$. The scattering geometry is shown in Fig. 2.1a. The wave vectors $\boldsymbol{K}_0$ and $\boldsymbol{K}_H$ of the incident and scattered

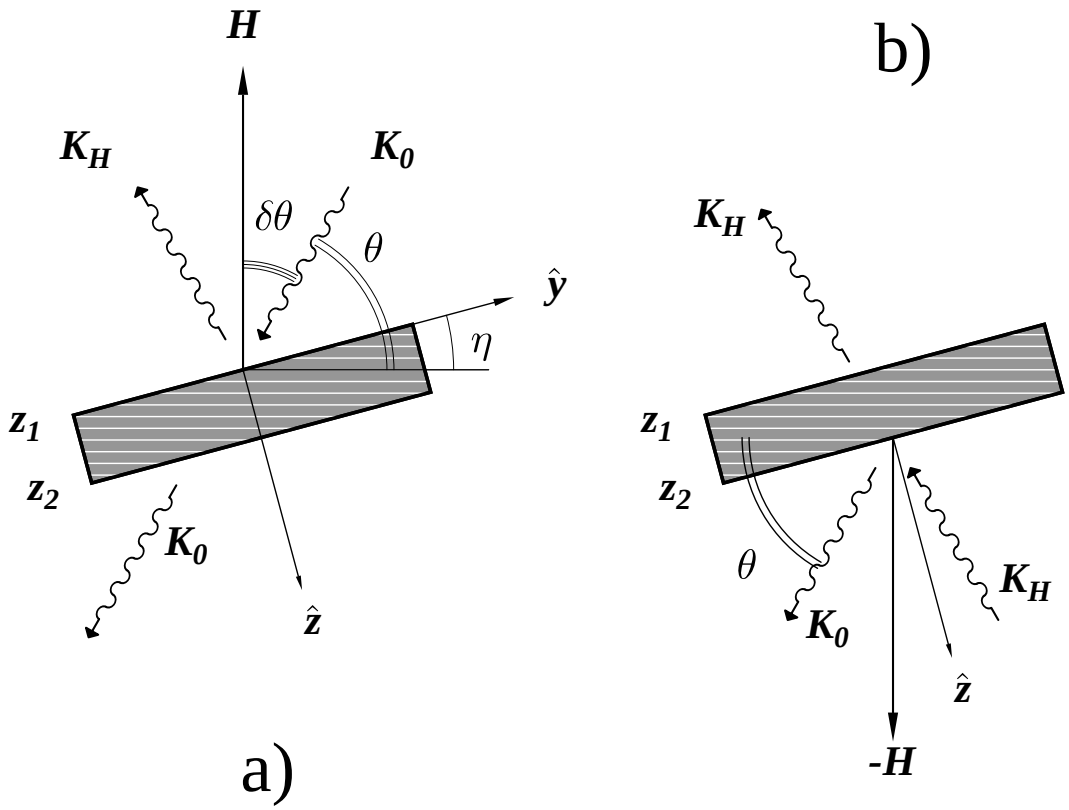

Figure 2.1: Bragg scattering geometries: a) front surface incidence, b) rear surface incidence.

radiation in vacuum define the scattering plane $(\boldsymbol{K}_0, \boldsymbol{K}_H)$. The glancing angle of the wave vector $\boldsymbol{K}_0$ with respect to the reflecting atomic planes is θ. The angle $\delta\theta = \pi/2 - \theta$ is the incidence angle, which is a measure of deviation from normal incidence to the reflecting atomic planes. The unit vector $\hat{\boldsymbol{z}}$ is an internal normal to the front crystal surface.

Because of the crystal susceptibility, although small, the in-crystal wave vectors $\boldsymbol{k}_0$ and $\boldsymbol{k}_H$ differ from those in vacuum $\boldsymbol{K}_0$ and $\boldsymbol{K}_H$, respectively. The condition of continuity of the tangential component of the electric field at the vacuum-crystal interface requires: $\boldsymbol{k}_0 = \boldsymbol{K}_0 + \delta\,\hat{\boldsymbol{z}}$, i.e., the wave vectors differ only along the surface normal by some value δ. A similar relation is valid for the in-crystal and vacuum wave vectors of the diffracted wave. These relations are applied in the subsequent discussion in the following form:

$$\boldsymbol{k}_0 = \boldsymbol{K}_0 + \frac{\varepsilon_0 K}{\gamma_0}\,\hat{\boldsymbol{z}} \tag{2.16}$$

$$\boldsymbol{k}_{H} \;=\; \boldsymbol{K}_{H} + \frac{\varepsilon_{H} K}{\gamma_{H}}\,\hat{\boldsymbol{z}}. \tag{2.17}$$

The corrections ε_0 and ε_H are unknowns which along with $\boldsymbol{\mathcal{D}}_0$ and $\boldsymbol{\mathcal{D}}_H$ have to be determined. As distinct from that, γ_0 and γ_H are defined by the scattering geometry. Here $\gamma_0 = \boldsymbol{K}_0\hat{\boldsymbol{z}}/K$ and $\gamma_H = (\boldsymbol{K}_0 + \boldsymbol{H})\hat{\boldsymbol{z}}/K$ are cosines of the angles between the surface normal and the wave vectors $\boldsymbol{K}_0$ and $\boldsymbol{K}_0 + \boldsymbol{H}$, respectively. By using Fig. 2.1, one can also obtain $\gamma_0 = \sin(\theta - \eta)$ and $\gamma_H = -\sin(\theta + \eta)$.

The corrections ε_0 and ε_H are not independent. By using the momentum conservation in crystals (2.10), the following relation can be obtained:

$$\boldsymbol{K}_{H} = \boldsymbol{K}_{0} + \boldsymbol{H} + K\left(\frac{\varepsilon_{0}}{\gamma_{0}} - \frac{\varepsilon_{H}}{\gamma_{H}}\right)\hat{\boldsymbol{z}}. \tag{2.18}$$

Furthermore, as long as the vacuum is isotropic and Bragg scattering is elastic, the magnitudes of the wave vectors of the incident and scattered radiation should be equal:

$$|\boldsymbol{K}_{H}|^2 = |\boldsymbol{K}_{0}|^2 = K^2. \tag{2.19}$$

By using (2.18) and (2.19), one obtains the relation between the corrections ε_0 and ε_H:

$$\varepsilon_{H} = \frac{\varepsilon_{0}}{b} + \frac{\alpha}{2}, \tag{2.20}$$

where

$$\alpha = \frac{2\boldsymbol{K}_{0}\boldsymbol{H} + \boldsymbol{H}^2}{K^2}, \tag{2.21}$$

and

$$b \;=\; \frac{\gamma_{0}}{\gamma_{H}} \;\equiv\; -\frac{\sin(\theta - \eta)}{\sin(\theta + \eta)}. \tag{2.22}$$

As a result, the wave vector of the diffracted wave in vacuum is

$$\boldsymbol{K}_{H} = \boldsymbol{K}_{0} + \boldsymbol{H}', \qquad \boldsymbol{H}' = \boldsymbol{H} - K\frac{\alpha}{2\gamma_{H}}\,\hat{\boldsymbol{z}}. \tag{2.23}$$

Thus, the momentum transfer for radiation waves in vacuum is $\boldsymbol{H}'$ and not $\boldsymbol{H}$ as for the radiation in the crystal, see eq. (2.10). If $\boldsymbol{H} \nparallel \hat{\boldsymbol{z}}$ then also $\boldsymbol{H} \nparallel \boldsymbol{H}'$. This implies that the crystal reflects from virtual planes perpendicular to $\boldsymbol{H}'$, rather than from the real atomic planes perpendicular to $\boldsymbol{H}$. By virtue of eq. (2.23) the angle between the virtual and the atomic planes (the angle between $\boldsymbol{H}'$ and $\boldsymbol{H}$) is a function of α and is given by

$$\Psi \;=\; \frac{K|\alpha|}{2H|\gamma_{H}|}\,\sin\eta. \tag{2.24}$$

The dimensionless parameter α (2.21) plays an important role in the subsequent discussion since the reflectivity and transmissivity of the crystal can be expressed as functions of only this parameter. It will be addressed in more detail in sec. 2.2.3.

The parameter b (2.22) characterizes how symmetric the wave vectors of the incident and reflected radiations are directed with respect to the normal of the crystal surface $\hat{\boldsymbol{z}}$. It is therefore often referred to as an asymmetry parameter. In the subsequent discussion the Bragg-case scattering geometry is considered, in which the incident and diffracted waves are on the same side of the vacuum-crystal interface, as in Fig. 2.1. In this case $\gamma_0 = \sin(\theta - \eta) > 0$, $\gamma_H = -\sin(\eta + \theta) < 0$, and the asymmetry parameter takes arbitrary negative values. If the wave vectors of the incident and reflected beams make the same angle with the normal to the crystal surface, then $b = -1$. This is always the case for exact backscattering ($\theta = \pi/2$).

Combining all these equations with eqs.(2.14)-(2.15), neglecting terms quadratic with respect to ε_0 and ε_H, one obtains the following system of equations

$$2\varepsilon_0 \, \mathcal{D}_0^s \;=\; \chi_0 \, \mathcal{D}_0^s \,+\, \chi_{\bar{H}} C^s \, \mathcal{D}_H^s \tag{2.25}$$

$$(2\varepsilon_0/b + \alpha) \, \mathcal{D}_H^s \;=\; \chi_H C^s \, \mathcal{D}_0^s \,+\, \chi_0 \, \mathcal{D}_H^s . \tag{2.26}$$

Here $\mathcal{D}_{0,H}^s$ are the linearly polarized components $s = \{\pi, \sigma\}$ of the electric vectors $\boldsymbol{\mathcal{D}}_{0,H} = \boldsymbol{e}_{0,H}^{\pi} \mathcal{D}_{0,H}^{\pi} + \boldsymbol{e}_{0,H}^{\sigma} \mathcal{D}_{0,H}^{\sigma}$. As usual the σ-polarization unit vectors $\boldsymbol{e}_{0,H}^{\sigma}$ are directed perpendicular to the scattering plane, while the π-polarization unit vectors $\boldsymbol{e}_{0,H}^{\pi}$ lie in the plane. The polarization factor $C^{\sigma} = 1$ and $C^{\pi} = \cos 2\theta$. As long as the primary interest here is backscattering, for which $|\cos 2\theta| \simeq 1$, the following discussion ignores the different polarization components and the polarization index s is omitted for simplicity.

The compatibility conditions for the set of linear equations (2.26) determines two possible values of ε_0:

$$2\varepsilon_{0(\nu)} - \chi_0 \;=\; \sqrt{C^2 |b| \, \chi_H \chi_{\bar{H}}} \;\left[-y \pm \sqrt{y^2 - 1} \right], \tag{2.27}$$

with $\nu = 1$ or $\nu = 2$ and

$$y \;=\; \frac{\chi_0(1-b) + \alpha b}{2\sqrt{C^2 |b| \, \chi_H \chi_{\bar{H}}}}. \tag{2.28}$$

It is assumed that the imaginary part of the root in eq.(2.27) is positive and index $\nu = 1$ corresponds to the sign "+" in eq. (2.27). As a result: $\mathrm{Im}(\varepsilon_{0(1)} - \varepsilon_{0(2)}) > 0$.

2.2.2 Wave fields in a crystal and in vacuum.

Front surface incidence

Because of the two solutions for ε_0, the expression (2.9) for the radiation field in the crystal is:

$$\mathcal{D}(\boldsymbol{r}) \;=\; \mathrm{e}^{\mathrm{i}\boldsymbol{K}_0\boldsymbol{r}}\;\left[\mathcal{D}_0(z)+\mathcal{D}_H(z)\,\mathrm{e}^{\mathrm{i}\boldsymbol{H}\boldsymbol{r}}\right], \tag{2.29}$$

with

$$\mathcal{D}_0(z) \;=\; \sum_{\nu=1,2}\mathrm{e}^{\mathrm{i}\delta_\nu z}\mathcal{D}_{0(\nu)}, \quad \mathcal{D}_H(z) \;=\; \sum_{\nu=1,2}\mathrm{e}^{\mathrm{i}\delta_\nu z}\mathcal{D}_{H(\nu)},$$

$$\delta_\nu = \frac{K}{\gamma_0}\varepsilon_{0(\nu)}. \tag{2.30}$$

By using eq.(2.26) one can determine the ratio of the amplitudes $\mathcal{D}_{0(\nu)}$ and $\mathcal{D}_{H(\nu)}$:

$$R_\nu = \frac{\mathcal{D}_{H(\nu)}}{\mathcal{D}_{0(\nu)}} = \frac{2\varepsilon_{0(\nu)}-\chi_0}{C\chi_{\bar{H}}}. \tag{2.31}$$

To determine the amplitudes $\mathcal{D}_{0(\nu)}$ and $\mathcal{D}_{H(\nu)}$ themselves the boundary condition $\boldsymbol{\mathcal{E}}(\text{vacuum side}) = \mathcal{D}(\text{crystal side})$ has to be used.

For the beam propagating in the forward direction, the boundary condition at the front surface $\boldsymbol{r} = \boldsymbol{r}_1$ is: $\mathcal{E}_0^{(in)}\,\exp(\mathrm{i}\boldsymbol{K}_0\boldsymbol{r}_1) = \exp(\mathrm{i}\boldsymbol{K}_0\boldsymbol{r}_1)\mathcal{D}_0(z_1)$. There is no incident beam with wave vector $\boldsymbol{K}_H$ at the rear surface. Therefore, for the in-crystal reflected beam the boundary condition at the rear surface $\boldsymbol{r} = \boldsymbol{r}_2$ is: $\exp\left[\mathrm{i}(\boldsymbol{K}_0+\boldsymbol{H})\boldsymbol{r}_2\right]\mathcal{D}_H(z_2) = 0$. By using eqs.(2.30), these relations can be rewritten as

$$\begin{array}{lcll} \mathcal{D}_{0(1)}\exp[\mathrm{i}\delta_1 z_1] & + & \mathcal{D}_{0(2)}\exp[\mathrm{i}\delta_2 z_1] & = \mathcal{E}_0^{(in)} \\ \mathcal{D}_{H(1)}\exp[\mathrm{i}\delta_1 z_2] & + & \mathcal{D}_{H(2)}\exp[\mathrm{i}\delta_2 z_2] & = 0. \end{array} \tag{2.32}$$

As a result, the forward $\mathcal{D}_0(z)$ and Bragg scattered $\mathcal{D}_H(z)$ components of the radiation field (2.29) inside the crystal at a depth z are given by

$$\mathcal{D}_0(z) = \mathcal{E}_0^{(in)}\,\frac{R_1\exp\left[\mathrm{i}\delta_2(z-z_2)\right]-R_2\exp\left[\mathrm{i}\delta_1(z-z_2)\right]}{R_1\exp\left[\mathrm{i}\delta_2(z_1-z_2)\right]-R_2\exp\left[\mathrm{i}\delta_1(z_1-z_2)\right]} \tag{2.33}$$

$$\mathcal{D}_H(z) = \mathcal{E}_0^{(in)}\,\frac{R_1R_2\left\{\exp\left[\mathrm{i}\delta_2(z-z_2)\right]-\exp\left[\mathrm{i}\delta_1(z-z_2)\right]\right\}}{R_1\exp\left[\mathrm{i}\delta_2(z_1-z_2)\right]-R_2\exp\left[\mathrm{i}\delta_1(z_1-z_2)\right]}. \tag{2.34}$$

The problem is to find general expressions for the transmission and reflection amplitudes of the system.

From (2.29), (2.33), and (2.34), the radiation field component propagating in the forward direction and the reflected radiation field component are given at the rear and at the front surface by

$$\begin{aligned} \mathcal{D}(\boldsymbol{r}_2)_{\text{forward}} &= \mathcal{E}_0^{(in)}\, t_{00}\, \mathrm{e}^{\mathrm{i}\boldsymbol{K}_0\boldsymbol{r}_2} \\ \mathcal{D}(\boldsymbol{r}_1)_{\text{reflected}} &= \mathcal{E}_0^{(in)}\, r_{0H}\, \mathrm{e}^{\mathrm{i}(\boldsymbol{K}_0+\boldsymbol{H})\boldsymbol{r}_1}. \end{aligned} \tag{2.35}$$

Here

$$t_{00} = \mathrm{e}^{\mathrm{i}\delta_1 d}\frac{R_2 - R_1}{R_2 - R_1\mathrm{e}^{\mathrm{i}(\delta_1-\delta_2)d}}, \tag{2.36}$$

$$r_{0H} = R_1R_2\frac{1-\mathrm{e}^{\mathrm{i}(\delta_1-\delta_2)d}}{R_2 - R_1\mathrm{e}^{\mathrm{i}(\delta_1-\delta_2)d}}. \tag{2.37}$$

are the transmission and reflection amplitudes measured at the rear and the front surfaces. They are obtained from eqs. (2.33),(2.34), and (2.35) and by using $d = z_2 - z_1$ as the crystal thickness.

The continuity of the wave fields at the vacuum-crystal interfaces yield the transmitted and reflected wave fields at an arbitrary point $\boldsymbol{r}$ in vacuum:

$$\begin{aligned} \boldsymbol{\mathcal{E}}_0(\boldsymbol{r}) &= \mathcal{D}(\boldsymbol{r}_2)_{\text{forward}}\, \mathrm{e}^{\mathrm{i}\boldsymbol{K}_0(\boldsymbol{r}-\boldsymbol{r}_2)}, \\ \boldsymbol{\mathcal{E}}_H(\boldsymbol{r}) &= \mathcal{D}(\boldsymbol{r}_1)_{\text{reflected}}\, \mathrm{e}^{\mathrm{i}\boldsymbol{K}_H(\boldsymbol{r}-\boldsymbol{r}_1)}. \end{aligned} \tag{2.38}$$

By using eqs. (2.35) and (2.23), the wave fields in vacuum can be written as follows:

$$\boldsymbol{\mathcal{E}}_0(\boldsymbol{r}) = \mathcal{E}_0^{(in)}\, t_{00}\, \mathrm{e}^{\mathrm{i}\boldsymbol{K}_0\boldsymbol{r}}, \tag{2.39}$$

$$\boldsymbol{\mathcal{E}}_H(\boldsymbol{r}) = \mathcal{E}_0^{(in)}\, \rho_{0H}\, \mathrm{e}^{\mathrm{i}\boldsymbol{K}_H\boldsymbol{r}}, \tag{2.40}$$

where

$$\rho_{0H} = r_{0H}\, \exp\left(\mathrm{i}\frac{Kz_1}{2\gamma_H}\alpha\right) \tag{2.41}$$

is the reflection amplitude measured in vacuum from the front crystal surface side. The transmission amplitudes at the crystal surface and in vacuum are equal.

Rear surface incidence

For the problem of the x-ray Fabry-Pérot resonator addressed in Chapter 5, it is helpful to consider the case of the rear surface incidence. In this case , the incident radiation wave

$$\boldsymbol{\mathcal{E}}(\boldsymbol{r},t) = \boldsymbol{\mathcal{E}}_{\boldsymbol{H}}^{(\boldsymbol{in})} \exp[\mathrm{i}(\boldsymbol{K}_H\boldsymbol{r} - Et/\hbar)] \tag{2.42}$$

with wave vector $\boldsymbol{K}_{H}$ strikes the rear surface of the crystal at $\boldsymbol{z}_2$ - Fig. 2.1b.

Under these conditions, the field inside the crystal is

$$\mathcal{D}(\boldsymbol{r}) \;=\; \mathrm{e}^{\mathrm{i}\boldsymbol{K}_{H}\boldsymbol{r}} \;\left[\mathcal{D}_{H}(z) \;+\; \mathcal{D}_{0}(z)\mathrm{e}^{-\mathrm{i}\boldsymbol{H}\boldsymbol{r}}\right], \tag{2.43}$$

and the boundary conditions are written as

$$\begin{array}{rcll} \mathcal{D}_{0(1)}\exp[\mathrm{i}\delta_1 z_1] & + & \mathcal{D}_{0(2)}\exp[\mathrm{i}\delta_2 z_1] & = 0 \\ \mathcal{D}_{H(1)}\exp[\mathrm{i}\delta_1 z_2] & + & \mathcal{D}_{H(2)}\exp[\mathrm{i}\delta_2 z_2] & = \mathcal{E}_{H}^{(in)}\,. \end{array} \tag{2.44}$$

All other variables are defined as previously. As a result, one obtains for the field components inside the crystal

$$\mathcal{D}_{0}(z) = \mathcal{E}_{H}^{(\mathrm{in})}\,\frac{\exp\left[\mathrm{i}\delta_2(z-z_1)\right] - \exp\left[\mathrm{i}\delta_1(z-z_1)\right]}{R_2\exp\left[\mathrm{i}\delta_2(z_2-z_1)\right] - R_1\exp\left[\mathrm{i}\delta_1(z_2-z_1)\right]}, \tag{2.45}$$

$$\mathcal{D}_{H}(z) = \mathcal{E}_{H}^{(\mathrm{in})}\,\frac{R_2\exp\left[\mathrm{i}\delta_2(z-z_1)\right] - R_1\exp\left[\mathrm{i}\delta_1(z-z_1)\right]}{R_2\exp\left[\mathrm{i}\delta_2(z_2-z_1)\right] - R_1\exp\left[\mathrm{i}\delta_1(z_2-z_1)\right]}, \tag{2.46}$$

and

$$t_{HH} = \mathrm{e}^{-\mathrm{i}\delta_2 d}\frac{R_2 - R_1}{R_2 - R_1\mathrm{e}^{\mathrm{i}(\delta_1-\delta_2)d}}, \tag{2.47}$$

$$r_{H0} = \frac{1 - \mathrm{e}^{\mathrm{i}(\delta_1-\delta_2)d}}{R_2 - R_1\mathrm{e}^{\mathrm{i}(\delta_1-\delta_2)d}}, \tag{2.48}$$

for the transmission and reflection amplitudes measured at the crystal surfaces, respectively.

The vacuum wave fields are obtained as follows:

$$\boldsymbol{\mathcal{E}}_{H}(\boldsymbol{r}) \;=\; \mathcal{E}_{H}^{(\mathrm{in})}\,t_{HH}\;\mathrm{e}^{\mathrm{i}\boldsymbol{K}_{H}\boldsymbol{r}}, \tag{2.49}$$

$$\boldsymbol{\mathcal{E}}_{0}(\boldsymbol{r}) \;=\; \mathcal{E}_{H}^{(\mathrm{in})}\,\rho_{H0}\;\mathrm{e}^{\mathrm{i}\boldsymbol{K}_{0}\boldsymbol{r}}, \tag{2.50}$$

where

$$\rho_{H0} \;=\; r_{H0}\;\exp\left(-\mathrm{i}\frac{Kz_2}{2\gamma_{H}}\alpha\right) \tag{2.51}$$

is the reflection amplitude measured in vacuum from the rear crystal surface side. The transmission amplitudes at the crystal surface and in vacuum are equal.

Effect of crystal translations

For the problem of the x-ray Fabry-Pérot resonator discussed in Chapter 5, it is also important to understand how the Bragg reflection and transmission amplitudes are transformed by crystal translations.

If the scattering medium is shifted by the translation vector $\boldsymbol{U}$ the electric susceptibility becomes $\chi(\boldsymbol{r}+\boldsymbol{U})$. As a result the Fourier components of the susceptibility transform to

$$\chi_{_H} \Rightarrow \chi_{_H}\, \mathrm{e}^{\mathrm{i}\boldsymbol{HU}}. \tag{2.52}$$

As a consequence $R_\nu \Rightarrow R_\nu \exp(\mathrm{i}\boldsymbol{HU})$ and the reflection amplitudes become

$$\tilde{r}_{_{0H}} = r_{_{0H}}\, \mathrm{e}^{\mathrm{i}\boldsymbol{HU}}, \qquad \tilde{r}_{_{H0}} = r_{_{H0}}\, \mathrm{e}^{-\mathrm{i}\boldsymbol{HU}}. \tag{2.53}$$

In a particular case of the translation vector $\boldsymbol{U} = n_1\boldsymbol{a}_1 + n_2\boldsymbol{a}_2 + n_3\boldsymbol{a}_3$, where $\boldsymbol{a}_i$ are the basis vectors of the crystal unit cell, and n_i any integer, the scalar product $\boldsymbol{HU} = 2\pi m$, where $m = 0, \pm1, \pm2, ...$ Thus, in this particular case the reflection amplitudes (2.53) are invariant to such a translation. In contrast, transmission amplitudes $t_{_{00}}$ and $t_{_{HH}}$ are always invariant to crystal translations.

The reflection amplitudes $\rho_{_{0H}}$ and $\rho_{_{H0}}$ measured in vacuum contain explicitely the coordinates z_1 and z_2 of the front and rear surfaces, respectively. Therefore they are transformed as follows:

$$\begin{aligned}
\tilde{\rho}_{_{0H}} &= r_{_{0H}}\ \exp\left(\mathrm{i}\frac{K\tilde{z}_1}{2\gamma_{_H}}\alpha\right)\ \mathrm{e}^{\mathrm{i}\boldsymbol{HU}} \\
\tilde{\rho}_{_{H0}} &= r_{_{H0}}\ \exp\left(-\mathrm{i}\frac{K\tilde{z}_2}{2\gamma_{_H}}\alpha\right)\ \mathrm{e}^{-\mathrm{i}\boldsymbol{HU}}.
\end{aligned} \tag{2.54}$$

Here $\tilde{z}_1 = U_z + z_1$ and $\tilde{z}_2 = U_z + z_2$ are the new coordinates of the front and rear surfaces, respectively. Because of the additional phase factor the amplitudes $\rho_{_{0H}}$ and $\rho_{_{H0}}$ possess no translational invariance.

2.2.3 Reflectivity of thick crystals

The reflectivity of the crystal is the ratio of reflected and the incident beam fluxes. Taking into account eqs. (2.40), (2.41), and the asymmetry parameter b, it is given by

$$R = \frac{1}{|b|}|r_{_{0H}}|^2. \tag{2.55}$$

As follows from (2.37), in the case of a thick crystal with $d \gg d_e$, where $d_e = \mathrm{Im}(\delta_1 - \delta_2)^{-1}$, or

$$d_e(y) = \mathrm{Im}\,\frac{\gamma_0}{K\sqrt{C^2|b|\chi_{_H}\chi_{_{\bar{H}}}}}\,\frac{1}{\sqrt{y^2-1}} \tag{2.56}$$

as the extinction length, the reflection amplitude $r_{_{0H}}$ does not depend on d and can be approximated with good accuracy by $r_{_{0H}} = R_1$. In this case the reflectivity becomes $R = |R_1|^2/|b|$. By using additionally eqs.(2.27) and (2.31) we obtain the well known expression for the reflectivity in the approximation of a semi-infinite crystal:

$$R = \left|\frac{\chi_{_H}}{\chi_{_{\bar{H}}}}\right| \left|-y \pm \sqrt{y^2-1}\right|^2. \tag{2.57}$$

The reflectivity is a function of the parameter y alone. Furthermore, in the case of vanishing photo-absorption ($\chi_{_0}'' \simeq 0$ and $\chi_{_H}'' \simeq 0$) there is a region of total reflection with $R = 1$ given by the condition $-1 \le y \le 1$. It is also assumed here that the relation $\chi_{_H} = \chi_{_{\bar{H}}}$ holds, which is true for centrosymmetric crystals. By using the notation $y = \cos\phi_r$ the reflection amplitude reads

$$r_{_{0H}} = -\sqrt{|b|}\exp(-\mathrm{i}\phi_r) \tag{2.58}$$

The phase jump ϕ_r varies in the region of total reflection from $-\pi$ to 0, as y changes from -1 to 1.

From eq.(2.28) the region of total reflection in terms of the parameter α can be defined as:

$$\alpha_{-1} \le \alpha \le \alpha_{+1}, \tag{2.59}$$

$$\alpha_{\pm 1} = \alpha_{\mathrm{c}} \pm 2|C\chi_{_H}|/\sqrt{|b|}, \tag{2.60}$$

$$\alpha_{\mathrm{c}} = \chi_{_0}'\left(1 - \frac{1}{b}\right). \tag{2.61}$$

The center of the region of total reflection is at α_{c}. The width of the region of the total reflection is

$$\Delta\alpha = \alpha_{+1} - \alpha_{-1} = 4|C\chi_{_H}|/\sqrt{|b|} \tag{2.62}$$

and has an order of magnitude of $|\chi_{_H}|$ which is typically $\le 10^{-5}$ for x rays of energy $E \simeq 15$ keV.

Thus, tiny variations of α and consequently of E, θ or T produce sizable changes in reflectivity. These variations leave the components of the electric

susceptibility χ_0, χ_H, asymmetry parameter b, polarization factor C, which enter the parameter y practically unchanged. From this, one may conclude that the reflectivity can be expressed as a function the universal parameter α. If $R(\alpha)$ is known, then by using the relation $\alpha = f(\theta, E, T)$ derived in the next section, the reflectivity as a function of the glancing angle θ, the photon energy E, and the crystal temperature T can be obtained immediately.

Parameter of deviation from Bragg's condition

In this section, the physical interpretation and different representations of the parameter α are discussed. If $\alpha = 0$ then following eq. (2.21)

$$2\boldsymbol{K}_0\boldsymbol{H} + \boldsymbol{H}^2 = 0. \tag{2.63}$$

By using Fig. 2.1 one obtains $\boldsymbol{K}_0\boldsymbol{H} = -HK\sin\theta$. From eq. (2.8) $H = 2\pi/d_H$. As a result

$$\lambda = 2d_H \sin\theta_{\mathrm{B}}, \tag{2.64}$$

which is called Bragg's law. In the kinematic theory of Bragg diffraction, see, e.g., James (1950), which takes no multiple scattering effects into account, Bragg's law relates the radiation wavelength λ to the glancing angle, termed Bragg angle θ_{B}, at which the radiation is reflected from the atomic planes. There is a similar relation between the glancing angle and x-ray energy E:

$$E_H = E\sin\theta_{\mathrm{B}} \tag{2.65}$$

where

$$E_H = \frac{1}{2}H\hbar c \equiv \frac{hc}{2d_H} \tag{2.66}$$

is termed the Bragg energy. X rays with this energy are reflected backwards (in the kinematic approximation).

Eq. (2.63) can be regarded as a kinematic Bragg's law in vector form. It implies, that those wave-vectors $\boldsymbol{K}_0$ fulfill Bragg's condition, which start at the perpendicular bisector of the vector $\boldsymbol{H}$, i.e., those wave-vectors $\boldsymbol{K}_0$ which start from a facet of the Brillouin zone normal to $\boldsymbol{H}$.

Bragg's law provides only a simplified picture of diffraction in crystals. As will be shown, the dynamical theory strictly speaking gives a different relation between the glancing angle and radiation wavelength (energy).

As long as eq. (2.64) is fulfilled when $\alpha = 0$, one can interprete α as a measure of the deviation from the Bragg's condition. For the subsequent discussion it is important to establish the relations between the parameter α and

the physical parameters of the problem, i.e., the energy (or wavelength) of the incident plane wave, the glancing angle, and the crystal temperature.

By using definition (2.21) and Fig. 2.1 one obtains

$$\alpha \;=\; \frac{1}{K^2}\,\left(-2KH\sin\theta \;+\; H^2\right). \tag{2.67}$$

Next, by using definition (2.66) of the Bragg energy, one can establish the following relation between α and the glancing angle θ, x-ray energy E, and crystal temperature T:

$$\alpha \;=\; 4\,\frac{E_{_H}(T)}{E}\;\left[\,\frac{E_{_H}(T)}{E}\;-\;\sin\theta\,\right]. \tag{2.68}$$

Here it was assumed that the interplanar distance $d_{_H}(T)$ and consequently the Bragg energy $E_{_H}(T)$ are temperature dependent.

The above expression is valid for any glancing angle θ, including $\theta = \pi/2$. It is the required general dependence $\alpha = f(E,\theta,T)$ for a given value of the Bragg energy $E_{_H}$. Equivalently α can be expressed via the x-ray wavelength λ:

$$\alpha \;=\; \frac{2\lambda}{d_{_H}(T)}\;\left[\,\frac{\lambda}{2d_{_H}(T)}\;-\;\sin\theta\,\right]. \tag{2.69}$$

By using Bragg's law (2.64), α can be expressed in angles:

$$\alpha \;=\; 4\sin\theta_{\rm B}\;\left[\,\sin\theta_{\rm B}-\sin\theta\,\right]. \tag{2.70}$$

These exact expressions for α were given by Shvyd'ko et al. (1998) and Shvyd'ko and Gerdau (1999).

Assuming that $|\theta_{\rm B}-\theta| \ll 1$ one can easily derive from (2.70) an approximated expression for α:

$$\alpha \;=\; 2\;(\theta_{\rm B}-\theta)\;\sin 2\theta_{\rm B}, \tag{2.71}$$

which is used as a rule in the standard texts of the dynamical theory – see, e.g., Zachariasen (1945), Batterman and Cole (1964), Pinsker (1978), and others. However, this expression fails in the region of backscattering: $\theta_{\rm B} = \pi/2$.

As was shown by Caticha and Caticha-Ellis (1982) another approximation

$$\alpha \;=\; 2\,\left[\,\delta\theta^2\;-\;2\epsilon\,\right]. \tag{2.72}$$

is applicable for backscattering. This expression is readily derived from the general expression (2.68), assuming $|\delta\theta| \ll 1$ and $|\epsilon| \ll 1$, where $\epsilon \equiv (E - E_{_H})/E_{_H}$ is the relative deviation of the x-ray energy from Bragg's energy $E_{_H}$.

As mentioned previously, the interplanar distance $d_{_H}$ and the Bragg energy are temperature dependent. Taking into account that the variation of the Bragg energy in a small temperature range can be expressed as

$$E_{_H}(T+\delta T) \;=\; E_{_H}(T)\,(1-\beta_{_H}\,\delta T), \tag{2.73}$$

with

$$\beta_{_H} = \frac{1}{d_{_H}(T)}\,\frac{\mathrm{d}d_{_H}}{\mathrm{d}T} \tag{2.74}$$

as the linear temperature expansion coefficient in the direction of $\boldsymbol{H}$, one can generalize eq. (2.72) in the following way:

$$\alpha \;=\; 2\delta\theta^2 \;-\; 4\,\left[\frac{\delta E}{E_{_H}(T)} + \beta_{_H}(T)\,\delta T\right]. \tag{2.75}$$

Here $\delta E = E - E_{_H}(T)$. The equation shows that in the backscattering region α varies linearly both with x-ray energy and crystal temperature and quadratically with the angular deviation $\delta\theta$.

Equation (2.75) can be used to establish the equivalence of the variations of the x-ray energy and the crystal temperature. Those values of E and T are equivalent which result in the same reflectivity. As long as the reflectivity of x rays is solely a function of α, the $E-T$ equivalence relation reads

$$\delta E \;=\; E_{_H}(T)\,\beta_{_H}(T)\,\delta T. \tag{2.76}$$

Center of the region of total reflection

Using eq. (2.69), which is valid in the whole range of glancing angles and photon energies, one can rewrite eq. (2.61) defining the center of the region of total reflection as

$$\frac{2\lambda_{\mathrm{c}}}{d_{_H}}\,\left[\frac{\lambda_{\mathrm{c}}}{2d_{_H}} \;-\; \sin\theta_{\mathrm{c}}\right] \;=\; \chi_0'\,\left(1-\frac{1}{b}\right). \tag{2.77}$$

By using the definition of χ_0 - eq. (2.4) - it can be written as

$$2d_{_H}\,\sin\theta_{\mathrm{c}} \;=\; \lambda_{\mathrm{c}}(1+w_{_H}), \tag{2.78}$$

where

$$w_{_H} \;=\; -\chi_0'\,\frac{d_{_H}^2}{\lambda^2}\,\left(1-\frac{1}{b}\right) \;=\; r_{\mathrm{e}}\frac{d_{_H}^2}{\pi V}\,F_0'\,\left(1-\frac{1}{b}\right). \tag{2.79}$$

Alternatively, for the center, E_{c}, of the region of total reflection on the energy scale one obtains

$$E_{\mathrm{c}}\,\sin\theta_{\mathrm{c}} \;=\; E_{_H}(1+w_{_H}). \tag{2.80}$$

Expressions (2.78) and (2.80) relate the radiation wavelength λ_c (energy E_c) and its glancing angle θ_c at the center of the region of total reflection. The region of total reflection from (2.78) in the whole of (λ, θ) space is shown in

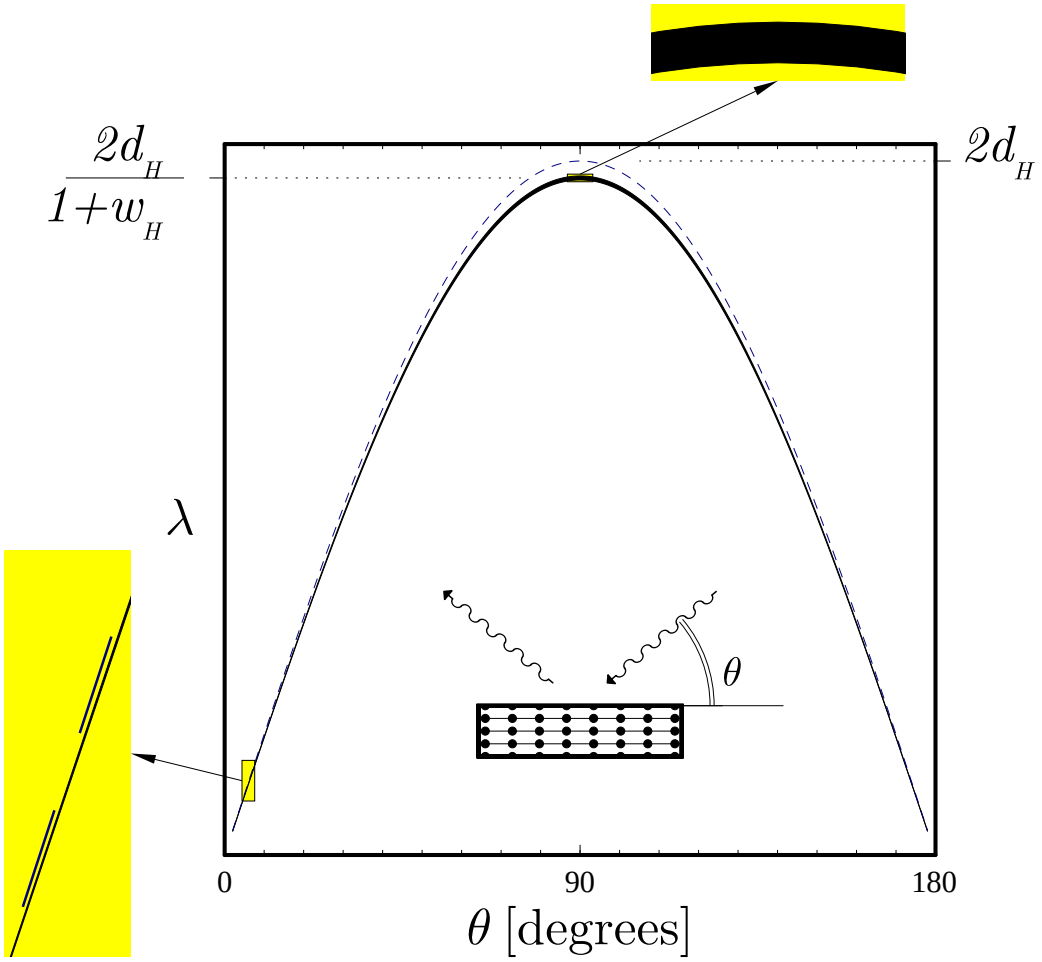

Figure 2.2: Solid line: the region of total reflection of x rays given by the two-beam dynamical Bragg diffraction; θ is the glancing angle to the reflecting atomic planes (hkl) in the crystal with interplanar distance d_H and λ is the wavelength of the x rays. The curve is given by (2.78). The spectral width of the curve is defined by (2.84). The enlarged parts of the diagram display the advantages of backscattering: high reflectivity in a broad angular region with a narrow spectral width. Dashed line: the trace of the Bragg peak reflectivity in the (λ, θ) space as given by kinematic Bragg's law (2.64).

Fig. 2.2. Equation (2.78) looks like Bragg's law (2.64), however, not exactly. There is a small but significant correction $w_{_H}$. Typically $w_{_H} \simeq 10^{-4} - 10^{-6}$. Since $w_{_H}$ is positive, it shifts the reflectivity peak to higher angles $\theta_{\rm c}$ or higher energies $E_{\rm c}$ than it is given by Bragg's law. Henceforth, relation (2.78) or (2.80), is referred to as the modified (or dynamical) Bragg's law. The general expression for α (2.69) allows us to formulate the dynamical Bragg law in a generalized form valid in the whole range of glancing angles without division into "standard" and "backscattering" regimes.

The correction $w_{_H}$ can be considered constant in a relatively large spectral range for a given Bragg reflection. The only energy (wavelength) dependence comes from the anomalous scattering corrections $f'(\lambda)$ to $F'_{_0}$, see eqs. (2.5)-(2.6). E.g., in the spectral range $\lambda_{\rm M} - 0.01$ Å $\leq \lambda_{\rm c} \leq \lambda_{\rm M} + 0.01$ Å where $\lambda_{\rm M} = 0.86$ Å, the anomalous scattering corrections for silicon f' varies at most by ± 0.003 about its average value of 0.119 (Deutsch and Hart 1988), and thus $w_{_H}$ varies by less than 10^{-8} compared to the leading term 1.

Due to the presence of the correction $w_{_H}$ the glancing angle at the center of the total-reflection region deviates from the Bragg angle by

$$\sin\theta_{\rm c} - \sin\theta_{\rm B} \;=\; w_{_H}\frac{\lambda_{\rm c}}{2d_{_H}}, \tag{2.81}$$

for a given wavelength $\lambda_{\rm c}$. Similarly, for a given glancing angle the radiation wavelength which is reflected at the center of total-reflection region

$$\lambda_{\rm c} \;=\; \frac{\lambda}{1+w_{_H}}, \tag{2.82}$$

deviates from the wavelength λ given by Bragg's law. The wavelength of the reflected radiation determined in the dynamical theory is always smaller, as if Bragg's law has to be fulfilled for the wavelength $\lambda_{\rm c}(1+w_{_H})$ and not for λ. This is usually attributed to refraction. However, such an interpretation is too simplified. Indeed, by virtue of (2.13) the in-crystal wavelength is larger than the vacuum wavelength. However, the correction in (2.13), although similar, is not equal to $w_{_H}$. The absence of the λ^2 dependence in $w_{_H}$ is the most significant difference. Only under exact backscattering conditions ($\lambda = 2d_{_H}$ and $b = -1$) are these corrections equal.

Spectral width of the region of total reflection

Let us define the relative spectral width of the Bragg reflection as

$$\epsilon_{_H} \;=\; \frac{\Delta\lambda}{\lambda} \;\equiv\; \frac{\Delta E}{E}. \tag{2.83}$$

By using (2.62) and (2.69) one readily obtains:

$$\epsilon_{_H} \;=\; \frac{\Delta\alpha}{4\sin^2\theta} \;=\; \frac{|C\chi_{_H}|}{\sin^2\theta\,\sqrt{|b|}}. \tag{2.84}$$

The equation is valid for all glancing angles except $\theta = 0$. One may think that the consequence of eq. (2.84) is that the highest relative spectral width is achieved at exact Bragg backscattering ($\theta = \pi/2$), where $\sin\theta$ takes its largest value. A more thorough analysis shows that in reality, for a given Bragg reflection, the *relative spectral width is constant* independent of the glancing angle θ. Indeed, according to (2.4) $\chi_{_H} \propto \lambda^2$. Thus $\epsilon_{_H} \propto \lambda^2/\sin^2\theta = (2d_{_H})^2 = \mathrm{const}$. The Debye-Waller factor as well as the atomic scattering amplitude, which enter $\chi_{_H}$ have the same $\lambda/\sin\theta$ dependence and therefore are also constant for a given reflection.

By using (2.56) the extinction length at the center $y = 0$ of total-reflection region

$$d_e(0) = \gamma_0/(K|C\chi_{_H}|\sqrt{|b|}). \tag{2.85}$$

Combining (2.85) with (2.84) and assuming the symmetric diffraction geometry ($b = -1$) one obtains

$$\epsilon_{_H} \;=\; \frac{d_{_H}}{\pi d_e(0)} \;=\; \frac{1}{\pi N^*}. \tag{2.86}$$

Here $N^* = d_e(0)/d_{_H}$ is the number of reflecting planes within the extinction length. Thus the relative spectral width of a Bragg reflection is the reciprocal of the effective number of diffracting atomic planes contributing to Bragg diffraction. The general tendency is - the higher the x-ray energy (the smaller the wavelength) the larger is the extinction length and therefore the smaller is the relative spectral width.

For x rays with $E \simeq 15$ keV the extinction lengths are typically in the range of $d_e(0) \approx 10 - 100$ μm. Thus the relative energy resolution achievable with single Bragg reflections in this energy range is $\approx (10 - 1) \times 10^{-7}$. This corresponds to energy widths of $\Delta E \simeq 10 - 1$ meV, respectively. One can improve on these numbers by using asymmetric Bragg reflections. For more details see the review paper of Toellner (2000) and references therein.

The *relative* spectral width of a Bragg reflection with a given scattering vector $\boldsymbol{H}$ is a constant independent of θ or λ. This implies that the *absolute* value of the spectral width of the Bragg reflection in terms of energy units takes its smallest value for the smallest photon energy, i.e., at normal incidence ($\theta = \pi/2$). Figure 2.2 illustrates this statement.

Angular width of the region of total reflection

There is no simple analytical expression for the angular width of the region of total reflection valid across the whole range of glancing angles. For $\theta \leq \pi/2$ where the approximation (2.71) is valid the angular width is

$$\Delta\theta \;=\; \frac{\Delta\alpha}{2\sin 2\theta} \;=\; \frac{2|C\chi_{_H}|}{\sin 2\theta\,\sqrt{|b|}}. \tag{2.87}$$

Since $\chi_{_H} \propto \lambda^2$ and $\sin\theta/\lambda = \mathrm{const}$, one can deduce from (2.87) that for a given Bragg reflection the angular acceptance $\Delta\theta$ increases as $\tan\theta$ with increasing glancing angle θ. This agrees with Fig. 2.2 in the whole angular range except $\theta \simeq \pi/2$ ($\delta\theta \simeq 0$).

In the backscattering region the representation (2.72) of α should be used. At the x-ray energy $E = E_{_H}(1-\alpha_{\mathrm{c}}/4) \equiv E_{_H}(1-\chi_{_0}'/2)$ the center of the angular range of total reflection is exactly at $\delta\theta = 0$ and its width is

$$\Delta\theta \;=\; \sqrt{\Delta\alpha} \;=\; 2\sqrt{|C\chi_{_H}|}. \tag{2.88}$$

As distinct from (2.87) the angular width at exact backscattering is proportional to the square root of $|\chi_{_H}|$. Taking into account that $|\chi_{_H}| \lesssim 10^{-6}$, the angular width increases drastically at $\delta\theta \simeq 0$. The reason for this is the quadratic angular dependence at $\delta\theta \simeq 0$ ($\theta \simeq \pi/2$) as one can clearly see in Fig. 2.2.

By using eq. (2.84) one can rewrite eq. (2.88) as

$$\Delta\theta \;=\; 2\sqrt{\epsilon_{_H}} \tag{2.89}$$

The relation is valid at near-normal incidence to the reflecting planes. It demonstrates one of the most striking features of Bragg backscattering. The angular acceptance scales with the *square root* of the relative spectral width! This implies that, Bragg reflections with a relative spectral width as small as $\epsilon_{_H} = 10^{-9}$ are still not blurred by an x-ray beam of a $\lesssim 60$ μrad divergence.

Summary of the properties of Bragg backscattering

The main results of the dynamical theory relevant to Bragg backscattering from a semi-infinite non-absorbing crystal are summarized graphically in Fig. 2.3. In fact it is the part of Fig. 2.2 about $\theta \simeq \pi/2$ drawn on different axes. The ordinate of the graph is $(E - E_{_H})/E_{_H}$ - the deviation of the x-ray energy E from the Bragg energy $E_{_H}$ measured in units of $E_{_H}$. The abscissa is the square of the angular deviation from normal incidence $\delta\theta^2$. The spectral-angular region

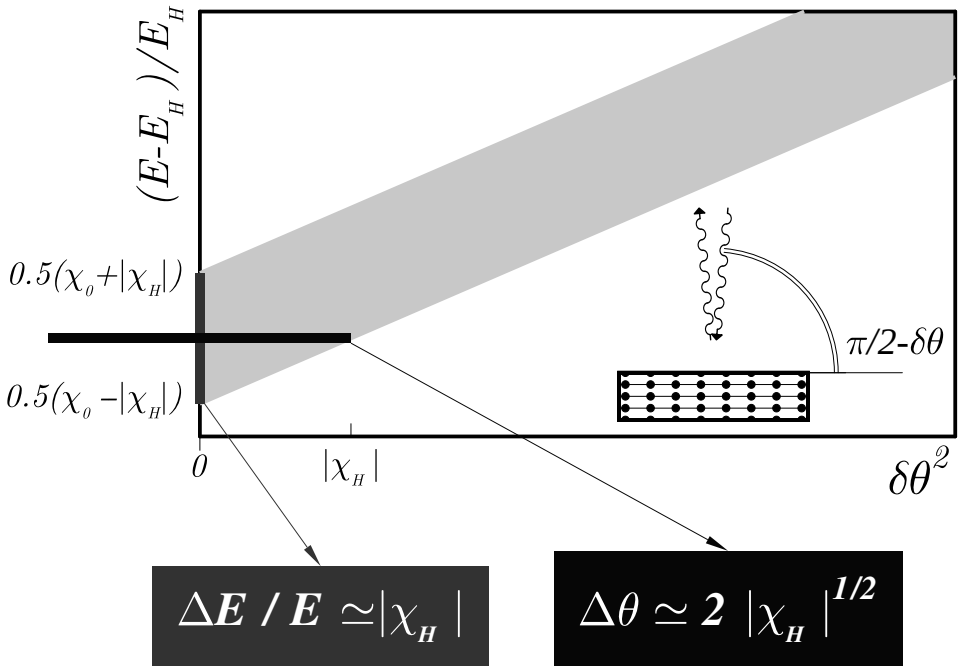

Figure 2.3: Spectral-angular region of total reflection of backscattering. Note that the abscissa scales with $\delta\theta^2$.

of total reflection for a perfect non-absorbing crystal - a kind of DuMond diagram - is given in this representation by the straight grey strip, according to eqs. (2.62), (2.72). The width of the grey strip along both axes scales with $\chi_{_H}$ - the Fourier component of the electric susceptibility, eqs. (2.3), (2.4).

At normal incidence ($\delta\theta = 0$) x-rays which are reflected backwards are centered around the energy $E = E_{_H}(1 - \chi_0'/2)$ slightly larger than $E_{_H}$. The relative width of the region on the energy scale is $\Delta E/E \simeq \chi_{_H}$.

An important feature of the DuMond diagram for backscattering is that the angular scale - the abscissa - has a $\delta\theta^2$ dependence, resulting in an unusually large width of the angular region of total reflection of $\Delta\theta \simeq 2\sqrt{\chi_{_H}}$.

Reflectivity including photo-absorption

Photo-absorption and finite crystal thickness makes the analysis of the Bragg reflectivity more complicated. Peak reflectivity, its position $\alpha_{\rm c}$, as well as the width of the reflection curve $\Delta\alpha = \alpha_{+1} - \alpha_{-1}$ can be derived by numerical calculations. $\Delta\alpha$ differs from (2.62), but it is still of the order of $|\chi_{_H}| \simeq 10^{-6}$. The conclusion that the reflectivity is solely a function of α remains valid.

From numerical calculations one defines $R(\alpha)$, peak reflectivity $R(\alpha_{\rm c})$, with

position α_c and half-width $\Delta\alpha$. The values and dependence on θ, E, or T can be obtained from the valid relation $\alpha = f(\theta, E, T)$.

The energy and angular dependence of Bragg reflectivity for an absorbing crystal calculated by the dynamical theory are shown in Fig. 2.4 with solid lines. The Bragg reflection $(0\ 0\ 0\ 30)$ in an α-Al_2O_3 crystal is used as an example with the following values for the coefficients of the dynamical equations:

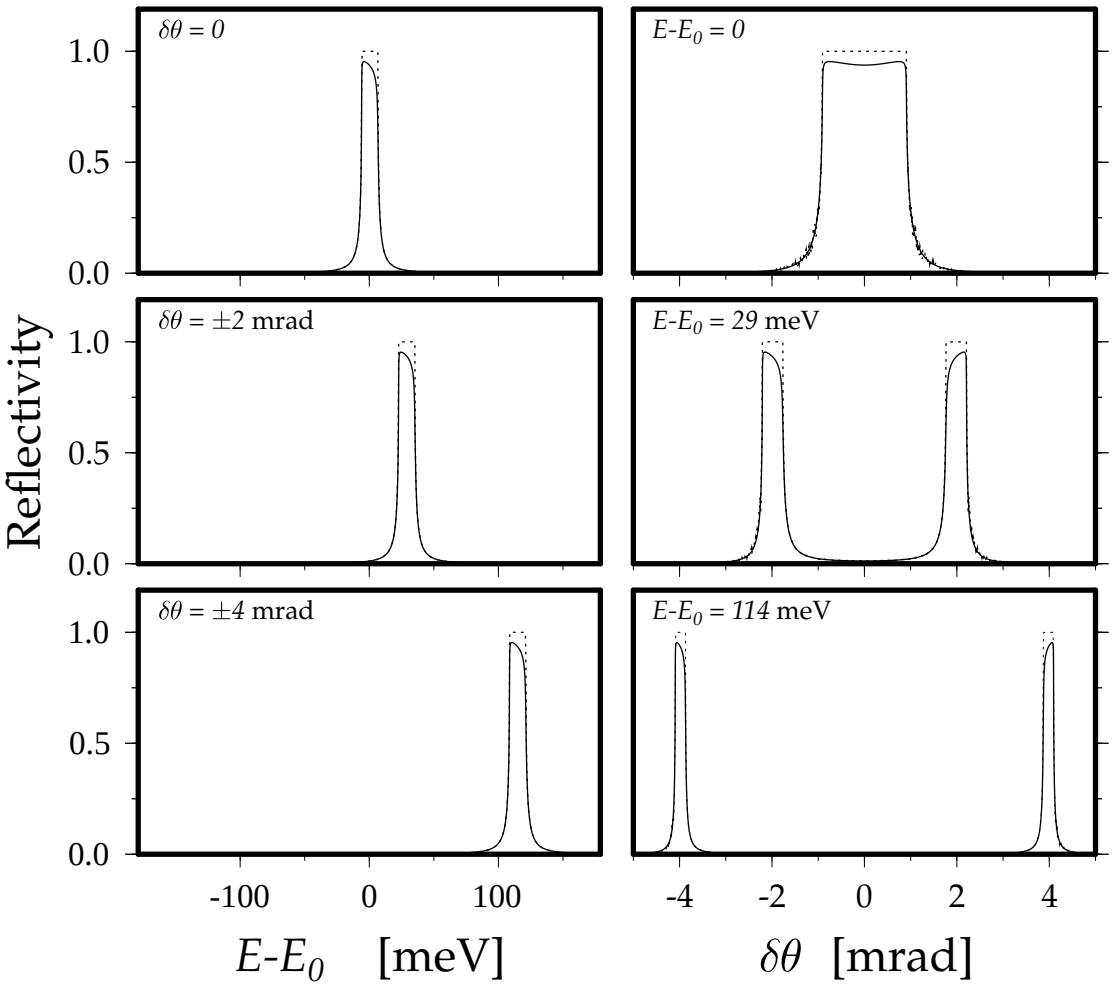

Figure 2.4: Bragg reflectivity of a semi-infinite crystal vs x-ray energy E for a fixed angle of incidence $\delta\theta$ (left panels), and vs incidence angle $\delta\theta$ for a fixed x-ray energy E (right panels). Bragg reflection $(0\ 0\ 0\ 30)$ in α-Al_2O_3 is used in the dynamical theory calculations with photo-absorption taken into account (solid lines). Dashed lines show the results of the same calculations with zero photo-absorption. At normal incidence to the $(0\ 0\ 0\ 30)$ atomic planes ($\delta\theta = 0$) x rays are reflected at an energy of $E_0 = 14.315$ keV.

$\chi_0 = (-7.96 + \mathrm{i}\,0.0297) \times 10^{-6}$, $\chi_H = (-8.63 + \mathrm{i}\,0.209) \times 10^{-7}$, $\chi_{\bar{H}} = \chi_H$. The coefficients are calculated by using the crystallographic data of Kirfel and Eichhorn (1990). The crystals for which $\chi_0' \gg \chi_0''$ and $\chi_H' \gg \chi_H''$ are termed weakly-absorbing. Silicon, sapphire (α-Al_2O_3), and diamond belong to this class of crystals, provided hard x rays (≥ 5 keV) are considered.

The dashed lines in Fig. 2.4 show the result of the same calculations but with zero photo-absorption, i.e., with the imaginary parts dropped in χ_0, χ_H, and $\chi_{\bar{H}}$. As is clearly seen, photo-absorption reduces the peak reflectivity and makes the reflectivity curve asymmetric in the region of "total" reflection. However, the reflectivity curves have the same width and are practically unshifted. This implies that the simple equation (2.78) determining the center of the region of total reflection for non-absorbing crystals as well as the expressions (2.84), (2.87) for the angular and energy widths can also be used with high precision for weakly-absorbing crystals.

2.2.4 Asymptotic solutions for parallel-sided crystals

Another case, relevant to the experiments discussed in the present report, is Bragg diffraction in thin crystals which – as will be clear from the following – is mathematically equivalent to asymptotic solutions for parallel-sided crystals. The thin crystal limit is defined as

$$Kd\sqrt{\chi_H \chi_{\bar{H}}} \ll 1. \tag{2.90}$$

Physically this means that the crystal thickness is much smaller than the Bragg scattering length. By virtue of (2.90), the phases in the exponents $\exp\{\mathrm{i}(\delta_1 - \delta_2)d\}$ in (2.36) and (2.37) change significantly only if the parameter $|y| \gg 1$. This further implies that the Bragg reflectivity profiles are much broader for thin crystals than they are for thick ones, as in the latter case significant changes happen for $|y| \lesssim 1$, see sec. 2.2.3. One can apply the condition $|y| \gg 1$ also to the parallel-sided crystals of any thickness. The approximations obtained under this condition describe the asymptotics (wings) of the Bragg reflectivity.

To calculate the reflectivity, we make use of eq. (2.55). For $|y| \gg 1$ the variables R_1, R_2 and the phase $(\delta_1 - \delta_2)$ take the form:

$$R_1 \simeq -\frac{1}{2y}\sqrt{|b|\,\chi_H/\chi_{\bar{H}}} \simeq \frac{C\,\chi_H}{\tilde{\alpha}}. \tag{2.91}$$

$$R_2 \simeq -2y\sqrt{|b|\,\chi_H/\chi_{\bar{H}}}. \tag{2.92}$$

$$\delta_2 - \delta_1 \simeq -\frac{K}{2\gamma_0}\sqrt{C^2|b|\,\chi_H\chi_{\bar{H}}}\;2|y| \simeq -\frac{K}{2|\gamma_H|}\;|\tilde{\alpha}| \tag{2.93}$$

Here we have defined $\tilde{\alpha} = \alpha - \chi_0(1 - 1/b)$. By virtue of these relations, $|R_2| \gg |R_1|$. As a result the reflection amplitude (2.37) is

$$r_{0H} \simeq R_1 \left[1 - \mathrm{e}^{\mathrm{i}(\delta_1 - \delta_2)d}\right]. \tag{2.94}$$

Finally one obtains for the reflectivity

$$R \simeq \frac{4|R_1|^2}{|b|} \sin^2 \frac{(\delta_1 - \delta_2)d}{2} = \frac{|\chi_H|^2 C^2 K^2 d^2}{4|\gamma_H|\gamma_0} \frac{\sin^2 \xi}{\xi^2}, \tag{2.95}$$

where

$$\xi = \frac{K|\tilde{\alpha}|d}{4|\gamma_H|}. \tag{2.96}$$

By using the representation (2.69) of the parameter α and the definition (2.79) of the parameter w_H, it follows immediately that

$$\xi = \pi N \left| (1 + w_H) \frac{\lambda}{2d_H} - \sin\theta \right|. \tag{2.97}$$

Here

$$N = \frac{d}{d_H|\gamma_H|} \tag{2.98}$$

is the number of reflecting planes throughout the crystal thickness. The reflectivity given by (2.95) has the form of the diffraction function well known in optics. The solution (2.95) is identical to the result derived by the kinematic theory, see, e.g., (Azaroff et al. 1974). The peak reflectivity is achieved at $\xi = 0$. The condition $\xi = 0$ perfectly coincides with the modified Bragg law (2.78). The peak reflectivity is proportional to the square of the crystal thickness d^2 and to the square of the scattering amplitude $|\chi_H|^2$. Due to (2.98), the peak reflectivity is also proportional to N^2 - the square of number of reflecting atomic planes. This is typical for coherent scattering.

The width of the reflection curve (2.95) is $\Delta\xi \simeq \pi$, or equivalently

$$\Delta\alpha \simeq |\gamma_H| \frac{2\lambda}{d}. \tag{2.99}$$

The wings of the reflectivity curve decay as $\propto 1/\xi^2$ ($\propto 1/|\alpha|^2$) and oscillate with a period of $\delta\xi = \pi$ or equivalently

$$\delta\alpha = |\gamma_H| \frac{2\lambda}{d}. \tag{2.100}$$

Thus, the width of the reflection curve $\Delta\alpha$ and the period of oscillation $\delta\alpha$ are equal. By using (2.97), it follows that for a given glancing angle θ the period of

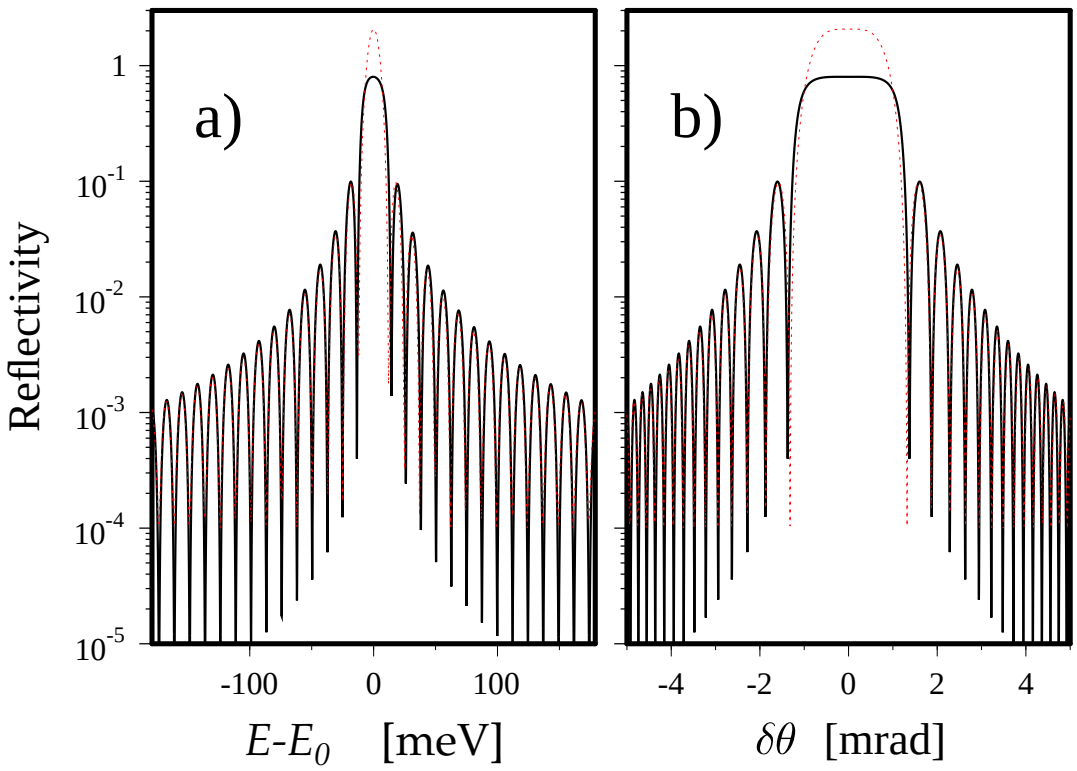

Figure 2.5: Bragg reflectivity of a parallel-sided α-Al_2O_3 crystal of thickness $d = 50$ μm as a function of a) x-ray energy E and b) incidence angle $\delta\theta$, calculated for the Bragg reflection $(0\ 0\ 0\ 30)$. The solid lines - calculations with rigorous expressions of the dynamical theory. The dashed lines - calculations by using the asymptotic approximation (2.95)-(2.97). At normal incidence $\delta\theta = 0$ to the $(0\ 0\ 0\ 30)$ atomic planes x-rays with energy $E_0 = 14.315$ keV are reflected. The calculations are performed in the angular and energy ranges corresponding to an equal variation of the α-parameter.

oscillations $\delta\lambda$ (and equivalently the width $\Delta\lambda$) measured in units of $2d_H$ is a constant independent of the wavelength λ:

$$\frac{\delta\lambda}{2d_H} = \frac{d_H|\gamma_H|}{d(1+w_H)} = \frac{1}{N(1+w_H)}. \tag{2.101}$$

It is determined only by the number of reflecting planes N. On the energy scale, the period of oscillations (and also the reflection width) is

$$\delta E = \Delta E = \frac{hc}{2d(1+w_H)}\frac{|\gamma_H|}{\sin^2\theta}. \tag{2.102}$$

At exact backscattering it is simply $\delta E = hc/2d(1+w_H)$. The thinner the crystal the larger the width. Thus, unlike the thick-crystal limit, the width of the curve

in the thin-crystal limit is independent of χ_H and extinction length. The width of the reflection curve is determined by the crystal thickness d.

Similarly, eqs. (2.95) and (2.97) describe angular dependence of the reflectivity. However - as can be seen from (2.97) - the oscillations are aperiodic on the angular scale. The aperiodicity is especially pronounced at glancing angles close to $\pi/2$, i.e., in the backscattering geometry.

Figure 2.5 shows the reflectivity of a parallel-sided α-Al_2O_3 crystal of thickness $d = 50$ μm as a function of a) x-ray energy E and b) incidence angle $\delta\theta$, calculated for the Bragg reflection $(0\ 0\ 0\ 30)$. Calculations performed with rigorous expressions of the dynamical theory are given by the solid lines. The dashed lines represent results of calculations using the asymptotic approximation (2.95)-(2.97). The comparison shows that the approximated expressions describe perfectly the wings of the Bragg reflection curves. In the limit of a very thin crystal (2.90) the asymptotic approximation can be applied in the whole energy (angular) range.

The intensity oscillation is an effect of crystal thickness. It occurs due to interference of the waves created at the entrance and rear surfaces, see, e.g. (Azaroff et al. 1974) for more discussion. This effect could be especially well recognized in the time dependence of Bragg diffraction, as will be discussed shortly in the following section.

2.2.5 Time dependence

How long does this scattering process, known as Bragg diffraction, last?

The answer to this question is of interest not only on its own. A similar question arises in conjunction with scattering in x-ray Fabry-Pérot resonators, see sec. 5.3. However, since the components of a resonator are single crystals, one should at the outset be able to answer the former question. There exists another reason why it is important to address this question. The upcoming fourth generation synchrotron radiation sources based on free electron lasers will generate radiation pulses as short as 100 fs (LCLS 1998, Materlik and Tschentscher 2001). How will the Bragg crystal optics affect such short radiation pulses? This problem was also addressed in publications by Chukhovskii and Förster (1995), Missalla et al. (1999), Shastri et al. (2001b), Shastri et al. (2001a).

The elementary scattering process from a single atom is very short. Typical widths of atomic resonances are in the eV-range. Thus, from the energy-time uncertainty relation, one should expect that the typical scattering times are less than 1 fs, provided the photon energy is close to an absorption edge. Under

"off-resonance" condition, which is typical for Bragg diffraction, the scattering time should be even shorter. Note, that the dependence of the collision time on the proximity to resonance was experimentally investigated by Smirnov and Shvyd'ko (1989) using the example of long-lived nuclear resonances.

At this point it is important to mention that the distance that light covers in 1 fs is about 0.3 μm, which is much smaller than typical extinction lengths. Thus, the collision time with a single scatterer *is not* the main contribution to the duration of x-ray Bragg diffraction. This is, by the way, very different from the case of nuclear resonant Bragg diffraction from Mössbauer nuclei, where the collision time with a single scatterer determines the time scale of Bragg diffraction (Kagan et al. 1979, Smirnov and Shvyd'ko 1986, Rüffer et al. 1987, van Bürck et al. 1987, Shvyd'ko and Smirnov 1990).

The basic physical phenomenon underlying Bragg diffraction in thick perfect crystals is multiple scattering. Due to multiple scattering and because of time delays for the radiation to propagate from one scatterer to another, Bragg diffraction occupy a finite duration independent of the duration of the elementary scattering process. One can roughly estimate the typical duration of Bragg diffraction as a time lag $\Delta t \sim d_e(0)/c$ for the radiation to cover the penetration length which is determined by the extinction length $d_e(0)$ - eq. (2.85). By virtue of the relation $\Delta E = \hbar c/d_e(0)\sin\theta$ (cf., eqs. (2.83)) and (2.86)) between the energy width of a Bragg reflection and its extinction length, it follows that $\Delta t \sim \hbar/\Delta E \sin\theta$. The latter expression (up to the constant factor $\sin\theta$) could have been derived directly from the uncertainty relation $\Delta t \Delta E = \hbar$. This fact shows that indeed multiple scattering, whose spatial extent is given by the extinction length, determines the duration of Bragg scattering. These facts suggest also a technique for the rigorous calculation of the time dependence of Bragg scattering - the Fourier transform of the energy dependence of Bragg diffraction.

The time dependence of the reflection amplitude $r_{0H}(t)$ is calculated as a Fourier transform of the energy dependence of the reflection amplitude $r_{0H}(E)$:

$$r_{0H}(t) = \int_{-\infty}^{\infty} \frac{\mathrm{d}E}{2\pi\hbar}\, \mathrm{e}^{-\mathrm{i}Et/\hbar}\, r_{0H}(E). \tag{2.103}$$

$r_{0H}(t)$ represents the response amplitude of the system to the instantaneous excitation with a δ-function type radiation pulse. The time dependence of the Bragg reflectivity, similar to eq. (2.55), is given by $R(t) \propto |r_{0H}(t)|^2$. Similar relations can be used to calculate the time dependence of transmission through a single crystal.

Figure 2.6 shows an example of the numerical dynamical theory calcula-

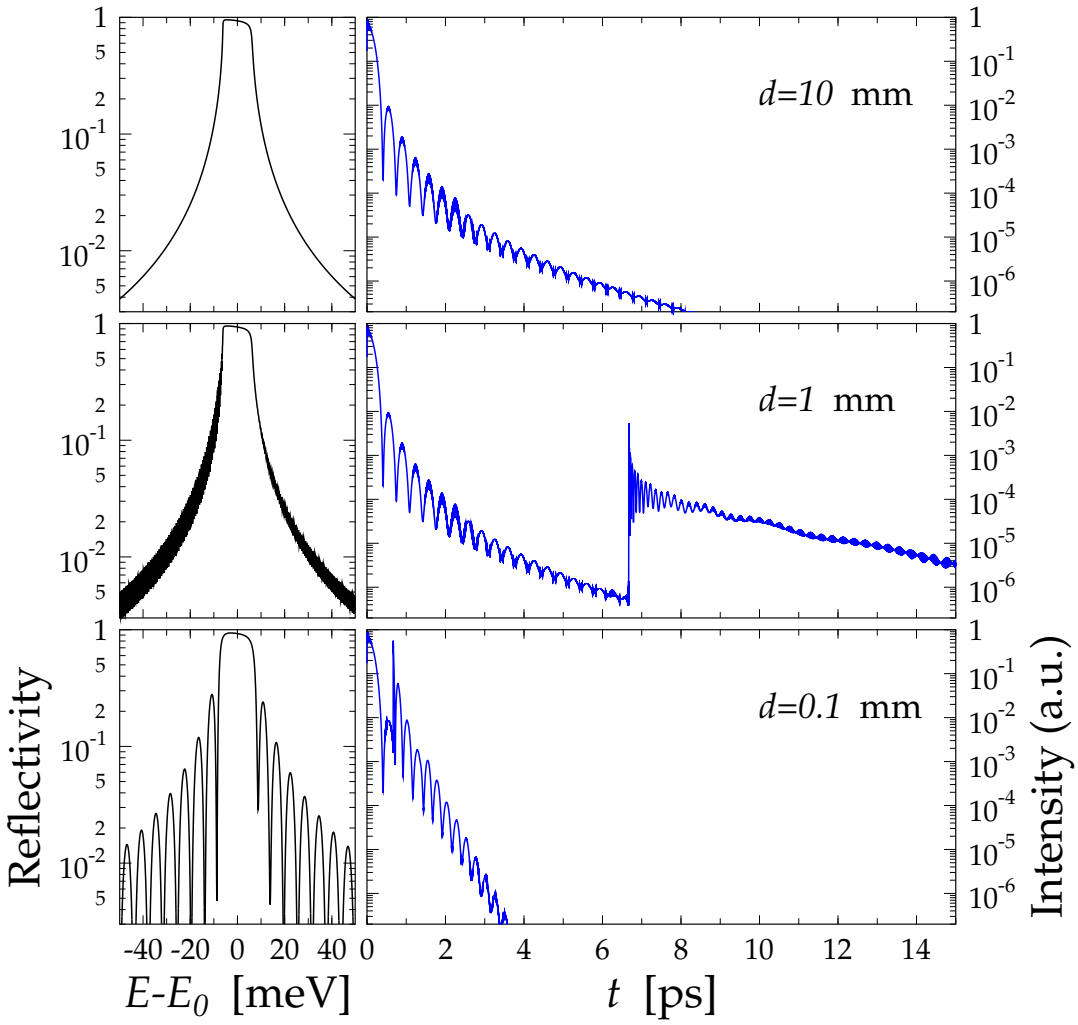

Figure 2.6: Left: Bragg reflectivity vs x-ray energy E for crystals of different thickness d. Right: time dependence of Bragg diffraction. It represents the time response to the instantaneous excitation with a δ-function type x-ray radiation pulse. Bragg reflection $(0\ 0\ 0\ 30)$ in α-Al_2O_3 is used in the dynamical theory calculations. X rays are at normal incidence ($\theta = \pi/2$) to the $(0\ 0\ 0\ 30)$ atomic planes, $E_0 = 14.315$ keV.

tions for the Bragg reflection $(0\ 0\ 0\ 30)$ in α-Al_2O_3 crystals of different thicknesses. The extinction length for this reflection $d_e(0) = 16.0\ \mu$m. For clarity, x rays are assumed to be incident normal ($\theta = \pi/2$) to the $(0\ 0\ 0\ 30)$ atomic planes. The left panels in Fig. 2.6 represent energy dependence of Bragg reflectivity with peaks at $E_0 = 14.315$ keV. Examples are given for three different

crystal thicknesses d, beginning with a thick one $d \gg d_e(0)$ and ending with $d \sim d_e(0)$.

From the aforementioned value of the extinction length one expects an energy width of $\Delta E = \hbar c/d_e(0) = 12.5$ meV, which agrees with 13.0 meV ascertained from the numerical calculations in Fig. 2.6 ($d = 10$ mm). Similarly, one can estimate that the response time $\simeq c/d_e(0) = 0.055$ ps. One obtains practically the same value from the uncertainty relation $\simeq \hbar/\Delta E = 0.051$ ps. However, the duration – full width at half maximum (FWHM) – of the time response ascertained from the numerical calculations in Fig. 2.6 ($d = 10$ mm) turns out to be $\simeq 0.17$ ps, which is a factor π larger.

This discrepancy can be attributed to the fact, that the "classical" uncertainty energy-time relation $\Delta E \Delta t \simeq \hbar$ is valid only for the wave-packets with Lorentzian energy and exponential time distributions. The energy dependence of the Bragg reflectivity is nearly rectangular. The Fourier transform of the rectangular energy dependence of a width ΔE is proportional to $\sin(\Delta E t/2\hbar)/\Delta E t$. As a result, the time dependence of the response is proportional to $[\sin(\Delta E t/2\hbar)/\Delta E t]^2$ with a response time Δt (FWHM) given by the "corrected" uncertainty energy-time relation for Bragg reflections

$$\Delta t \, \Delta E = \pi \hbar. \tag{2.104}$$

The oscillation accompanying the subsequent decay has a period of

$$T = 2\pi\hbar/\Delta E.$$

By using theses relations one obtains estimates for the response time of Bragg diffraction, $\Delta t = 0.17$ ps, and for the period of subsequent oscillations $T = 0.34$ ps, which agree with the values obtained from the rigorous numerical calculations in Fig. 2.6 ($d = 10$ mm).

The following expressions can be derived to estimate the energy width and the response time of Bragg diffraction by using the extinction length with arbitrary glancing angle θ:

$$\Delta E = \frac{\hbar c}{d_e(0)} \frac{1}{\sin\theta} \qquad \Delta t = \pi \frac{d_e(0)}{c} \sin\theta. \tag{2.105}$$

According to the definition - eq. (2.85) - the extinction length $d_e \propto \gamma_0$. In the case of symmetric Bragg diffraction the latter equals $\sin\theta$. Therefore, the response time Δt scales as $\sin^2\theta$ with glancing angle θ. Thus, the smaller the glancing angle (Bragg angle) the smaller is the response time for a given Bragg reflection.

The next graph in Fig. 2.6 is calculated for a thinner crystal with $d = 1$ mm. A remarkable feature appears in this case - an intensity jump at $t = 6.7$ ps. This is an effect due to the wave-field being reflected from the rear surface of the crystal. It appears at a time, which equals the back and forth time-of-flight $2d/c$ through the crystal. A jump of the same origin is observed at $t = 0.67$ ps in Fig. 2.6 ($d = 0.1$ mm) with a more pronounced amplitude. The thinner the crystal - the larger the amplitude of the field reaching the rear surface, because of the weaker influence of both extinction and photo-absorption.

2.3 Backscattering experimental techniques

The observation of exact 180°-scattering has an obvious experimental difficulty. Either the x-ray source or the detector is blocking the reflected or the incident x rays. There are two possibilities to overcome this problem.

Transparent x-ray source

One option is to use a transparent x-ray source, wiggler or undulator, as proposed by Graeff and Materlik (1982), Caticha-Ellis et al. (1990). The construction of an exact backscattering beamline was announced by Moncton (1996) at the Advanced Photon Source (APS) at the 1-ID beamline. The first experiments were performed in 2000 by the High-Resolution X-ray Scattering group at APS, led by Ercan Alp, with participation of the HfWW group of the Hamburg University (NID 2000-2001). A backscattering α-Al_2O_3 crystal was placed downstream of the 1-ID front end and the Si(111) double crystal high-heat-load monochromator, see Fig. 2.7. An undulator was used as a source. The sapphire crystal selected photons with a meV bandpass and sent them back through the Si(111) monochromator and undulator. The photon beam was observed from the other side of the undulator in the normal incidence diffraction station (NID-X). The distances from the undulator to the observation point and to the sapphire crystal were 44 m and 57 m, respectively.

The flux and energy width of x rays using different back reflections were characterized. We have observed, e.g., 4×10^9 photons/s within an energy bandpass of 13 meV at 14.315 keV using the α-$Al_2O_3(0\ 0\ 0\ 30)$ reflection. The

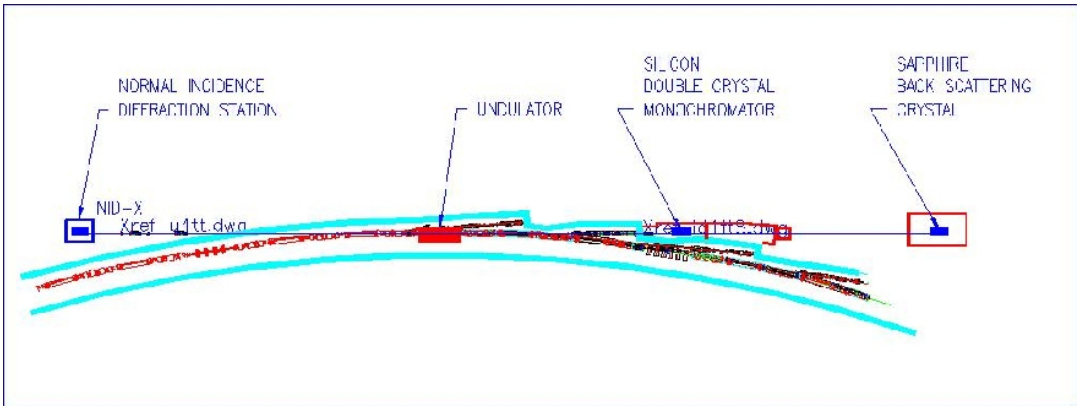

Figure 2.7: An exact backscattering beamline at the APS (Argonne). (Thanks to E. Alp, APS)

incident flux measured downstream of the high-heat-load monochromator was 2.5×10^{12} photons/s/2 eV. The available spectral flux would be 3.2×10^{10} photons/s. The losses in various windows, and air gaps were estimated to sum up to a factor of four. Thus, about half of the photons available back into the NID-X station were obtained in the first attempt.

Semitransparent detector

Another possible way, which was implemented by Cusatis et al. (1996), is to use a semitransparent detector. This technique was used also by Sutter et al. (2001). In this case the reflected radiation is observed on the strong background of the incident radiation.

To discriminate against this background Shvyd'ko et al. (1998) have proposed employing a semitransparent detector with good time resolution and making use of the pulsed structure of synchrotron radiation. The time-of-flight $\tau = 2L/c$ to the crystal and back to the detector, separated by a distance L, allows one to distinguish between the incident and reflected radiation pulses as shown in Fig. 2.8.

A semitransparent detector with good time resolution becomes an essential element of the backscattering experiment - Fig. 2.9. An avalanche photo diode (APD) EG&G[2] C30703F with a 100 μm thick sensitive Si wafer serves as the semitransparent detector[3]. A sensitive silicon wafer of 100 μm thickness absorbs $\simeq 35\%$ of the incident 14 keV photons. The size of the diode is $15 \times 15 \times 2.5$ mm^3 with a sensitive area of 10×10 mm^2. Its time resolution is 0.7 ns. This allows one to distinguish between the incident pulse and the pulse reflected from a crystal placed as close as $L \geq 0.5$ m from the detector. The diode in combination with the timing electronics is able to detect a photon flux up to $\simeq 10^8$ Hz. The application of these APDs for experiments with synchrotron radiation was recently reviewed by Baron (2000).

Setup

The experiments further described in this Chapter were performed at the wiggler beam line BW4 at HASYLAB. Depending on requirements the flight path

[2]Since 1999 a change from EG&G to Perkin-Elmer occurred. Perkin-Elmer, 22001 Dumberry Rd., Vaudreuil J7V 8P7 Quebec. However, we continue to refer to EG&G, as all the devices were purchased from this company.

[3]We are indebted to Dr. Henri Dautet from the EG&G Optoelectronics Ltd., Vaudreuil, Quebec, for delivering photodiodes without ceramic stiffener in the back and without backcover.

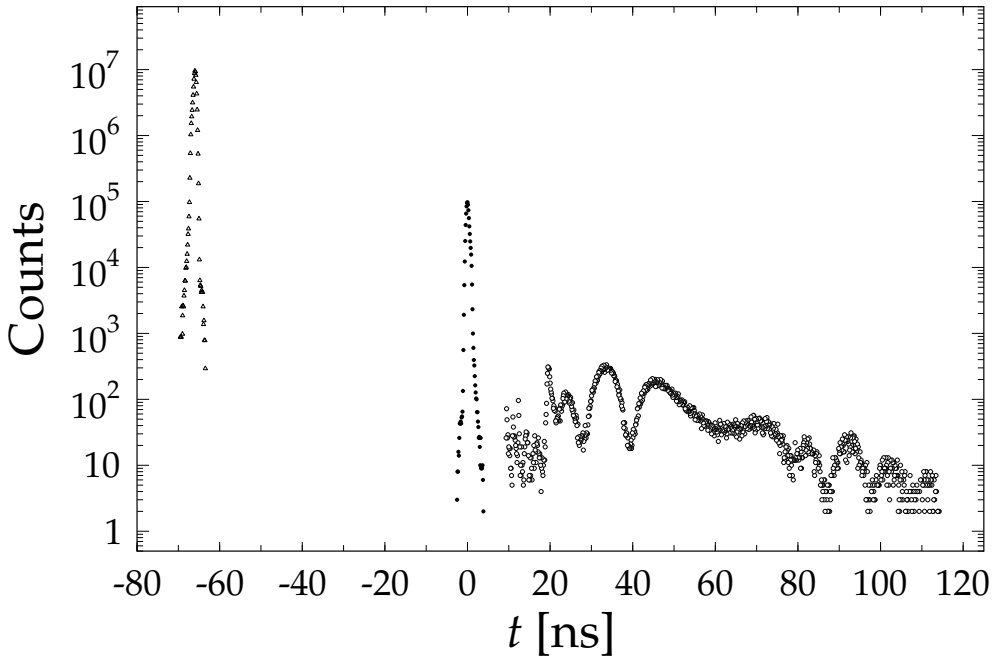

Figure 2.8: Counts in the semitransparent detector as seen on the time scale. The detector is placed at a distance of $L \simeq 10$ m from the reflecting crystal - Fig. 2.9. Primary radiation pulse at $t \simeq -66$ ns; back reflected radiation pulse at $t \simeq 0$; back reflected resonant radiation at $t > 0$.

was varied from $L = 10$ m ($\tau = 66.7$ ns) to $L = 1.0$ m ($\tau = 6.7$ ns). The DORIS-III positron storage ring was operated in five-bunch mode producing synchrotron radiation pulses from the wiggler every 192 ns. The pulse duration was $\simeq 150$ ps. A high-heat-load Si(111) monochromator (M) provided 14 keV radiation with $\simeq 3$ eV bandwidth. The beam divergence was typically 20 μrad in the vertical and 80 μrad in the horizontal plane.

Monochromatic x rays

The typical energy width of Bragg back reflections is in the meV-range. Therefore, to study Bragg backscattering one needs radiation of highest monochromaticity. Two different techniques were used to generate monochromatic x rays.

In the first case 14.4 keV Mössbauer radiation of ^{57}Fe nuclei was used for this purpose. The energy spectrum of the Mössbauer radiation, even for the largest observed broadening and splitting is within a band of 1 μeV width, which can be considered as quasi mono-energetic relative to the energy widths

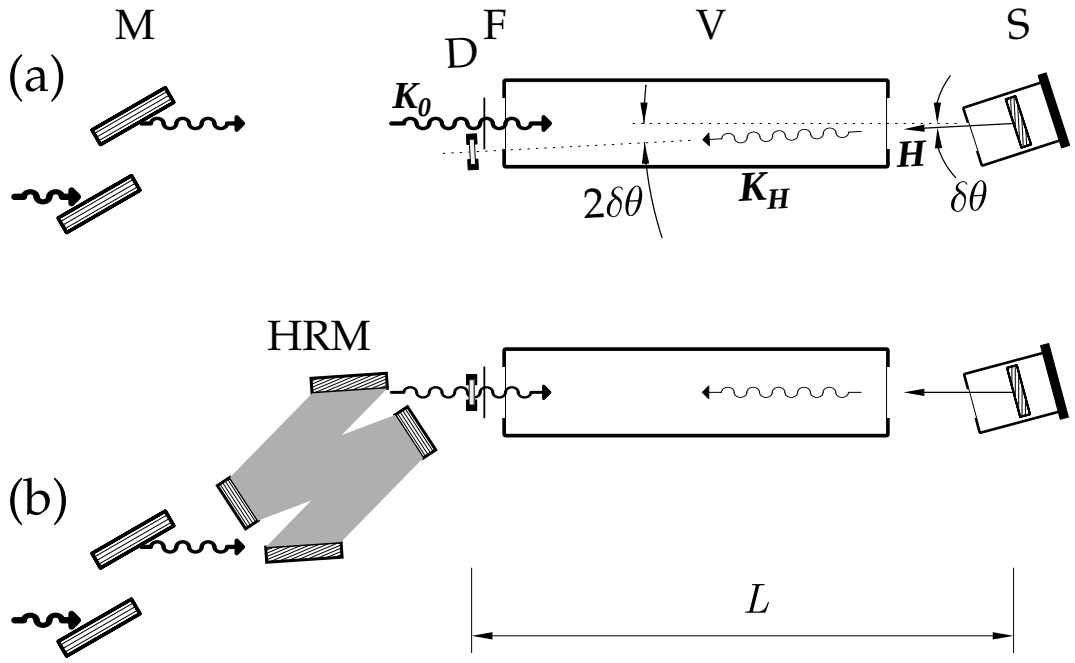

Figure 2.9: Schematics of backscattering experiments. (a) M is the Si(111) high-heat-load monochromator; D is a semitransparent x-ray detector; F is a 10 μm thick ^{57}Fe foil; V is a vacuum flight tube of 1-10 m length; S is a backscattering single crystal in an oven; $\delta\theta$ is the angle between the wave vector $\boldsymbol{K}_0$ of the incident radiation and the scattering vector $\boldsymbol{H}$; $\boldsymbol{K}_H = \boldsymbol{K}_0 + \boldsymbol{H}$ is the wave vector of the scattered radiation. (b) The high energy resolution monochromator (HRM) reduces the incident radiation to a meV bandwidth.

of backscattering reflections. A collimated beam of Mössbauer photons is generated by spatially coherent excitation with synchrotron radiation pulses of the 14.4 keV resonance of ^{57}Fe nuclei placed in a solid state matrix (Hastings et al. 1991). Due to coherent enhancement the ensemble of excited ^{57}Fe nuclei emits photons in the direction of the incident beam (Shvyd'ko et al. 1991) with a delay of ≈20-50 ns. We have used a 10 μm thick iron foil (F in Fig. 2.9). The iron foil was enriched in ^{57}Fe to a level of 95%. The time spectrum of the radiation scattered in forward direction is shown in Fig. 2.8. Mössbauer photons are re-emitted with a delay, which allows one to discriminate them from the prompt pulse containing most of the incident photons. Thus the time resolution of the APD is used twice. First, to distinguish between the incident and the reflected radiation pulses. Second, to count only 14.4125 keV photons in the 0.5 μeV energy band, scattered by ^{57}Fe nuclei in the forward direction.

Being bound to the fixed energy of the Mössbauer radiation, the standard measurement of the reflectivity as a function of the x-ray energy E is replaced by the equivalent reflectivity measurement as a function of the crystal temperature T. The $T-E$ equivalence relation is given by eq. (2.76). Let us consider as an example the $(1\ 3\ \overline{4}\ 28)$ back reflection in α-Al_2O_3 crystals. As will be shown, this reflection matches the 14.4125 keV Mössbauer radiation at $T \simeq 371.6$ K. By using the value of the temperature expansion coefficient of sapphire in the direction [1 3 $\bar{4}$ 28] (Shvyd'ko et al. 2002) one obtains

$$\frac{\mathrm{d}E}{\mathrm{d}T} = -0.094\ \mathrm{eV/K}. \tag{2.106}$$

The second and more general way of monochromatization uses so-called in-line nested monochromators proposed by Ishikawa et al. (1992). By using this technique one could obtain x-ray beams with a bandwidth of $\simeq 0.6$ meV. Recent advances in this field were reviewed by Toellner (2000). The high energy resolution monochromator used in the experiments at HASYLAB built with channel-cut Si(4 2 2) and Si(12 2 2) crystals in a nested geometry was designed by E. Gerdau, R. Rüffer and H.D. Rüter in 1992 for experiments with 14.4 keV Mössbauer radiation. It reduces the energy band of the incident beam from $\simeq 2$ eV to $\simeq 7$ meV. The energy of transmitted x rays can be tuned over a range of 160 eV.

Depending on the situation we use one of these methods of monochromatization.

Temperature control

The most important part of the setup is the backscattering crystal. At least two parameters must be controlled - the crystal temperature and the angular orientation of the atomic planes to the incident beam.

The temperature determines the crystal lattice constants and thus the spectrum of the backscattered radiation. The precision of the temperature control δT is defined by the relative energy width $\Delta E/E_{_H}$ of the chosen reflection and the temperature expansion coefficient β_H of the crystal in the direction of the scattering vector $\boldsymbol{H}$. From eq. (2.76) $\delta T \ll \beta_{_H}^{-1}\,\Delta E/E_{_H}$. By using a typical relative width of $\Delta E/E_{_H} \simeq 3\times 10^{-7}$ for the backscattering reflections in Si with $E_{_H} \simeq 15$ keV and the thermal expansion coefficient $\beta_{_H} = 2.65\cdot 10^{-6}$ K^{-1}, one obtains the following estimation $\delta T \ll 0.1$ K. Thus the accuracy of the temperature control should be in the mK range. In the experiments described in this report this was achieved by placing the crystals into ovens or cryostats. The technical design of an oven or of a cryostat was aimed at allowing temperature

homogeneity within a few mK. The temperature in the oven was stabilized with an accuracy of 1 mK by using computer control (Lucht 1998). A platinum resistor PT100 was used as a temperature sensor.

The ovens for the backscattering experiments were specially designed and built in the Institut für Experimentalphysik, Uni. Hamburg. It was possible to change the temperature from 285 to 470 K, and in a special case up to 800 K. The continuous flow cryostat (KONTI-cryostat for x-ray measurements, Kom. Nr.:5974) was designed specially for backscattering experiments by CryoVac[4] to access temperatures from 4 to 300 K.

Searching for back reflections

Finally, the crystal maintained at the required temperature should be adjusted in such a way that the reflecting atomic planes are normal, or nearly normal, to the incident beam. Very often the reflecting atomic planes are not parallel to the crystal surface. How then does one adjust the crystal? A typical situation which is encountered in the experiments is explained by the following example. Backscattering of the 14.4125 keV Mössbauer radiation from the $(1\ 3\ \overline{4}\ 28)$ atomic planes in an α-Al_2O_3 crystal is sought. The crystal plate is cut parallel to the (0 0 0 1) atomic planes.

At first the $[0\ 0\ 0\ 1]$ crystal axis is oriented parallel to the incident beam by detecting the exact back reflection (0 0 0 30) of x rays with energy E =14.315 keV (crystal at room temperature). For this, all photons are counted except those incident at $t \simeq -66$ ns, see Fig. 2.8. Then the $(1\ 3\ \overline{4}\ 28)$ atomic planes are set perpendicular to the incident beam by detecting the exact back reflection of the 14.4125 keV photons. It is known from the crystal structure that the angle ψ between the [0 0 0 1] and [1 3 $\bar{4}$ 28] directions is 22.091°. There are other 5 reciprocal vectors equivalent to [1 3 $\bar{4}$ 28]. They lie on the surface of a cone with opening angle ψ and rotation axis parallel to [0 0 0 1]. Back reflections corresponding to these reciprocal vectors are found easily by directing the incident beam at an angle of ψ to the [0 0 0 1] axis and by rotating the crystal around the [0 0 0 1] direction. The angular position of the crystal, at which it reflects these x rays back into the detector with maximum intensity, is taken as the reference point for exact backscattering - $\theta = \pi/2$ or $\delta\theta = 0$. The smaller the solid angle of the detector seen from the crystal the more exact the reference point can be determined. One can increase the precision by installing a pinhole straight after the detector or by increasing the flight path L.

[4]CryoVac Gesellschaft für Tieftemperaturtechnik mbH & Co. KG, D-53842 Troisdorf, Heuserweg 14, Germany.

At this stage of the adjustment procedure the Mössbauer photons generated in the iron foil do not necessarily fall into the energy band of the $(1\,3\,\overline{4}\,28)$ back reflection. As a next step the temperature of the crystal is scanned until the events within a time window of 20-120 ns are detected - Fig. 2.8. This signals that the crystal reflects Mössbauer photons backwards.

A similar procedure is used if the photons are monochromatized with a high energy resolution monochromator. Only the last step is different. Instead of tuning the crystal temperature the monochromator is tuned.

2.4 Experiments on exact Bragg backscattering

Bragg backscattering close to normal incidence, though not exactly at normal incidence, have been studied in numerous experiments starting from the pioneering work of Graeff and Materlik (1982). In almost all investigations Si or Ge single crystals were used. Cusatis et al. (1996) took advantage of the (1 1 1) reflection to study angular dependence of the *exact* Bragg backscattering with 1.9 keV x rays. The choice of this reflection was not accidental. Together with the other low-order (2 2 0) Bragg reflection, these are the only two reflections in Si and Ge and other crystals with the diamond structure which belong to the two-beam Bragg diffraction case. All other reflections belong to the multiple-beam reflection case, as discussed in the following sec. 2.4.3.

To avoid multiple-beam diffraction systematically, crystals possessing lower than cubic symmetry should be applied. Rhombohedral sapphire (α-Al_2O_3) single crystals are of this kind. In the present section the energy and angular dependence of Bragg reflectivity at normal incidence are studied by way of the example of α-Al_2O_3 single crystals. The results presented are based on the original publications of Shvyd'ko et al. (1998) and Shvyd'ko and Gerdau (1999) and on some unpublished material.

2.4.1 Temperature and angular dependence

The Bragg reflection from the $(1\ 3\ \overline{4}\ 28)$ atomic planes in α-Al_2O_3 was chosen. Exact backscattering of the ^{57}Fe 14.4125 keV Mössbauer radiation is predicted for this set of planes at a crystal temperature of $\simeq 372$ K. The extinction length is $d_e(0) = 37\ \mu$m. Sapphire crystals of 1 mm thickness were employed in the form of a 15 mm disk cut perpendicular to the axis $[0\ 0\ 0\ 1]$ [5]. The dislocation density in the crystals was typically about 10^3 cm^{-2}, see sec. 3.4.

A sapphire crystal was placed in the oven on a four-circle diffractometer at the end of the vacuum flight tube, Fig. 2.9a. The incident radiation was monochromatized by using nuclear resonant scattering from ^{57}Fe nuclei in the iron foil. As the photon energy was fixed, the variation of the photon energy was replaced by the variation of the sapphire crystal temperature. The APD was placed as close as possible to the incident beam. The deviation from exact backscattering in this geometrical arrangement can be chosen as small as 0.2 mrad, which in the present case is almost equivalent to exact backscattering since the widths of the measured angular dependence are typically 1 mrad.

[5] These particular crystals were obtained from ESCETE B.V. Single Crystal Technology, Schiffstraat 220, NL-7574 RD Enschede, the Netherlands.

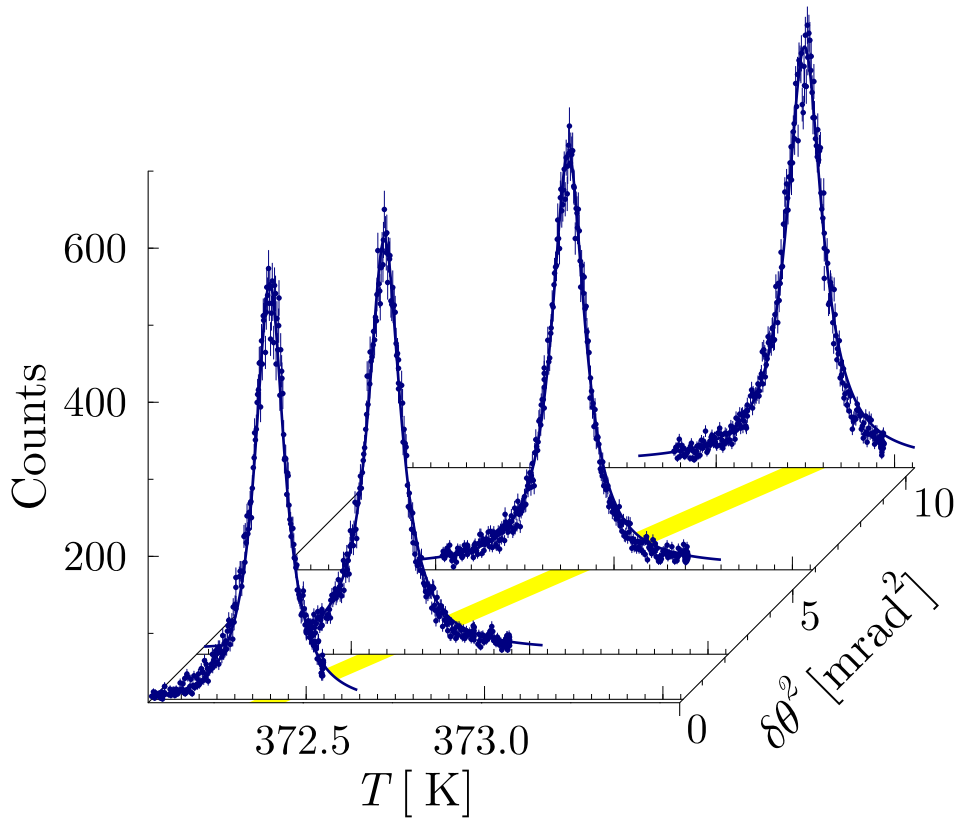

Figure 2.10: Temperature dependence of Bragg scattering of 14.4125 keV photons with 0.5 μeV bandwidth from an α-Al_2O_3 crystal measured at different angular deviations $\delta\theta$ from normal incidence to the $(1\,3\,\overline{4}\,28)$ reflecting planes. Solid lines are fits with Lorentzians. The width of the curve at $\delta\theta = 0.2$ mrad is 100 mK (equivalent to a 9.4 meV x-ray energy bandwidth).

Temperature dependence

Figure 2.10 shows temperature dependence of the reflectivity recorded at different angular deviations $\delta\theta$ from normal incidence to the $(1\,3\,\overline{4}\,28)$ planes.

At $\delta\theta = 0.2$ mrad (i.e. almost at normal incidence) the maximum reflectivity is achieved at $T_H = (372.40 \pm 0.01)$ K [6]. The width of the reflection curve is 100 mK corresponding to an energy width of $\simeq 9.4$ meV. This is more than the 5.9 meV expected theoretically.

With increasing $\delta\theta$ the temperature width changes insignificantly. This

[6]The temperature values given here are based on the calibration of the PT100 provided by the producer. With the PT100 sensor calibrated at Physikalisch-Technische Bundesanstalt (PTB) a slightly different value was measured - $T_H = 371.582(8)$ K, cf., sec. 4.6.

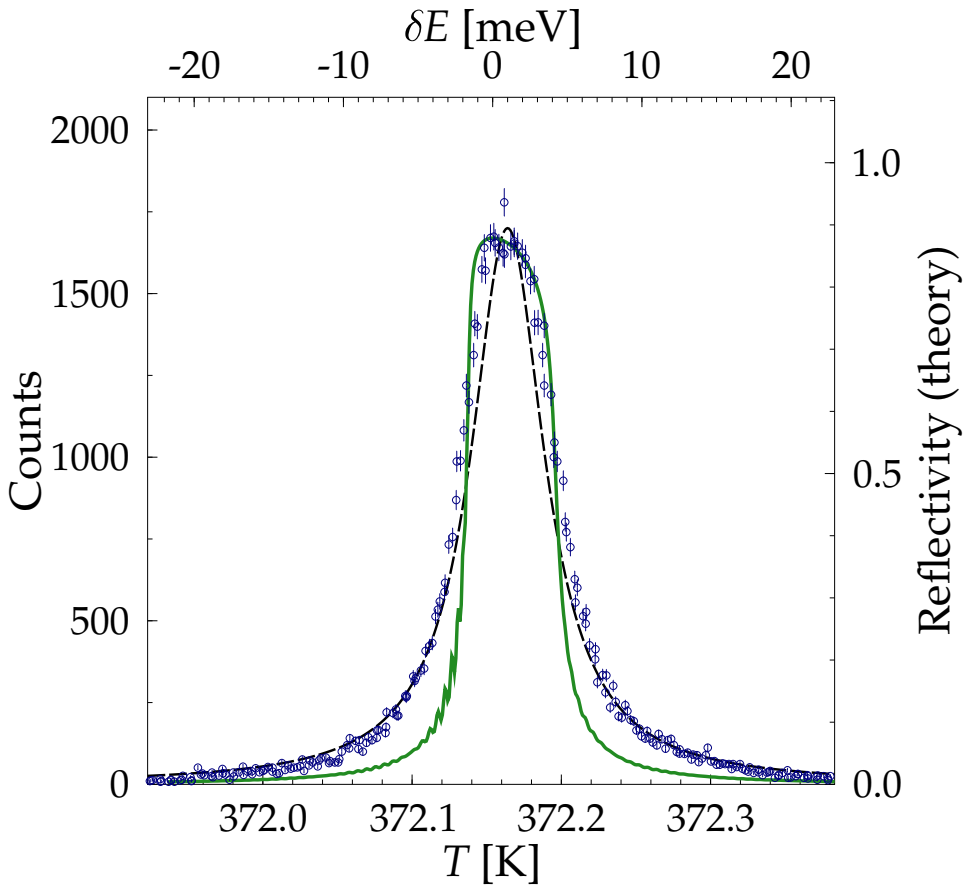

Figure 2.11: Reflectivity of α-Al_2O_3 (circles) vs. the crystal temperature T at almost exact backscattering ($\delta\theta = 0.2$ mrad). The upper scale is the photon energy variation equivalent to the temperature change. The solid line is the calculation according to the dynamical theory for an ideal crystal of α-Al_2O_3 1 mm thick and an incident monochromatic plane wave. The dashed line is a Lorentzian with a width of 6.2 meV.

agrees with the dynamical theory which predicts that for a given Bragg reflection the relative energy width, i.e., also the relative temperature width is a constant independent of incidence angle, see eqs. (2.84) and (2.86). This implies that $\Delta E \propto E$. By using Bragg's law one obtains $\Delta E \propto (\sin\theta)^{-1} = (1 + (\delta\theta)^2/2)^{-1}$ - a very weak angular dependence in agreement with the experiment.

The temperature dependence of almost exact backscattering was measured in sapphire single crystals grown in different ways. The width and the form of the temperature dependence served as a test of crystal quality. Czochralski

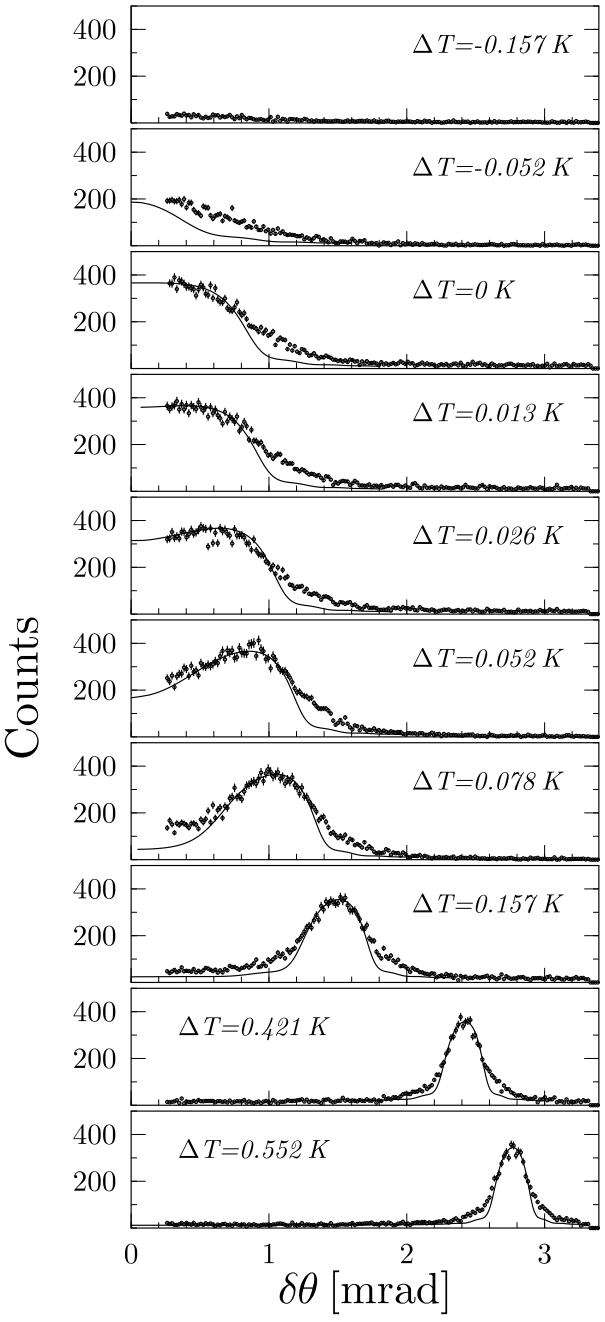

Figure 2.12: Angular dependence of Bragg backscattering of monochromatic 14.4125 keV x rays with 0.5 μeV bandwidth measured at different temperatures T of an α-Al_2O_3 crystal utilizing the $(1\,3\,\overline{4}\,28)$ reflection. $\delta\theta$ is the angular deviation from normal incidence of the x rays to the $(1\,3\,\overline{4}\,28)$ reflecting planes. $\Delta T = T - T_H$ where T_H=372.40 K. Solid lines are fits using the dynamical theory of Bragg diffraction.

grown crystals showed energy widths of typically about 40-50 meV. Sapphire crystals grown using heat-exchange method (HEM) (Schmid et al. 1994, Khattak and Schmid 2001) showed significantly narrower reflection curves with widths from 20 meV down to the nearly theoretical value of 6.2 meV, see Fig. 2.11. The factors influencing the energy width will be addressed in more details in sec. 3.4.

Yet another interesting feature can be observed in Fig. 2.10. With increasing $\delta\theta$ the peak reflectivity shifts to higher energies as $(\delta\theta)^2$. This square dependence is a property of backscattering. It has has a remarkable consequence, namely an extraordinarily large angular acceptance of the Bragg back reflections.

Angular dependence

Figure 2.12 shows the angular dependence of Bragg scattering of 14.4125 keV resonant radiation measured at different temperatures T of the same α-Al_2O_3 crystal. The angle $\delta\theta$ of deviation from normal incidence was varied in one direction from normal incidence. Because of the symmetry with respect to $\delta\theta = 0$ this is equivalent to a variation in any other direction.

Below T_H, i.e., at $T - T_H = \Delta T < 0$ Bragg scattering scarcely takes place. Approaching T_H Bragg scattering builds up with its maximum of reflectivity at $\delta\theta = 0$ and the largest angular width of 1.7 mrad at $\Delta T = 0$ (full width at half maximum). With a further increase of the temperature the peak reflectivity shifts off normal incidence, the rocking curve narrows, and gradually acquires the form known in conventional Bragg scattering. Nevertheless, the width of the Bragg reflection at $\delta\theta = 2.8$ mrad still has the extraordinarily large value of 0.24 mrad.

Peak reflectivity at normal incidence

The peak reflectivity is constant at different deviations $\delta\theta$ from normal incidence, see Fig. 2.12. To measure the absolute value of the peak reflectivity at normal incidence, a high energy resolution monochromator was installed, see Fig. 2.9(b). This reduces the flux without loss of 'good' photons to such a low level that it allows one to place the semitransparent detector into the incident beam. The iron foil in this measurement is placed upstream of the detector. Now, the time spectrum of nuclear forward scattering from the iron foil appears twice in the detector with a $2L/c$ separation in time. The ratio of the time integrated count rates of both time spectra gives the reflectivity of sapphire multiplied by the transmissivity of the detector. The transmissivity is

easily measurable. The reflectivity of the sapphire crystal for the 14.4125 keV nuclear resonant radiation is found to be 64%. This value applies to the sample used in the measurements shown in Fig. 2.10 and Fig. 2.12. This value is fairly close to the value of 87% calculated for perfect crystals.

Evaluation of data and discussion

Temperature dependence

All measured temperature dependences of backscattering can be fitted by Lorentzian curves (cf. Fig. 2.10) having a width larger than predicted for a perfect crystal. The only exception is the temperature dependence in Fig. 2.11. The width and the central part of the experimental curve fits well to the theoretical Darwin-Prins curve calculated with the dynamical diffraction theory. However, the tails tend to fit more closely to a Lorentzian.

The Lorentzian distribution which are observe cannot be caused by an energy or angular distribution of the incident beam, as our measurements were performed with almost monochromatic and well collimated x rays. This is an unusual line form which differs significantly from the Darwin-Prins curve predicted by the dynamical theory of diffraction in perfect crystals. Most probably the Lorentzian line shape is a result of crystal imperfections. As is shown in the next section, the reflectivity curves of the better quality crystals do not show this Lorentzian behaviour. Still, the challenge to theoretically account for the observed Lorentzian distribution remains.

Angular dependence

The results shown in Fig. 2.12 were compared with the angular dependence calculated by the dynamical theory. Certain assumptions were made to reproduce the observed broadening of the temperature and angular curves. A simplified model of crystal defects causing the broadening was used. It was assumed that the defects subdivide the crystal into blocks of finite but different thicknesses. The signals originating from different blocks were added incoherently. The thinner the block the broader is the partial reflectivity curve. It was found that the calculated angular dependence homogeneously averaged over block thicknesses in the range from 0 to $d = 140$ μm describe satisfactorily the experimental results shown by the solid lines in Fig. 2.12. Still, the fit is not perfect and the tails of the experimental dependence decay more slowly than those of the theoretical curves.

The following parameters were used in the calculations: $E = 14.4125$ keV, $\chi_0 = (-78.4 + \mathrm{i}\, 0.29) \times 10^{-7}$, $\chi_H = (-4.04 + \mathrm{i}\, 0.13) \times 10^{-7}$, $b = -1$.

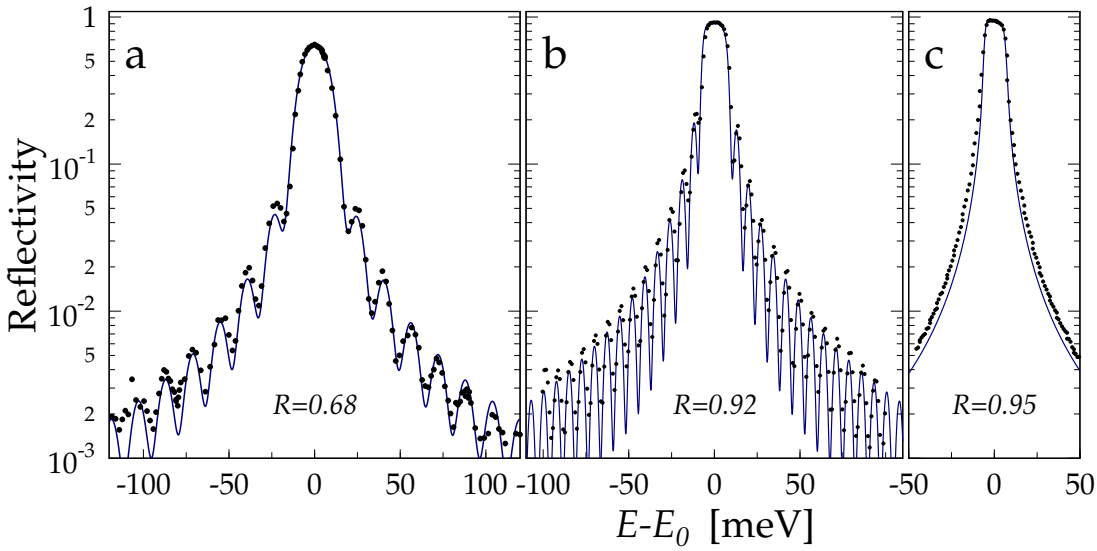

Figure 2.13: Bragg reflectivity vs x-ray energy E of parallel-sided α-Al_2O_3 crystals of different thicknesses: (a) $d = 0.039$ mm , (b) $d = 0.084$ mm, and , (c) $d = 2.5$ mm. X rays are at normal incidence to the $(0\ 0\ 0\ 30)$ atomic planes, $E_0 = 14.315$ keV. Solid lines are dynamical theory calculations for the incident plane wave packet with an energy bandwidth of (a) 6 meV and (b-c) 2 meV.

2.4.2 Energy and thickness dependence

In the following examples the energy dependence of reflectivity under exact Bragg backscattering conditions were studied in α-Al_2O_3 crystals of different thickness. The $(0\ 0\ 0\ 30)$ back reflection was used. Its Bragg energy is $E_H = 14.315$ keV at T=295 K. The expected peak reflectivity for a thick crystal is 95%, the energy width $\Delta E = 13.1$ meV, and the extinction length $d_e(0) = 16\ \mu$m. The dynamical theory calculations for this Bragg reflection in thin and thick crystals are shown in Figs. 2.4 and 2.5, respectively.

To measure the energy dependence, the nested monochromator was employed - see Fig. 2.9b - which provides photons with a 7 meV bandwidth. The HEM sapphire crystals with low dislocation density were used, see sec. 3.4. Figure 2.13 shows the energy dependence of reflectivity under exact Bragg backscattering conditions. The thicknesses of the samples used to measure the reflectivity curves in panels (a), (b) and (c) were $0.039(1)$, $0.055(1)$, and 2.5 mm, respectively. The first two values were obtained by theoretical fits of the measured reflectivity curves. The measured peak reflectivities are 0.68, 0.83 and 0.86, respectively.

The experimental results show that the thicker the crystal the higher the

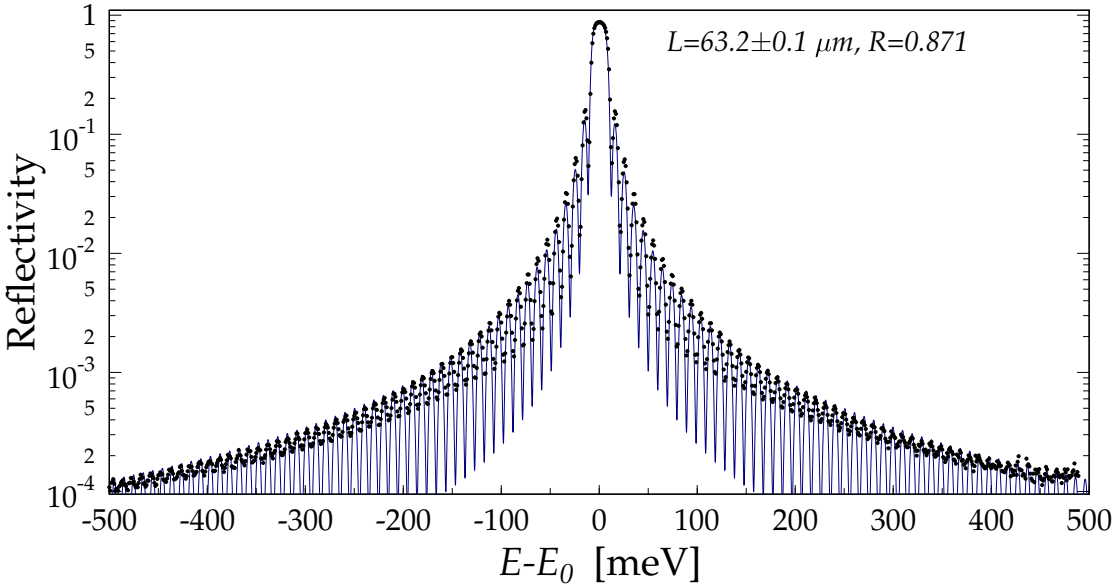

Figure 2.14: Bragg reflectivity vs x-ray energy E of parallel-sided α-Al_2O_3 crystal of a thicknesses $d = 0.063$ mm. X rays are at normal incidence to the $(0\ 0\ 0\ 30)$ atomic planes, $E_0 = 14.315$ keV. Solid line is a dynamical theory calculation for the incident plane wave packet with an energy bandwidth of 2 meV.

peak reflectivity R and the smaller is the energy width observed. This observation agrees with the dynamical theory calculations. The only disagreement observed is for the peak reflectivity of the thickest crystal, which is measured to be 10% smaller than the theoretical value. This can be attributed to the fact that the bandwidth of the incident photons is too broad compared with the energy width of the reflection curve.

Another remarkable feature observed in Fig. 2.13a and 2.13b is the intensity oscillations in the tails of the reflection curves. The thicker the sample, the shorter is the period of these oscillations. In Fig. 2.13b they are less pronounced than in Fig. 2.13a since the period of oscillations becomes comparable with the bandwidth of the monochromator. On the right tail of Fig. 2.13b they are hardly visible at all. The latter could be due to residual crystal defects. No oscillations can be resolved on the reflection curve of the 2.5 mm thick crystal. All these observations are in a good agreement with the dynamical theory calculations for perfect crystals.

As was mentioned in sec. 2.2.4, the intensity oscillations on the tails of the Bragg reflection curves are due to the interference of the radiation fields

reflected from the front and rear surfaces of a parallel sided crystal. They can be refered to as "thickness" oscillations. The thickness of the samples can be directly determined with eq. (2.102) from the period of oscillations δE as $d = hc/2\delta E(1 + w)$. Alternatively, an absolute energy calibration of the monochromator can be performed if the crystal thickness is known.

The thickness oscillations have been observed earlier for the angular dependence of the Bragg reflection curves by Batterman and Hilderbrandt (1967) and Batterman and Hilderbrandt (1968). They have been observed as a function of crystal thickness by Hashizume et al. (1970) and compared with the dynamical theory by Wilkins (1978). These oscillations should not be mixed up with those originating from the Pendellösung effect, which takes place in the Laue-scattering geometry, see, e.g., (Pinsker 1978). The oscillating angular dependence of Laue-case rocking curves has been used by Teworte and Bonse (1983) and Deutsch and Hart (1985) for very precise determination of the structure factors F_H of silicon.

The thickness oscillations are observed both on the energy (wavelength) and the angular scale. According to eqs. (2.95)-(2.97), they are described universally via the α parameter which contains both the energy (wavelength) and angular variables. With todays technology, angular measurements are extremely precise. The aforementioned universality could be therefore employed to carry out very precise wavelength calibrations of monochromators or wavelength-meters. To do so, the Bragg reflectivity curve should be measured twice. First - as a function of incidence angle $\delta\theta$, and second - as a function of x-ray wavelength λ. These curves could be translated one into another by using eqs. (2.96)-(2.97) and thus the relative wavelength (energy) scale calibration could be performed. If the Bragg energy is known the relative calibration could be converted to the absolute one. The backscattering geometry is most favorable for such measurements, due to the $(\delta\theta)^2$ stretching of the angular scale.

In summary, the results of the present section demonstrate that sapphire single crystals can be used as normal incidence mirrors of high reflectivity.

2.4.3 Multiple-beam effects in Bragg backscattering

As was originally pointed out by Steyerl and Steinhauser (1979), for crystals with the diamond structure, e.g. Si, Ge, etc., and for the exact backscattering condition, parasitic reflections occur for all allowed orders of reflection. There are only two reflections which are not influenced by multiple beam diffraction. These are the (1 1 1) and (2 2 0) reflections.

For crystals with cubic symmetry the following rule is observed. The wave vector $\boldsymbol{K}_0$ of the incident radiation fulfilling Bragg's condition for backscattering with diffraction vector $\boldsymbol{H}$ always originates at an intersection of facets of one of the Brillouin zones of the reciprocal lattice – Fig. 2.15. The intersection point is marked with P in Fig. 2.15. As a result, the condition for Bragg scattering is automatically fulfilled for other diffraction vectors $\boldsymbol{G}$, $\boldsymbol{F}$, etc, which are perpendicular to those facets of the Brillouin zone crossing at P. Scattering chan-

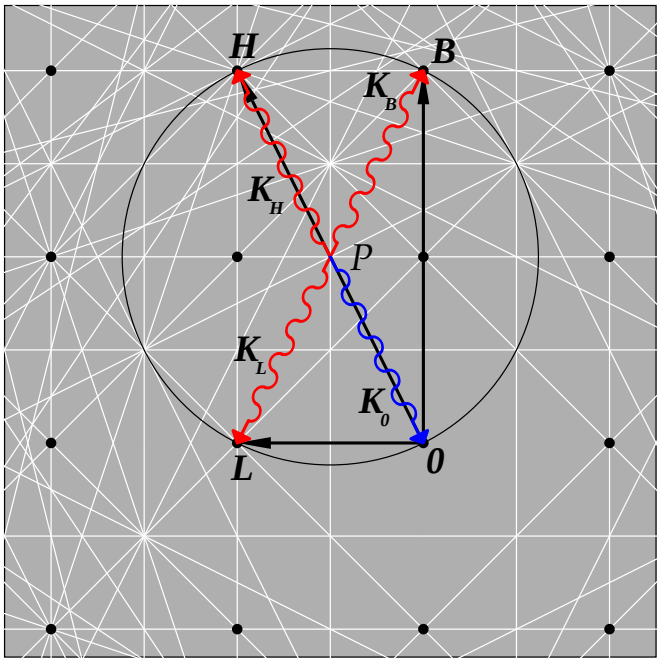

Figure 2.15: Multiple-beam effects in Bragg backscattering from a two-dimensional square lattice. $\boldsymbol{H}$, $\boldsymbol{G}$, $\boldsymbol{F}$ are reciprocal lattice vectors. The white lines are perpendicular bisectors of the reciprocal lattice vectors, which compose the Brillouin zones. $\boldsymbol{K}_0$ is the wave vector of the incident radiation fulfilling Bragg's condition for backscattering with diffraction vector $\boldsymbol{H}$: $\boldsymbol{K}_H = -\boldsymbol{K}_0 = \boldsymbol{H}/2$. Scattering channels are open not only with wave vector $\boldsymbol{K}_H$ but also with wave vectors $\boldsymbol{K}_G$ and $\boldsymbol{K}_F$.

nels become open not only for the back reflected radiation with wave vector $\boldsymbol{K}_H = -\boldsymbol{K}_0 = \boldsymbol{H}/2$, but also for the radiation with wave vectors $\boldsymbol{K}_G = \boldsymbol{K}_0 + \boldsymbol{G}$, $\boldsymbol{K}_F = \boldsymbol{K}_0 + \boldsymbol{F}$, etc. In crystals with cubic symmetry, exact backscattering thus co-exists with multiple beam Bragg scattering.

This particular case can be generalized to any reciprocal lattice. To discuss this point, we shall use the kinematical approximation. By using the kinematical Bragg law in vector form $2\boldsymbol{K}_0\boldsymbol{G} + \boldsymbol{G}^2 = 0$, as given by eq. (2.63), and the Bragg backscattering condition $\boldsymbol{K}_0 = -\boldsymbol{H}/2$, one can find the following relation between the diffraction vector $\boldsymbol{H}$ for the back reflection and the diffraction vector $\boldsymbol{G}$ for the accompanying parasitic reflection

$$\boldsymbol{G}\boldsymbol{H} = \boldsymbol{G}^2. \tag{2.107}$$

The relation is valid in the kinematical approximation for any reciprocal lattice. It is still an open question, whether for a certain vector $\boldsymbol{H}$ there exist any vector $\boldsymbol{G}$ fulfilling (2.107). However, if a such vector exists, relation (2.107) implies that the vectors $\boldsymbol{H}$, $\boldsymbol{G}$, and $\boldsymbol{H} - \boldsymbol{G}$ compose a right-angle triangle with a right angle between the vectors $\boldsymbol{G}$, and $\boldsymbol{H} - \boldsymbol{G}$ as illustrated in Fig. 2.15. Moreover, if the relation (2.107) is valid for the vectors $\boldsymbol{H}$ and $\boldsymbol{G}$, a similar relation $\boldsymbol{F}\boldsymbol{H} = \boldsymbol{F}^2$ is valid for the reciprocal vector $\boldsymbol{F} = \boldsymbol{H} - \boldsymbol{G}$. Thus, if a back reflection with diffraction vector $\boldsymbol{H}$ is accompanied by a parasitic reflection with diffraction vector $\boldsymbol{G}$, it is also accompanied by the parasitic reflection with diffraction vector

$$\boldsymbol{F} = \boldsymbol{H} - \boldsymbol{G}. \tag{2.108}$$

Such "conjugate pairs" of the parasitic reflections were discussed by Sutter (2000) for a particular case of normal incidence to the (12 4 0) planes in Si. Our analysis shows that this is a general property independent of the reflection and crystal symmetry.

Parasitic reflections appear always in conjugate pairs, whereas the vectors $\boldsymbol{H}$, $\boldsymbol{G}$, and $\boldsymbol{F}$ compose a right-angle triangle. The latter implies that the parasitic reflections appear systematically in rectangular reciprocal lattices. However, they can also appear in non-rectangular reciprocal lattices, if a rectangular lattice occurs as a sublattice. Such a case is shown in Fig. 2.16 by example of a hexagonal lattice.

By using eq. (2.108) and the relations $\boldsymbol{K}_G = \boldsymbol{K}_0 + \boldsymbol{G}$, $\boldsymbol{K}_F = \boldsymbol{K}_0 + \boldsymbol{F}$ one readily obtains

$$\boldsymbol{K}_G = -\boldsymbol{K}_F. \tag{2.109}$$

The wave vectors $\boldsymbol{K}_G$ and $\boldsymbol{K}_F$ are exactly opposite to each other. In other words, the radiation waves in the "parasitic" channels propagate in opposite

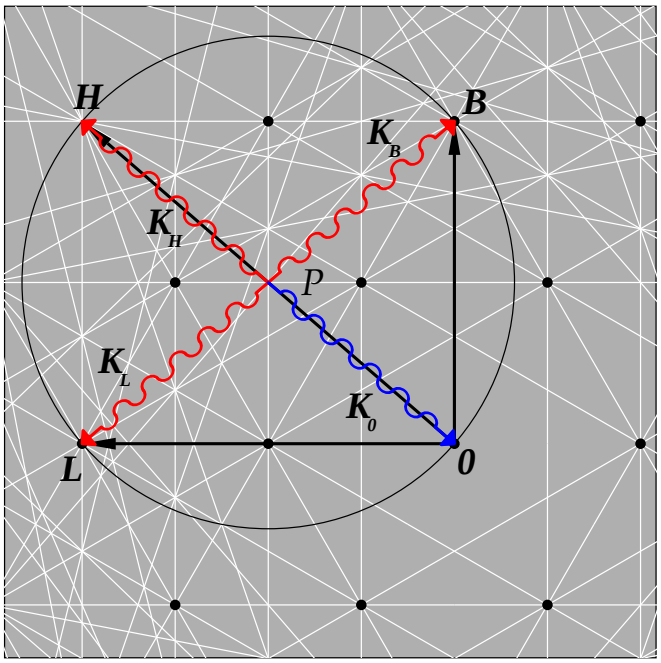

Figure 2.16: Multiple-beam effects in Bragg backscattering from a hexagonal lattice. Notations as in Fig. 2.15.

directions. This is also clearly seen in Figs. 2.15 and 2.16. This property could be used to generate coherent photons propagating in opposite directions.

One can ascertain numerically by using eq. (2.107) whether for a given back reflection with diffraction vector $\boldsymbol{H}$ there exist any parasitic reflections with diffraction vector $\boldsymbol{G}$. For example, for the (12 4 0) back reflection in Si, another 22 reflections are allowed simultaneously: (0 2 2), (0 4 0), (4 2 6), (4 8 0), (6 0 6), (8 8 0) etc. Thus, approaching normal incidence to the (12 4 0) planes, new reflection channels for x rays open up. One expects a reduced reflectivity in the backscattering channel and a complicated energy dependence.

The results of studies of Bragg scattering at normal incidence to the $(12\ 4\ 0)$ atomic planes are shown in Figs. 2.17 and 2.18 (Shvyd'ko and Gerdau 1999). The x rays are monochromatized to an energy bandwidth of 7 meV and scanned about $E_0 \simeq 14.438$ keV by using the high energy resolution monochromator as shown in Fig. 2.9b.

The two-dimensional angular dependence shown in Fig. 2.17 and a one-dimensional angular dependence measured at $\delta\chi = 0$ shown in Fig. 2.18 demonstrate a mrad-broad region of high reflectivity which collapses while approaching normal incidence. The angular range of low reflectivity is ± 0.2 mrad.

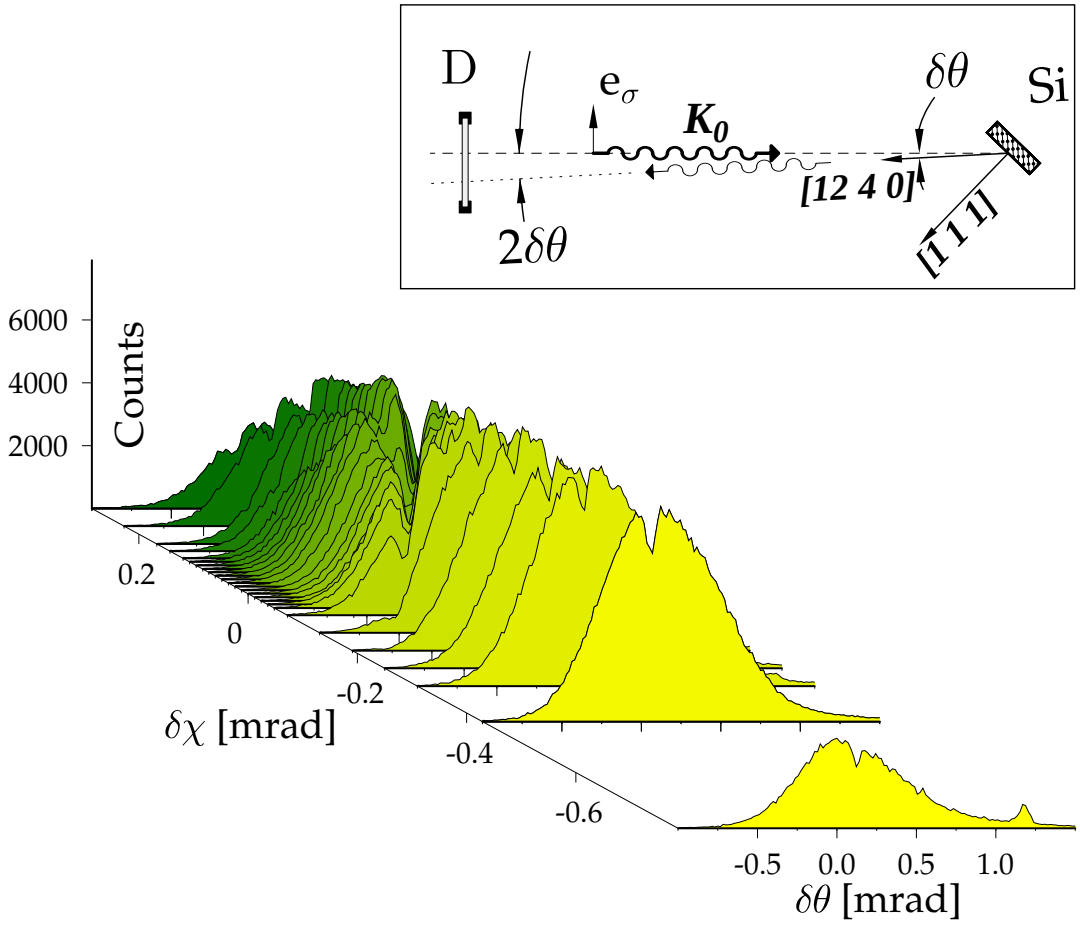

Figure 2.17: Two-dimensional angular dependence of the reflectivity of a Si single crystal for incoming x rays close to normal incidence to the (12 4 0) atomic planes and a schematic of the experimental setup for its observation (see inset). The angular divergence of the x rays is $\simeq 20 \times 20$ μrad^2. $\delta\theta$ and $\delta\chi$ are deviations from normal incidence to $(12\,4\,0)$ in the $[1\,1\,1], [12\,4\,0]$ plane and in the plane perpendicular to it, respectively. The x rays are monochromatized to an energy band of 7 meV width. The semitransparent detector D is placed at a distance of 0.8 m from the Si crystal.

The reflectivity at normal incidence is about half of its maximum value at $\delta\theta \simeq 0.2$ mrad. The effect becomes even more pronounced if it is observed by using incident radiation with a smaller bandwidth. Sutter et al. (2001) have observed nearly zero reflectivity at normal incidence of x rays with 2 meV bandwidth.

In addition, while approaching normal incidence the energy dependence of the reflectivity experiences dramatic changes. At 0.2 mrad off normal in-

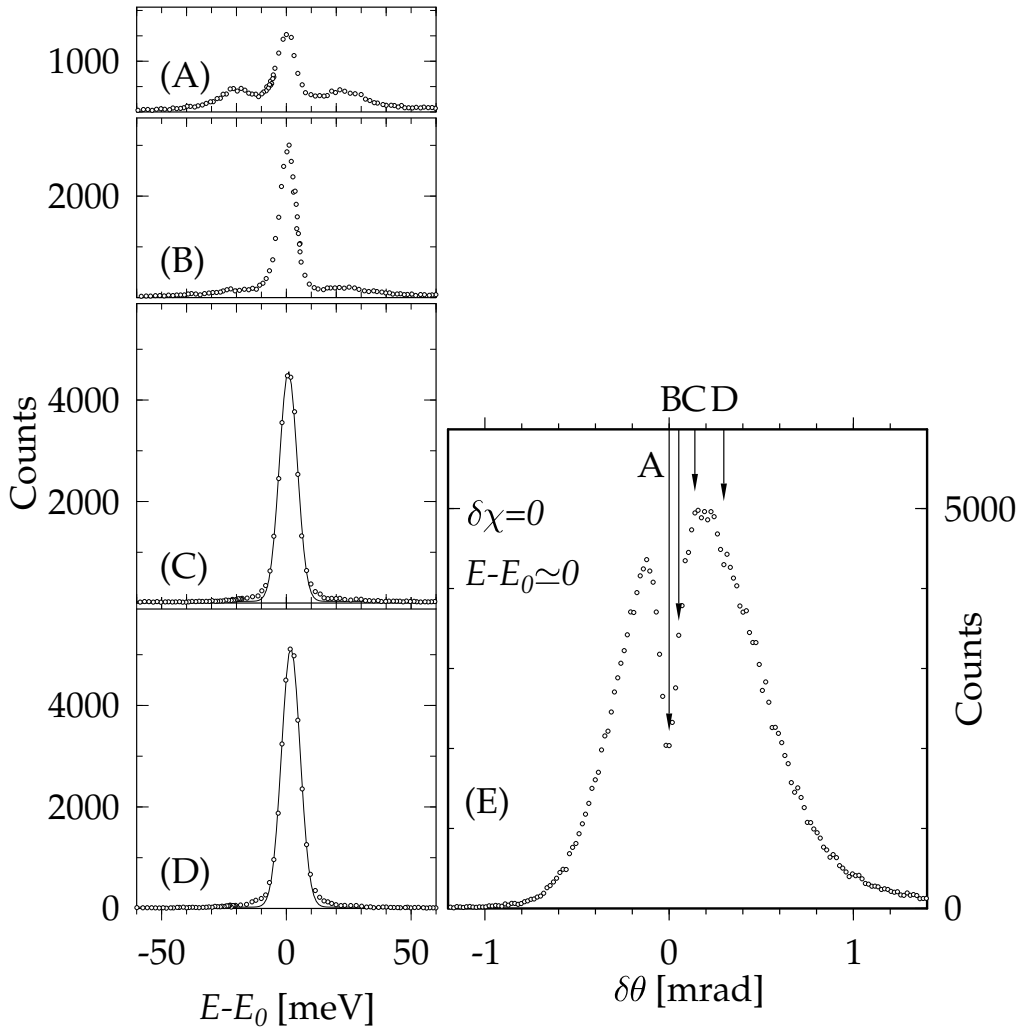

Figure 2.18: Energy (A),(B),(C),(D) and angular (E) dependence of the reflectivity of a Si single crystal for incoming x rays close to normal incidence to the (12 4 0) atomic planes with $\delta\chi = 0$. A,B,C and D in (E) mark the $\delta\theta$ angular positions at which the energy spectra (A),(B),(C) and (D) are measured. Solid lines in (C) and (D) are fits with 8.5 meV broad Gaussians.

cidence the energy dependence shows a few meV-wide narrow single peak, Fig. 2.18(D). At normal incidence the spectrum changes drastically and displays a triple peak structure, Fig. 2.18(A), which is most probable due to multiple-beam diffraction.

This very interesting mode of Bragg scattering deserves comprehensive experimental and theoretical studies of its own. However, they are beyond the scope of this report. Theoretical studies of the Si(9 9 1) backscattering case

were presented by Kohn et al. (1999). Comprehensive experimental and theoretical studies by examining the Si(12 4 0) backscattering case were presented by Sutter (2000) and Sutter et al. (2001).

One should note additionally that a similar drastic suppression of reflectivity have been observed also in experiments for the (777), (991) and (975) Bragg back reflections in Si. These results definitively suggest that Si single crystals are not suitable for normal incidence x-ray mirrors because of their low reflectivity. A recent attempt by Liss et al. (2000) to build an x-ray resonator consisting of silicon mirrors by using the (888) Bragg back reflection confirms this statement as well. After the first two bounces most of the incident radiation, i.e., $\simeq 99.9\%$ according to Fig. 3 of Liss et al. (2000), disappears in side channels.

Chapter 3

Normal incidence x-ray mirrors

In the present chapter we address practical issues of selecting materials for elements of Bragg back-reflection optics. It will be shown that sapphire (α-Al_2O_3) crystals are advantageous for this role. Sapphire crystals are presumed to play an important part in the role of normal incidence mirrors for x-ray resonators, high energy resolution monochromators and analyzers with meV and μeV bandpasses. The quality of commercially available sapphire is also assessed.

3.1 Why not perfect Si?

Among commercially available single crystals those manufactured of Si have the highest quality. Their use in high resolution crystal x-ray optics is well established. It turns out that for Bragg reflection optics at normal incidence hexagonal crystals Be, BeO, rhombohedral α-Al_2O_3 (sapphire), hexagonal or rhombohedral polytypes of silicon carbide (4H-SiC, 6H-SiC, 15R-SiC, etc) are a better choice. There are several reasons for this.

The main reason is the suppression of reflectivity at normal incidence because of multiple-beam diffraction, as discussed in sec. 2.4.3. However, there exists another reason why Si or any other crystal with a diamond structure, e.g., C, Ge, GaAs, etc., is not so favorable for this role.

First, it is difficult to find Bragg energies in these crystals matching the chosen x-ray energy. In crystals with a cubic unit cell the interplanar distance is

$$d_{_H} = \frac{a}{\sqrt{h^2 + k^2 + l^2}}, \tag{3.1}$$

where a is the lattice constant, and h, k, l are Miller indices. It is easy to see that the same value of $d_{_H}$ and accordingly the same Bragg energy $E_{_H} = hc/d_{_H}$ can

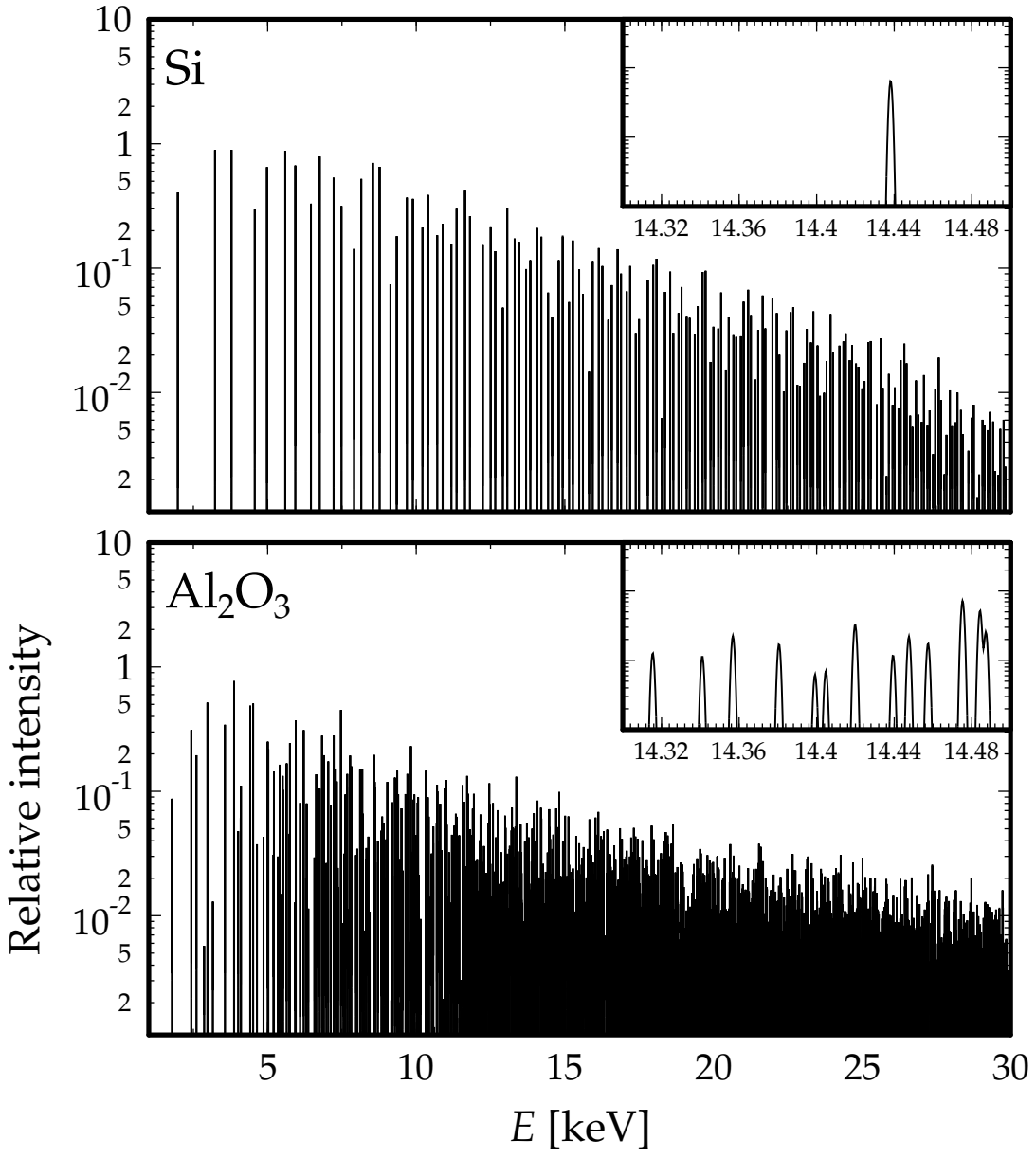

Figure 3.1: Bragg backscattering spectra of Si and α-Al_2O_3 single crystals. Calculations are performed by the dynamical theory of diffraction for single crystal plates of 1 mm thickness. The height and width of the peaks result from the convolution of the energy profile of the theoretical reflectivity curve with the energy profile of the incident radiation, which is assumed to be 2 eV broad. Peaks corresponding to n-times degenerate Bragg energies are taken to have n-times greater height. The insets show expanded spectra in the range 14.3-14.5 keV.

belong to reflections with different Miller indices. The Bragg energies in cubic crystals are therefore highly degenerate and the number of different Bragg energies is rather low. Typically there is only one Bragg energy per $\simeq 500-250$ eV interval in the range $10-25$ keV. This is illustrated in Fig. 3.1(Si), which shows the spectrum of Bragg energies in Si. A measured backscattering spectrum will be presented in sec. 4.7, Fig. 4.9. Matching an x-ray energy to the nearest Bragg energy is equivalent to tuning of the lattice constant which for practical reasons means a variation of the temperature. The temperature expansion coefficient in Si at room temperature is $\beta_{_H} = 2.65 \cdot 10^{-6}$ K^{-1}. Thus, $\mathrm{d}E_{_H}/\mathrm{d}T = 0.038$ eV/K for $E_{_H} \simeq 15$ keV. To shift $E_{_H}$ by 100 eV, the temperature would have to be changed by an unrealistic 2600 K. Therefore, one can conclude that Si single crystals allow backscattering only in limited regions of the x-ray spectrum.

Secondly, their relatively low reflectivity hampers further the application of Si crystals as backscattering mirrors. Peak reflectivity of all allowed Bragg back reflections exceeding the 10% level in Si with Bragg energies $E_{_H}$ in the range from 0 to 50 keV are shown in Fig. 3.2(Si). The upper left panel shows the results of calculations at crystal temperature $T = 295$ K. Two distinctly separate sets of points represent even (higher points) and odd (lower points) reflections. It is clearly seen that a reflectivity of more than 90% is achievable at room temperature for x-rays only in the range from 3 to 8 keV.

Calculations were performed for crystal parameters at $T = 295$ K using dynamical theory. The crystals were assumed to be infinitely thick. The B-factor in the expression for the Debye-Waller factor (2.7) was taken to be 0.4632 Å^2 (Deutsch and Hart 1985). This value corresponds to a Debye temperature of $\Theta_{\mathrm{D}} = 530$ K. The low reflectivity at high energies, i.e. for reflections with small interplanar distance $d_{_H}$ is a consequence of the relatively large B-factor. The latter physically corresponds to large amplitudes of thermal vibrations in Si. The crystal is too "soft". One could partly improve the situation by cooling the crystal. This is demonstrated by the results of calculations at crystal temperature $T = 4$ K in the upper right panel of Fig. 3.2(Si).

3.2 Non-cubic α-Al_2O_3.

These aforementioned problems can be circumvented by choosing crystals i) with lower crystal symmetry, ii) with higher Debye temperature and iii) with low photo-absorption. Hexagonal Be, BeO or rhombohedral sapphire (α-Al_2O_3) crystals, hexagonal and rhombohedral polytypes of silicon carbide (4H-SiC, 6H-SiC, 15R-SiC, etc) are the materials of choice. In the following,

we shall discuss the properties of sapphire, since the quality of commercially available sapphire crystals is the best of these materials.

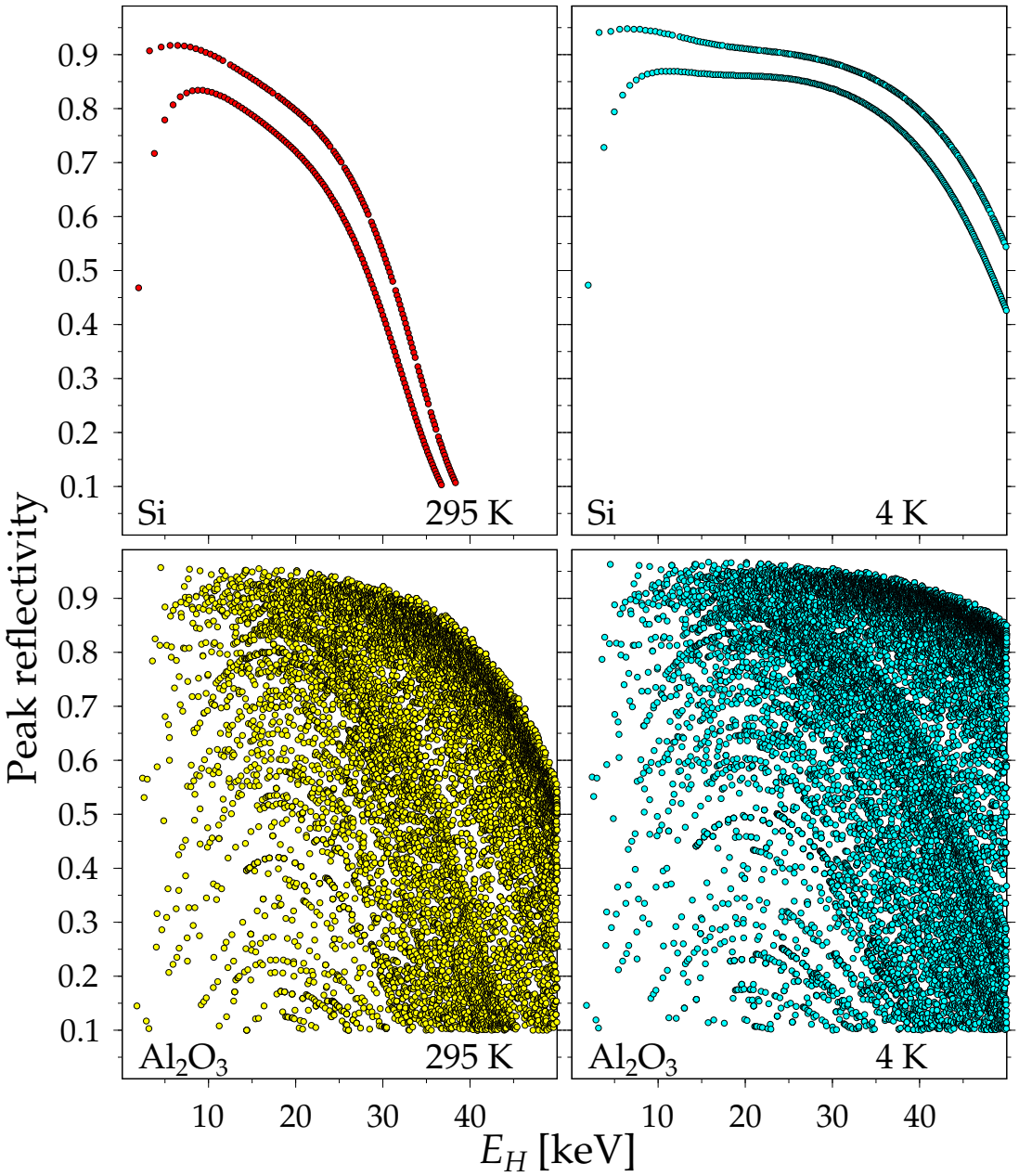

Figure 3.2: Peak reflectivity of Bragg back reflections in Si (upper panels) and in α-Al_2O_3 (lower panels) at $T = 295$ K (left) and at $T = 4$ K (right), respectively. All allowed reflections are shown with Bragg energies E_H in the range from 0 to 50 keV and reflectivity exceeding 10%.

Sapphire (α-Al_2O_3) has a rhombohedral crystal lattice and belongs to the space group $R\overline{3}c$ (D^6_{3d}) (No. 167). It is usually specified with hexagonal axes of reference $\boldsymbol{a}$, $\boldsymbol{b}$, $\boldsymbol{c}$, where the $\boldsymbol{c}$-axis is directed along the 3-fold symmetry axis, see, e.g., (Burns and Glazer 1978). There are two independent lattice constants a and c ($a = b$). For convenience, one uses four Miller indices $(hkil)$, to specify atomic planes in the hexagonal basis, where the additional index i is redundant and is given by: $i = -(h + k)$. The interplanar distance in a hexagonal lattice is given by:

$$d_{_H} = \frac{ac}{\sqrt{4c^2\left(h^2 + k^2 + hk\right)/3 + a^2l^2}}. \tag{3.2}$$

The interplanar distances $d_{_H}$ and hence Bragg energies $E_{_H} = hc/d_{_H}$ are much less degenerate in the rhombohedral lattice (of α-Al_2O_3) than in the cubic lattice (of Si). Sapphire single crystals allow exact backscattering with a density of reflections of at least one per $\simeq$ 15 eV in the range $10 - 25$ keV and even more often for harder x rays, see Fig. 3.1(Al_2O_3). A measured backscattering spectrum is presented and discussed in sec. 4.7, Fig. 4.10. By heating or cooling α-Al_2O_3 by no more than 100 K from room temperature one can fulfil the backscattering condition for any x-ray energy above 10 keV.

As was already discussed in sec. 2.4.1, there are much less systematic problems with multiple-beam diffraction and consequently with suppression of reflectivity at normal incidence in non-cubic sapphire crystals. There exist many more two-beam Bragg back diffraction cases in α-Al_2O_3 than in Si.

Peak reflectivity of all allowed Bragg back reflections exceeding the 10% level in α-Al_2O_3 with Bragg energies $E_{_H}$ in the range from 0 to 50 keV are shown in Fig. 3.2(Al_2O_3). The left panel shows the results of calculations at a crystal temperature $T = 295$ K. Calculations were performed by using the dynamical theory for an infinitely thick crystal. Crystal parameters (coordinates of atoms, thermal parameters, lattice constants) were used based on single crystal measurements of Kirfel and Eichhorn (1990) at room temperature. Similar crystal parameters were reported also by Brown et al. (1992) based on powder diffraction measurements. The anisotropy of the thermal parameters in α-Al_2O_3 is small (Kirfel and Eichhorn 1990, Brown et al. 1992). As a result, to a fairly good approximation the B-values in eq. (2.7) could be taken as isotropic with $B_{\rm Al} = 0.195$ Å^2, $B_{\rm O} = 0.274$ Å^2. These values were used to calculate the Debye-Waller factors at room temperature. By using these values, the effective Debye temperatures can also be estimated for the sub-lattice of aluminum atoms $\Theta_{\rm D}({\rm Al}) = 890$ K, and for the sub-lattice of oxygen atoms $\Theta_{\rm D}({\rm O}) = 995$ K. These temperatures will be used in the subsequent considerations to extrapolate the Debye-Waller factors to other temperatures in the

framework of the Debye model (Ziman 1969).

The energy dependent parts of the structure factor - eqs. (2.5)-(2.6) - were calculated for α-Al_2O_3 with f'_n and f''_n obtained from the library of anomalous scattering factors (Kissel and Pratt 1990, Kissel et al. 1995).

Reflections with a peak reflectivity of more than 90% are observed in a broad range from 5 to 35 keV. For Si this is not possible even at $T = 4$ K. The much higher peak reflectivity is first of all due to the smaller amplitudes of thermal vibration in α-Al_2O_3. The crystal lattice of α-Al_2O_3 is much more rigid than that of Si. At 4 K the high reflectivity range extends even more up to 45 keV, as can be seen in the right panel of Fig. 3.2(Al_2O_3).

Figure 3.3 shows the energy width ΔE of Bragg back reflections in Si (upper panel) and in α-Al_2O_3 (lower panel). All allowed reflections are shown with Bragg energies E_H in the range from 0 to 50 keV and peak reflectivities exceeding 10%. The plots of the energy widths demonstrate another advantage of α-Al_2O_3crystals. For a given Bragg energy E_H, they offer reflections with energy widths both larger and smaller than those of the Si crystals. The choice of reflections in α-Al_2O_3 is more versatile, which makes it easier to find the right one for a certain application. This property is due to strong structure factor variations resulting from the more complicated structure of α-Al_2O_3.

All the aforementioned facts confirm that sapphire single crystals are more attractive for x-ray crystal optics applications than Si crystals. Higher reflectivity values can be achieved over a broad spectral range. It is easy to match Bragg energies and desired x-ray energies. These crystals offer more versatile properties, such as higher tunability of energy widths of the Bragg back reflections. Sapphire could be considered as a new material with great potential for x-ray crystal optics, especially attractive for Bragg backscattering mirrors of x-ray resonators, high energy resolution monochromators and analyzers.

There are also drawbacks to α-Al_2O_3. The most serious one is the insufficient perfection of commercially available crystals. The quality is inferior to that of Si crystals. However, one should not regard the situation too pessimisticly. Industrial society's dependence on solid-state microelectronics advances not only semiconductor technology. Sapphire crystals are of great importance in modern optics and microelectronics. Sapphire is widely used in scientific, industrial, and military applications as an excellent optical material (Schmid et al. 1994, Khattak and Schmid 2001). In the microelectronics industry, sapphire is a widely used substrate material for epitaxial growth, for example, in blue laser and light emitting diode technologies (Ambacher 1998). Crystal growth techniques are also improving steadily. However at present, applications of α-Al_2O_3 in x-ray crystal optics would still require careful in-

spection and selection of samples. In sec. 3.4 we address techniques of quality

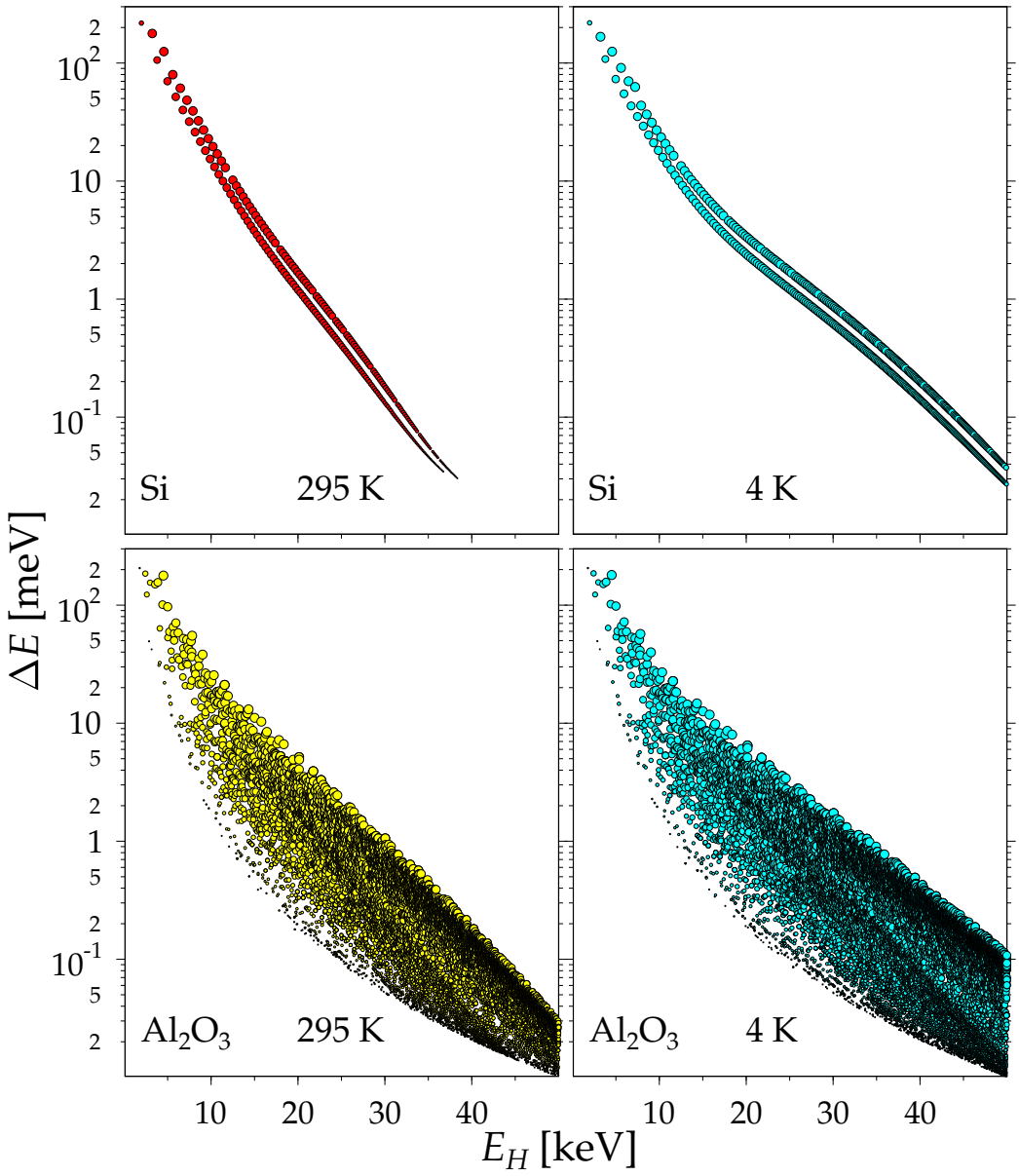

Figure 3.3: Energy width ΔE of Bragg back reflections in Si (upper panels) and in α-Al_2O_3 (lower panels) at $T = 295$ K (left) and at $T = 4$ K (right), respectively. All allowed reflections are shown with Bragg energies E_H in the range from 0 to 50 keV and reflectivity larger than 10%. The diameter of each point is proportional to the peak reflectivity of the corresponding back reflection. The smallest point corresponds to a reflectivity of 10% and the largest to 95%.

assessment adequate for applications of sapphire crystals in x-ray optics.

Another problem is that the crystal data for α-Al_2O_3 are not well known. In particular, predictions of the Bragg energies are greatly hampered by the lack of precise data on the crystal lattice constants in α-Al_2O_3 at different temperatures. To improve the situation, we have performed $\lesssim 1$ ppm-precise measurements of crystal lattice parameters in α-Al_2O_3. The results are presented in sec. 4.5.

3.3 α-Al_2O_3 as a universal meV-monochromator

In the previous section it was argued that α-Al_2O_3 single crystals offer a greater diversity of possibilities compared to Si crystals. According to Fig. 3.1 it should be easy to find a matching Bragg back reflection in α-Al_2O_3 for any desired x-ray energy above 10 keV. The back reflections select x rays with a very small energy bandwidth – see Fig. 3.3. To select photons with narrow bandwidth, one has not necessarily use exact backscattering. But to render simultaneously significant angular acceptance, especially at high x-ray energies, one has to use exact backscattering. With a single α-Al_2O_3 crystal in backscattering geometry one could access practically continuously different photon energies (by changing Bragg back reflections and crystal temperature) and select photons with a narrow spectral bandwidth. Thus, a single sapphire single crystal could serve as a universal high energy resolution monochromator with large angular acceptance tunable over a broad energy range. Such a monochromator would be extremely useful, e.g., for nuclear resonant scattering experiments with synchrotron radiation, which operate at special photon energies. In particular, we mention the potential of such monochromators for nuclear resonance hyperfine spectroscopy in the time domain and for phonon spectroscopy by using nuclear resonance inelastic scattering; see (Gerdau and de Waard 1999/2000) for review papers. This statement will be illustrated here by example of Mössbauer photon energies, whose values are scattered over the range from a few keV to about 50 keV.

Table 3.1 shows selected Mössbauer transition energies E. Not all known Mössbauer photon energies are included. Only those are given whose values are known precisely enough. For each selected energy we provide Miller indices $(hkil)$ of atomic planes for α-Al_2O_3 which back reflect photons with such an energy. Also, the attendant crystal temperatures $T_{_H}$ are provided at which the back reflection takes place. In this report, $T_{_H}$ is referred to as the Bragg temperature which clearly applies to a selected set of atomic planes (hkl) and to a selected x-ray energy. For each reflection the table provides the calculated angular width $\Delta\theta$, the energy bandwidth ΔE, the peak reflectivity, the extinction length $d_e(0)$ - eq. (2.85) - and the variation of the reflection peak position on the energy scale with crystal temperature $\mathrm{d}E/\mathrm{d}T$.

The calculations were performed using the dynamical theory for an infinitely thick perfect crystal. The coordinates of atoms in the unit cell were taken from the measurements of Kirfel and Eichhorn (1990). The Debye-Waller factors at different temperatures were calculated in the framework of the Debye model with the effective Debye temperatures $\Theta_{\mathrm{D}}(\mathrm{Al}) = 890$ K and $\Theta_{\mathrm{D}}(\mathrm{O}) =$

Nucleus	E	$(hkil)$ hexagonal	T_H	$\Delta\theta$	ΔE	Reflectivity	Extinction length	$\mathrm{d}E$ $\mathrm{d}T$
	keV		K	μrad	meV		mm	eV/K
^{181}Ta	6.2155	$(2\ 1\ \overline{3}\ 10)$	228.4	3355	59	.89	.004	-.027
^{169}Tm	8.4103	$(1\ 5\ \overline{6}\ 2)$	600.0	1322	4.0	.31	.058	-.067
^{73}Ge	13.275	$(8\ 1\ \overline{9}\ 7)$	337	1248	5.6	.82	.038	-.078
^{57}Fe	14.4125	$(1\ 3\ \overline{4}\ 28)$	371.6	1001	5.9	.87	.036	-.094
		$(1\ 6\ \overline{7}\ 22)$	161	719	1.9	.63	.111	-.037
^{151}Eu	21.5414	$(11\ 2\ \overline{13}\ 24)$	221.2	526	2.8	.93	.075	-.085
		$(3\ 2\ \overline{5}\ 43)$	287.1	324	.56	.64	.371	-.125
^{149}Sm	22.496	$(3\ 13\ \overline{16}\ 8)$	134	597	2.7	.93	.077	-.036
^{119}Sn	23.8795	$(1\ 9\ \overline{10}\ 40)$	286.9	440	1.8	.91	.120	-.131
		$(6\ 5\ \overline{11}\ 40)$	286.9	353	1.1	.85	.197	-.131
^{161}Dy	25.6513	$(14\ 5\ \overline{19}\ 0)$	342.2	341	1.1	.88	.197	-.149
		$(3\ 2\ \overline{5}\ 52)$	374.6	301	.66	.80	.319	-.166
^{129}I	27.77	$(11\ 10\ \overline{21}\ 10)$	344	296	.82	.87	.259	-.162
^{40}K	29.8299	$(5\ 15\ \overline{20}\ 26)$	214	273	.68	.88	.310	-.110
^{201}Hg	32.138	$(2\ 17\ \overline{19}\ 36)$	100.4	201	.38	.83	.559	-.030
^{125}Te	35.4919	$(11\ 6\ \overline{17}\ 68)$	4	168	.36	.90	.575	-.0001
^{161}Dy	43.8211	$(15\ 17\ \overline{32}\ 28)$	155	93	.10	.77	2.05	-.094
^{238}U	44.915	$(8\ 25\ \overline{33}\ 4)$	73	111	.16	.86	1.32	-.019
^{183}W	46.4839	$(7\ 12\ \overline{19}\ 82)$	76.0	88	.10	.80	2.13	-.028

Table 3.1: Mössbauer photon energies E for selected Mössbauer isotopes and matching Bragg back reflections $(hkil)$ and temperatures T_H in α-Al_2O_3. For each reflection the table provides the calculated angular width $\Delta\theta$, the energy bandwidth ΔE, the peak reflectivity, the extinction length $d_e(0)$ - eq. (2.85) - and the variation of the reflection peak position on the energy scale with crystal temperature $\mathrm{d}E/\mathrm{d}T$.

995 K (see sec. 3.2). The crystal lattice parameters in the relevant temperature range were taken from the recent measurements of Shvyd'ko et al. (2002) (see also sec. 4.5) and Lucht et al. (2001). It is noteworthy that the values of the lattice parameters are now known to a greater accuracy due to the mentioned publications, and ,therefore, one can predict back reflections and relevant crystal temperatures matching a certain photon energy more precisely than before. For this reason, the values in table 3.1 are somewhat different from those given earlier by Shvyd'ko and Gerdau (1999), which were based on older data for thermal expansion coefficients (Aldebert and Traverse 1982) and lattice constants (Kirfel and Eichhorn 1990).

According to this table, for x rays matching the 14.4125 keV Mössbauer transition in ^{57}Fe nuclei, the $(1\ 3\ \overline{4}\ 28)$ back reflection can be predicted at T_H=371.6 K with an angular acceptance of 1.0 mrad, an energy bandwidth of 5.9 meV, and 87% reflectivity.

It is remarkable that even for x rays with relatively high energy, e.g., the 46.4837 keV Mössbauer transition in ^{183}W, sapphire offers a reflection with high reflectivity, with an angular acceptance much larger than the divergence of radiation from present day undulator based x-ray sources, and with an energy bandpass as low as 100 μeV. However, for this to be realized, a perfect sapphire crystal more than 5 mm thick and kept in an environment with mK-stable temperature has to be used.

The higher the photon energy the easier it is to find a back reflection with matching Bragg energy and temperature. Generally speaking, more than one set of reflecting atomic planes matches each selected photon energy. Data are presented for only one set with the highest reflectivity and with the Bragg temperature falling into the temperature range from 4 K to 400 K. In some cases the data for another reflection are presented as well, if this reflection is encountered later.

At high photon energies however another problem appears - lower peak reflectivity. The solution is known - the crystals should be cooled – see Fig. 3.2. A very interesting case would be, e.g., the Mössbauer resonance in ^{67}Ni at 67.41 keV. However, we do not list back reflections for photon energies above 50 keV. The photon energies should be known accurately to correctly select a Bragg reflection with significant reflectivity and reasonable Bragg temperature.

The high energy limit of photons which can be selected with the backscattering sapphire monochromator is estimated to be $\simeq 70$ keV. Above this limit, even at 4 K, the reflectivity of the strongest reflections decreases to $\simeq 10\%$ and the extinction length increases to $\simeq 100$ mm.

Table 3.1 demonstrates that one single α-Al_2O_3 crystal can monochromatize x rays at energies of the Mössbauer transitions in the range from 6 to at least 50 keV with meV and sub-meV bandwidths. To select a new photon energy, one has only to rotate the crystal and change its temperature. Such a monochromator could be a very effective alternative to the multibounce high energy resolution monochromators (Ishikawa et al. 1992, Toellner 2000). The latter require for each Mössbauer transition energy a new set of specially cut crystals. Besides, it is difficult to make them applicable at energies higher than 30 keV. The highest photon energy at which they presently operate is 25.6 keV (Chumakov et al. 2001, Baron et al. 2001a). The most effective use of such

monochromators would be at backscattering beamlines, whose prototype was described in sec. 2.3.

The first applications of α-Al_2O_3 crystals as a universal high energy resolution monochromator will be addressed in secs. 4.8 and 4.6. A broader application is hindered at the moment by the lack of millimeter thick perfect sapphire crystals. We are hopeful of finding the solution of the problem in the near future. Altogether, whatever application of α-Al_2O_3 crystals in x-ray crystal optics is considered, the assessment of their crystal quality acquires great significance.

3.4 Quality assessment of α-Al_2O_3 crystals

Two x-ray diffraction techniques are used for the quality assessment of sapphire crystals: (i) reflectivity and energy width measurements of Bragg back reflections, and (ii) white beam x-ray topography. The first technique is the most appropriate for our purposes. Essentially, it was presented in secs. 2.3 and 2.4.1. However, it requires monochromatic x rays, and it is time consuming. X-ray topography, especially white beam backscattering x-ray topography, is much faster and requires minimum instrumentation. Yet, a priori, it is not clear whether it gives adequate information. The results presented here of the application of white beam x-ray topography to the quality assessment of sapphire crystals are based mostly on the original publications of Chen et al. (2001b) and Chen et al. (2001a).

Sapphire crystals grown by different techniques are commercially available (Dobrovinskaya et al. 2002). Our very first studies (Shvyd'ko et al. 1998) have indicated that the crystals grown by the heat-exchange method (HEM) have on average a better quality. It is for this reason that they are predominantly studied here. For comparison, samples grown with the modified Czochralski method (MCM) are inspected as well.

The heat-exchange method has been developed to grow high-quality sapphire crystals of large size for industrial applications (Schmid et al. 1994, Khattak and Schmid 2001). Crystals of different quality are available from the producer: HEMEX, HEMLITE, etc.. The premium grade HEMEX sapphire is grown from CSI ultra high purity material[1] and selected by the producer using visible light optical techniques. However, visible light optical tests are not sufficient to characterize crystals destined for applications in x-ray crystal optics. For this one has to use x-ray diffraction techniques as well.

3.4.1 Preparation of samples

Before going into the details of the crystal quality studies, a few words should be mentioned about the preparation of the sapphire samples for the x-ray measurements.

The crystal surface is treated by chemical polishing in order to remove any possible defective layers or stresses which have been introduced due to preceeding mechanical treatment (cutting, polishing, etc.). Typically $100\ \mu$m of the surface layer are removed. The polishing is performed in a 1:1 H_2SO_4:

[1] HEMEX, HEMLITE, etc., and "CSI ultra high purity" are trademarks of Crystals Systems, 27 Congress Street, Salem, MA 01970, USA.

H_3PO_4 solution at 560 K, as described by Reisman et al. (1971). The temperature of the solution is controlled with an accuracy of 1 K. The removal rate in the $[0\ 0\ 0\ 1]$ direction is about 8.5 μm/hour (for each side of the sample). The polishing in this solution is anisotropic. More experimental details including the setup for chemical polishing have been presented by Lerche (2000).

3.4.2 White beam x-ray topography technique

X-ray topography is a fast non-destructive technique, which can provide a map of the strain or defect distribution in crystals, such as dislocations, planar defects, stacking faults, domain walls in ferroelectric and magnetic materials, growth defects or large precipitates, see, e.g., Bowen and Tanner (1998). In white beam mode under weak absorption conditions this technique is sensitive to strain fields extending over more than several microns. The white beam backscattering x-ray topography technique was introduced by Tuomi et al. (1974). In addition, when used in Bragg reflection mode, one can obtain depth information for defect distributions inside the sample by examining different reflections, as the penetration depths for different reflections differ from each other. It can provide depth information from several to several hundred microns from the sample surface.

White beam backscattering x-ray topography is recorded like a usual Laue diagram in backscattering geometry - Fig. 3.4. Each spot on the photo plate corresponds to a certain Bragg reflection $(hkil)$. The spot dimensions is given by the incident beam cross-section. Each single spot is a topograph. The spots are not equivalent, since Bragg reflections show different sensitivity to defects of different origin. Examples of such topographs are shown in Figs. 3.5-3.10.

The geometrical resolution of x-ray topography depends on a number of factors, including angular source size, the source to sample distance and the sample to photo plate distance. For the conditions used in this experiment the resolution usually lies in the micron range.

The synchrotron x-ray topography experiments were performed at HASYLAB (DESY), Hamburg, at the bending magnet beamline F1 utilizing the continuous spectrum of synchrotron radiation from the DORIS-III storage ring. The beam size for the "large area" topography experiments was about 2.1×1.7 mm^2. The distance from sample to photo plate was 45 mm. For "small area" section topography in transmission geometry the beam was limited by a vertical slit of height approximately 20 μm and length 1.5 mm. The distance from sample to photo plate was set to 80 mm.

The aforementioned large area Bragg patterns of topographs were recorded

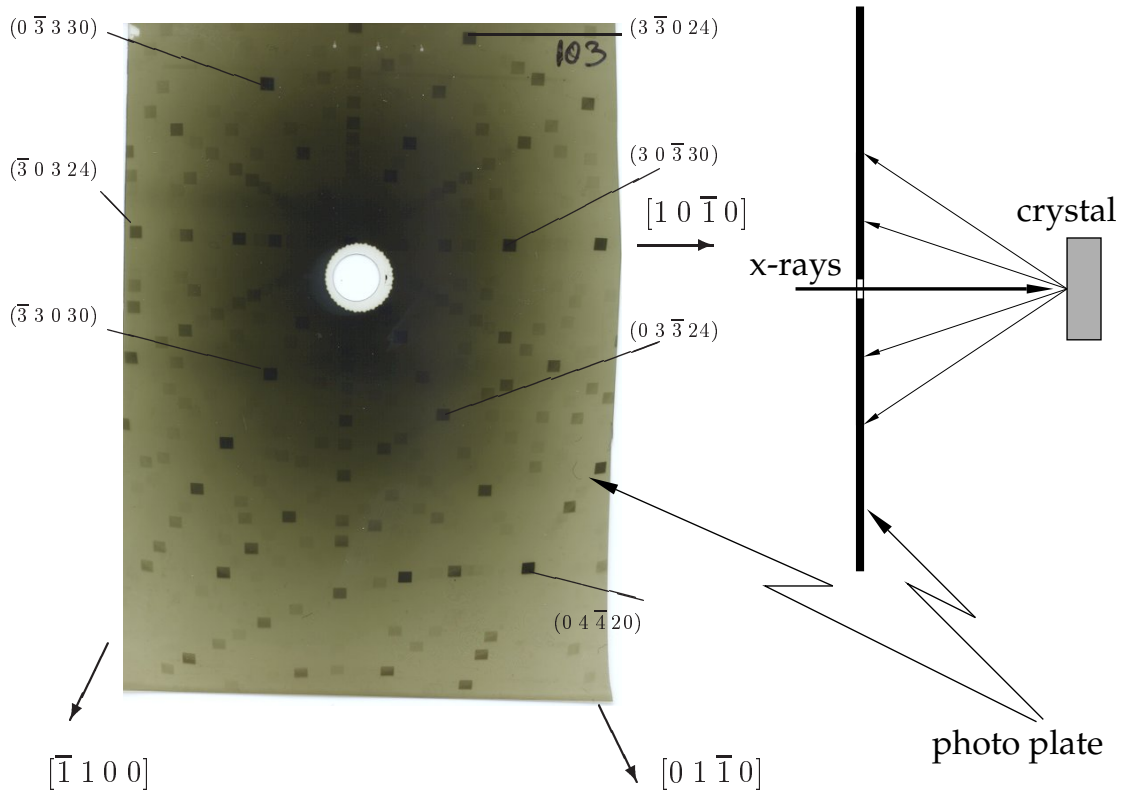

Figure 3.4: Schematic of the backscattering white beam x-ray topography technique. The topography spots corresponding to different Bragg reflections $(hkil)$ are recorded on a high-resolution photo plate (left) in backscattering geometry (right). The spot size is determined by the incident beam cross-section.

on Geola VRP-M photo plate[2] having an emulsion grain size of about 0.05 μm. Spatial resolution of the photo plate is $\simeq 3000$ lines/mm. The small area section topographs were recorded on Kodak Industrex SR photo plate. The pictures, which appear in this report, have been generated on a system comprising of a CCD camera, frame-grabber and appropriate software.

Dislocation distribution and density

X-ray topographs show that dislocations exist in most of the sapphire wafers. However, in all samples discrete dislocation lines can be discerned, which indicates the relatively low dislocation density and high sapphire quality. The

[2]VPR-M Green Sensitive Emulsion, Slavich, PO Box 343, Vilnius 2006, Lithuania, geola@post.omnitel.net, www.slavich.com

dislocation density in the studied sapphire can vary significantly from sample to sample, especially between samples produced with different methods.

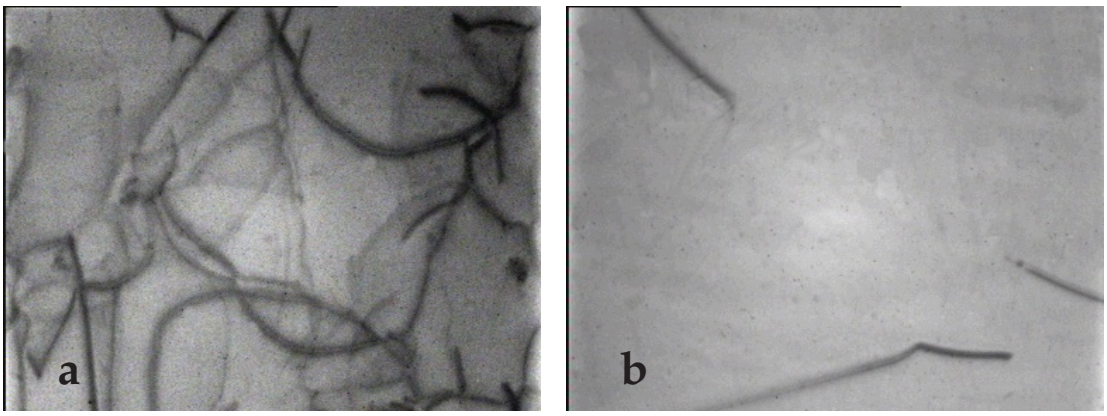

Figure 3.5: Back-reflection topographs of HEMEX sapphire wafers cut from different boules show different dislocation densities: (a) $\simeq 10^3$ cm^{-2}, (2 2 $\bar{4}$ 24) reflection; (b) much lower dislocation density, (3 0 $\bar{3}$ 18) reflection. Sample area illuminated by x rays is 2.1×1.7 mm^2.

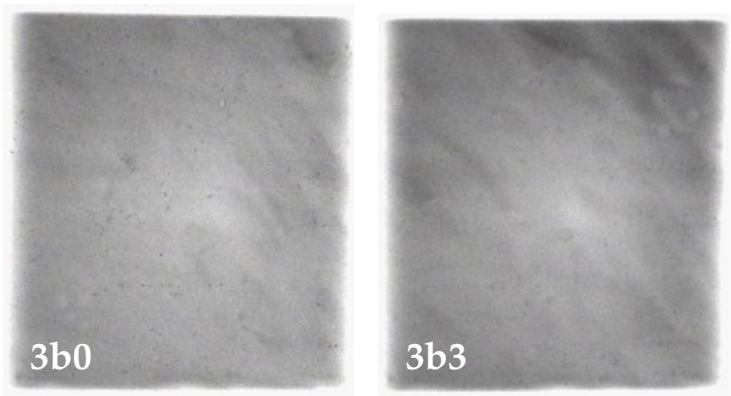

Figure 3.6: Back-reflection topographs of HEMEX sapphire crystals with no dislocations, (2 $\bar{2}$ 0 16) reflection. The thickness of the sample is 0.04 mm. Sample area illuminated by x rays is 1.2×1.2 mm^2. These crystals were used in the first experiments with the x-ray Fabry-Pérot interferometer - sec. 6.3.

The nominally highest quality HEMEX sapphire shows typically a dislocation density in the order of 10^3 cm^{-2} - see Fig.3.5(a). In samples cut from a different boule a much lower dislocation density was detected - see Fig.3.5(b). In some regions of these samples no dislocations were detected at all - see Fig.3.6. Pendellösung fringes were observed in the corresponding transmis-

sion section topographs (Fig.3.7), which confirms the very high quality of the sapphire wafer.

Figure 3.7: (0 $\bar{1}$ 1 1) transmission section topography at a region in HEMEX sapphire with no dislocations. Sample thickness is 0.1 mm. (Note: the black spots in the image are due to defects in the photo plate)

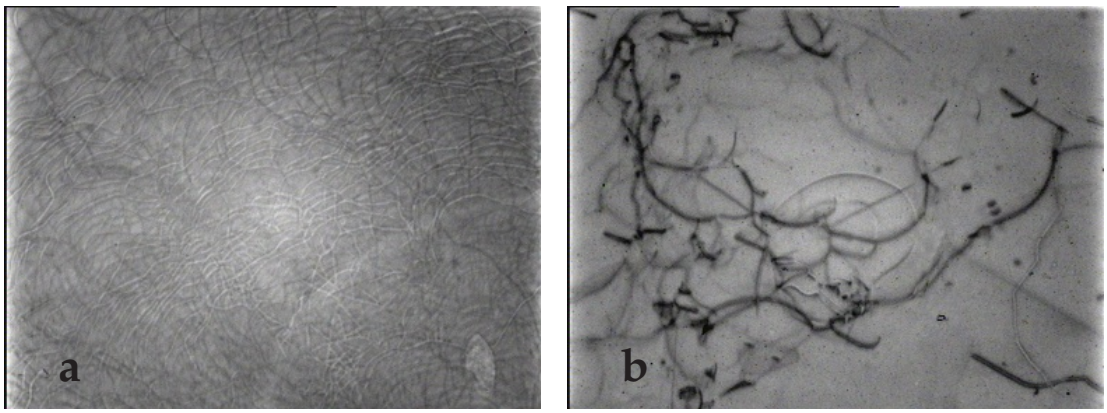

Figure 3.8: Back reflection topographs of a MCM sapphire wafer at regions with different dislocation densities: (a) Center part of the wafer, (2 0 $\bar{2}$ 14) reflection ; (b) Edge part of the wafer, (3 0 $\bar{3}$ 18) reflection. Sample area illuminated by x rays is 2.1×1.7 mm^2, the thickness of sample is about 0.3 mm.

The topograph of Fig.3.8(a) was taken from the center part of a MCM wafer. The dislocation density is high: $\simeq 9 \times 10^4$ cm^{-2}. It can be observed from Fig.3.8(a) that two sets of dislocations exist in this wafer, which run roughly in the direction of [0 1 $\bar{1}$ 0] and [1 $\bar{1}$ 0 0] respectively. An examination of the edge region of the same wafer indicates a higher crystal quality, as a lower dislocation density $\simeq 4 \times 10^3$ cm^{-2} was detected in its corresponding topographs - see Fig.3.8(b).

Dislocation densities were calculated using the equation

$$\rho_{\mathrm{D}} = \frac{L}{V} \tag{3.3}$$

where V is the volume of the sapphire wafer exposed to the x rays during the experiment and L is the total dislocation line length in that volume. V is calculated using the extinction length (penetration depth) and the beam size.

Determination of the Burgers vectors

When examining dislocations in different reflections from the same sample, one may notice that their contrast changes with each reflection. Occasionally, the dislocation contrast disappears in certain reflections. Examples of this fact are shown in Figs. 3.9 (a)-(c). Dislocation A appears in the (2 $\bar{1}$ $\bar{1}$ 0) reflection, but disappears in the (2 0 $\bar{2}$ $\bar{1}$) and (3 0 $\bar{3}$ 0) reflections. Similarly, dislocation B appears in the (2 0 $\bar{2}$ $\bar{1}$) and (3 0 $\bar{3}$ 0) reflection, but disappears in the (2 $\bar{1}$ $\bar{1}$ 0) reflection. By applying the criterion $\boldsymbol{H}\boldsymbol{b} = 0$, where $\boldsymbol{H}$ is the X ray diffraction vector and $\boldsymbol{b}$ is the Burgers vector of the dislocation, one can in principle determine the Burgers vector of individual dislocations. The Burgers vector of some dislocations in the sapphire wafers are calculated, which are [$\bar{1}$ $\bar{1}$ 2 0], [$\bar{1}$ 2 $\bar{1}$ 0], [2$\bar{1}$ $\bar{1}$ 0], [$\bar{1}$ $\bar{1}$ 2 0], and [1 $\bar{1}$ 0 $\bar{1}$], respectively. Most of them are mixed type dislocations.

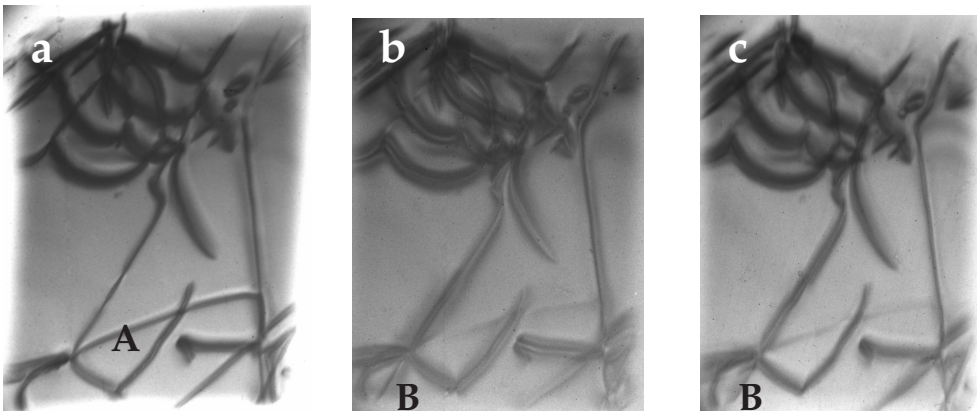

Figure 3.9: Dislocation contrast variations with different reflections (a) (2 $\bar{1}$ $\bar{1}$ 0), (b) (2 0 $\bar{2}$ $\bar{1}$), and (c) (3 0 $\bar{3}$ 0). The sample thickness is about 0.05 mm.

Stacking faults

One prominent feature observed in the sapphire samples is the occurrence of numerous stacking faults. Stacking faults are found in most topographs and in all wafers inspected in this study. Some topographs of the stacking faults are shown in Fig. 3.10(a)-(b), which comprise of two reflections from the same experimental spot. If the phase shift α ($\alpha = 2\pi\boldsymbol{H}\boldsymbol{r}$, where $\boldsymbol{r}$ refers to the fault

vector) between the diffraction vector and the stacking faulted region is not an integer times 2π (Bowen and Tanner 1998), the fault contrast in the topographs can be easily observed as seen in Fig. 3.10.

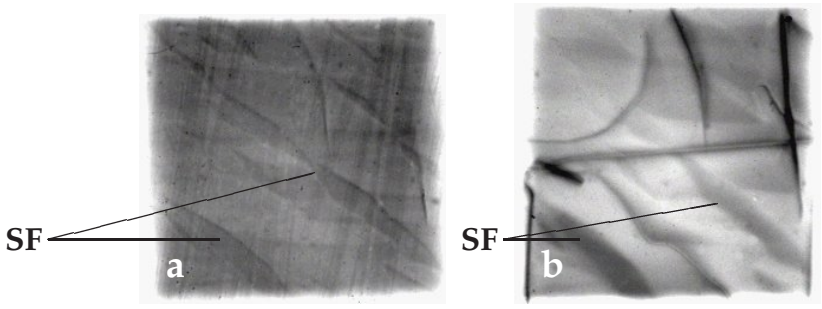

Figure 3.10: Stacking fault (SF) features in a sapphire wafer as seen in reflections (a) (3 3 $\bar{6}$ 30), and (b) (1 1 $\bar{2}$ 12). The sample thickness is about 0.05 mm.

In some samples, no dislocations were detected, but many stacking faults were discernible - see Fig. 3.6.

3.4.3 Bragg reflectivity vs. dislocation density

Figure 3.11 shows energy dependence of the reflectivity of two sapphire crystals for x rays at normal incidence to the (0 0 0 30) atomic planes. The extinction length for this reflection is 16 μm. The x rays were monochromatized to an energy band of 7 meV width and scanned around $E_0 \simeq 14.315$ keV by using a high energy resolution monochromator described in detail in sec. 2.3. The reflectivity curve shown in Fig. 3.11a was measured for the same region of the HEMEX α-Al_2O_3 crystal where few dislocations were detected - as shown in Fig. 3.5b. The reflectivity curve shown in Fig. 3.11b was measured from the same region of the MCM α-Al_2O_3 crystal where the high dislocation density was detected - see Fig. 3.5a. The HEMEX sapphire shows a high peak reflectivity of $\simeq 86\%$ and a small width of 13 meV (FWHM) which fits well to the profile (solid line) calculated with the dynamical theory of x ray diffraction in perfect crystals. The MCM sapphire shows a much lower peak reflectivity of $\simeq 14\%$ and a large width of $\simeq 50$ meV (FWHM).

Another example is shown in Fig. 3.12 where the reflectivity was measured for x rays of the higher energy $E_0 \simeq 21.630$ keV at normal incidence to the (1 1 $\bar{2}$ 45) atomic planes. The measurements were carried out at the undulator beamline 3-ID at the Advanced Photon Source (Alp et al. 2000a). The x rays

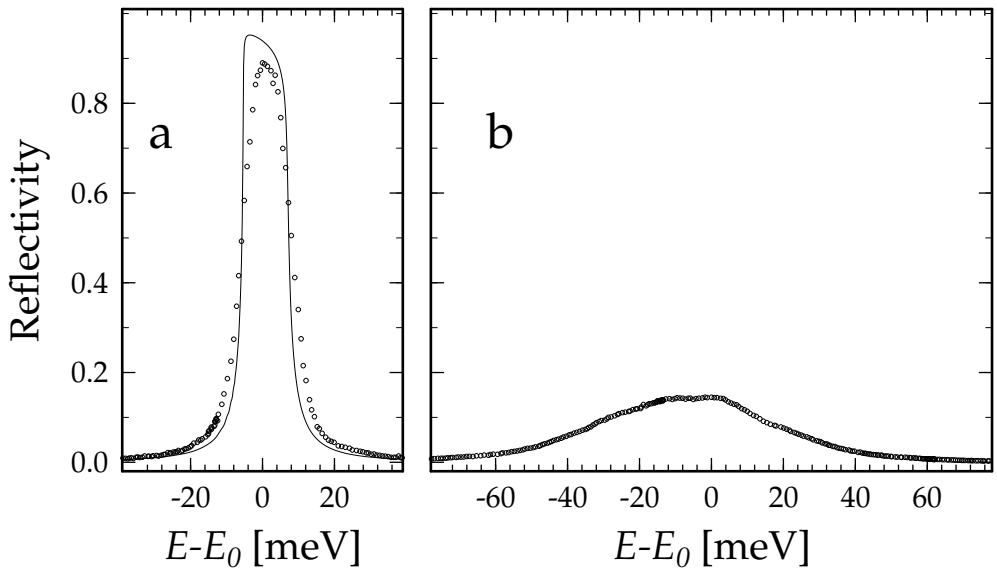

Figure 3.11: Energy dependence of the Bragg reflectivity of sapphire crystals for x rays at normal incidence to the (0 0 0 30) atomic planes, $E_0 \simeq 14.315$ keV. (a) HEMEX low dislocation density sapphire; its topograph is shown in Fig. 3.5b. Circles are measured values, the solid line is the calculated profile from the dynamical theory of diffraction for perfect crystals (b) MCM sapphire with high dislocation density; its topograph is shown in Fig. 3.8a.

were monochromatized to an energy bandwidth of 1 meV and scanned around 21.630 keV by using a high energy resolution monochromator designed by Toellner et al. (2000).

The dynamical theory predicts a peak reflectivity of 84.2% and an energy width of 1.5 meV. The extinction length for this reflection is 144 μm, which is much larger than in the previous case. One should expect that a higher crystal quality would be required to achieve theoretically predicted values of the reflectivity and energy width.

The reflectivity curve shown in Fig. 3.12a was measured from the same region of the HEMEX α-Al_2O_3 crystal where the standard ($\simeq 10^3$ cm^{-2}) dislocation density was detected - see Fig. 3.5a. The reflectivity curve shown in Fig. 3.12b was measured for the same region of the HEMEX α-Al_2O_3 crystal where few dislocations were detected (Fig. 3.5b). The HEMEX sapphire with standard dislocation density shows a low peak reflectivity of $\simeq 25\%$ and a broad reflection curve with a width of $\simeq 7.8$ meV. The HEMEX sapphire with

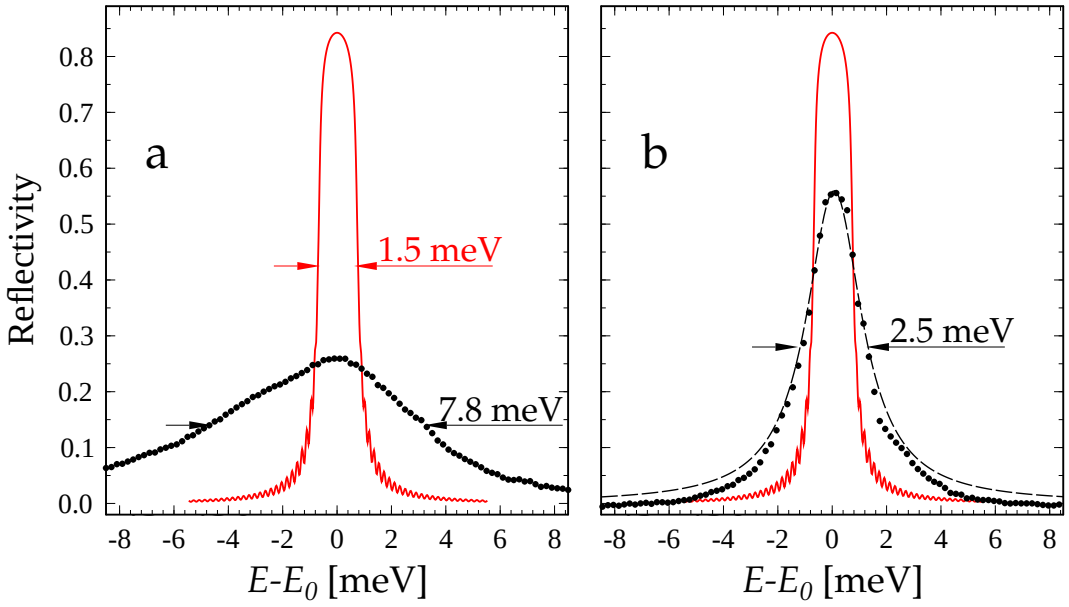

Figure 3.12: Energy dependence of the Bragg reflectivity of sapphire crystals for x rays at normal incidence to the (1 1 $\bar{2}$ 45) atomic planes, $E_0 \simeq 21.629$ keV. (a) HEMEX standard dislocation density sapphire, its topograph is shown in Fig. 3.5a; (b) HEMEX low dislocation density sapphire, its topograph is shown in Fig. 3.5b. Circles are measured values, the solid line is the calculated profile from the dynamical theory of diffraction for perfect crystals. The dashed line in (b) is a fit with a Lorentzian.

lower dislocation density shows a peak reflectivity of $\simeq 55\%$ and the reflection curve - circles in figure 3.12b - with a width of 2.5 meV. In both cases the theoretical values for a perfect crystal are not achieved. Yet, the HEMEX sapphire with lower dislocation density shows much better performance.

A comparison of the reflectivity and topography results thus shows that the white-beam x-ray topography technique provides information which correlates with the reflectivity measurements. This allows one to use the more rapid white-beam x-ray topography technique to assess the quality of the sapphire material for backscattering x-ray mirrors.

Chapter 4

Selected applications of backscattering

4.1 Introduction

In this chapter we present some applications of Bragg backscattering. These deal primarily with precise measurements of lattice constants and radiation wavelengths in the x-ray spectral region, as well as with applications of sapphire crystals for a high energy resolution x-ray monochromator.

Diverse techniques exist to measure lattice constants and radiation wavelength in the x-ray spectral region. Whatever technique is used, it should rely on some length standard. Up to the 1980s, the set of wavelengths of the K_α characteristic x rays of atoms was used for this purpose (Bearden 1965, 1967). Since the 1980s, the silicon lattice constant took over the role of the most precise and reliable length standard for atomic scales (Deslattes and Henins 1973, Becker et al. 1981, Basile et al. 1994, Mohr and Taylor 2000). In sec. 4.2 we argue, why nevertheless a precise and easy reproducible *wavelength* standard is still required, and why the wavelength of the ^{57}Fe Mössbauer photons can fulfill this role.

A backscattering technique is introduced in sec. 4.3 for measuring radiation wavelengths and lattice constants relying on the Mössbauer wavelength standard. This technique is applied in the following sections to measure the wavelength of Mössbauer photons and lattice constants of α-Al_2O_3.

First, the absolute value of the wavelength λ_{M} of the ^{57}Fe Mössbauer radiation must be ascertained with sub-ppm accuracy. Two independent experiments by Shvyd'ko et al. (2000a) and Xiaowei et al. (2000) have reported such results. Xiaowei et al. (2000) have measured λ_{M} with a relative uncertainty of 0.6 ppm using the method of Siddons et al. (1988) by comparing λ_{M} with the

lattice constants of different silicon crystals. The averaged value reported by the authors is $0.8602557(5) \times 10^{-10}$ m.

Shvyd'ko et al. (2000a) measured λ_{M} with a relative uncertainty of 0.19 ppm using almost exact Bragg backscattering of x rays from a calibrated reference silicon crystal kept in an environment with precisely controlled temperature and pressure - sec. 4.4. Its value is determined as $\lambda_{\mathrm{M}} = 0.86025474(16) \times 10^{-10}$ m. The details of this experiment are presented in sec. 4.4. Some popular scientific journals have reported these new developments in nano-metrology (Irion 2000, Burgess 2000, Chin 2000).

The values reported in the two publications differ by 1.1 ppm. This is a reliable base for precise absolute measurements with the new wavelength standard. It is applied in the following sections.

As was argued in the previous chapter, sapphire crystals have the potential to become the workhorse of high energy resolution Bragg back-reflection x-ray optics in the 10-50 keV spectral range. For this purpose precise data on crystal lattice constants are required. We present in sec. 4.5 measurements of the lattice constants of α-Al_2O_3 crystals in a temperature range from 286 to 374 K. All measured values are expressed both in units of λ_{M} and in meters.

A precise knowledge of the lattice constants in sapphire across a broad temperature range as well as the ability of sapphire crystals to back-reflect x rays of any energy in the 10-50 keV spectral range is used in sec. 4.6 to determine the wavelength of Mössbauer photons of the following nuclei: ^{151}Eu, ^{119}Sn, and ^{161}Dy. The wavelengths are measured with sub-ppm accuracy. The wavelengths of these Mössbauer photons provide a set of reference wavelengths in the hard x-ray range with a uniquely small uncertainty and easy reproducibility.

Powder diffraction is a powerful tool in x-ray crystallography. In sec. 4.7 we study the potential of this technique in backscattering geometry.

The first applications of sapphire as a backscattering monochromator are presented in sec. 4.8. With its help, nuclear resonant scattering of synchrotron radiation from the 25.6 keV level of ^{161}Dy is studied by employing two techniques: nuclear forward scattering (NFS) and nuclear incoherent scattering (NIS). NIS energy spectra reveal scattering with participation of phonons in Dy_2O_3. Electron spin dynamics in Dy-metal in the slow-relaxation regime is observed and studied using NFS.

4.2 Why do we need a new wavelength standard?

Precise length measurements are of great importance in natural science.

The definition of the meter as a standard for length measurements evolved with our growing knowledge of the basic laws of physics. In 1799 a platinum bar made equal as closely as possible to the one ten-millionth part of the polar quadrant of the earth passing through Paris was defined as one meter and deposited as a reference in the French National Archive. Replaced in 1899 by an 'International Prototype Meter' in the form of an alloy bar of platinum (90%) and iridium (10%), it served as a length standard until 1960, when the wavelength of the orange line from a ^{86}Kr standard lamp took over its role. Since 1983, the meter has been defined as the distance traveled by light in 1/299 792 458 of a second. The speed of light c is made a fixed constant and a wavelength standard λ_{s} is established via the measured frequency f_{s} of an iodine stabilized He-Ne laser such that $\lambda_{\mathrm{s}} = c/f_{\mathrm{s}}$. This becomes possible due to the ability to measure laser frequencies relative to the ^{133}Cs standard second, due to the narrowness of the laser radiation line itself and due to the ability to stabilize its frequency to a few parts in 10^{11}.

However, the 633 nm wavelength of the He-Ne laser is too long to be used to measure interatomic distances, which are typically 10000 times smaller. Therefore, a secondary shorter length standard is necessary for such purposes.

Bonse and Hart (1965b) proposed the use of a combination of Michelson visible-light and triple-Laue-case (LLL) x-ray interferometers to measure the lattice constant of high quality silicon single crystals in terms of the wavelength of the He-Ne laser. In the following years the Si lattice constant as a secondary length standard was measured in a series of experiments of Deslattes and Henins (1973) and Becker et al. (1981) with steadily increasing accuracy, which now has reached a relative uncertainty of 0.029 ppm (Basile et al. 1994). The following value of the lattice constant of silicon $a = 5.43102088(16) \times 10^{-10}$ m at $22.500\,^{\circ}$C is accepted nowadays as a length standard for interatomic measurements (Mohr and Taylor 2000).

However, to reproduce its value even with a moderate relative uncertainty of 1 ppm is not effortless. Chemical purity, crystal perfection, absolute temperature and pressure have to be precisely controlled. This is possible in well equipped laboratories but otherwise is not trivial. Besides, to gauge interatomic distances, one needs *radiation* with a well-defined wavelength rather than an etalon of a well-defined material.

Thus, it is desirable to have access to an easy reproducible wavelength standard for atomic scales. In fact the solution to this problem is known. It is re-

lated to the Mössbauer effect and Mössbauer radiation, widely known since 1958 to have an unprecedentedly narrow spectral line and both precise and stable wavelength.

The most famous is the Mössbauer radiation originating from the decay of the first excited state of ^{57}Fe nuclei. The energy of the excited state and the energy of the Mössbauer photons is $E_{\rm M} \simeq 14.4$ keV. The radiation wavelength $\lambda_{\rm M} \simeq 0.86 \times 10^{-10}$ m is perfectly suited to use as a wavelength standard for atomic scales.

The spectral linewidth Γ of the ^{57}Fe Mössbauer radiation, determined by the lifetime of the excited state $\tau = 141$ ns via the uncertainty relation $\Gamma\tau = \hbar$, is as small as 4.8×10^{-9} eV. Thus the relative uncertainty of the radiation energy is $\Gamma/E_{\rm M} \simeq 3 \times 10^{-13}$ and the same relative uncertainty corresponds to the Mössbauer wavelength $\lambda_{\rm M}$. A potential source of line broadening originates in interaction of the nuclei with the environment, e.g., the electrons of the atomic shell. These so-called hyperfine interactions may deteriorate the spectral purity of the Mössbauer radiation by a factor of about 100. Thus, even if nothing is known about the hyperfine interactions, the relative uncertainty and reproducibility is still $\simeq 10^{-11}$. This outstandingly small uncertainty is a gift of nature and makes Mössbauer radiation an attractive wavelength standard.

To use such a wavelength standard, one needs easily available, strong and well collimated sources of Mössbauer photons. 35 years ago Bearden considered the possibility of introducing a γ-ray wavelength standard, attempting to measure the wavelength of 14.4 keV Mössbauer radiation of ^{57}Fe nuclei with a relative accuracy of 10 ppm (Bearden 1965). His conclusion was: to make the Mössbauer standard experimentally feasible the brightness of the radioactive source would have to be increased by a factor of 100 beyond his 200 mCi activity (Bearden 1965, 1967).

Until recently this was a problem. The brightness of radioactive sources is limited by self-absorption. This limitation can be overcome if one uses synchrotron radiation as a source. Mössbauer photons are filtered from the synchrotron radiation spectrum by coherent nuclear resonant scattering, see Gerdau and de Waard (1999/2000) for a review. Any ^{57}Fe-containing substance exposed to synchrotron radiation in the 14.4 keV spectral range becomes a strong source of Mössbauer photons preserving the collimation of the incident beam. Such a source is free of radioactive contaminations. Since the pilot experiment of Gerdau et al. (1985) in 1984 the rate of the 14.4 keV Mössbauer photons available has increased from 0.1 Hz to $\simeq 10^4$ Hz within a solid angle of 20×20 μrad^2 at modern third generation synchrotron radiation facilities. The synchrotron-based sources of Mössbauer photons are already $\simeq 10^6$

times brighter than the 200 mCi radioactive source used by Bearden and will be much brighter with forthcoming x-ray free-electron laser facilities (Materlik and Tschentscher 2001). The availability of such sources has stimulated our attempts to establish this standard.

After realizing the potential of the Mössbauer wavelength standard, an important first step leading to practical use is the precise measurement of the absolute value of the wavelength[1]. There are at least two options. One could measure the Mössbauer wavelength directly in terms of the wavelength of the He-Ne laser. Another less direct way, is to measure the Mössbauer wavelength with respect to the silicon lattice constant, using silicon as a transfer standard. We have chosen the second approach.

[1]At the beginning of these studies, the wavelength, and thus the energy of the ^{57}Fe Mössbauer radiation was acknowledged to be known with a relative accuracy of only 10 ppm: $E_{\mathrm{M}} = 14413.00(15)$ eV (Firestone et al. 1996).

4.3 Measuring lattice constants and wavelengths

Before going into details, a technique which enables precision measurements of lattice constants and wavelengths to better than 0.1 ppm is presented, which relies on the Mössbauer wavelength standard λ_{M}. It is based on the publications (Shvyd'ko et al. 2000a, 2002).

Basic principle

The basic idea underlying the experimental technique exploits the fact that the spectrum of the radiation reflected backwards from the atomic planes with Miller indices (hkl) and interplanar distance $d_{_H}$ is centered at

$$\lambda_{\mathrm{c}} \,=\, 2d_{_H}\,\left[1-\frac{1}{2}\delta\theta^2-w_{_H}\right]. \tag{4.1}$$

This expression is derived from Bragg's law (2.78) under the assumption of a small angular deviation from normal incidence: $\delta\theta = \pi/2-\theta \ll 1$. If $\delta\theta \leq \sqrt{2\epsilon}$, where ϵ is the required relative uncertainty of measurements, the simple relation $\lambda = 2d_{_H}(1-w_{_H})$ is valid even for a relatively coarse angular setting. E.g., for $\delta\theta \leq 100$ μrad it yields a relative uncertainty of better than $\epsilon \simeq 10^{-8}$.

This property is used to transfer the regular $d_{_H}$ pattern onto the scale of the instrument which selects and measures x-ray wavelengths, the λ-meter. Once the Mössbauer wavelength is measured also using the λ-meter, the lattice constants $d_{_H}$ can be determined in terms of λ_{M}. If the crystal structure and thus the relations between the interplanar distances $d_{_H}(a,b,c)$ and the lattice constants a, b, c are known, the lattice constants can thus be ascertained.

The opposite is also true. If the values of $d_{_H}$ or a, b, c are known, the radiation wavelengths can be measured using the λ-meter.

Determination of lattice constants

In the following, the theoretical background and sources of possible uncertainties of the measurements of lattice constants in terms of λ_{M} are discussed.

The λ-meter in our experiments is a silicon channel-cut crystal calibrated in units of λ_{M}, see, e.g., Fig. 4.1 of the next section. X rays are reflected from atomic planes of the λ-meter with the interplanar distance $d_{_{H^*}}$. At a certain glancing angle θ they are reflected within a spectral range centered at λ_{c}, as given by the modified Bragg law - eq. 2.78.

λ_{c} is changed by rotating the λ-meter. The variation of the rotation angle ψ can be measured in the experiment. The angles ψ and θ are identical only if the

rotation axis is perfectly perpendicular to the incident beam $\boldsymbol{k}_0$ and parallel to the reflecting atomic planes. If ξ and η are the angles of deviation from perfect alignment then the relation between θ and ψ is: $\sin\theta = \sin\psi\cos\eta\cos\xi + \sin\eta\sin\xi$. Combining this expression with eq. 2.78 one obtains the relation between the rotation angle ψ and the wavelength $\lambda_{\rm c}$ selected by the λ-meter:

$$\sin\psi \;=\; \frac{\lambda_{\rm c}}{2d^*} - \zeta\,. \tag{4.2}$$

Here $\zeta = \tan\eta\tan\xi$ is a parameter which allows for a non-perfect alignment of the λ-meter. d^* is another instrumental parameter of the λ-meter given by $d^* = d_{H^*}\cos\eta\cos\xi/(1+w_{H^*})$. It is assumed to be constant in the spectral range $\lambda_{\rm M} - 0.01$ Å $\leq \lambda_{\rm c} \leq \lambda_{\rm M} + 0.01$ Å investigated in the following experiments. This is justified as $f'_{\rm Si}(\lambda_{\rm c})$ varies in this range at most by ± 0.003 about its average value of 0.119 (Deutsch and Hart 1984, 1988), and thus w_{H^*} varies by less than 10^{-8} compared to the leading term 1. The instrumental parameter d^* is determined in the experiments.

Now the equations describing the measurement procedure can be obtained. The rotation angle ψ_H of the λ-meter at which it selects x rays matching the backscattering reflection (hkl) is given by

$$\sin\psi_H \;=\; 2x\tilde{d}_H(\tilde{a},\tilde{b},\tilde{c})\,(1-w_H) - \zeta\,. \tag{4.3}$$

This relation is obtained by inserting eq. (4.1) into eq. (4.2) and introducing length variables measured in terms of $\lambda_{\rm M}$: $\tilde{d}_H = d_H/\lambda_{\rm M}$, $\tilde{a} = a/\lambda_{\rm M}$, $\tilde{b} = b/\lambda_{\rm M}$, $\tilde{c} = c/\lambda_{\rm M}$, and $x = \lambda_{\rm M}/2d^*$. Here we have neglected the small correction $\delta\theta^2$ in eq. (4.1). As was already mentioned, a deviation from normal incidence even by an angle of, e.g., $\delta\theta \simeq 0.1$ mrad, changes the wavelength of the reflected radiation by only $5\cdot 10^{-9}\lambda_{\rm c}$. If necessary, it can be taken into account.

Equation (4.2) allows one to determine the rotation angle $\psi_{\rm M}$ at which the λ-meter selects the radiation with the reference wavelength $\lambda_{\rm M}$:

$$\sin\psi_{\rm M} \;=\; x - \zeta\,. \tag{4.4}$$

The difference $\psi_H - \psi_{\rm M} \;=\; \delta\psi_H$, is measured in the experiment. By using eqs. (4.3) and (4.4) we obtain the equation

$$\delta\psi_H = \arcsin\left\{2x\tilde{d}_H(\tilde{a},\tilde{b},\tilde{c})\,(1-w_H) - \zeta\right\} - \arcsin\left\{x-\zeta\right\}, \tag{4.5}$$

which is used for the data evaluation. Here $\tilde{a}$, $\tilde{b}$, $\tilde{c}$, x, and ζ are unknowns which should be determined.

In principle, five independent measurements of $\delta\psi_{_H}$ are necessary for this. The number of unknowns and thus the number of measurements can be reduced to four provided the λ-meter is well aligned. As is ascertained by the numerical analysis of eq. (4.5) the parameter ζ can be omitted without changing the result of $\tilde{a}$, $\tilde{b}$, and $\tilde{c}$ by more than 10^{-10} in relative units if the alignment parameter $\zeta \leq 10^{-5}$. The λ-meter in the experiments presented in the following sections was aligned better.

The technique described relies on the strict fulfillment of the relation $d_{_H}(a, b, c)$ between the interplanar distances and lattice constants. This should be the case in absolutely perfect crystals. Defects violate the periodicity of the crystal structure and thus the relation $d_{_H}(a, b, c)$. The validity of the relation and the errors in determining the lattice constant can be checked by measuring $\delta\psi_{_H}$ for more back reflections (hkl) than required by the number of unknowns in the set of equations (4.5). Several independent sets of equations (4.5) can be then composed to determine the values of the lattice constants. The dispersion of lattice constants determined from the independent sets will give an error in the periodicity averaged over the crystal volume and the uncertainty in the determination of the lattice constants by this method for the particular sample.

Determination of wavelengths

The backscattering condition (4.1) can be used to measure a radiation wavelength. Following the procedure described in the pervious section, one determines for which reflection (hkl) and at what crystal temperature exact back reflection occurs for the radiation in question and then measures the crystal lattice parameters at this temperature in terms of λ_{M}. From the measured interplanar distance $d_{_H}$ the wavelength is readily determined by (4.1).

4.4 γ-ray wavelength standard for atomic scales

The absolute wavelength value λ_{M} of the ^{57}Fe Mössbauer radiation is measured in terms of the silicon lattice constant a by using the experimental technique presented in sec. 4.3.

4.4.1 Setup

Figure 4.1 shows the schematic of the experimental setup. As a reference a silicon single crystal (Si) was used, whose lattice constant $a = 5.43102030(36) \cdot 10^{-10}$ m has been calibrated against a silicon standard crystal (Becker et al. 1981) with a relative uncertainty of 0.07 ppm at 22.500°C in vacuum. To reproduce this value of a in the present experiment the crystal is kept in an evacuated thermostat at 22.500°C (295.650 K) with an accuracy of ≤ 5 mK and a stability of ≤ 1 mK (Lucht 1998). The thermostat is installed on a 4-circle goniometer and can be oriented to allow back reflections of x rays which have passed the λ-meter (λ). We use back reflections with $2d_{_H}$ close to λ_{M}: (11 5 3), (12 4 0), and (9 9 1) - Fig. 4.2. Any pair of these reflections allows one to calibrate the λ-meter in terms of the lattice constant a.

An α-Fe foil (F) was installed in the beam to generate the Mössbauer pho-

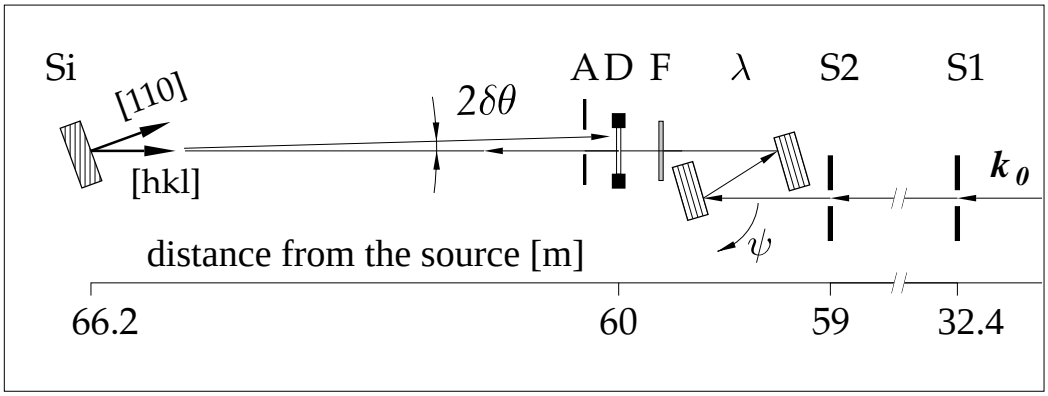

Figure 4.1: Schematic of the experiment: the radiation after a high-heat-load premonochromator (not shown) passes through the vertical slits S1 and S2, λ: λ-meter; F: ^{57}Fe foil used as a source of Mössbauer radiation; D: semitransparent avalanche photo-diode with 1 ns time resolution; A: 4 mm aperture, Si: reference silicon single crystal with (110) surface in an evacuated thermostat on a 4-circle goniometer. The distances from the APS source are given.

tons. The foil is 6 μm thick, enriched to 95% in ^{57}Fe. At some angle of the λ-meter the wavelength of the transmitted radiation coincides with $\lambda_{\rm M}$ - Fig. 4.2. At precisely this angle resonant excitation of the ^{57}Fe nuclei occurs and photons are re-emitted with a delay of typically 140 nanoseconds relative to the incident synchrotron radiation pulse. The delayed emission permits discrimination and provides a clear signal of nuclear resonant excitation. Once the Mössbauer wavelength is also measured using the λ-meter, the relation between a and $\lambda_{\rm M}$ can be established.

The detector is a semitransparent APD, as described in sec.2.3.

The λ-meter in our experiment is a silicon channel-cut crystal. Its temperature is kept at 303.8 K with a stability of 2 mK. The symmetric Bragg reflection (777) is used. The wavelength λ at the exit of the λ-meter varies as a function of the angle of incidence θ of the beam to the (777) atomic planes. The variation of the wavelength is performed by rotation of the channel-cut crystal mounted on a high-angular resolution rotation stage (KOHZU KTG-15) with a step of 25 nrad. The rotation angle ψ is measured with a Heidenhain ROD800C angle encoder and AWE1024 interpolation electronics, which has a resolution of 0.175 μrad. Figure 4.2 shows the detected back-reflected radiation as well as the Mössbauer radiation on the ψ-scale.

The intrinsic relative width of the (777) reflection on the wavelength scale for x rays with $\lambda \simeq 0.86$ Å is $\Delta\lambda/\lambda \simeq 3.5 \cdot 10^{-7}$. The center of the reflection profile can be determined much more exactly. This allows one to measure wavelengths with a relative uncertainty of better than 10^{-7} using a third reflection. To achieve this precision two conditions have to be fulfilled: i) the divergence of the incident beam in the plane of dispersion should be less than the angular width of the (777) reflection - 1.2 μrad, and ii) the direction of the incident beam should be kept constant *independent* of the wavelength of the x rays. To ensure this a system of two slits S1 and S2 of appropriate widths at a large mutual separation is used.

As was discussed in sec. 2.4.3, at exact Bragg backscattering in silicon, multiple-beam scattering takes place and more complex equations should be used in place of (4.1). To avoid this problem, we perform the measurements off normal incidence at $\delta\theta = 0.3$ mrad where the multiple-beam effects vanish – see Fig. 2.18 – and apply eq. (4.1) with the precisely known small $\delta\theta^2$-correction[2]. The $\delta\theta = 0.3$ mrad offset is adjusted with the help of a 4 mm aperture (A) installed downstream of the detector.

The rotation angle $\psi_{_H}$ of the λ-meter at which it transmits x rays matching

[2]Due to the $\delta\theta^2$-dependence in (4.1) a deviation from normal incidence by $\delta\theta \simeq 0.3$ mrad changes the wavelength by only $4.5 \cdot 10^{-8}\lambda_{\rm c}$.

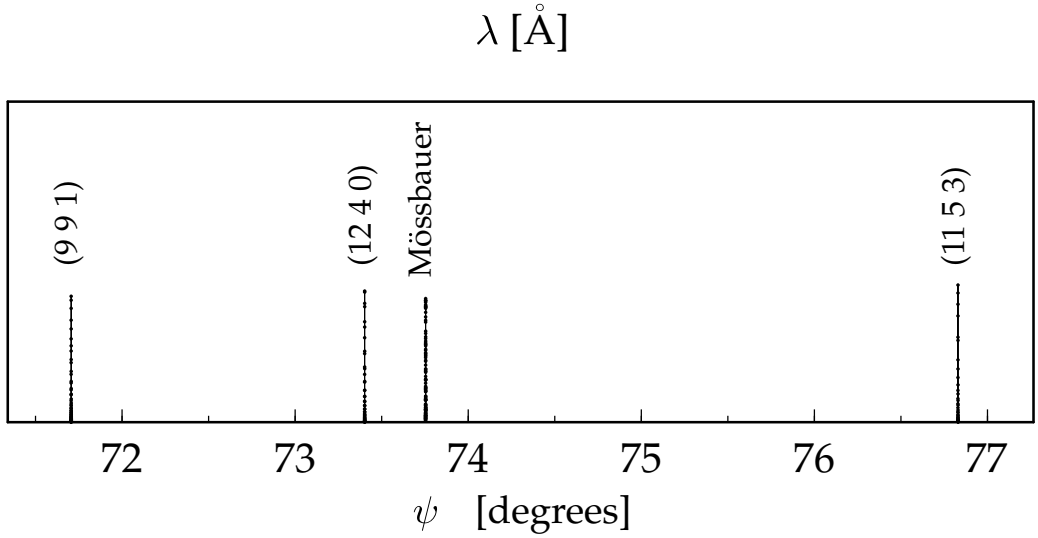

Figure 4.2: Back-reflected and Mössbauer radiation in the detector vs the rotation angle ψ of the λ-meter. The wavelength scale is calculated according to eq. (4.2)

the backscattering reflection (hkl) is calculated by using eqs. (4.2) and (4.1). Eq. (4.2) allows one to determine the rotation angle $\psi_{\rm M}$ at which the λ-meter transmits the Mössbauer radiation. For the difference $\psi_{_H} - \psi_{\rm M} = \delta\psi_{_H}$, which is measured in the experiment, we obtain:

$$\delta\psi_{_H} = \arcsin\left[\frac{2\tilde{a}\,x}{\sqrt{h^2+k^2+l^2}} - \zeta\right] - \arcsin\left[x-\zeta\right]. \tag{4.6}$$

This expression is a particular case of eq. (4.5) valid for backscattering from crystals with the cubic unit cell. Here $\tilde{a} = a\left[1-\delta\theta^2/2-\delta(\lambda_{\rm M})\right]/\lambda_{\rm M}$, $x = \lambda_{\rm M}/2d^*$, and ζ are free parameters. The λ-meter was adjusted so that $\zeta \leq 10^{-4}$ ($\mid \xi \mid, \mid \eta \mid \leq 10$ mrad). It was ascertained by numerical analysis of eq. (4.6) that ζ in this case can be taken as zero without changing the value of $\tilde{a}$ by more than $10^{-8}\tilde{a}$. Thus for the determination of $\tilde{a}$ and x, $\delta\psi_{_H}$ has to be measured for two independent reflections (hkl).

4.4.2 Experimental details and discussion

The experiments with ^{57}Fe Mössbauer nradiation were performed at two synchrotron radiation facilities.

At the wiggler beamline BW4 at HASYLAB (DESY, Hamburg) the vertical source size was $\simeq 0.8$ mm. A compromise between high count rate and small beam divergence allowed us to use only relatively large vertical apertures $\simeq 100$ μm for the slits S1 and S2, separated by a distance of 19.9 m. The vertical divergence of the beam was 12 ± 2 μrad, derived from the width of the angular dependence of transmission of Mössbauer photons through the λ-meter. The count rate of Mössbauer photons was 5 Hz. The $\delta\psi_{_H}$ values were measured for the $(12\,4\,0)$ and $(9\,9\,1)$ back reflections at different temperatures of the reference crystal. Results of the evaluation of $\tilde{a}$ are given in Fig. 4.3 (full circles). They fit well to the solid line, given by the thermal expansion of silicon (Okada and Tokumaru 1984). The value of $\tilde{a}$ at $t = 22.500$°C is determined as $\tilde{a} = 6.3132545(85)$ (average over 4 measurements). The 1.3 ppm uncertainty is due to the relatively large divergence of the beam and low count rate.

To improve this result, another experiment was carried out at the undulator beamline 3-ID at the Advanced Photon Source (Argonne). The source size was 120 μm (FWHM). A system of two roller-blade slits S1 and S2 , similar to those describe by Libbert et al. (1997), was used at a distance of $\simeq 26.6$ m to collimate the beam. The smallest beam divergence of 4.5 μrad was achieved with vertical apertures of the slits of $S1 = 40$ μm and $S2 = 75$ μm, respectively. The smaller divergence and the higher count rate ($\simeq 100$ Hz for Mössbauer photons) in this experiment allowed one to achieve a higher accuracy for $\tilde{a}$. Open circles in Fig 4.3 represent results of evaluations of the APS measurements by using the pair of $(12\ 4\ 0)$ and $(9\ 9\ 1)$ back reflections. The crosses show the average for three independent pairs of back reflections: $(11\ 5\ 3)$, $(12\ 4\ 0)$ and $(9\ 9\ 1)$. The dashed lines in the inset limit the significant error corridor for the APS data. By interpolation we obtain at $t = 22.500(5)$°C:

$$\tilde{a} = 6.3132548 \pm 0.0000012. \tag{4.7}$$

This value agrees with the value determined from the HASYLAB measurements and is 7 times more accurate. By using the value of a for the reference crystal, we obtain

$$\lambda_{\mathrm{M}} = (86.025474 \pm 0.000016) \cdot 10^{-12}\ \mathrm{m}, \tag{4.8}$$

for the wavelength of the ^{57}Fe Mössbauer radiation, and

$$E_{\mathrm{M}} = (14412.497 \pm 0.003)\ \mathrm{eV}. \tag{4.9}$$

for its energy $E_{\mathrm{M}} = hc/\lambda_{\mathrm{M}}$ with Planck's constant $h = 4.13566727(16) \cdot 10^{-15}$ eV s (Mohr and Taylor 2000). It is noteworthy that our value $E_{\mathrm{M}} = 14412.497(3)$ eV

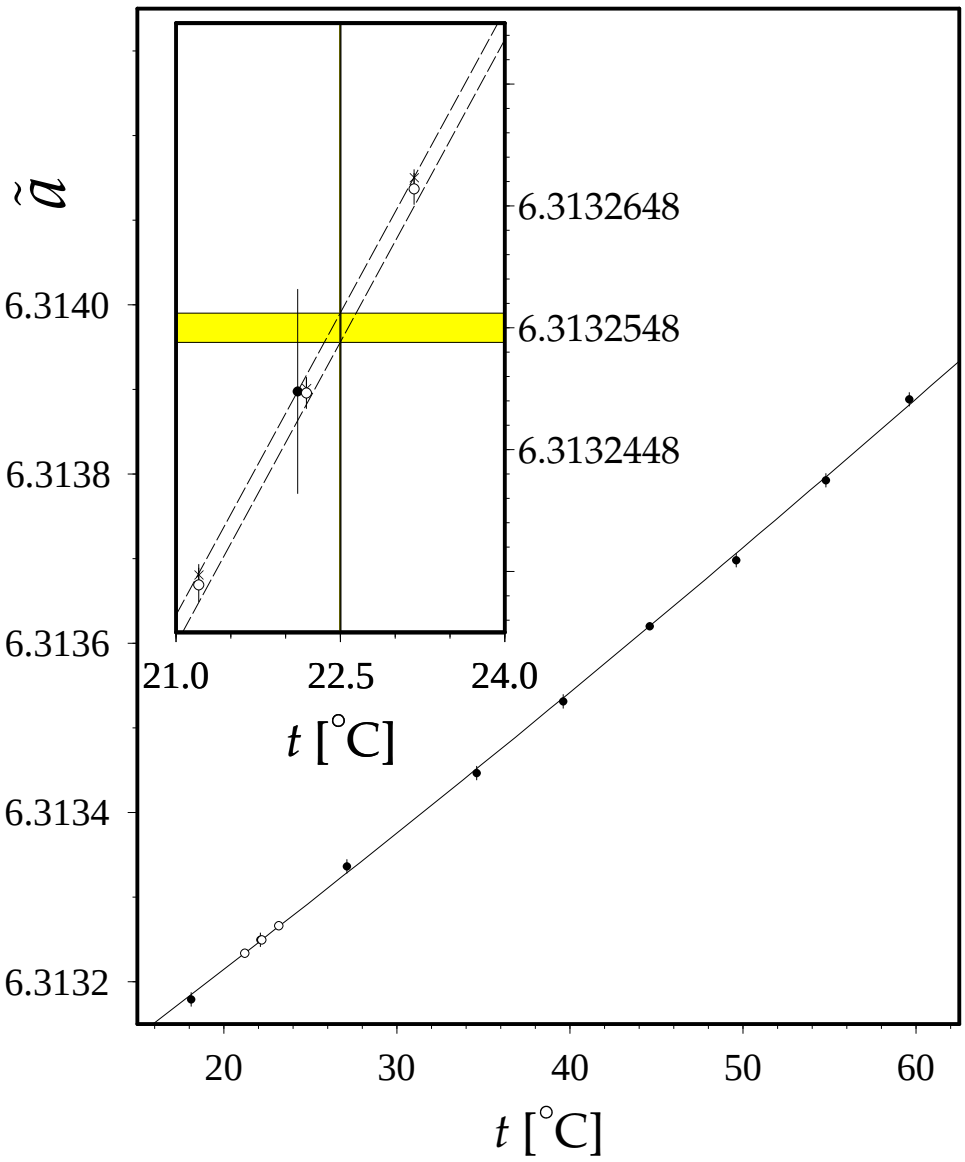

Figure 4.3: The ratio $\tilde{a}$ of the lattice constant a of the reference silicon crystal to the wavelength λ_{M} of the ^{57}Fe Mössbauer radiation in silicon measured at different temperatures of the crystal. Full ($\bullet$) and open ($\circ$) circles represent the results of evaluations of the HASYLAB and APS measurements respectively by using the pair of $(12\ 4\ 0)$ and $(9\ 9\ 1)$ reflections. The crosses ($\times$) show the results of evaluations of these measurements by using three reflections: $(11\ 5\ 3)$, $(12\ 4\ 0)$ and $(9\ 9\ 1)$. The solid line is the temperature dependence of a (Okada and Tokumaru 1984). The dashed lines in the inset limit the significant error corridor for the APS data.

agrees much better with the value $14412.47(29)$ eV used in the previous seventh edition of "Table of Isotopes" (Lederer and Shirley 1976) derived from the 35 year old measurements of Bearden (1965), than with 14413.00(15) eV from the newest edition (Firestone et al. 1996).

The accuracy can be improved by at least an order of magnitude if the beam divergence is reduced to a sub-μrad level. Future x-ray free-electron laser sources with much better emittance will certainly allow this.

4.5 α-Al_2O_3 lattice constants

As was argued in chapter 3, sapphire is a potential new material for x-ray crystal optics, especially attractive for backscattering mirrors for interferometers, high energy resolution monochromators and analyzers, since it permits (unlike silicon) exact Bragg backscattering with high reflectivity for x rays in the 10-50 keV spectral range. Precise values of the sapphire lattice constants and their temperature dependence are required to predict the Miller indices (hkl) of back reflections and relevant crystal temperatures for desired x-ray energies. However, lattice constants and thermal expansion data for α-Al_2O_3 reported in the literature (Kirfel and Eichhorn 1990, Brown et al. 1992, Aldebert and Traverse 1982, Lewis et al. 1982, Yim and Paff 1973) differ by up to 100 ppm. This imposes large uncertainties in the predicted back reflections and relevant crystal temperatures. To ensure more precise predictions the lattice constants of sapphire have been measured here with a relative uncertainty of up to 0.1 ppm in the temperature range from 286 to 374 K. Recently these measurements have been extended to the 4-290 K range (Lucht et al. 2001). The experimental method was presented in sec. 4.3, the experimental details are described in sec. 4.5.1 and the results are presented in sec. 4.5.2 All the measured values are given both in λ_{M} units and in meters.

4.5.1 Experimental details

The experiments were performed at the undulator beamline 3-ID at the Advanced Photon Source (Argonne). Practically the same experimental setup was used as outlined in sec. 4.4, Fig. 4.1. The differences are presented in the following.

The reference Si crystal is replaced by an α-Al_2O_3 single crystal in the furnace on the 4-circle goniometer. Exact Bragg backscattering ($\delta\theta = 0$) is employed. The Bragg back reflections in α-Al_2O_3 used in the experiment are listed in Tab. 4.1. The sapphire crystal grown by the heat-exchange method (Schmid et al. 1994) is employed in the present studies. The dislocation density in the sample is $\simeq 3 \times 10^3$ cm^{-2} as measured with white beam backscattering x-ray topography (sec. 3.4). The lattice constants are measured at different crystal temperatures in the range from 286 to 374 K. The crystal in the furnace is maintained at a fixed temperature with a stability of ≤ 1 mK.

A PT100 thermo-resistor is used for the measurement of the crystal temperature. It has been calibrated in the Physikalisch-Technische Bundesanstalt (Braunschweig, Germany) over the temperature range 291.3–299.2 K with an

$(hkil)$	λ [pm]	$\widehat{[000\,1][hkil]}$ [degrees]	$\widehat{[10\bar{1}0][hkil]}$ [degrees]	ΔE [meV]
(0 0 0 30)	86.60572	0.0	0.0	13.2
(1 6 $\bar{7}$ 22)	86.07066	43.2162	52.4109	1.8
(1 3 $\bar{4}$ 28)	85.97935	22.0934	46.1021	6.1
(2 6 $\bar{8}$ 20)	85.81588	48.6577	46.1021	4.5

Table 4.1: Miller indices $(hkil)$ of selected reflections in α-Al_2O_3 with backscattering wavelengths $\lambda = 2d_{_H}/(1 + w_{_H})$ close to $\lambda_{\rm M}$. The λ values are calculated by using the lattice constants at $T = 287.3$ K as obtained in the present studies. The angular deviation of the diffraction vector from the main crystallographic directions as well as the expected theoretical energy widths are given as well.

accuracy of better than 10 mK, and at 373 K with an accuracy of 10 mK. Using this calibration a linear correction was applied to the $T(R)$ characteristic curve of the PT100 thermo-resistor as given by the IEC751 standard.

The λ-meter is the same Si(777) channel-cut crystal. As previously mentioned, the channel-cut crystal is mounted on a high-angular resolution KOHZU KTG-15 rotation stage with a step width of 25 nrad. The rotation angle ψ is measured with the new IK320 interpolation electronics, rendering an improved angular resolution of 43 nrad.

Although the same roller-blade slits are implemented at the same distance of $\simeq 26$ m, the actual divergence was measured to be 9 μrad. It is twice as large as in the previous experiment and four times as large as one would expect from the opening of the slits and their separation. Presumably, this higher divergence results from scattering on Be-windows which are installed between the experimental hutches. This larger than expected divergence deteriorates the accuracy of the measurement.

A semitransparent detector was placed immediately after the α-Fe foil and $L = 6.2$ m upstream from the backscattering crystal. The detector's aperture was $D^2 = 10 \times 10$ mm^2. Thus only those x rays which deviated from exact backscattering by a maximum of $\delta\theta = D/4L = 0.4$ mrad were detected. The relative energy variation due to the angular dispersion was small $(\delta\theta)^2/2 \leq 8 \times 10^{-8}$, cf. eq. (4.1), and was neglected in the data evaluation.

For each temperature of the sapphire crystal the angles $\psi_{_H}$ as well as the reference angle $\psi_{\rm M}$ of the λ-meter were measured. For a perfectly stable setup $\psi_{\rm M}$ should be constant. Figure 4.4 shows the values of $\psi_{\rm M}$ from run to run. The typical duration of one run (measurements at one temperature) is 4-5 hours.

This relatively long duration was due to the slow motion of the high-angular resolution KOHZU KTG-15 rotation stage. The graph demonstrates the stability of the experimental setup.

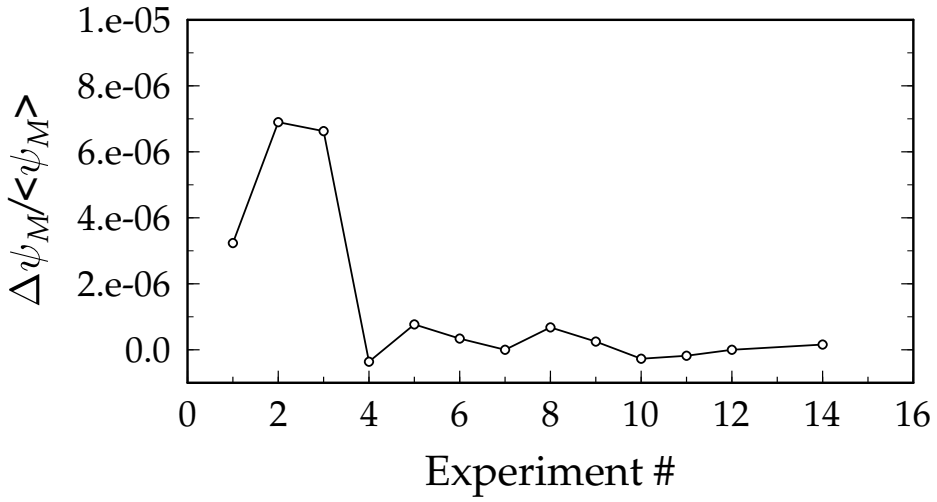

Figure 4.4: Relative variation (from run to run) of the reference angle ψ_{M} - the angle of the λ-meter at which it selects the Mössbauer radiation.

4.5.2 Data evaluation

Sapphire has a rhombohedral lattice, which can be specified in hexagonal axes of reference with two independent lattice constants $a = b$ and c. The interplanar distance in a hexagonal lattice is given by eq. (3.2). Thus the three unknowns a, c, and d^* enter eq. (4.5). To be able to determine the three unknowns, the angular difference $\delta\psi_H$ has to be measured for at least three different back reflections for each crystal temperature. In the present experiment, four angular differences $\delta\psi_H$ for four Bragg reflections are measured, as listed in Tab. 4.1. This allows us to compose four independent sets, each with three equations of type (4.5), yielding a solution for the three unknowns.

From the four independent solutions the averaged values of a and c and their standard errors are computed. However, the solution resulting from the combination of $(0\ 0\ 0\ 30)$, $(2\ 6\ \overline{8}\ 20)$, and $(1\ 6\ \overline{7}\ 22)$ reflections is ignored, since it yielded systematically significantly different values. This is attributed to the fact that the $(2\ 6\ \overline{8}\ 20)$ and $(1\ 6\ \overline{7}\ 22)$ atomic planes are nearly parallel (only $\approx 7^\circ$ apart, see Tab. 4.1) which – in combination with the insufficient crystal quality

T [K]	$\widetilde{a}$ [λ_{M}]	$\widetilde{c}$ [λ_{M}]	a [Å]	c [Å]	$\delta a/a$ $\times 10^{-7}$	$\delta c/c$ $\times 10^{-7}$
.						
286.143(8)	5.532056(5)	15.101192(2)	4.758977(4)	12.990872(2)	8.4	1.5
286.968(8)	5.532080(10)	15.101262(5)	4.758998(9)	12.990932(4)	18.9	3.1
287.125(8)	5.532083(12)	15.101278(6)	4.759001(10)	12.990946(5)	21.0	3.9
288.108(8)	5.532106(9)	15.101369(5)	4.759020(8)	12.991024(4)	16.8	3.1
312.533(9)	5.532822(6)	15.103584(2)	4.759636(5)	12.992930(2)	10.5	1.5
322.359(9)	5.533110(3)	15.104526(1)	4.759884(3)	12.993740(1)	6.3	0.77
332.184(9)	5.533428(5)	15.105504(2)	4.760158(4)	12.994581(2)	8.4	1.5
342.010(9)	5.533741(6)	15.106472(2)	4.760427(5)	12.995414(2)	10.5	1.5
351.836(9)	5.534064(9)	15.107456(3)	4.760705(8)	12.996261(3)	16.8	2.3
361.661(9)	5.534379(3)	15.108467(1)	4.760976(3)	12.997130(1)	6.3	0.77
371.339(10)	5.534699(3)	15.109478(2)	4.761251(3)	12.998000(2)	6.3	1.5
375.000(10)	5.534768(1)	15.109658(1)	4.761310(1)	12.998155(1)	2.1	0.77
374.287(10)	5.534804(1)	15.109758(1)	4.761341(3)	12.998241(1)	6.3	0.77

Table 4.2: Lattice constants of Al_2O_3 in the temperature range 286.1–374.3 K.

– may cause a large error. Mean values and standard errors of a and c are given in Tab. 4.2 for different temperatures, in units of λ_{M} and Å. The errors of a and c are primarily due to the averaging process, as described above. Other error sources, namely the uncertainties in T and λ_{M}, are about two orders of magnitude smaller.

A 6^{th}-order polynomial was used to fit the experimental data. The polynomial coefficients are given in Tab. 4.3. One should note that these formulae are not suitable for extrapolation of the lattice constants outside the 285.9–374.3 K temperature range, and do not correspond to any theoretical model for thermal expansion. Mean values of the lattice constants and the polynomial fit are shown in Fig. 4.5.

By using the polynomial fit, one can calculate at room temperature $T = 295.65$ K the lattice parameters

$$a = 4.759213(8)\,\text{Å} \tag{4.10}$$

$$c = 12.991586(4)\,\text{Å} \tag{4.11}$$

and linear thermal expansion coefficients

$$\beta_{[10\overline{1}0]} = 5.22 \cdot 10^{-6}\ \mathrm{K}^{-1} \tag{4.12}$$

$$\beta_{[0001]} = 5.92 \cdot 10^{-6}\ \mathrm{K}^{-1}, \tag{4.13}$$

respectively.

The relative deviations of the measured data from the values calculated with the interpolation formula is shown in Fig. 4.6. Large deviations of the data calculated by using the ignored combination of $(0\ 0\ 0\ 30)$, $(1\ 6\ \overline{7}\ 22)$, and $(2\ 6\ \overline{8}\ 20)$ reflections is clearly seen here. Table 4.2 and Fig. 4.6 also reveal larger

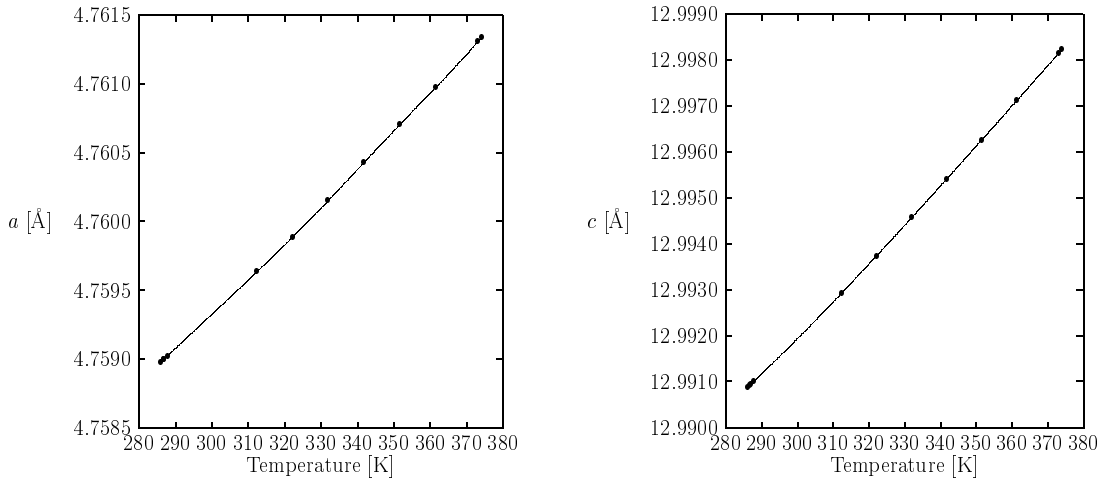

Figure 4.5: Lattice constants a and c of α-Al_2O_3. Solid line is a 6^{th}-order polynomial fit with the parameters given in Tab. 4.3.

a[Å]	=	$\sum_{i=0}^{6} p_i\,(T[\mathrm{K}])^i$	c[Å]	=	$\sum_{i=0}^{6} q_i\,(T[\mathrm{K}])^i$
p_0	=	16.5918	q_0	=	13.0572
p_1	=	-0.2211998	q_1	=	$-8.89587 \cdot 10^{-4}$
p_2	=	$1.73069 \cdot 10^{-3}$	q_2	=	$3.92279 \cdot 10^{-6}$
p_3	=	$-7.17791 \cdot 10^{-6}$	q_3	=	$-7.03958 \cdot 10^{-9}$
p_4	=	$1.67047 \cdot 10^{-8}$	q_4	=	$4.76801 \cdot 10^{-12}$
p_5	=	$-2.06828 \cdot 10^{-11}$	q_5	=	$-5.35555 \cdot 10^{-19}$
p_6	=	$1.06437 \cdot 10^{-14}$	q_6	=	$6.78943 \cdot 10^{-22}$

Table 4.3: Interpolation formulae for lattice constants of α-Al_2O_3 in the temperature range 285.8–374.3 K.

errors for a and c at lower temperatures. This is attributed to the stronger variation of the reference angle of the λ-meter, ψ_{M}, at the beginning of the experiment (see Fig. 4.7). The smaller relative error in the determination of c compared with that of the a lattice parameter is evidently due to the fact that all reciprocal lattice vectors of the back reflections used in the measurements are much closer to the c-axis of the crystal.

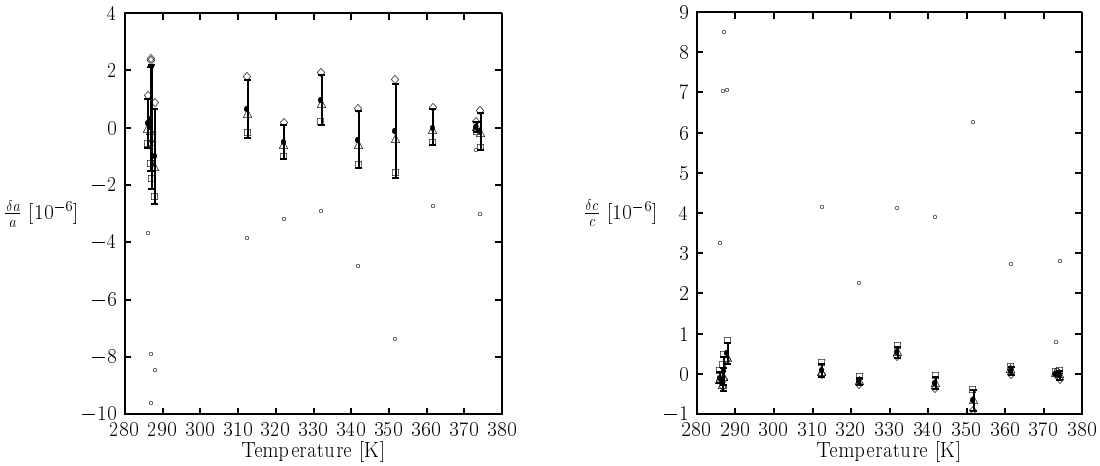

Figure 4.6: Relative deviation of the 6^{th}-order polynomial fit (Tab. 4.3) from the a and c values evaluated from: □ – $(1\ 3\ \overline{4}\ 28)$, $(0\ 0\ 0\ 30)$, and $(1\ 6\ \overline{7}\ 22)$ back reflections; ◇ – $(1\ 3\ \overline{4}\ 28)$, $(0\ 0\ 0\ 30)$, $(2\ 6\ \overline{8}\ 20)$ back reflections; △ – $(1\ 3\ \overline{4}\ 28)$, $(2\ 6\ \overline{8}\ 20)$, $(1\ 6\ \overline{7}\ 22)$ back reflections; ○ – $(0\ 0\ 0\ 30)$, $(1\ 6\ \overline{7}\ 22)$, $(2\ 6\ \overline{8}\ 20)$ back reflections (ignored in the calculation of the average values). The average of the □, ◇ and △ values is shown by •.

4.5.3 Discussion and conclusions

A γ-ray wavelength standard was used to measure the lattice constants of α-Al_2O_3 in the temperature range from 286 to 374 K by using exact Bragg backscattering. All the measured values are given both in λ_{M} units and in meters. Therefore, should the λ_{M} value be refined, the values of the lattice constants could be recalculated. Lucht et al. (2001) have recently extended these measurements into the 4-290 K temperature range.

The relative experimental uncertainty in the determination of the lattice constant c of α-Al_2O_3 is in the range 0.4-0.1 ppm. The relative uncertainty in the determination of the lattice constant a is in the range 2-0.6 ppm. The main factors, which have deteriorated the accuracy were: (i) the divergence of the

beam (9 μrad instead of expected 2 μrad), and (ii) the lack of crystal perfection of the α-Al_2O_3 sample. A perfect crystal would have allowed 10 times more precise measurements.

The measured temperature dependence of the lattice constants of α-Al_2O_3 are important for the design of high energy resolution monochromators and analyzers. The data obtained allow one to predict more precisely Miller indices of back reflections and relevant crystal temperatures for desired x-ray energies. As an example, Tab. 3.1 lists Miller indices $(hkil)$ of atomic planes and attendant temperatures T_H of α-Al_2O_3 for which the energies of peak reflectivity at normal incidence match energies of selected Mössbauer transitions.

4.6 Wavelengths of the ^{151}Eu, ^{119}Sn, and ^{161}Dy Mössbauer photons

Precise values of the sapphire lattice constants, as presented in the previous section, as well as the ability of sapphire crystals to back-reflect x rays of any energy in the 10-50 keV spectral range, are used here to determine the wavelengths of ^{151}Eu, ^{119}Sn, and ^{161}Dy Mössbauer radiations. Mössbauer radiation of different nuclei can provide a set of reference wavelengths in the hard x-ray range with a uniquely small uncertainty and easy reproducibility. In current crystallography studies, x-ray and nuclear spectroscopy use the set of wavelengths of K_α characteristic x rays of atoms (Bearden 1965, 1967). A set of Mössbauer wavelengths can take over this role as brilliant Mössbauer radiation sources are available at synchrotron radiation facilities worldwide. Mössbauer radiation has at least 10^6 times smaller spectral width and is much less perturbed by variations of external conditions. However, the relative uncertainty in the knowledge of the absolute values of the wavelengths other than ^{57}Fe Mössbauer radiation is in the best cases about 10 ppm: (Kikuta 1994, Leupold et al. 1996, Koyama et al. 1996). The results of measurements with a relative uncertainty $\simeq 0.8 - 0.4$ ppm are reported here for the wavelengths of the Mössbauer transitions in ^{151}Eu, ^{119}Sn, and ^{161}Dy nuclei. They are based on the publication of Shvyd'ko et al. (2002). All the measured values are given both in λ_{M} units and in meters.

4.6.1 Experimental details

Figure 4.7 shows the schematic of the experimental setup for the observation of Bragg backscattering of Mössbauer radiation. The experiment is a continuation of the measurements presented in the previous section. Synchrotron radiation pulses from the undulator are monochromatized at Mössbauer energies to a bandwidth of ≈ 1 eV width with a diamond high-heat-load monochromator (not shown in Fig. 4.7). The radiation is further aimed at the target (T) containing the Mössbauer nuclei. For selected nuclei Tab. 4.4 provides the energy E, lifetime τ, natural spectral width $\Gamma = \hbar/\tau$ of the relevant excited nuclear state, and the target used to generate Mössbauer photons.

The nuclei excited by 150 ps radiation pulses emit photons in a narrow energy band of $\approx \Gamma$ (5-50 neV) with a delay $\approx \tau$ (10-150 ns). The detector is installed slightly off the incident beam axis, so as not to be overloaded with the high photon flux of the 1 eV beam. The prompt and the delayed radiation components hit the sapphire crystal.

Isotope	E [keV]	τ [ns]	Γ [neV]	Target
^{57}Fe	14.4	141.2	4.7	α-^{57}Fe
^{151}Eu	21.5	13.8	47.5	EuO
^{119}Sn	23.8	26.0	25.3	$^{119}Sn_20$
^{161}Dy	25.6	41.0	15.7	Dy (at 20K)

Table 4.4: Excitation energy E, lifetime τ, natural energy width Γ, and target composition of selected Mössbauer nuclei (Firestone et al. 1996) .

In accordance with the selected isotope, the atomic planes $(hkil)$ of the α-Al_2O_3 sample as given in Tab. 4.5 are adjusted to a position almost normal to the incident beam by observing the corresponding Bragg back reflections. The angular deviation from exact backscattering is $\delta\theta = 0.4$ mrad. The correction factor $\delta\theta^2/2 = 8 \times 10^{-8}$ in eq. 4.1 is ignored in the following.

The energy widths of the back reflections are in the meV-range: Tab. 4.5. The temperature variation of the backscattering energies in α-Al_2O_3 is typically 0.1 eV/K. Thus to observe backscattering of the prompt radiation component having an energy bandwidth of 1 eV the crystal temperature should be correct within ≈ 10 K, which is easy. However, to observe backscattering of the Mössbauer radiation the crystal temperature must be tuned to the correct temperature with mK-accuracy.

The crystal temperatures T at which backscattering of the Mössbauer pho-

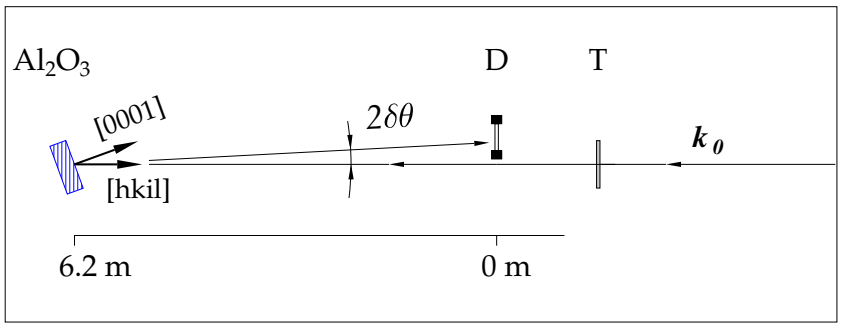

Figure 4.7: The schematic of the setup for observation of backscattering of the Mössbauer radiation. The target (T) contains Mössbauer nuclei which are excited by the incident radiation pulse. The Mössbauer photons emerging from the target are reflected from the sapphire single crystal α-Al_2O_3 and detected by the avalanche photo-diode (D).

Isotope	$(hkil)$	T [K]	ΔT (exp) [mK]	ΔE (exp) [meV]	ΔE (theory) [meV]
^{57}Fe	$(1\ 3\ \overline{4}\ 28)$	371.582(8)	66	6.5	5.8
^{151}Eu	$(3\ 2\ \overline{5}\ 43)$	287.125(8)	67	8.3	0.6
^{119}Sn	$(6\ 5\ \overline{11}\ 40)$	286.968(10)	109	14.5	1.1
^{161}Dy	$(3\ 2\ \overline{5}\ 52)$	374.624(40)	46	7.6	0.7

Table 4.5: Miller indices $(hkil)$, crystal temperature T, temperature width ΔT and energy width ΔE (as measured and as expected from the dynamical theory) of backscattering reflections in α-Al_2O_3 for the ^{57}Fe, ^{151}Eu, ^{119}Sn, and ^{161}Dy Mössbauer radiation.

tons is observed and their widths ΔT are given in Tab. 4.5. The corresponding energy widths ΔE are computed from ΔT by using eq. (2.76) with $d_{_H}(T)$ values as obtained in sec. 4.5. The experimental energy widths of the back reflections are an order of magnitude larger than the expected theoretical values. This is attributed to a relatively high dislocation density in the crystal used. The crystal quality is a serious factor that deteriorates the accuracy of the present measurements.

The nuclear resonance in ^{161}Dy was observed in another experiment at the undulator beamline PETRA-1 (DESY, Hamburg) with a similar backscattering setup and with the same sapphire crystal, see sec. 4.8 or (Shvyd'ko et al. 2001). Backscattering of the ^{161}Dy Mössbauer radiation was observed from the $(3\ 2\ \overline{5}\ 52)$ atomic planes in sapphire at a temperature which was $\delta T = 3.04(1)$ K above the temperature of backscattering of the ^{57}Fe Mössbauer radiation from the $(1\ 3\ \overline{4}\ 28)$ atomic planes. This precisely known temperature difference together with the crystal temperature for backscattering of the ^{57}Fe Mössbauer radiation obtained in the present experiment (Tab. 4.5) are used to determine the absolute crystal temperature for backscattering of the ^{161}Dy Mössbauer radiation.

4.6.2 Wavelengths of the ^{151}Eu, ^{119}Sn, and ^{161}Dy Mössbauer radiation

With the measured lattice parameters of sapphire (Tabs. 4.2, and 4.3), the temperatures for backscattering of the Mössbauer radiation (Tab. 4.5), and using eqs. (3.2), and (4.1), it is possible to determine the wavelengths of the ^{151}Eu, ^{119}Sn, and ^{161}Dy Mössbauer radiation. The results are presented in Tab. 4.6.

Isotope	$\tilde{\lambda}$ [λ_{M}]	$\delta\tilde{\lambda}/\tilde{\lambda}$ $\times 10^{-7}$	λ [Å]	$\delta\lambda/\lambda$ $\times 10^{-7}$	E [eV]
^{57}Fe	1.0	0	0.86025474(16)	1.9	14412.497(3)
^{151}Eu	0.66905978(28)	4.1	0.57556185(27)	4.7	21541.418(10)
^{119}Sn	0.60355158(43)	7.1	0.51920811(39)	7.4	23879.478(18)
^{161}Dy	0.56186073(18)	3.3	0.48334336(19)	4.0	25651.368(10)

Table 4.6: Wavelengths λ and energies E of the ^{151}Eu, ^{119}Sn, and ^{161}Dy Mössbauer radiation as determined by exact backscattering from α-Al_2O_3 crystal. The λ and E data for ^{57}Fe are from (Shvyd'ko et al. 2000a).

The major source of the errors for the $\tilde{\lambda}$ values expressed in λ_{M} units are the uncertainties in the lattice parameters of sapphire $\tilde{a}$ and $\tilde{c}$. The uncertainty of λ given in meters and of E given in eV includes additionally the uncertainty of λ_{M}.

Our results agree well with the Mössbauer energy values previously reported by Koyama et al. (1996): $E = 21541.49(16)$ eV and Leupold et al. (1996): $E = 21541.7(5)$ eV for ^{151}Eu, by Kikuta (1994) for ^{119}Sn: $E = 23879.5(5)$ eV, and by Koyama et al. (1996) for ^{161}Dy: $E = 25651.29(16)$ eV. The relative accuracy of our data is better by more than one order of magnitude.

4.6.3 Discussion and conclusions

The γ-ray wavelength standard was used to measure the wavelengths of the Mössbauer radiation of ^{151}Eu: 57.556185(27) pm, ^{119}Sn: 51.920811(39) pm, and ^{161}Dy: 48.334336(19) pm. All the measured values are given both in λ_{M} units and in meters. Therefore, should the λ_{M} value be refined, the values of the wavelengths can be recalculated.

The relative uncertainty achieved in the determination of the wavelength of Mössbauer radiation is in a range of 0.4-0.7 ppm. The main factors, which have deteriorated the accuracy were: (i) the divergence of the beam (9 μrad instead of expected 2 μrad), and (ii) the lack of crystal perfection of the α-Al_2O_3 sample. Perfect crystals would have allowed 10 times more precise measurements.

The measured wavelengths of the Mössbauer photons could be used as a

set of reference wavelengths in the hard x-ray range of the electromagnetic radiation spectrum providing a uniquely small uncertainty and easy reproducibility.

4.7 Powder Bragg backscattering spectroscopy

Powder diffraction is a powerful tool in x-ray crystallography. The potential of this technique in extreme backscattering geometry has been studied by Shvyd'ko et al. (2000b) and is presented in this section in more detail.

Powder backscattering spectroscopy means that in contrast to standard powder diffraction technique the scattering angle is kept fixed at 180° and the x-ray energy is tuned. One expects several advantages in comparison to the standard technique. The simple geometrical arrangement of backscattering with only one path for the incoming and outgoing beams enables access to samples with very small angular aperture. This is important if the samples are placed in a pressure cell, cryostat, or furnace, etc. As the scattering geometry does not change the extinction corrections are not required. The highest possible momentum transfer and thus the highest possible spatial resolution is achieved in backscattering.

Another important point is that a very simple Bragg's law for backscattering (4.1) may be used for simple and accurate measurements of crystal structure parameters as well as for x-ray wavelengths. In most cases one can use the simplest relation $2d_{_H} = \lambda$ without account of the incidence angle $\delta\theta$. As distinct from the single crystal measurements presented in the previous sections, it does not require tedious angular adjustment of the samples and, what is of even more importance, it does not require single crystal samples. The payoff for this is clearly a lower accuracy of measurements than with single crystals. This is illustrated in Fig. 2.13. The thinner (or the smaller) the sample the broader are the diffraction peaks and thus the smaller is the accuracy in determination of their positions.

The accuracy of measurements is limited:
1. By the angular deviation $\delta\theta$ from normal incidence, which is also defined by the detector aperture. $\delta\theta$ can be easily made less than 10^{-3}, so that the accuracy of the backscattering relation $2d_{_H} = \lambda$ can be made better than 1 ppm, cf. eq. (4.1).
2. By the energy resolution of the λ-meter which selects and tunes the wavelength (energy) of the incident x rays. Presently it can be chosen in the range from $\simeq 1$ eV down to $\simeq 1$ meV.
3. By the energy width of the backscattering reflections. For thick single crystals it is in the meV range. However, for small ($\simeq 1$ μm) powder particles the energy width may increase to about 1 eV.

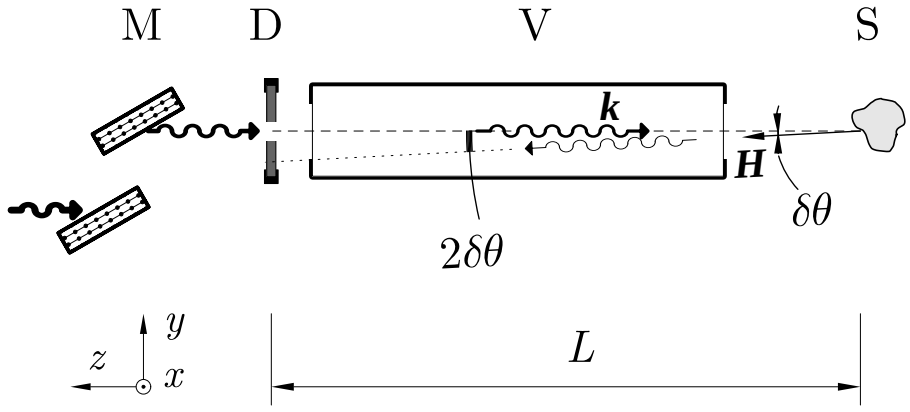

Figure 4.8: The schematic of the experiment. M: tunable high heat load diamond C(111) monochromator used as λ-meter; D: x-ray detector with a time resolution of $\simeq 0.7$ ns; V: vacuum flight tube; S: powder sample; $\delta\theta$: angle between the wave vector $\boldsymbol{k}$ of the incident radiation and the scattering vector $\boldsymbol{H}$; $L \simeq$6 m.

4.7.1 Experimental details

The experiments were performed at the undulator beamline 3-ID at the APS (Argonne). Figure 4.8 shows the schematic of the experimental setup. A diamond C(111) high-heat-load monochromator, used as the λ-meter, transmits x rays with a bandwidth of 1 eV and is tuned in the range of 14 to 15 keV.

The detector should be put as close to the incident beam as possible to achieve $\delta\theta < 10^{-3}$. This leads, however, to an enormous background and thus hinders the performance of experiments in the backscattering geometry. The problem is solved by exploiting the pulse structure of the synchrotron radiation and by using a detector with good time resolution. Because the background arises from the incident pulse going to the sample and the signal consists of the pulse reflected from the sample, a time delay $\tau_{\rm d} = 2L/c$ exists between the background and the signal. This enables the discrimination of the signal from the background, cf. sec. 2.3 and Fig. 2.8.

The detector employed in the experiment consists of two avalanche photodiodes, with a time resolution of $\simeq 0.7$ ns, as described in sec. 2.3, placed 2 mm above and below the incident beam, at a distance of $L = 6$ m upstream from the sample. Under these conditions $\delta\theta < 0.4$ mrad and $\tau_{\rm d} \simeq 40$ ns.

4.7.2 Results and discussion

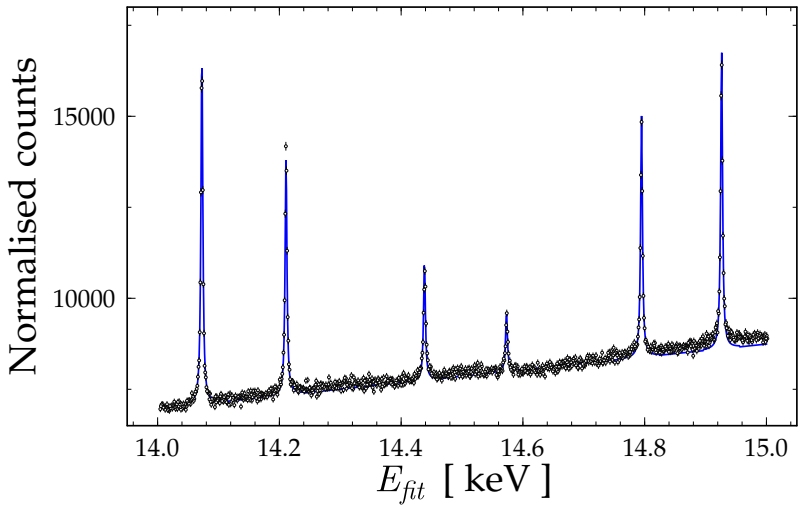

Figure 4.9: Bragg backscattering spectrum from Si powder sample (circles). As the lattice constant of silicon $a = 5.4310196$ Å is precisely known a fit of the theoretical backscattering spectrum (solid line) to the experimental points determines the energy scale E_{fit} of the λ-meter.

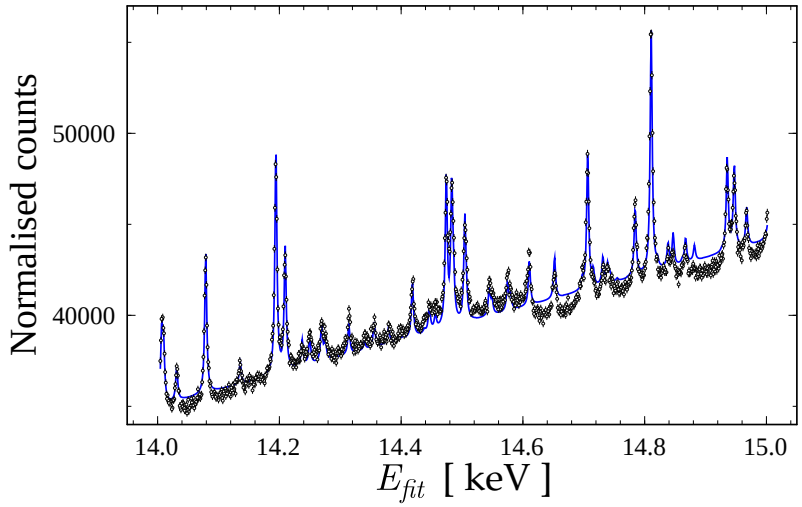

Figure 4.10: Bragg backscattering spectrum from α-Al_2O_3 powder sample. The solid line was calculated with program package BASS.

Figures 4.9 and 4.10 show results of measurements of the standard NIST powder samples of Si and α-Al_2O_3, respectively. The radiation flux was $\simeq$

10^{12} photons/s. The spectral lines in case of the Si sample are more intense and the signal to noise ratio is much better, since Bragg reflections are strongly degenerate. The data at each point were collected for about 0.5 s in case of the Si and 3 s in case of the α-Al_2O_3 sample and normalized to the incident flux. To average the orientation of the powder particles, the samples were rotated about an axis perpendicular to the beam. The spectra recorded without rotating the sample show the spectral lines at the same positions but with changed strengths.

The strength of the spectral lines is given by eq. (2.95), which describes the reflectivity of a thin crystal. The strength is proportional to $|\chi_H|^2$ and thus to the square of the structure factor F_H, which contains crystal structure information. Thus, the backscattering powder diffraction spectra provide information similar to that of the usual angular dispersive powder diffraction.

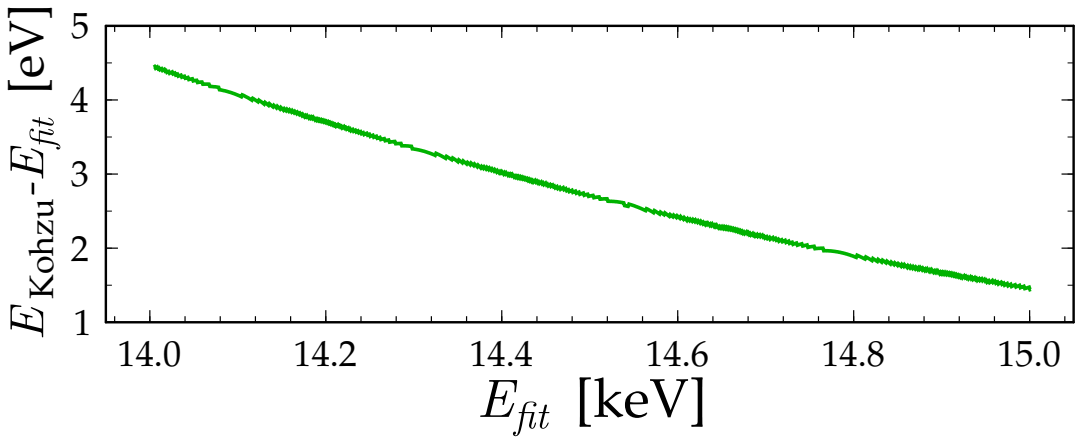

Figure 4.11: Difference in values of the x-ray energy of the KOHZU high-heat-load monochromator read-back E_{Kohzu} and the x-ray energy E_{fit} obtained from the fit of the Si backscattering spectrum in Fig.4.9.

The line form is very close to a Lorentzian. This is typical for Bragg backscattering spectra in non-perfect crystals, see sec. 2.4.1. The linewidth is typically 4 eV. This is more than the 1 eV width of the incident radiation. Presumably it is determined by the size of the particles. To cause such a broadening the particles should have a diameter of $\simeq 150$ nm, see eq.(2.102).

The evaluation of the spectra was performed with the program package BASS (Shvyd'ko 1998). The lattice constant of silicon is well known. This allows one to ascertain the energy scale of the λ-meter from the fit of the experimental spectrum - Fig. 4.9. Figure 4.11 shows the difference between the fit val-

ues and the internal calibration of the monochromator. This is in fact a demonstration of a technique by which it is possible to calibrate x-ray monochromators in a simple way and is much more exact than using the K-edges.

The best fit of the α-Al_2O_3 Bragg backscattering spectrum is achieved for the lattice parameters $a = 4.75931(4)$, $c = 12.9920(1)$. The accuracy is $\simeq 10$ ppm, which is high for a powder diffraction technique. It is limited by the 4 eV linewidth and the capability of measuring the position of lines with better than 0.2 eV accuracy. The data are in agreement with the single crystal data at $T \simeq 300$ K of sec. 4.5. The other crystallographic parameters obtained from the fit of the intensities of lines – positions of atoms in the unit cell and anisotropic thermal parameters – are in agreement with the angle-dispersive powder diffraction measurements of Brown et al. (1992).

4.8 Nuclear Resonant Scattering from ^{161}Dy

The sapphire backscattering monochromator is employed here to study nuclear resonant scattering of synchrotron radiation from the 25.6 keV level of ^{161}Dy. Two techniques are used: nuclear forward scattering (NFS) and nuclear incoherent scattering (NIS). NFS time spectra of Dy-metal are measured at temperatures ranging from 15 K to 80 K. They reveal electron spin relaxation in ferromagnetic Dysprosium with long relaxation times of $\simeq 10 - 30$ ns. NIS energy spectra of Dy_2O_3 at room temperature are measured with meV-resolution. Scattering accompanied by phonon excitation is observed. The results presented here are based on the original publication of Shvyd'ko et al. (2001).

4.8.1 Overview of the field

Mössbauer studies with Dy nuclei have been performed since the early 1960s. Dy compounds are attractive due to their magnetic properties. Dy metal shows a helical-type arrangement of atomic moments (Wilkinson et al. 1961, Andrianov et al. 1991). The hyperfine magnetic field at the nucleus due to the 4f electrons is about 600 T and is among the strongest static magnetic fields observed (Ofer et al. 1965, Bowden et al. 1967). Dy metal possess unusual thermal properties at magnetic phase transitions (Gschneider et al. 1997).

The ^{161}Dy isotope is favorable for Mössbauer spectroscopy. Its natural isotopic abundance is 18.8 %. There are several nuclear excited states which can be used. Most attractive is the first excited state with an energy of 25.6 keV which decays via an E1 transition to the ground state. (Firestone et al. 1996). The natural linewidth of the transition $\Gamma_0 = 15.7$ neV deduced from the lifetime of $\tau_0 = 42.0$ ns is only about three times larger than the width of the famous 14.4 keV transition in ^{57}Fe. High resolution hyperfine spectroscopy is therefore possible. However, ^{161}Dy Mössbauer sources are strongly broadened to about $10 - 20\Gamma_0$. Still they allow one to observe the huge magnetic hyperfine splittings of about $\pm 1000\Gamma_0$ caused by the extremely large hyperfine magnetic field. Dramatic line-broadening effects due to strong spin relaxation phenomena were also observed by Khurgin et al. (1970), Loh et al. (1974), and Tappert et al. (1996). However, studies of hyperfine interactions with a natural-width resolution ($\simeq \Gamma_0$) in Dy compounds were not possible. Nuclear resonance of a natural linewidth and "soft" relaxation phenomena in the nanosecond range were never reported to our knowledge.

The problem caused by broadened sources could be overcome by using

pulsed synchrotron radiation instead of radioactive Mössbauer sources. Very short $\simeq 50 - 150$ ps radiation pulses are available at modern synchrotron radiation facilities. They make possible high resolution hyperfine spectroscopy in the time domain, pioneered by Gerdau et al. (1986) and Hastings et al. (1991). See also review articles in (Gerdau and de Waard 1999/2000). Time spectra of nuclear forward scattering (NFS) provide information similar to that of Mössbauer absorption spectra. The resolution of this technique at low-frequencies is only limited by the width of the time window of observation of the nuclear response after excitation with synchrotron radiation pulses. Additionally, synchrotron radiation sources allow phonon spectroscopy by measuring energy spectra of nuclear incoherent scattering (NIS), pioneered by Seto et al. (1995) and Sturhahn et al. (1995). See also review articles in (Gerdau and de Waard 1999/2000).

The first observation of the excitation of the 25.6 keV level of ^{161}Dy with synchrotron radiation was reported by Koyama et al. (1996). However, no spectroscopy studies were performed.

The present studies aim to demonstrate the feasibility of hyperfine spectroscopy in the time domain and phonon spectroscopy by using nuclear resonance scattering from ^{161}Dy nuclei.

4.8.2 Experimental setup

The measurements were carried out at the undulator beamline of the 12 GeV storage ring PETRA (DESY, Hamburg); see the paper of Franz et al. (2000) for more details on the beamline. The beam from the undulator was monochromatized to a bandwidth of about 2 eV with a high-heat-load monochromator. Two diamond single crystals in a Laue geometry were used with the (220) Bragg reflection. The energy calibration of the monochromator was performed with the absorption K-edge of Ag at 25.514 keV (Bearden and Blurr 1967). A bandwidth of 2 eV is still much larger than the μeV spectral range of the nuclear resonance. Also a photon flux of $\simeq 10^{11}$ photons/s after the monochromator is too high to be handled with a detector in forward scattering geometry. To reduce the photon flux further monochromatization to a meV-band is necessary. Milli-electronvolt monochromatization is also required for measurements of phonon spectra with nuclear incoherent scattering.

To achieve monochromatization of a few meV we used almost exact Bragg backscattering from a α-Al_2O_3 single crystal. As was argued in sec. 3.3, sapphire single crystals allow exact Bragg backscattering for x rays in the 10 - 50 keV spectral range with high reflectivity, small energy bandwidth and large

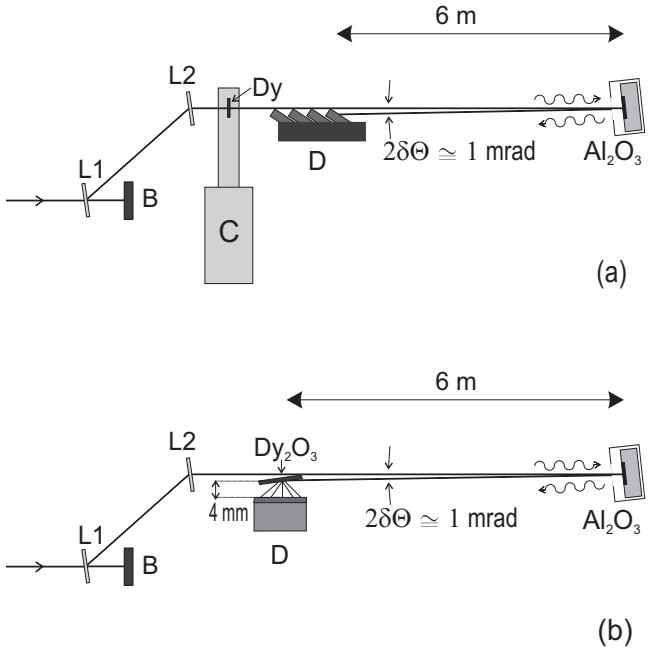

Figure 4.12: Experimental setup: a beam from the undulator (not shown) passes through the high heat-load monochromator consisting of two diamond crystals C(220) in Laue geometry (L1 and L2). Further monochromatization to meV-bandwidth is achieved by Bragg backscattering from a sapphire single crystal (α-Al_2O_3), reflection $(3\ 2\ \overline{5}\ 52)$. (a) Setup for nuclear forward scattering (NFS), (C) a cryostat with a Dy-metal foil as sample, (D) detector: a stack of four APDs. (b) Setup for nuclear incoherent scattering (NIS) with a Dy_2O_3 sample and a single APD as detector (D).

angular acceptance. The $(3\ 2\ \overline{5}\ 52)$ Bragg back reflection in sapphire at $\simeq 374.6$ K fits to the nuclear transition energy of ^{161}Dy, see Tab. 3.1. The calculated energy bandwidth of the reflection is 0.66 meV. The backscattering energy and the energy of the nuclear transition can be perfectly matched by tuning the crystal temperature. From the temperature dependence of the lattice constants of sapphire (Shvyd'ko et al. 2002) one obtains that the temperature variation of the energy of the $(3\ 2\ \overline{5}\ 52)$ back reflection is $\mathrm{d}E/\mathrm{d}T = -166$ meV/K. For a proper performance of the monochromator, mK-stability of the crystal temperature is required, as described in sec. 4.3. A sapphire crystal grown by the heat-exchange method (Schmid et al. 1994) with a dislocation density of $\simeq 3 \times 10^3$ cm^{-2} was used.

The setup for nuclear forward scattering measurements is shown in Fig.

4.12a. The beam passes through the sample, a 25 μm thick polycrystalline foil of Dy metal. The sample was placed in a closed-cycle cryostat downstream of the diamond monochromator. The temperature of the sample was changed in the range from 15 K to 80 K. Four avalanche photo diodes (APD), each with a 100 μm thick sensitive Si wafer inclined at an angle of 72°, served as detector. APDs of the type EG&G C30703F were used, see sec. 4.3. The time resolution was 0.8 ns and the overall detector efficiency 40%.

The setup for nuclear incoherent scattering measurements is shown in Fig. 4.12b. As distinct from the case of the NFS setup, the sample has to be placed downstream of the sapphire monochromator. A Dy_2O_3 powder sample was used. A single APD was placed close to the sample to detect isotropic nuclear resonance fluorescence. γ-resonant absorption in ^{161}Dy followed by internal conversion yields the 6.4 keV L_α and the 7.2 keV L_β fluorescence line of Dy-atoms (Bearden 1967). The fluorescence was detected with the Si-APD with an efficiency of about 85%.

While measuring NFS time spectra the energy (temperature) of the sapphire monochromator is fixed at the energy of the nuclear resonance. While measuring NIS energy spectra, the energy of the monochromator is scanned across the nuclear resonance by changing the temperature of the sapphire crystal.

The performance of the sapphire monochromator was tested with the help of the NFS setup. Delayed photons from the Dy-foil reflected from the α-Al_2O_3 single crystal were counted as a function of the crystal temperature (Fig. 4.13). The largest reflectivity was observed at a temperature of $T_0 = 374.624(40)$ K. This value was ascertained in the following way. Backscattering of the ^{161}Dy Mössbauer radiation was observed at a temperature which was $\delta T = 3.04(1)$ K above the temperature of backscattering of the ^{57}Fe Mössbauer radiation from the $(1\ 3\ \overline{4}\ 28)$ atomic planes. This precisely known temperature difference together with the crystal temperature for backscattering of the ^{57}Fe Mössbauer radiation obtained in the experiment described in sec. 4.6 were used to determine the crystal temperature for backscattering of the ^{161}Dy Mössbauer radiation.

The energy of x rays selected at the temperature T_0 ws associated with the energy E_0 of the nuclear resonance in ^{161}Dy. The width of the curve is 46 mK, corresponding to an energy width of 7.8 meV. It is $\simeq 10$ times larger than the expected theoretical width. The main reason for this is a relatively high dislocation density in the sapphire single crystal used.

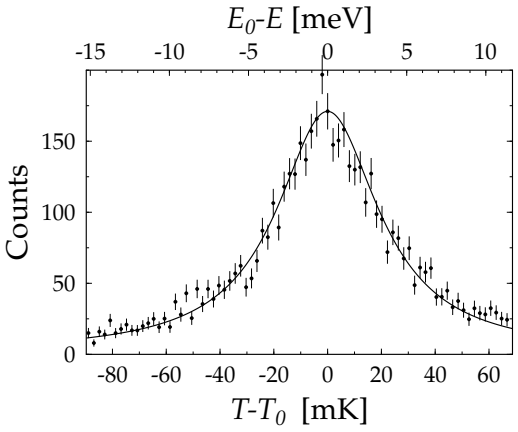

Figure 4.13: Number of delayed 25.6 keV photons vs. the temperature of the sapphire crystal as measured with the NFS setup (Fig. 4.12a). $T_0 = 374.624(40)$ K. The energy scale is calculated by using the conversion 0.17 meV/mK valid for the reflection $(3\ 2\ \overline{5}\ 52)$ in α-Al_2O_3.

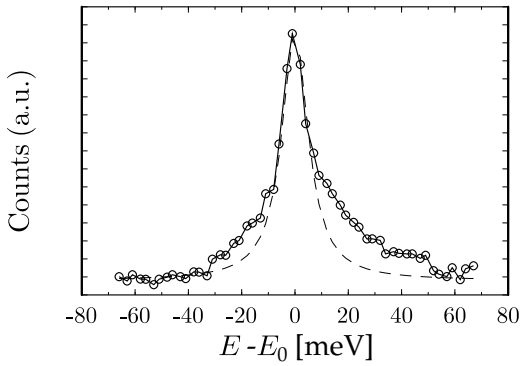

Figure 4.14: NIS energy spectrum of a Dy_2O_3 powder sample at room temperature (circles). The dashed line is the instrumental function of the sapphire monochromator as in Fig. 4.13.

4.8.3 NIS energy spectra of Dy_2O_3

Figure 4.14 shows the NIS energy spectrum of a Dy_2O_3 powder sample at room temperature. The dashed line is the instrumental function of the sapphire monochromator equivalent to that in Fig. 4.13. The observed additional intensity in the wings of the NIS spectrum is caused by excitation (annihilation) of phonons in Dy_2O_3 in the process of nuclear resonant scattering. The effect is more pronounced at photon energies above the nuclear resonance energy, at which phonon creation takes place. Typical phonon energies are $\simeq 15$ meV. The inadequate energy resolution of the monochromator, however, does not allow us to resolve details in the spectrum. The high-quality crystals are badly needed to achieve the potentially high energy resolution of the sapphire backscattering monochromator.

In the recent publications of Chumakov et al. (2001) and Baron et al. (2001a) an energy resolution of 1 meV and 0.5 meV, respectively, was achieved by using in-line nested silicon monochromators for 25.6 keV x rays. Such a high energy resolution have allowed the authors to study with high precision phonon spectra in a Dy metal and in a Dy_2O_3 powder.

At this point is is important to stress once more, that despite deficient per-

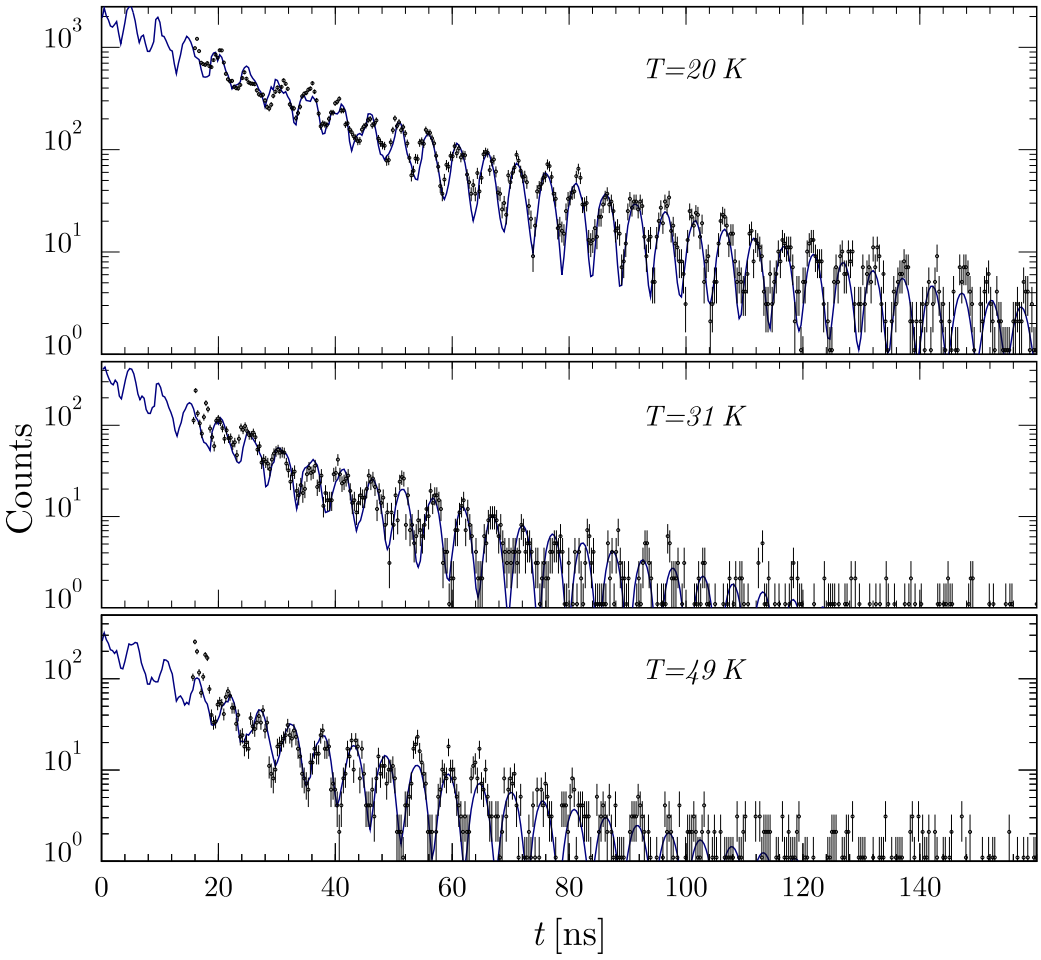

Figure 4.15: NFS time spectra of metallic Dy at different temperatures. Solid lines are fits with the NFS theory.

fection of the commercially available sapphire crystals, the sapphire backscattering monochromator has a great potential because of it universal applicability in a broad x-ray energy range, as was discussed in sec. 3.3.

4.8.4 NFS time spectra of metallic Dy

NFS time spectra of metallic Dy at different sample temperatures are shown in Fig. 4.15. The time response is an almost exponential decay function with superimposed quantum beats. Both the period of the quantum beats and the decay rate increase with temperature. The most drastic effect is observed for

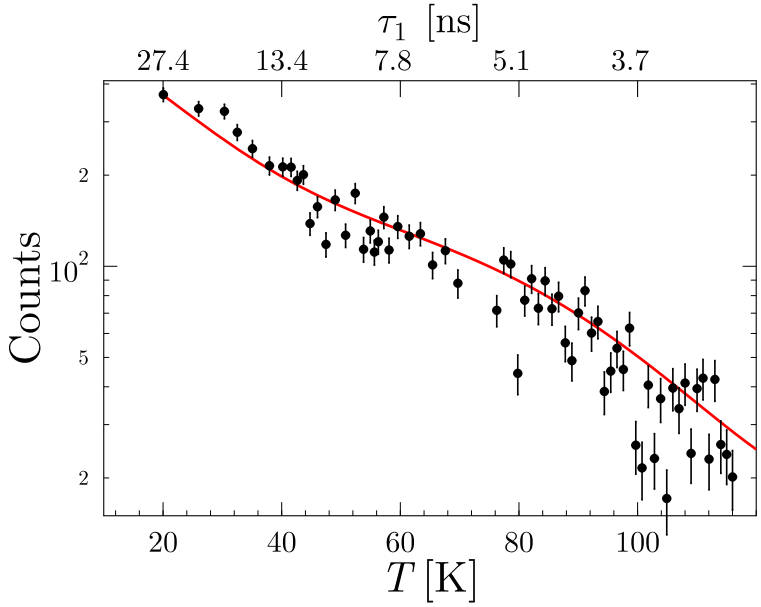

Figure 4.16: Number of counts in the time window 20-200 ns vs. the temperature T of metallic Dy (circles). The spin relaxation time scale τ_1 relates to T via eq. (4.20). It is deduced from the fit of the observed curve to the theoretical one - solid line - calculated with the stochastic relaxation model.

the time integrated count rate of NFS, which drops exponentially with sample temperature, see Fig. 4.16.

The Lamb-Mössbauer factor f_{LM} can not account for such a drastic effect, as it changes in accordance with the Debye model, by less than 10% in this temperature range. The decreasing count rate can be a consequence of the increasing decay rate. Both effects can be attributed to electron spin relaxation. Spin-relaxation broadens the nuclear resonance line and thus leads to a faster time response and a decreased count rate. The influence of spin relaxation in magnetically ordered rare-earth compounds on the line shape of Mössbauer spectra was first reported as early as 1966 by Nowik and Wickman (Nowik and Wickman 1966).

The measured spectra in Fig. 4.15 are compared to the time spectra calculated by using the NFS theory taking into account spin relaxation. Following (Shvyd'ko 1999) the time spectrum $S(t)$ is

$$S(t) \propto |E(t)|^2,$$

$$E(t) = \exp\left[-\xi \int_0^t K(t-t')\mathrm{d}t'\right] \delta(t'),$$

$$K(t) = \sum_{\ell} \mathcal{A}_\ell K_\ell(t), \tag{4.14}$$

with $K(t)$ as the nuclear time correlation function, ξ as the effective resonance thickness parameter; ℓ indexes all possible hyperfine nuclear transitions, $\mathcal{A}_\ell$ represents the nuclear transition amplitude, and $K_\ell(t)$ the time correlation function for a particular transition. In the absence of relaxation $K_\ell(t) = \exp\left[-\left(\mathrm{i}\Omega_\ell + \Gamma_0/2\hbar\right)t\right]$, with Γ_0 as the natural linewidth of the nuclear excited state, and $\Omega_\ell = \Omega_\ell^{\mathrm{e}} + \Omega_\ell^{\mathrm{m}}$ as the correction to the unperturbed nuclear transition frequency ω_0 with the components Ω_ℓ^{e}, Ω_ℓ^{m} arising due to the electric and magnetic hyperfine interactions, respectively. E.g.,

$$\hbar\Omega_\ell = \left(\mu_{\mathrm{g}} m_{\mathrm{g}}/J_{\mathrm{g}} - \mu_{\mathrm{e}} m_{\mathrm{e}}/J_{\mathrm{e}}\right) B, \tag{4.15}$$

where B is the magnetic field at the nuclear site, J_λ is the nuclear spin, μ_λ is the nuclear magnetic moment, m_λ is the magnetic quantum number in the excite λ =e or in the ground λ =g state, respectively, and ℓ is a joint index for the nuclear transition $J_{\mathrm{g}}, m_{\mathrm{g}} \Rightarrow J_{\mathrm{e}}, m_{\mathrm{e}}$. For more details on $\mathcal{A}_\ell$, Ω_ℓ, ξ, etc., see (Shvyd'ko 1999) and (Shvyd'ko 2000).

Electron spin relaxation is taken into account in the framework of the Kubo-Anderson stochastic model (Abragam 1961) in the presentation of Wickman (Wickman et al. 1966, Wickman 1966, Nowik 1967). Relaxation between the two lowest ionic sublevels $J_z = \pm 15/2$ of Dy^{+3} split by exchange interaction is considered therein. The relaxation times of the sublevels are τ_1 and τ_2, respectively. For a magnetically ordered material one expects $\tau_1 > \tau_2$. The populations of the ionic levels are then defined as $p_1 = \tau_1/(\tau_1+\tau_2)$ and $p_2 = \tau_2/(\tau_1+\tau_2)$. Due to relaxation, each nuclear transition ℓ is accompanied by radiation at two frequencies: $\omega_0 + \Omega_\ell^{\mathrm{e}} + \Omega_\ell^{\mathrm{m}}$ and $\omega_0 + \Omega_\ell^{\mathrm{e}} - \Omega_\ell^{\mathrm{m}}$.

By using the rate equations of Wickman et al. (1966),Wickman (1966), and Nowik (1967) we have derived the following time correlation function:

$$K_\ell(t) \;=\; \exp\left[-\left(\mathrm{i}\Omega_\ell^{\mathrm{e}} + \gamma\right)t\right]\left[a_\ell \exp(\mathrm{i}\mu_\ell t) + b_\ell \exp(-\mathrm{i}\mu_\ell t)\right], \tag{4.16}$$

$$a_\ell \;=\; \frac{\mu_\ell - \delta_\ell + \Omega_\ell^{\mathrm{m}}\tau/\tau_1}{2\mu_\ell} \qquad b_\ell \;=\; \frac{\mu_\ell + \delta_\ell - \Omega_\ell^{\mathrm{m}}\tau/\tau_1}{2\mu_\ell}, \tag{4.17}$$

$$\gamma = (\Gamma_0/\hbar + 1/\tau)/2, \quad \tau = \frac{2\tau_1\tau_2}{\tau_1+\tau_2}, \tag{4.18}$$

$$\mu_\ell \;=\; \sqrt{\delta_\ell^2 \;-\; \mathrm{i}\Omega_\ell^{\mathrm{m}}/\tau_1}, \quad \delta_\ell = \Omega_\ell^{\mathrm{m}} + \mathrm{i}/2\tau. \tag{4.19}$$

These expressions are consistent with those derived by Wickman et al. (1966), and Wickman (1966) to describe the nuclear resonance absorption spectra.

The code MOTIF (Shvyd'ko 2000) is used to fit the time spectra with the time correlation function given by eqs. (4.16)-(4.19). A set of hyperfine parameters reported by Bowden et al. (1967) are used as initial values for the fit. The energy spectra of NFS, calculated by using the parameters obtained from the best fit of the time spectra are shown in Fig. 4.17. They reveal hyperfine splittings as large as $\Delta E \simeq 2400\ \Gamma_0$, which is in agreement with the experimental observations of Bowden et al. (1967). This should result in a beat period of $2\pi\hbar/\Delta E = 0.11$ ns. Our detector allows us to resolve beat periods > 0.8 ns corresponding to nuclear transitions split by less than $300\ \Gamma_0$, e.g., those at the center of the spectra. The calculated time spectra in Fig. 4.15 are convolved with the detector instrumental function. As a result, the fast quantum beats are not resolved there as well. Because of the convolution, the time spectra are practically insensitive to the quadrupole interaction.

The parameters $\xi = 2.75$ and $\tau = 0.37$ ns were obtained from the fit of the spectrum at $T = 20$ K and were kept constant in all other calculations. The parameters B, τ_1, and $f_{\rm LM}$ were fitted for each temperature independently. The best fit parameters are given in table 4.7. The population $p_2 = \tau/2\tau_1$ of the first

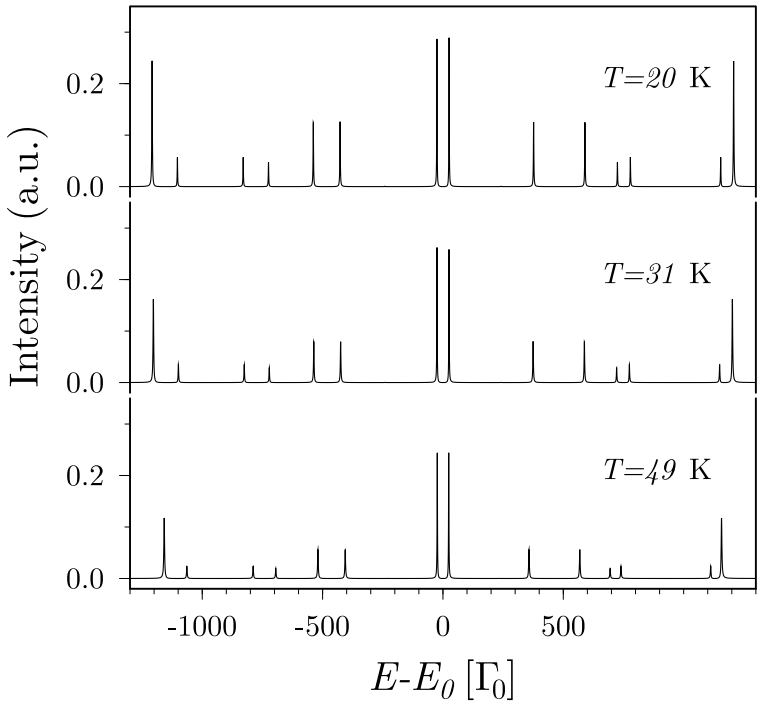

Figure 4.17: Simulation of the NFS energy spectra of metallic Dy. Hyperfine parameters are used as determined from the fit of the NFS time spectra.

excited ionic level is presented in the table as well.

T [K]	B [T]	f_{LM}	τ_1 [ns]	p_2
20	578.9(2)	0.78(5)	27(1)	0.0068
31	577.6(4)	0.76(2)	16(1)	0.0118
49	554.7(5)	0.74(2)	11(1)	0.0164

Table 4.7: A set of the best fit parameters.

The time-integrated NFS intensity in Fig. 4.16 can be also simulated by the aforementioned model. The theoretical curve is calculated as a function of the relaxation time τ_1 with the value of τ fixed. It fits the experimental data provided

$$\tau_1 = \frac{\tau}{2} \exp\left[\frac{\epsilon}{k_{\text{B}}(T + T_1)}\right], \tag{4.20}$$

with $\epsilon = 52(3)$ meV and $T_1 = 100(5)$ K. The fits to the time spectra in Fig. 4.15 and those in Fig. 4.16 provide consistent values for the relaxation time τ_1. If the temperature dependence of the spin relaxation times given by eq. (4.20) is also valid at temperatures lower than 20 K, then the formula predicts the spin relaxation time $\tau_1 \simeq 75$ ns in Dy metal at $T = 0$, i.e., spin relaxation in Dy metal does not cease even close to absolute zero.

The results of the calculations demonstrate the sensitivity of the time spectra to spin relaxation in Dy metal. It should be noted, that the influence of spin relaxation has not previously been reported for the Mössbauer absorption spectra in bulk Dy metal in this temperature range (Khurgin et al. 1970). Mössbauer absorption spectra have revealed only a slight change of the hyperfine splitting (Bowden et al. 1967). Spin relaxation was observed only in the antiferromagnetic phase between 85 K and 178.5 K (Khurgin et al. 1970, Loh et al. 1974). In the ferromagnetic phase it was observed recently in very thin layers of Dy in the FeDy multilayer system (Tappert et al. 1996). However, much shorter relaxation times - $\tau = 0.03$ ns - were reported.

4.8.5 Conclusions

In summary, we have demonstrated the feasibility of hyperfine spectroscopy with ^{161}Dy nuclei in the time domain by using pulsed synchrotron radiation as a source. Spin relaxation is observed in ferromagnetic Dy metal with relaxation times as long as 27 ns, which have not been reported previously. This example

shows the very high sensitivity of time domain spectroscopy with synchrotron radiation.

Energy spectra of nuclear incoherent scattering of Dy_2O_3 have been measured by using the sapphire backscattering monochromator with an energy resolution of 7.8 meV. With this resolution we were able to resolve inelastic phonon scattering. The development of α-Al_2O_3 backscattering monochromators with improved energy resolution is in progress.

Chapter 5

Theory of x-ray Fabry-Pérot resonators

5.1 Introduction

Steyerl and Steinhauser (1979) pioneered the idea of a Fabry-Pérot-type interference filter for x rays and performed the first theoretical analysis. They have applied the dynamical theory of Bragg diffraction. A matrix approach of matching boundary conditions was employed. A particular case of *exact* normal incidence to the reflecting atomic planes was considered. The transmission energy spectrum with a single sharp transmission peak was calculated at 17.4 keV for the (14 6 0) reflection in silicon. The calculated resolution of the transmitted peak was $E/\Delta E \approx 5 \times 10^7$. Interestingly, the first theory of the x-ray Fabry-Pérot resonator by Steyerl and Steinhauser (1979) was developed at a time when there was no consistent theory of Bragg backscattering.

Caticha and Caticha-Ellis (1990b) extended the theoretical treatment to an arbitrary angle of incidence. They also introduced an additional parameter allowing for the possible relative shift of the crystal plates. A similar matrix approach was used to match the boundary conditions. The matrix technique for a system of N thin parallel crystals diffracting at near-normal incidence was formulated. Numerical simulations of the energy dependence of the transmissivity of the x-ray Fabry-Pérot resonator were performed. It was shown that for crystal plates with low absorption, the transmission function has sharp resonances of defined energy that can be controlled by tuning the gap of the x-ray resonator. The theory of a thermal neutron resonator of Fabry-Perot type was presented by the same authors (Caticha and Caticha-Ellis 1996). The matrix technique is convenient for numerical calculations and it can be easily applied to systems containing many diffracting crystals. However, it does not allow

simple analytical analysis.

To overcome this drawback Caticha et al. (1996) applied a geometrical approach, which is often used in theories of the optical resonator (Born and Wolf 1980, Vaughan 1989). A summation of the multiple reflection amplitudes from the crystal plates was used to calculate the reflectivity and transmissivity of the system. The reflection and transmission amplitudes of the resonator elements - the crystal plates - were calculated by the dynamical theory of Bragg diffraction (Caticha and Caticha-Ellis 1990a). The transmission spectra of the x-ray resonator were also calculated.

Unfortunately, numerous misprints do not allow one to reproduce reliably the results of the paper. An attempt to calculate the reflectivity of the x-ray resonator by using the formulae of Caticha et al. (1996) lead to altogether non-physical effects. For this reason, Shvyd'ko and Gerdau (1999) revised the theory of Caticha et al. (1996). Additionally, a very important phase factor was introduced that was lacking in the previously mentioned theories. Numerical calculations for an x-ray Fabry-Pérot resonator built of sapphire single crystals were performed. Both transmission and reflection intensities were calculated as a function of x-ray energy and incidence angle. The validity of the newly incorporated phase factor was rigorously substantiated by Kohn et al. (2000).

Kohn et al. (2000) have developed the theory of the x-ray Fabry-Pérot resonator as a particular case of the dynamical theory of x-ray Bragg diffraction in layered crystalline systems. It has been shown that the performance of the x-ray resonator is similar to that of the optical Fabry-Pérot resonator. Both show a fine resonance structure in the transmission and reflection dependence. However, for the x-ray Fabry-Pérot resonator this occurs only inside the region of the Bragg back diffraction peak. The influence of possible imperfections, such as the roughness of the crystal plate surfaces and the error in the parallelism of the atomic planes has been discussed. Numerical estimations for the sapphire x-ray resonator have been given.

In the present report the theory of the x-ray Fabry-Pérot resonator is developed following the results of the original papers of Shvyd'ko and Gerdau (1999) and Kohn et al. (2000). Initially, a perfect x-ray resonator, is considered: the x-ray Fabry-Pérot resonator built as a system of two perfect crystal plates parallel to each other, playing the role of resonator mirrors. The derivation of the mathematical expressions for the transmissivity and reflectivity of the perfect x-ray resonator uses the geometrical approach based on the summation of the probability amplitudes of multiple reflections from the crystal plates. The single reflection and transmission amplitudes of the crystal plates are calculated using the dynamical theory of x-ray Bragg diffraction, as described in

sec. 2.2.2. A detailed analytical analysis of the obtained expressions is performed. In particular, the position and width of the Fabry-Pérot transmission resonances are estimated analytically as a function of the gap between the mirrors, the x-ray energy, the angle of incidence, and the temperature. Numerous results of computer simulations of the energy, time and angular dependence are presented to illustrate the performance of the x-ray Fabry-Pérot resonator.

A new problem, which was not addressed in the theoretical papers, the time response of the x-ray Fabry-Pérot resonator, is described in this report. This new aspect is of particular interest as the time response plays an important role in the experiments on x-ray Fabry-Pérot resonators presented in sec. 6.3. An analytical expression for the time response of an x-ray Fabry-Pérot resonator to an excitation with a short radiation pulse is derived. Examples of numerical calculations of the time response are also presented.

The influence of possible imperfections, such as roughness of the crystal surfaces, error in the parallelism of the atomic planes, and unequal crystal temperatures is discussed in sec. 5.4. It is shown that these factors may significantly deteriorate the performance of the x-ray resonator. Analytical estimations are given.

In conclusion to this chapter, some model applications of x-ray Fabry-Pérot resonators are discussed.

Before going into detail, it is worthwhile to recall the theory of the optical Fabry-Pérot resonator and to discuss especially the effect of multiple-beam interference underlying this theory. This will allow us to reveal similarities and differences between the optical Fabry-Pérot resonator and its x-ray counterpart and thus to gain deeper insight into the physical nature of the theoretical results.

5.2 Multiple-beam interference in optics

Multiple-beam interference is the main distinguishing feature of Fabry-Pérot resonators.

The purpose of this paragraph is to give a short account of the theory of multiple-beam interference in visible-light optics and, based upon that, high resolution interference filters. A more detailed treatment can be found, e.g., in the standard optics texts such as Born and Wolf (1980), Vaughan (1989), or Hecht and Zajac (1974). Plane parallel (Fabry-Pérot) and wedge (Fizeau) multiple-beam resonators are discussed to provide a link between optical and x-ray multiple-beam interference devices.

5.2.1 Plane resonators

Consider a plate of a thickness $d_{\rm g}$ with parallel surfaces coated with thin layers of high reflectivity which play the role of mirrors, see Fig. 5.1. These could be thin metal films or multi-layer dielectric films. It is assumed here for simplicity, that the mirrors are infinitely thin and are not absorbing. The refractive index of the medium filling the gap between the mirrors is $n_{\rm g}$, and of the surrounding medium is n, respectively. Let the amplitude-reflection coefficients of the mirrors be r and the amplitude-transmission coefficients be t, for a wave traveling from the surrounding medium to the reflecting plates. Similarly, let $\tilde{r}$ and $\tilde{t}$ be the corresponding coefficients for a wave traveling from the gap to the surrounding medium.

The transmission of a plane monochromatic wave through the system of two mirrors is considered in terms of the wave frequency ω, amplitude E_0, glancing angle θ, gap width $d_{\rm g}$, and some other parameters.

The radiation passing through the first mirror experiences multiple reflections between the mirrors before it escapes through one of them, as is shown schematically in Fig. 5.1. It should be noted that the rays are actually lines drawn perpendicular to the wavefronts and thus to the optical fields.

The amplitude of the transmitted wave after having experienced p successive reflections at each mirror is $E_{pt} = E_0\, t\, (\tilde{r})^{2p}\, \tilde{t}\, \exp(\mathrm{i}\, p\, \delta\varphi)$. Here $\delta\varphi = K\Lambda$ is the phase difference between adjacent rays, with Λ being the difference in optical path lengths between adjacent rays, $K = 2\pi/\lambda$ is the wavenumber, and $\lambda = \omega/2\pi c$ is the wavelength. It is readily shown (see Fig. 5.1) that $\Lambda = n_{\rm g}(AB + BC) - nAD = 2d_{\rm g} n_{\rm g} \sin\theta_{\rm g}$. Expressed in terms of the glancing

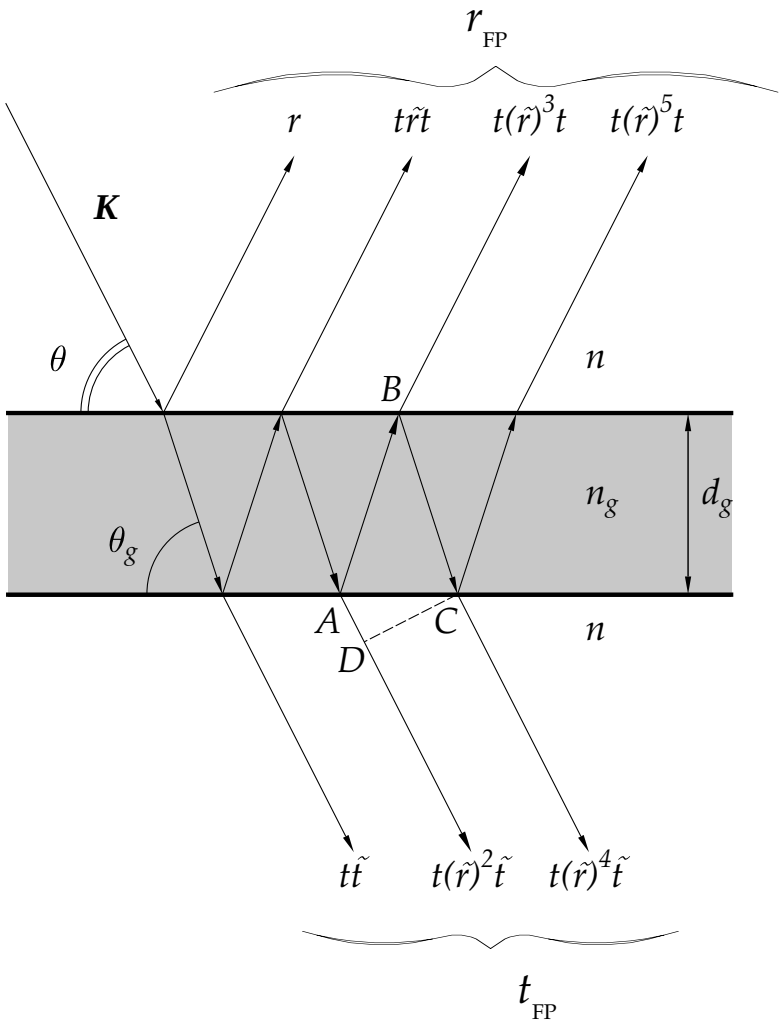

Figure 5.1: Scheme of formation of multiple-beams in an optical Fabry-Pérot resonator.

angle θ, the optical path difference reads

$$\Lambda = 2d_{\mathrm{g}}\sqrt{n_{\mathrm{g}}^2 - n^2\cos^2\theta}. \tag{5.1}$$

The total amplitude of the radiation transmitted through the system of two reflecting mirrors is the sum of all possible multiply-reflected waves:

$$E_t = \sum_{p=0}^{\infty} E_{pt} = E_0 \sum_{p=0}^{\infty} t\,(\tilde{r})^{2p}\,\tilde{t}\exp(\mathrm{i}\,p\,\delta\varphi). \tag{5.2}$$

The summation of the geometrical series results in

$$E_t \;=\; E_0 \frac{t\tilde{t}}{1 \,-\, \tilde{r}^2 \,\exp(\mathrm{i}\,\delta\varphi)}. \tag{5.3}$$

Let us term the reflectivity of the mirrors $\mathcal{R} = |\tilde{r}^2|$, transmissivity $\mathcal{T} = |t\tilde{t}|$, the phase jump on reflection $\phi_{\mathcal{R}} = \arg[\tilde{r}^2]$, and the phase jump on transmission $\phi_{\mathcal{T}} = \arg[t\tilde{t}]$. Using these notations one arrives at the following expression for the amplitude-transmission coefficient of the system

$$t_{\scriptscriptstyle \mathrm{FP}} \;=\; \frac{E_t}{E_0} \;=\; \frac{\mathcal{T}\,\exp(\mathrm{i}\,\phi_{\mathcal{T}})}{1 \,-\, \mathcal{R}\,\exp(\mathrm{i}\,\varphi)}, \tag{5.4}$$

where

$$\varphi \;=\; 2\,K\,d_{\mathrm{g}}\,\sqrt{n_{\mathrm{g}}^2 \,-\, n^2\cos^2\theta} \;+\; \phi_{\mathcal{R}} \tag{5.5}$$

will be termed henceforth the Airy phase.

The transmissivity of the system $T_{\scriptscriptstyle \mathrm{FP}} = |t_{\scriptscriptstyle \mathrm{FP}}|^2$ is the ratio of the incident flux density $I_0 \;=\; |E_0|^2/2$ to the transmitted flux density $I_t \;=\; |E_t|^2/2$. Using (5.4) one obtains

$$T_{\scriptscriptstyle \mathrm{FP}} \;=\; \frac{\mathcal{T}^2}{1 + \mathcal{R}^2 \,-\, 2\mathcal{R}\,\cos(\varphi)} \;=\; \frac{\mathcal{T}^2}{(1-\mathcal{R})^2 \,+\, 4\mathcal{R}\,\sin^2(\varphi/2)}. \tag{5.6}$$

Defining the parameters

$$F \;=\; \frac{4\mathcal{R}}{(1-\mathcal{R})^2}, \qquad H \;=\; \frac{\mathcal{T}^2}{(1-\mathcal{R})^2} \tag{5.7}$$

one arrives at the expression

$$T_{\scriptscriptstyle \mathrm{FP}} \;=\; \frac{H}{1 \,+\, F\sin^2(\varphi/2)}. \tag{5.8}$$

One should note that in the absence of absorption, which was assumed previously, the parameter $H \;=\; 1$. Equation (5.8) is widely known in optics as the Airy formula, which describes the intensity distribution of the transmitted pattern due to multiple reflections in a system of two parallel plane reflecting surfaces.

By using similar considerations and summations of the reflected wave trains one can obtain the equation for the reflectivity of the system of the two mirrors. In the absence of absorption, however, it can be easily calculated using $R_{\scriptscriptstyle \mathrm{FP}} = 1 - T_{\scriptscriptstyle \mathrm{FP}}$.

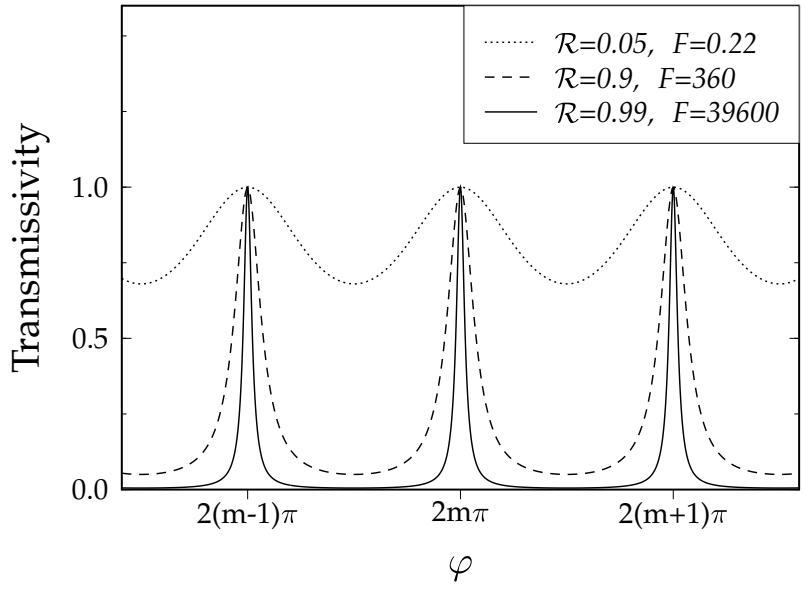

Figure 5.2: Multiple-beam fringes in transmitted light as a function of the Airy phase φ shown for a few orders of interference m. The curves are calculated according to eq. (5.8) for different values of the mirrors' reflectivity $\mathcal{R}$ and F.

The behavior of transmissivity (5.8) as a function of the Airy phase is shown in Fig. 5.2, calculated for different values of $\mathcal{R}$ and F, respectively. The transmitted intensity is a periodic function of φ with a period of 2π. The fringes of the order of interference $m-1$, m, and $m+1$ are shown. The transmission maxima (interference fringes) are sharper the higher the reflectivity of the mirrors $\mathcal{R}$. Alternatively, the higher the reflectivity, the more multiply-reflected waves contribute to the net signal, and the sharper are the fringes. This demonstrates in particular the great significance of multiple-beam interference and its difference from the more usual two-beam interference. If the reflectivity approaches unity, the number of interfering beams increases and the transmission becomes very small except in the immediate vicinity of the maxima of total transmission. The interference pattern consists of narrow bright fringes on an almost completely dark background.

The ratio of the separation of adjacent fringes (2π) and the full-width at half-maximum $\Delta\varphi$ is called the *finesse*:

$$\mathcal{F} = 2\pi/\Delta\varphi. \tag{5.9}$$

For large F it is readily shown to be given by

$$\mathcal{F} = \frac{\pi\sqrt{F}}{2} = \frac{\pi\sqrt{\mathcal{R}}}{1-\mathcal{R}}. \tag{5.10}$$

Fabry and Pérot (1899) have proposed the use of two parallel mirrors of high reflectivity as a high-resolution spectrometer based on multiple-beam interference. Because of the extreme sharpness of the multiple-beam interference fringes, such devices have an enhanced resolving power.

One can observe interference fringes by changing the spacing $d_{\rm g}$ between the mirrors. If the spacing can be scanned, such devices are usually called Fabry-Pérot interferometers. Since the Airy phase φ is proportional to $d_{\rm g}$ - eq. (5.5) - the interference pattern on the $d_{\rm g}$-scale is similar to that of Fig. 5.2. Let us assume for simplicity that $n_{\rm g} = 1$ and $n = 1$, i.e., the mirrors are in vacuum. Then the interference fringes appear every time if the variation of the spacing $\delta d_{\rm g}$ obeys the following rule

$$2\,\delta d_{\rm g}\,\sin\theta = m\,\lambda, \quad m = 0, \pm 1, \pm 2, ... \tag{5.11}$$

Thus the highest transmittance is achieved if the condition of standing wave formation between the mirrors is fulfilled. This is the usual resonator condition in optics. It is equivalent to Bragg's law[1], see eq. (2.64). Due to this property and due to the enhanced resolving power, Fabry-Pérot resonators have been applied since their advent to the comparison of different wavelengths and to the measurement of wavelengths in terms of the standard meter. For more details see, e.g., (Vaughan 1989).

Alternatively, one can fix the spacing and change the frequency of the incident radiation. If the spacing is fixed, such devices are usually called Fabry-Pérot étalons [2]. Also in this case the interference pattern for transmitted light on the frequency (energy) scale will be similar to that of Fig. 5.2. The separation between the adjacent fringes on the energy scale is given by

$$E_{\rm f} = \frac{hc}{2d_{\rm g}\sin\theta}, \tag{5.12}$$

[1]One could think of the parallel atomic planes reflecting x-rays in a crystal in the Bragg diffraction mode as a kind of Fabry-Pérot resonator. A significant difference is the very low reflectivity of the atomic planes which is however compensated by their great number. In fact Bragg diffraction from a crystal could be compared with the performance of a multiple (consisting of many reflecting planes) Fabry-Pérot resonator.

[2]Unless otherwise indicated, the name Fabry-Pérot resonator or simply resonator is used for both options.

which is called the free spectral range. The width of the fringe on the energy scale is then

$$\Gamma = \frac{E_{\mathrm{f}}}{\mathcal{F}}. \tag{5.13}$$

One can estimate that at normal incidence with mirrors spaced by 1 cm the free spectral range is $E_{\mathrm{f}} = 62\ \mu$eV. With a reflectivity of $\mathcal{R} = 0.99$ the finesse $\mathcal{F} = 314$ and therefore the spectral width of the transmission lines is in the sub-micro-electronvolt range. This demonstrates the high resolving power of optical Fabry-Pérot resonators . It is for this reason, that they were intensively and extensively applied over the 20th century to study fine and hyperfine structure of atomic spectra, among other applications.

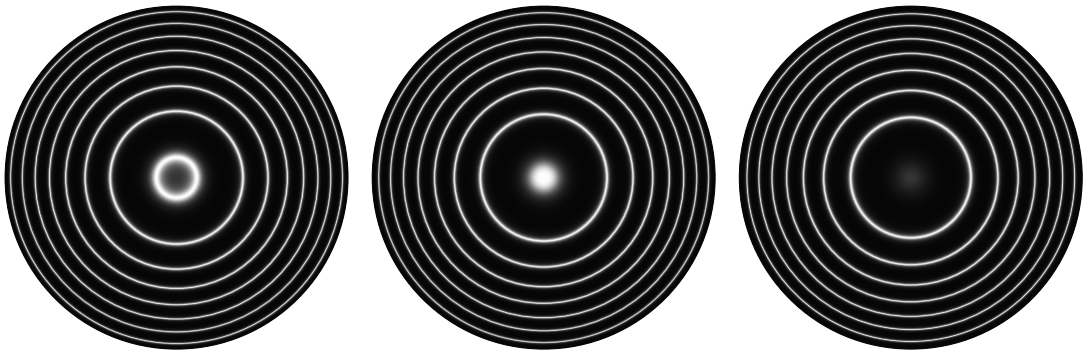

Figure 5.3: Simulations of the multiple-beam fringes of equal inclination in transmission.

The fringes can be also observed on the angular scale. Assuming monochromatic light and taking again for simplicity $n_{\mathrm{g}} = 1$, one obtains for the Airy phase $\varphi = 2\,K\,d_{\mathrm{g}}\,\sin\theta + \phi_{\mathcal{R}}$. Thus the fringes of equal inclination are observed at glancing angles, for which the order of interference is given by

$$m = \frac{\varphi}{2\pi} = \frac{2\,d_{\mathrm{g}}}{\lambda}\,\sin\theta + \frac{\phi_{\mathcal{R}}}{2\pi}. \tag{5.14}$$

Figure 5.3 shows simulations of the multiple-beam fringes of equal inclination using the Airy formula (5.8) with $F = 1520$ and $\mathcal{R} = 0.95$, respectively. The centers of the graphs correspond to normal incidence: $\delta\theta = \pi/2 - \theta = 0$. Figure 5.3a represents the case for which the interference order $m = 100$ appears nearest to the center ring. In Fig. 5.3b it is seen exactly at the center ($\delta\theta = 0$), while in Fig. 5.3c it does not appear at all. Physically these situations happen when the wavelength of the light increases gradually from (a) to (c), or equivalently, the spacing between the mirrors decreases from (a) to (c).

At near-normal incidence, where the approximation $\sin\theta \simeq 1 - (\delta\theta)^2/2$ is valid, the Airy phase has a quadratic dependence on the incidence angle $\delta\theta$. As a result the fringes of equal inclination are not equidistant, as is clearly seen in Fig. 5.3. Also, the angular widths of the fringes are larger the closer they are to normal incidence. For the fringe appearing at exact normal incidence the angular width is

$$\Delta\theta \;=\; 2\sqrt{\frac{\lambda}{2d_{\rm g}\,\mathcal{F}}}. \tag{5.15}$$

Equation (5.9) and the quadratic dependence of the Airy phase was used to derive this expression. For high interference orders $m \simeq 2d_{\rm g}/\lambda \gg 1$ the width of the central fringe can be given as $\Delta\theta \;=\; 2/\sqrt{m\mathcal{F}}$.

These formulae demonstrate that the use of the Fabry-Pérot resonator as a high resolution interference filter is most favorable under near-normal incidence conditions where the angular width of the transmission resonances is largest.

5.2.2 Wedge resonators

The discussion of multiple-beam interference in the preceeding section was confined to the condition of parallel mirrors. Naturally the question arises, what happens to multiple-beam interference if the mirrors are not parallel? It is of practical importance to obtain an answer to the question: what inclination of the mirrors do not yet destroy the very sharp Fabry-Pérot fringes?

For a fixed wavelength and a fixed incidence angle, the light is either transmitted or not through a Fabry-Pérot resonator, depending on how well it satisfies the resonator condition (5.11). If one of the plates is tilted slightly, the spacing varies across the plate, and transmission takes place if the condition (5.11) is fulfilled. Thus the transmission pattern observed behind the resonator is a contour map of the resonator spacing. If the plates are flat, the contours are straight lines. This arrangement of a Fabry-Pérot resonator with tilted plates, also called in the literature a multiple-beam Fizeau resonator, is most useful for testing surfaces (Tolansky 1960).

The first detailed study of the multiple-beam wedge fringes, was made by Brossel (1947a) and Brossel (1947b). As outlined in these papers, phase lag due to the wedge angle can create asymmetry and subsidiary fringes. The first detailed numerical evaluation of a multiple-beam fringe profile was carried out by Kinosita (1953). Rogers (1982) has performed more detailed calculations of the shape and location of multiple-beam transmission Fizeau fringes. Moos

et al. (1963) have demonstrated sharp wedge fringes for plate separations as large as 20 cm. A useful general account of multiple-beam interferometry can be found in (Born and Wolf 1980), (Polster 1969) and (Vaughan 1989).

5.3 Perfect x-ray Fabry-Pérot resonator

In the x-ray spectral region high reflectivity may be achieved either by employing scattering at grazing incidence or using Bragg diffraction from single crystals. In the latter case normal incidence to reflecting planes is possible. Thus in the x-ray spectral region, crystals should take over the role of high reflectivity mirrors.

5.3.1 General equations

The perfect x-ray Fabry-Pérot resonator is a device which consists of two perfectly parallel crystal plates of thicknesses d and $\tilde{d}$, separated by a gap of width d_{g} filled with a non-diffracting medium - Fig. 5.4a. It is assumed that the crystals are made of the same material. The reflecting atomic planes in the second crystal plate are assumed to be perfectly parallel to the planes in the first crystal plate and have the same temperature.

The relative position of the crystal plates in space can be described by a translation vector $\boldsymbol{u}$. The translation is defined in such a way that $\boldsymbol{u} = 0$ corresponds to a configuration where both crystals are composed of a single crystal of thicknesses $d + \tilde{d}$ - Fig. 5.4b. With this choice the gap is related to $\boldsymbol{u}$ by $d_{\mathrm{g}} = \boldsymbol{u}\hat{\boldsymbol{z}}$.

One can also introduce another translation vector $\boldsymbol{U}$ defined in such a way that $\boldsymbol{U} = 0$ corresponds to a configuration where the entrance surfaces (for the incoming x-rays) of both crystals coincide. Additionally, it is required that the positions of atoms coincide in the overlapping volumes of both crystals. The latter implies that $\boldsymbol{U} - \boldsymbol{u} = \boldsymbol{A}$, where $\boldsymbol{A} = \sum_{i=1}^{3} n_i \boldsymbol{a}_i$ is a translation period of the crystal lattice. As before, $\boldsymbol{a}_i$ are the basis vectors of the crystal unit cell, and n_i any integers. As vector $\boldsymbol{A}$ connects points on the front and the rear surface of the first crystal, one can write that $d = \boldsymbol{A}\hat{\boldsymbol{z}}$ or $d = U_z - d_{\mathrm{g}}$.

Bragg reflection from the crystals takes place. The incident beam is reflected either directly from the first crystal or after multiple reflections between the crystals of the resonator, see Fig. 5.5. Similarly, the incident beam is either transmitted directly or after multiple reflections between the crystals. The amplitude r_{FP} of the radiation field reflected from the x-ray Fabry-Pérot resonator and the amplitude t_{FP} of the radiation transmitted through the x-ray Fabry-Pérot resonator is a superposition of the probability amplitudes of all possible multiple scattering paths. With each path, a probability amplitude is associated with an incident beam for arrival at the detector. It is a product of successive reflection and transmission amplitudes related to both crystal plates and

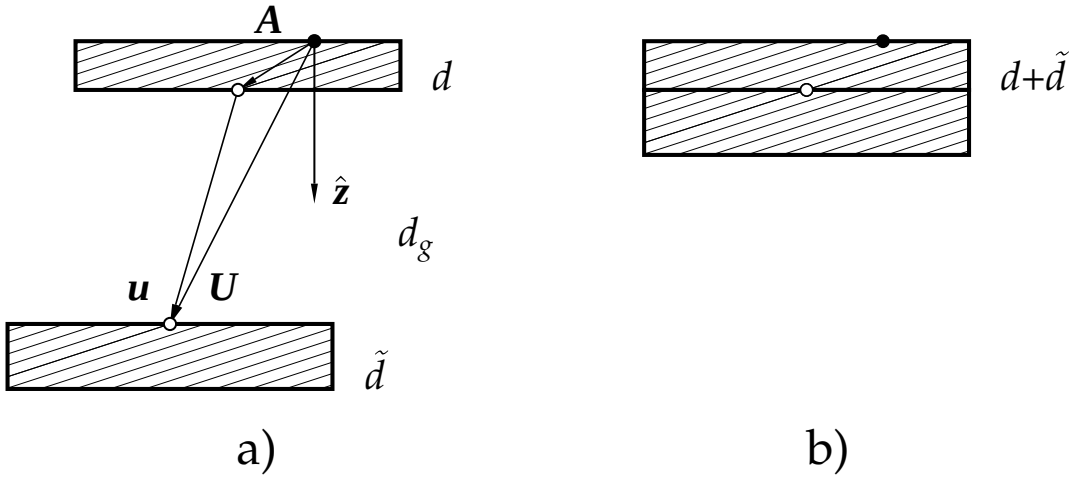

Figure 5.4: (a) Arrangement of crystals in an x-ray Fabry-Pérot resonator. Two parallel crystal plates of thicknesses d and $\tilde{d}$ are separated by a gap $d_{\rm g}$; $\hat{\boldsymbol{z}}$ is an internal normal to the crystal surface. Reflecting atomic planes are shown by the set of parallel lines. The relative position of the crystals can be described by two different translation vectors, which are, respectively, $\boldsymbol{u}$ and $\boldsymbol{U}$. Translation vector $\boldsymbol{U} = 0$ corresponds to a configuration where the front surfaces of both crystals and the reflecting atomic planes coincide in the overlapping volumes. Translation vector $\boldsymbol{u} = 0$ corresponds to a configuration where both crystals are composed of a single crystal of thickness $d + \tilde{d}$, as shown in panel (b). $\boldsymbol{A} = \boldsymbol{U} - \boldsymbol{u}$ is a translation period of the crystal lattice.

the gap. The scheme of multiple scattering paths and the amplitudes of the individual scattering events r_{0H}, $\tilde{r}_{0H}$, $\mathrm{e}^{\mathrm{i}\phi_{\rm g}}$, etc., are shown in Fig. 5.5.

The reflection amplitude $r_{0H}(d)$ and transmission amplitude $t_{00}(d)$ for radiation incident on the front surface of the first crystal are given by eqs. (2.37), and (2.36) of the dynamical theory, respectively. The reflection amplitude $r_{H0}(d)$ and transmission amplitude $t_{HH}(d)$ for radiation incident on the rear surface of the first crystal are given by eqs. (2.48), and (2.47), respectively.

The second crystal is shifted by the translation vector $\boldsymbol{U}$ from the position where the front surfaces and reflecting atomic planes coincide for both crystals. From eq. (2.53), the reflection amplitude $\tilde{r}_{0H}(\tilde{d}) = r_{0H}(\tilde{d})\,\exp(\mathrm{i}\boldsymbol{H}\boldsymbol{U})$ for the radiation incident on the front surface of the second crystal. As it was argued in sec. 2.2.2, the transmission amplitudes for the second crystal are given by the same expressions as for the first crystal, e.g., $\tilde{t}_{00}(\tilde{d}) = t_{00}(\tilde{d})$.

The transmission amplitudes for radiation propagating through the gap in the direction $\boldsymbol{K}_0$ of the incident and in the direction $\boldsymbol{K}_H$ of the reflected beam

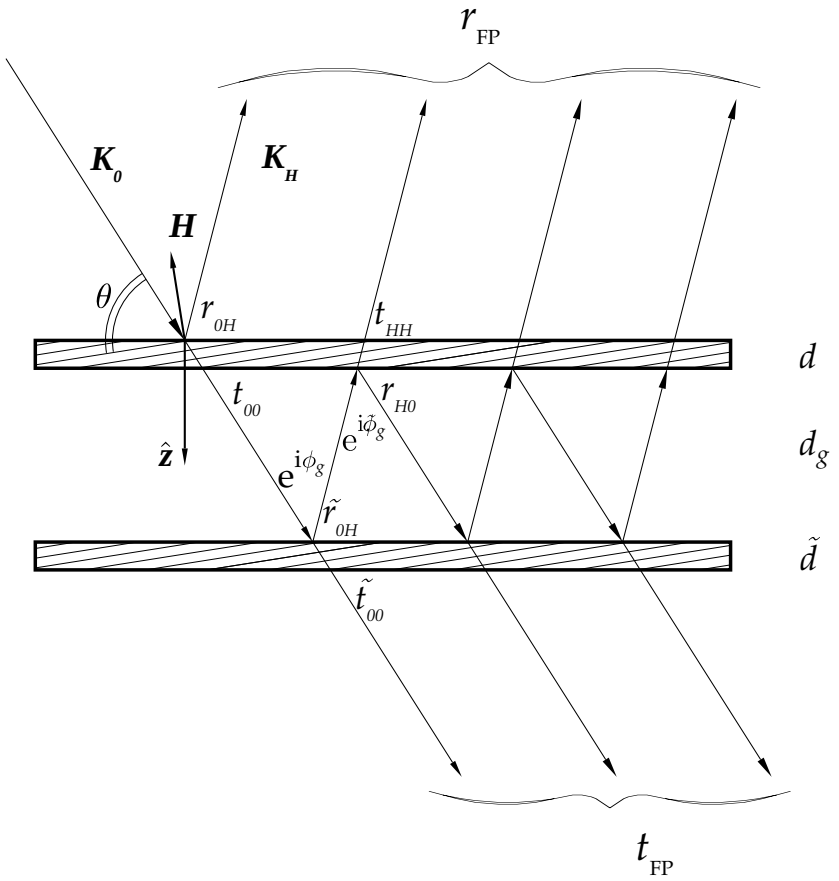

Figure 5.5: An x-ray Fabry-Pérot resonator with two parallel single crystal plates used as reflecting mirrors. The crystals are of a thickness d and $\tilde{d}$ separated by a gap $d_{\rm g}$ filled with non-diffracting medium. The scheme of multiple scattering and the amplitudes of the individual scattering events r_{0H}, r_{H0}, etc. are shown.

are given by $\mathrm{e}^{\mathrm{i}\phi_{\rm g}}$ and $\mathrm{e}^{\mathrm{i}\tilde{\phi}_{\rm g}}$, respectively. The complex phases $\phi_{\rm g}$ and $\tilde{\phi}_{\rm g}$ are:

$$\phi_{\rm g} = \frac{Kd_{\rm g}}{2\gamma_0}\chi_{\rm g}, \qquad \tilde{\phi}_{\rm g} = \frac{Kd_{\rm g}}{2\gamma_H}(\alpha - \chi_{\rm g}). \tag{5.16}$$

They are derived from eq. (2.36) and (2.47), respectively, by replacing χ_0 with $\chi_{\rm g}$ and taking $\chi_H = 0$. Here $\chi_{\rm g}$ is the Fourier component of zero order of the electric susceptibility of the medium filling the gap, cf. eq.(2.3), and (2.4).

By using the notation of Fig. 5.5, and assuming that all reflected and respectively transmitted beams are superimposed, one obtains for the reflection and

transmission amplitude coefficients the following infinite series

$$r_{\rm FP} \;=\; r_{0H} \;+\; t_{00}\mathrm{e}^{\mathrm{i}\phi_{\rm g}}\tilde{r}_{0H}\mathrm{e}^{\mathrm{i}\tilde{\phi}_{\rm g}}\left(t_{HH} + r_{H0}\mathrm{e}^{\mathrm{i}\phi_{\rm g}}\tilde{r}_{0H}\mathrm{e}^{\mathrm{i}\tilde{\phi}_{\rm g}}\left(t_{HH} + \ldots\right.\right., \tag{5.17}$$

$$t_{\rm FP} \;=\; t_{00}\mathrm{e}^{\mathrm{i}\phi_{\rm g}}\left(\tilde{t}_{00} + \tilde{r}_{0H}\mathrm{e}^{\mathrm{i}\tilde{\phi}_{\rm g}}r_{H0}\mathrm{e}^{\mathrm{i}\phi_{\rm g}}\left(\tilde{t}_{00} + \ldots\right.\right. . \tag{5.18}$$

The series can be readily transformed to the following form

$$r_{\rm FP} \;=\; r_{0H} \;+\; t_{00}\tilde{r}_{0H}t_{HH}\mathrm{e}^{\mathrm{i}(\phi_{\rm g}+\tilde{\phi}_{\rm g})}\;\left[1 + \sum_{m=1}^{\infty}\left(r_{H0}\,\tilde{r}_{0H}\,\mathrm{e}^{\mathrm{i}(\phi_{\rm g}+\tilde{\phi}_{\rm g})}\right)^{m}\right], \tag{5.19}$$

$$t_{\rm FP} \;=\; t_{00}\tilde{t}_{00}\mathrm{e}^{\mathrm{i}\phi_{\rm g}}\;\left[1 + \sum_{m=1}^{\infty}\left(r_{H0}\,\tilde{r}_{0H}\,\mathrm{e}^{\mathrm{i}(\phi_{\rm g}+\tilde{\phi}_{\rm g})}\right)^{m}\right]. \tag{5.20}$$

The summation of the series results in

$$r_{\rm FP} \;=\; r_{0H} \;+\; \frac{t_{00}\,t_{HH}\,\tilde{r}_{0H}\,\mathrm{e}^{\mathrm{i}(\phi_{\rm g}+\tilde{\phi}_{\rm g})}}{1 - r_{H0}\,\tilde{r}_{0H}\,\mathrm{e}^{\mathrm{i}(\phi_{\rm g}+\tilde{\phi}_{\rm g})}},$$

$$t_{\rm FP} \;=\; \frac{t_{00}\,\tilde{t}_{00}\,\mathrm{e}^{\mathrm{i}\phi_{\rm g}}}{1 - r_{H0}\,\tilde{r}_{0H}\,\mathrm{e}^{\mathrm{i}(\phi_{\rm g}+\tilde{\phi}_{\rm g})}}. \tag{5.21}$$

Combining eq. (5.21) with eqs. (2.36)-(2.37), (2.47)-(2.48), (2.53), and (5.16) one obtains for the reflection and transmission amplitudes of the x-ray Fabry-Pérot resonator

$$t_{\rm FP} \;=\; \frac{t_{00}(d)\,\tilde{t}_{00}(\tilde{d})\,\exp(\mathrm{i}\phi_{\rm g})}{1 - r_{H0}(d)\,r_{0H}(\tilde{d})\,\exp(\mathrm{i}\phi)}, \tag{5.22}$$

$$r_{\rm FP} \;=\; r_{0H}(d) \;+\; \frac{t_{00}(d)\,t_{HH}(d)\,r_{0H}(\tilde{d})\,\exp(\mathrm{i}\phi)}{1 - r_{H0}(d)\,r_{0H}(\tilde{d})\,\exp(\mathrm{i}\phi)} \tag{5.23}$$

with the complex phase

$$\phi \;=\; \boldsymbol{H}\boldsymbol{u} \;+\; \phi_{\rm g}\,(1-b) \;+\; \frac{Kd_{\rm g}}{2\gamma_{H}}\alpha, \qquad d_{\rm g} = \boldsymbol{u}\hat{\boldsymbol{z}}. \tag{5.24}$$

In the derivation of (5.24) use was made of the fact that $\exp(\mathrm{i}\boldsymbol{H}\boldsymbol{U}) = \exp(\mathrm{i}\boldsymbol{H}\boldsymbol{u})$ by virtue of $\boldsymbol{U} = \boldsymbol{u} + \boldsymbol{A}$ and $\exp(\mathrm{i}\boldsymbol{H}\boldsymbol{A}) = 1$.

One may verify that for zero gap ($d_{\rm g} = 0$) and in the absence of the translation of the second crystal relative to the first one ($\boldsymbol{u} = 0$), the reflection and transmission amplitudes satisfy the obvious relation

$$t_{\rm FP} = t_{00}(d + \tilde{d}), \qquad r_{\rm FP} = r_{0H}(d + \tilde{d}), \tag{5.25}$$

i.e. $t_{\rm FP}$ and $r_{\rm FP}$ are equal to the reflection and transmission amplitudes of a crystal with thickness $d + \tilde{d}$. The same result is obtained for a nonzero gap, provided $\phi = 2\pi n$ $(n = 0, \pm 1, \ldots)$ and $\chi_{\rm g} = 0$.

Let us introduce effective transmission and reflection coefficients of the crystal mirrors $\mathcal{T}$, $\mathcal{R}$

$$\begin{aligned} \mathcal{T} &= |t_{00}(d)\, t_{00}(\tilde{d})| \exp(-\phi''_{\rm g}), \\ \mathcal{R} &= |r_{H0}(d)\, r_{0H}(\tilde{d})| \exp\left[-\phi''_{\rm g}\,(1-b)\right], \end{aligned} \tag{5.26}$$

and relevant phases $\phi_{\mathcal{T}}$, $\phi_{\mathcal{R}}$:

$$\begin{aligned} \phi_{\mathcal{T}} &= \arg\left[t_{00}(d)\, \tilde{t}_{00}(\tilde{d})\right] + \phi'_{\rm g}, \\ \phi_{\mathcal{R}} &= \arg\left[r_{H0}(d)\, r_{0H}(\tilde{d})\right]. \end{aligned} \tag{5.27}$$

By using these notations and $\phi = \phi' + {\rm i}\,\phi''$, the transmission amplitude (5.22) can be written as

$$t_{\rm FP} = \frac{\mathcal{T} \exp({\rm i}\phi_{\mathcal{T}})}{1 - \mathcal{R} \exp({\rm i}\varphi)}, \tag{5.28}$$

where $\varphi = \phi' + \phi_{\mathcal{R}}$. From eq. (5.24) the phase φ can be presented in the form

$$\varphi = \boldsymbol{H}\boldsymbol{u} + \phi'_{\rm g}\,(1-b) + \phi_{\mathcal{R}} + \frac{K d_{\rm g}}{2\gamma_H}\alpha. \tag{5.29}$$

In a manner similar to the optical case discussed in sec. 5.2, the phase φ is termed as the x-ray Airy phase, or simply Airy phase unless this produces ambiguity.

Remarkably, the expression (5.28) for the transmission amplitude of the x-ray Fabry-Pérot resonator is identical to that of the optical Fabry-Pérot resonator, cf. eq. (5.4). What is different is the physical content of the parameters entering these formulae and their dependence on the incident photon energy, glancing angle, mirror characteristics, etc.

The reflectivity and transmissivity of the x-ray Fabry-Pérot resonator are calculated by

$$R_{\rm FP} = \frac{1}{|b|}|r_{\rm FP}|^2, \quad T_{\rm FP} = |t_{\rm FP}|^2. \tag{5.30}$$

With eqs.(5.22), (5.23) and (5.28), one may write the expressions for the transmissivity and the reflectivity in the form

$$T_{\rm FP} = \frac{H}{1 + F\sin^2(\varphi/2)}, \quad R_{\rm FP} = 1 - T_{\rm FP} - A_{\rm FP} \tag{5.31}$$

where $A_{\rm FP}$ is the amount of energy absorbed in the resonator,

$$H = \frac{\mathcal{T}^2}{(1-\mathcal{R})^2}, \quad \text{and} \quad F = \frac{2\mathcal{R}}{(1-\mathcal{R})^2}. \tag{5.32}$$

Within the Bragg diffraction region, $\mathcal{R}$ is close to unity and the parameter F has a large value. In this case, the transmissivity has sharp maxima when the condition

$$\varphi = 2\pi n \equiv \varphi_n, \qquad n = 0, \pm 1, \pm 2, \ldots. \tag{5.33}$$

is fulfilled. Hereafter, eq. (5.33) is called the "resonance condition".

For a negligible photo-absorption one can put $A_{\rm FP} = 0$ in eq.(5.31). As a result $R_{\rm FP} = 1 - T_{\rm FP}$. In this case the analysis of the transmissivity and reflectivity of the x-ray resonator is rather straightforward. In the following discussion we shall use this approximation to obtain analytical expressions which will allow us to gain deeper insight into the physics of x-ray Fabry-Pérot resonators. Rigorous equations are used in the following to perform computer simulations of the transmissivity and reflectivity of the x-ray Fabry-Pérot resonator. The theory is implemented in the computer code FPET, available from the author. As an example, the resonator composed of two α-Al_2O_3 single crystal plates with a $(0\ 0\ 0\ 30)$ Bragg reflection is considered.

At this point it is worth noting, that the expressions for the reflectivity and transmissivity of the x-ray Fabry-Pérot resonator obtained above, in particular eqs. (5.22)-(5.23) and (5.24) are somewhat different from those obtained by Caticha et al. (1996). The expression for the phase ϕ - eq.(5.24) contains an essential α-dependence, which is absent in the relevant formulae of Caticha et al. (1996). This may lead clearly to different predictions of the properties of the x-ray resonator.

5.3.2 Comparison with optical resonators

Equation (5.31) is similar to the Airy formula (5.8) which describes multiple-beam interference phenomena with two identical parallel non-absorbing mirrors of high reflectivity. The same Airy equation also describes the performance of optical Fabry-Pérot resonators. This means that x-ray and optical Fabry-Pérot resonators are described by similar or even identical formulas. However, one has also to observe significant differences.

First of all, the effective reflection coefficient $\mathcal{R}$ takes significant values only within the range of Bragg reflection and thus varies rapidly with x-ray energy E, glancing angle θ, crystal temperature, etc. Secondly, and this is even more important, the expression for the x-ray Airy phase φ given by eq. (5.29) differs

from the expression (5.5) known from the theory of the optical Fabry-Pérot resonator.

The difference starts with the first term $\boldsymbol{Hu}$ in eq. (5.29) which is unique in the case of x-ray resonators. This term appears due to the internal structure of the x-ray mirrors. It describes whether the reflecting atomic planes of the second crystal mirror are in perfect registry with the atomic planes in the first one. It describes how coherent the internal structure of the first mirror is with respect to the second one.

The fourth term in eq. (5.29) is also unique. The most pronounced energy, angular, and temperature dependence of the Airy phase are expressed via the α-parameter included in this term. A detailed analysis of the influence of different physical parameters on the Airy phase in the problem of the x-ray Fabry-Pérot resonator is given in the subsequent discussion.

The third term $\phi_{\mathcal{R}}$ in eq. (5.29) is a phase jump on Bragg reflections, which is similar to $\phi_{\mathcal{R}}$ in eq. (5.5) - the phase jump on reflection from optical mirrors. The latter is a constant, which takes the values 0 or π depending on the optical properties of the mirrors. Unlike this, $\phi_{\mathcal{R}}$ in Bragg reflection may change significantly within the range of total reflection. Indeed, for non-absorbing crystals one can approximate $\phi_{\mathcal{R}} = 2\phi_r$ where ϕ_r is given by eq. (2.58). As was discussed in sec. 2.2.3, for thick non-absorbing crystals the phase ϕ_r changes in the range from $-\pi$ to 0 within the Bragg reflection peak. Thus, $\phi_{\mathcal{R}}$ may change from -2π to 0 in the same range.

In particular cases, one can find similarities between the optical and x-ray Airy phases. For this one has to note that the magnitude of the scattering vector can be represented as $H = 2K\sin\theta$. Assuming that $\boldsymbol{H} \parallel \hat{\boldsymbol{z}}$ one can write for the first term in eq. (5.29): $\phi_1' = \boldsymbol{Hu} = 2Kd_{\mathrm{g}}\sin\theta$. If one then assumes symmetric diffraction, i.e., $b = -1$ and thus $\gamma_0 = \sin\theta$, the second term in eq. (5.29) can be written as $\phi_2' = \phi_{\mathrm{g}}(1-b) = Kd_{\mathrm{g}}\chi_{\mathrm{g}}/\sin\theta$. By using $n_{\mathrm{g}} = 1+\chi_{\mathrm{g}}/2$ for the refractive index in the gap and taking $|\chi_{\mathrm{g}}| \ll 1$ into account one can ascertain that under these conditions $\phi_1' + \phi_2' \simeq 2Kd_{\mathrm{g}}\sqrt{n_{\mathrm{g}}^2 - \cos^2\theta}$. Thus, in this particular case, the sum of the first and the second terms in eq. (5.29) can be reduced to the first term of the Airy phase known in the theory of the optical resonator - eq. (5.5).

5.3.3 Enhanced phase sensitivity

If one assumes (as a first approximation) that the effective reflection coefficient $\mathcal{R}$ is constant, then the transmissivity and reflectivity of the x-ray Fabry-Pérot resonator given by eqs. (5.31)-(5.32) varies only with changing Airy phase φ

(5.29) as is shown in Fig. 5.2. The relative position of the mirrors, given by the translation vector $\boldsymbol{u}$, the x-ray energy E (or wavelength λ), the glancing angle θ, the crystal temperature T, the refractive index of the material filling the gap $n_{\rm g} = 1 + \chi_{\rm g}/2$, and some other terms, have an effect on the phase φ.

The influence of each of these parameters on the phase φ and thus on the performance of the x-ray Fabry-Pérot resonator will be discussed. As a first step, however, the transmissivity of the x-ray Fabry-Pérot resonator is analyzed as a function of the Airy phase φ without specifying its dependence on any physical value.

As was already pointed out the transmissivity of the x-ray resonator has sharp transmission peaks - Fabry-Pérot resonances - when the Airy phase φ takes the values $\varphi_n = 2\pi n$ defined by the resonance condition (5.33). The resonance values of the phase are separated by 2π.

To analyse the shape of the transmission peak as a function of φ let us consider a small deviation of the phase from the resonance value φ_n, so that $|\varphi - \varphi_n| \ll 1$. By using this assumption one obtains from eq. (5.31)

$$T_{\rm FP}(\varphi) \simeq \left(\frac{\Delta\varphi}{2}\right)^2 \frac{H}{(\varphi - \varphi_n)^2 + (\Delta\varphi/2)^2}. \tag{5.34}$$

Thus the Fabry-Pérot resonances have a Lorentzian shape with a maximum value of H and phase width (FWHM) of the Fabry-Pérot resonance $\Delta\varphi = 4/\sqrt{F}$. From (5.32)

$$\Delta\varphi = \frac{2(1-\mathcal{R})}{\sqrt{\mathcal{R}}} = \frac{2\pi}{\mathcal{F}}. \tag{5.35}$$

Here $\mathcal{F}$ is the so-called finesse. As in the theory of the optical resonator the finesse $\mathcal{F}$ of the x-ray resonator is defined as a ratio of the resonance width to the separation between the resonances:

$$\mathcal{F} = \frac{2\pi}{\Delta\varphi} = \frac{\pi\sqrt{\mathcal{R}}}{1-\mathcal{R}}. \tag{5.36}$$

The higher the reflectivity of the crystal mirrors and the smaller the absorption in the gap, the larger is the effective reflection coefficient $\mathcal{R}$ (5.27), and as a consequence the larger is the finesse. For example, $\mathcal{F} = 29.8$ for $\mathcal{R} = 0.9$. As is discussed further, the finesse scales with the effective number $\mathcal{N}_s$ of multiple reflections within the gap: $\mathcal{F} = 2\mathcal{N}_s$, see sec. 5.3.9.

Equation (5.35) demonstrates the enhanced phase sensitivity of the x-ray Fabry-Pérot resonator. The enhancement factor is $\mathcal{F}$. The enhanced phase sensitivity is a general distinguishing feature of resonators of the Fabry-Pérot-type, which is due to *multiple*-beam interference.

The absolute positions of the Fabry-Pérot resonances on the phase scale are fixed, as given by the resonance condition (5.33). On the other hand, the Airy phase depends practically on all physical parameters of the problem: the energy of the x rays, the glancing angle, the gap width, the polarizabilities of the crystal and of the non-diffracting medium in the gap, the crystal temperature, etc. As a consequence, the absolute positions of the Fabry-Pérot resonances, for instance, on the x-ray energy scale, are a function of all other physical parameters. By the same arguments, the positions of the resonances on the angular scale are also a function of all other physical parameters (including the x-ray energy). Thus all the parameters should be precisely controlled, in order to observe the resonance behavior of the x-ray Fabry-Pérot resonator.

At this point let us proceed with detailed discussion of the influence of different physical parameters on the resonance behavior of x-ray Fabry-Pérot resonators.

5.3.4 Influence of the gap width

Three terms of the four in the expression for the Airy phase (5.29) depend on the relative position of the crystal mirrors, which is given by the translation vector $\boldsymbol{u}$. Thus the transmissivity of the x-ray resonator can be changed by shifting the mirrors relative to each other. Before going into further detail, let us specify the expression for the Airy phase. It is assumed that the glancing angle θ and the x-ray wavelength λ are fixed at the center of the region of total reflection ($\lambda = \lambda_{\rm c}$, $\theta = \theta_{\rm c}$, $\alpha = \alpha_{\rm c}$), as given by the modified Bragg law (2.78). From eqs. (5.29) and (5.16) the phase φ is given by

$$\varphi \;=\; \boldsymbol{H}\boldsymbol{u} \;+\; \frac{Kd_{\rm g}}{2\gamma_{_H}}\alpha_{\rm c} \;+\; \frac{Kd_{\rm g}}{2\gamma_0}\chi'_{\rm g}\;(1-b)\,. \tag{5.37}$$

The phase jump $\phi_{\mathcal{R}}$ is omitted in eq. (5.37) as it is not affected by crystal translations. By also using $\alpha_{\rm c} = \chi'_0\,(1-1/b)$ - eq. (2.61) - and $d_{\rm g} = \boldsymbol{u}\hat{\boldsymbol{z}}$ we arrive at the following expression for the Airy phase

$$\varphi \;=\; \boldsymbol{H}\boldsymbol{u} \;-\; \frac{K\boldsymbol{u}\hat{\boldsymbol{z}}}{2|\gamma_{_H}|}\;\left(\chi'_0 \;-\; \chi'_{\rm g}\right)\;\left(1-\frac{1}{b}\right). \tag{5.38}$$

The first term in (5.38) is henceforth called the "diffractive" phase and the second one - the "refractive" phase. The reasons for this are obvious. The diffractive phase depends on the diffraction vector $\boldsymbol{H}$, while the refractive phase depends on the difference of the refractive index $n = 1 + \chi_0/2$ of the crystals and the refractive index $n_{\rm g} = 1 + \chi_{\rm g}/2$ of the medium filling the gap. Both terms

in (5.38) depend on the translation vector $\boldsymbol{u}$. If the refractive indices in both media coincide, i.e., $\chi_0' = \chi_g'$, the refractive phase becomes zero.

The diffractive phase changes rapidly - a shift of one of the crystals by only $u = d_H$ along $\boldsymbol{H}$ alters the phase by 2π. This effect is seen clearly in the calculated transmission and reflection spectra in Fig. 5.7 (p. 149). The diffractive phase which can also be represented as $\boldsymbol{Hu} = 2\pi s$, describes the spatial coherence of the atomic planes in both crystal plates. If $s = n$, where $n = 0, \pm1, \pm2, \ldots$, the atomic planes in both crystals are in perfect registry relative to each other. The atomic planes, for instance, are always in perfect registry if the mirrors are monolithically cut out of a single crystal piece. It should be noted that a shift $\boldsymbol{u} \perp \boldsymbol{H}$ does not change the diffractive phase.

The refractive phase changes more slowly than the diffractive phase. To change the refractive phase by 2π the gap $d_g = \boldsymbol{u}\hat{\boldsymbol{z}}$ should be changed by $\delta d_g \simeq \lambda|\gamma_H|/|\chi_0' - \chi_g'|$. For $\lambda = 1$Å, $\chi_0' \approx 10^{-5}$ and $\chi_g' = 0$ one obtains $\delta d_g \approx 10$ μm. The refractive phase is $\approx 10^5$ less sensitive to translations than the diffractive phase.

A unique property of the x-ray Fabry-Pérot resonator shows up when the reflecting atomic planes and the crystal plate surface (or equivalently their normals $\hat{\boldsymbol{z}}$ and $\boldsymbol{H}$) are not parallel, as is shown in Fig. 5.5. Obviously, according to (5.41) it is then possible to add to $\boldsymbol{u}$ an additional shift $\delta\boldsymbol{u}$ with $\delta\boldsymbol{u}\hat{\boldsymbol{z}} = 0$ (i.e., parallel to the crystals surfaces) but $\delta\boldsymbol{u}\boldsymbol{H} \neq 0$. Thus the transmissivity of the x-ray resonator can be varied by transversal translation without varying the gap. This property is due to the intrinsic structure of the mirrors of the x-ray resonator.

Let us consider a particular case when $\hat{\boldsymbol{z}} \parallel \boldsymbol{H}$, i.e., the crystal surface and atomic planes are parallel to each other. As a result $b = -1$ and $|\gamma_H| = \sin\theta_c$. Additionally, it is assumed that there is vacuum in the gap, i.e., $\chi_g = 0$. The diffractive phase can then be presented in the form $\boldsymbol{Hu} = Hd_g = 2\pi d_g/d_H = 4\pi d_g \sin\theta_c/\lambda_c(1 + w_H)$. For the refractive phase: $-Kd_g\chi_0'(1 - 1/b)/2|\gamma_H| = 4\pi d_g \sin\theta_c w_H/\lambda_c(1 + w_H)^2$. Substituting both terms into eq. (5.38) one obtains for the Airy phase the expression

$$\varphi = 2\pi \frac{2d_g \sin\theta_c}{\lambda_c}. \tag{5.39}$$

It is valid with an accuracy of $w_H^2 \approx 10^{-10}$.

The Fabry-Pérot resonances appear every time when the gap width variation δd_g obeys the following rule

$$2\,\delta d_g \sin\theta_c = m\,\lambda_c. \tag{5.40}$$

The results expressed by eqs. (5.39) and (5.40) are remarkable in several ways. First, the Airy phase is a function of only the gap width and the x-ray wavelength in vacuum (for a fixed glancing angle). Second, the same resonance condition as (5.40) is valid for the visible-light Fabry-Pérot resonator with the optical wavelength substituted for the x-ray wavelength λ_{c}; see eq. (5.11). This fact opens up the possibility of direct comparison of the radiation wavelengths in visible and hard x-ray spectral regions. This problem is addressed in more detail in sec. 5.5.

5.3.5 Spectral dependence

Let us consider the wavelength (energy) dependence of the transmissivity of the x-ray resonator. In the subsequent discussion it is assumed for simplicity that there is a vacuum gap between the mirrors, i.e., $\chi_{\mathrm{g}} = 0$.

By using (2.69) the Airy phase (5.29) reads

$$\varphi \,=\, \boldsymbol{H}\boldsymbol{u} \,-\, 2\pi N_{\mathrm{g}} \left(\frac{\lambda}{2d_{_H}} \,-\, \sin\theta \right) \,+\, \phi_{\mathcal{R}}, \qquad N_{\mathrm{g}} = \frac{d_{\mathrm{g}}}{d_{_H}|\gamma_{_H}|}. \tag{5.41}$$

Here N_{g} is the effective number of interplanar distances $d_{_H}$ fitting into the gap of the x-ray Fabry-Pérot resonator. For a fixed glancing angle θ the center of the region of total reflection λ_{c} is given by the modified Bragg law (2.78). As a result we arrive at the expression for the Airy phase convenient for the current analysis:

$$\varphi(\lambda) \,=\, \boldsymbol{H}\boldsymbol{u} \,-\, 2\pi\, \frac{\lambda - \lambda_{\mathrm{c}}}{\lambda_{\mathrm{f}_0}} \,+\, \phi_{_H} \,+\, \phi_{\mathcal{R}}(\lambda), \qquad \phi_{_H} \,=\, 2\pi\, N_{\mathrm{g}}\, w_{_H}\, \sin\theta, \tag{5.42}$$

$$\lambda_{\mathrm{f}_0} \,=\, \frac{2d_{_H}}{N_{\mathrm{g}}} \,=\, \frac{2d_{_H}^2|\gamma_{_H}|}{d_{\mathrm{g}}}. \tag{5.43}$$

The correction $w_{_H}$, as well as the phase $\phi_{_H}$, can be considered constant within the broad spectral range, cf. discussion in sec. 2.2.3.

Positions of resonances

The positions of the Fabry-Pérot resonances on the wavelength (energy) scale are defined by eq. (5.42) and the resonance condition (5.33). The resonances can be shifted easily. They are most sensitive to the translation of mirrors, and this is expressed formally by the first term in (5.42), i.e., by the diffractive phase. The positions can also be easily shifted by changing the glancing angle. Unlike the absolute position values, the distance between resonances is

rather constant. Indeed, using the resonance condition (5.33) and neglecting for a moment the energy (wavelength) dependence of the phase $\phi_{\mathcal{R}}$ one obtains that the distance between two neighboring points of high transparency on the wavelength scale is λ_{f_0}.

In the theory of optical resonators λ_{f_0} is termed the free spectral range. It is worth noting that the expression for λ_{f_0} (5.43) is universal and depends neither on the glancing angle θ nor on the x-ray wavelength λ. As noteworthy is the fact that the expression for the free spectral range (5.43) is identical to the expression for the period of thickness oscillations in the wings of the Bragg reflection curves (2.101) for parallel-sided crystals. The only difference is that the gap width d_{g} is substituted in (5.43) for the crystal thickness d. The underlying physics is the same: interference of the radiation fields reflected from two surfaces at a distance d_{g} or d, respectively. The difference is in the number of reflections from the surfaces. In the case of the x-ray Fabry-Pérot resonator the number of reflections is large, which makes the transmission bandwidth narrow.

By replacing the wavelength λ in eq. (5.42) with the energy E, the expression for the Airy phase φ reads

$$\varphi(E) \,=\, \boldsymbol{Hu} \,+\, 2\pi\,\frac{E-E_{\mathrm{c}}}{E_{\mathrm{f}_0}} \,+\, \phi_{_H} \,+\, \phi_{\mathcal{R}}(E). \tag{5.44}$$

Here

$$E_{\mathrm{f}_0} \,=\, \frac{E_{_H}}{N_{\mathrm{g}}}\,\frac{1}{\sin^2\theta} \,\equiv\, \frac{hc}{2L_{\mathrm{g}}} \simeq \frac{0.6199\ \mathrm{meV\,mm}}{L_{\mathrm{g}}}. \tag{5.45}$$

is the free spectral range on the energy scale. The notation

$$L_{\mathrm{g}} = d_{\mathrm{g}}\frac{\sin^2\theta}{|\gamma_{_H}|} \tag{5.46}$$

is used to denote *half* of the optical delay for successive reflections. At normal incidence L_{g} equals simply the gap width d_{g}. Unlike eq. (5.43), the expression for the energy dependence of the Airy phase (5.44) is valid only for relatively small energy deviations $E - E_{\mathrm{c}} \ll E_{\mathrm{c}}$.

The weak energy dependence of the phase $\phi_{\mathcal{R}}$ was so far neglected in the analysis. To take it into account we consider the simplified case of crystal mirrors with a large thickness $d \,>\, d_e(0)$. Here $d_e(0) \,=\, \gamma_{_0}/(K|C\chi_{_H}|\sqrt{|b|})$ is the extinction length at the center $y = 0$ of the region of total reflection – eq. (2.85). In this case $\phi_{\mathcal{R}} \,=\, 2\phi_r$ where $\phi_r \,=\, \arg[r(d)]$. As pointed out in sec. 2.2.3 the phase ϕ_r changes from $-\pi$ to 0 within this region. Because of this phase an

additional transmission peak should appear within the Bragg peak. As a result, the actual free spectral range should be slightly less than that given by eq. (5.45)

The phase $\phi_r(E)$ can be approximated at the center of the Bragg peak, i.e. at $E = E_{\rm c}$, by a first-order Taylor expansion $\phi_r(E) \simeq \phi_r(E_{\rm c}) + (E - E_{\rm c})\,\partial\phi_r/\partial E$. By using $\cos\phi_r = y$, eqs. (2.28), (2.68), $\phi_r(E_{\rm c}) = -\pi/2$, and the definition of $d_e(0)$, one arrives at the following expression for the derivative: $\partial\phi_r/\partial E \simeq 4\pi d_e(0)\sin^2\theta/|\gamma_{_H}|hc = 2\pi\,E_{\rm f_0}\,(d_e(0)/d_{\rm g})$ at the center of the Bragg peak. Combining all these expressions and substituting them into eq. (5.44) one obtains for the Airy phase the following approximation

$$\varphi(E) \;=\; 2\pi\,\frac{E - E_{_0}}{E_{\rm f}}, \qquad E_{_0} \;= E_{\rm c} - \;E_{\rm f}\frac{\boldsymbol{H}\boldsymbol{u} \;+\; \phi_{_H} \;-\; \pi}{2\pi} \tag{5.47}$$

where

$$E_{\rm f} = \frac{hc}{2\tilde{L}_{\rm g}}, \qquad \tilde{L}_{\rm g} = L_{\rm g}\left(1 + \frac{2d_e(0)}{d_{\rm g}}\right) \tag{5.48}$$

is the improved approximation of the free spectral range. For x-rays with $E \simeq 15$ keV the extinction lengths are typically $10 - 100$ μm. Therefore, the modified free spectral range may differ considerably from (5.45), especially for a small gap width $d_{\rm g} \approx d_e(0)$. Equation (5.48) is similar to eq. (20) of Caticha et al. (1996). It is valid only within the central part of the Bragg reflection maximum. At the boundaries $\partial\phi_r/\partial E$ becomes strongly dependent on photoabsorption, crystal thickness, etc., and differs from the expression used. The approximation of a thick transparent mirror is no longer applicable.

It should be noted that the values of $\mathcal{T}$, $\mathcal{R}$, $\mathcal{F}$ vary slightly inside the Bragg reflection region that leads, for example, to different heights of the peaks. This is best seen from the results of the subsequent numerical calculations.

The results of the computer simulations of the energy dependence of transmission and reflection at normal incidence to the $(0\ 0\ 0\ 30)$ reflecting planes are shown in Fig. 5.6 (left and right panels respectively). The calculations for different values of the gap $d_{\rm g}$ between the sapphire mirrors are shown. The mirrors have the same thickness $d = \tilde{d} = 50\mu$m. The reflecting atomic planes in both crystals are assumed to be in perfect registry, i.e., $\boldsymbol{H}\boldsymbol{u} = 2\pi n$. This is, e.g., the case where the two thin parallel crystal plates are monolithically cut from a crystal block such that spatial lattice coherence between the two slabs is preserved. It is also assumed that it is vacuum between the crystal plates, i.e. $\chi_{\rm g} = 0$. Under these conditions only the third and the fourth terms of the Airy phase (5.29) are significant.

The dependence labeled with (a) correspond to the zero gap situation ($d_{\rm g} = 0$), i.e., to a single crystal plate of a thickness $d + \tilde{d}$. The dependence reveal the

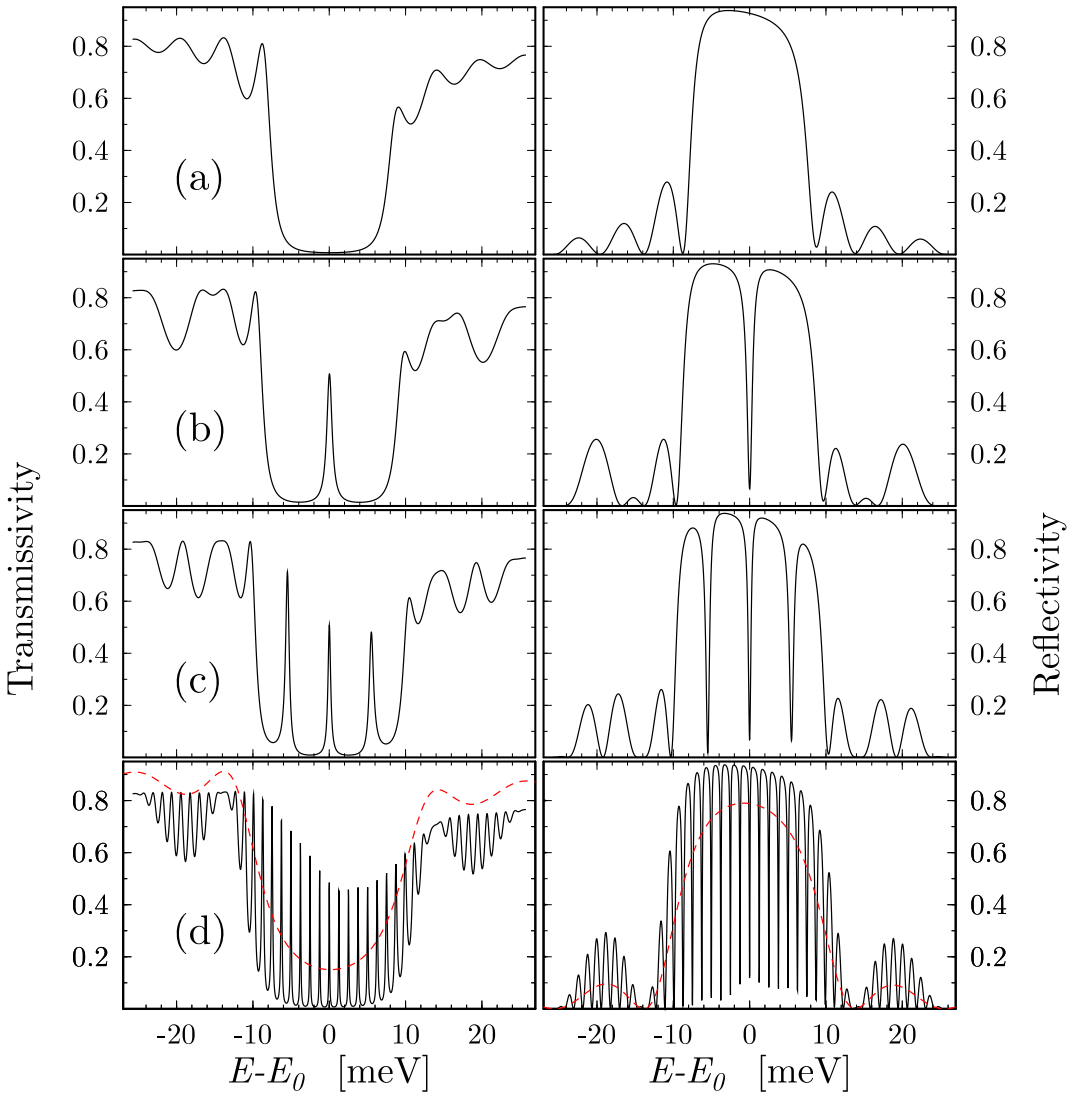

Figure 5.6: Energy dependence of transmission (left panels) and reflection (right panels) for an x-ray Fabry-Pérot resonator made of two single crystal plates of α-Al_2O_3. $E_0 = 14.3148$ keV. The incident radiation is a plane monochromatic wave at normal incidence ($\delta\theta = 0$) to the reflecting atomic planes $(0\ 0\ 0\ 30)$. The reflecting atomic planes in both crystal plates are in perfect registry relative to each other, i.e., $\boldsymbol{Hu} = 2\pi n$. The thicknesses of the crystal plates are $d = \tilde{d} = 50$ μm, and their temperature $T = 300$ K. The vacuum gap between the plates is taken to be (a) $d_g = 0$, (b) $d_g = 27.2$ μm, (c) $d_g = 81.6$ μm, (d) $d_g = 462.4$ μm. The appropriate individual crystal curves are shown for comparison with dashed lines in panels (d).

region of high reflectivity and respectively very low transmissivity, which are typical for Bragg diffraction as discussed, e.g., in sec. 2.2.2. For a zero gap the Bragg curve for backscattering is reproduced. The superimposed oscillation is a result of the finite crystal thickness $d + \tilde{d}$, cf. sec. 2.2.4.

The transmission spectra with non-zero gaps marked by (b),(c), or (d) in Fig. 5.6 show sharp maxima (resonances) in the region of initially low transmissivity. The spacing between the resonances decreases inversely proportional to the gap width. The reflection spectra show sharp minima at the same positions. The sum of both curves is not unity due to photo-absorption. For the resonator with a gap of 27.2 μm there is one transmission resonance with an energy width of $\simeq 800$ μeV – Fig. 5.6(b). The gap is chosen in such a way that the transmission resonance is exactly at the center of the region.

By increasing the gap the number of resonances increases. The resonator gaps in the subsequent examples of Fig. 5.6(c) and Fig. 5.6(d) are chosen as odd integer multiples of the gap used in the example of Fig. 5.6(b): $d_{\mathrm{g}}(\mathrm{c}) = 3d_{\mathrm{g}}(\mathrm{b})$; $d_{\mathrm{g}}(\mathrm{d}) = 17d_{\mathrm{g}}(\mathrm{b})$. Under these conditions the transmission resonances in the next graphs appear at the same positions and additionally in between.

The calculations demonstrate that in the region of high reflectivity the x-ray Fabry-Pérot resonator behaves similarly to the optical Fabry-Pérot resonator. At well defined x-ray energies a system of two strongly reflecting parallel Bragg mirrors becomes transparent.

Single crystal transmission and reflection curves are shown for comparison with dashed lines in the panels (d). In the very first approximation, the curves of the x-ray Fabry-Pérot resonator look like the reflection and transmission curves of an individual crystal modulated with a period, which depends on the distance between the mirrors. This resembles the situation with the diffraction patterns of a slit and a system of two slits, respectively, see e.g., Born and Wolf (1980) or Hecht and Zajac (1974).

The condition of perfect coherence $\boldsymbol{H}\boldsymbol{u} = 2\pi n$ between the atomic planes in both crystals was assumed in the simulations shown in fig 5.6. Figure 5.7 shows what happens if the perfect coherence is violated. This occurs when one of the mirrors is translated by a fraction of the interplanar distance. An additional shift of the crystal lattice of the second crystal leads to a shift of the diffractive phase and the transmission pattern on the energy scale. A shift of $u = d_{_H}$ along the diffraction vector $\boldsymbol{H}$ produces no change in the energy spectrum.

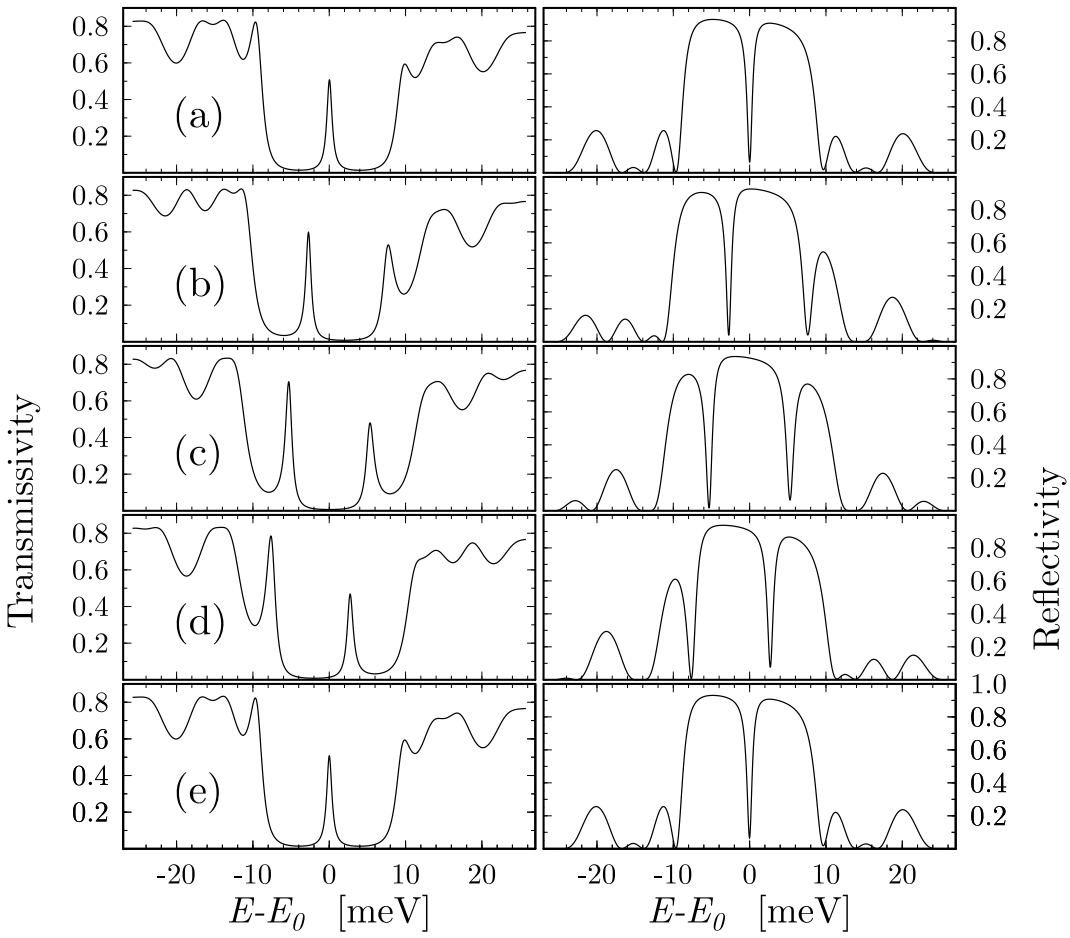

Figure 5.7: Energy dependence of transmission (left panels) and reflection (right panels) for an x-ray Fabry-Pérot resonator made of two single crystal plates of α-Al_2O_3. $E_0 = 14.3148$ keV. (a) The same as Fig. 5.6(b). (b) The crystals plates are shifted additionally relative to each other along the scattering vector $\boldsymbol{H}$ by a translation vector $\boldsymbol{u}$ of a magnitude $u = 0.25d_H$, (c) $u = 0.5d_H$, (d) $u = 0.75d_H$, (e) $u = d_H$, where $d_H = 0.433$ Å.

Resonance widths

The energy width of the resonances decreases with the gap width, as shown in Fig. 5.6. The resonances in Fig. 5.6(c) have a width of $\simeq 400$ μeV. The width of the resonances in Fig. 5.6(d) is $\simeq 100$ μeV. The spectra in Fig. 5.6 show that the x-ray Fabry-Pérot resonator acts as a high-resolution energy filter. The energy resolution can be improved by increasing the gap width, however, this increases the number of transmission resonances.

Such behavior is readily explained. The phase width of the Fabry-Pérot resonances is a constant determined only by the finesse, see (5.35). But on an energy scale, the free spectral range decreases with gap width. As a result the resonance width should also decrease. The analytical expression for the energy width Γ of a Fabry-Pérot resonance can be obtained from the phase width $\Delta\varphi$ (5.35) and from the linear dependence (5.47) of φ on E. The result is

$$\Gamma \;=\; E_{\rm f}/\mathcal{F}. \tag{5.49}$$

From eqs. (5.45) and (5.48) the energy width can also be presented in the form

$$\Gamma \;=\; \frac{E_{_H}}{\mathcal{F}\tilde{N}_{\rm g}}\,\frac{1}{\sin^2\theta} \;\equiv\; \frac{hc}{2\tilde{L}_{\rm g}\,\mathcal{F}}. \tag{5.50}$$

Here $\tilde{N}_{\rm g} \;=\; N_{\rm g}(1+2d_e(0)/d_{\rm g})$. The relative spectral width of the Fabry-Pérot resonances is then given by

$$\epsilon_{_{\rm FP}} \;=\; \frac{\Gamma}{E} \;\simeq\; \frac{1}{N_{\rm g}\,\mathcal{F}}\,\frac{|\gamma_{_H}|}{\sin\theta}. \tag{5.51}$$

Here we have neglected small extinction and refraction corrections.

The energy width is thus inversely proportional to the effective number $N_{\rm g}$ of interplanar distances fitting into the resonator gap. Additionally, this value is enhanced by the finesse $\mathcal{F}$, which in turn is defined by the reflectivity of the mirrors. The finesse increases with the reflectivity. For a fixed Bragg reflection this can be achieved either by increasing the thickness of the crystal mirrors or by cooling the crystals.

Making the Fabry-Pérot resonances sharper by changing the crystal thickness is illustrated in Fig. 5.8. The gap between the mirrors is now fixed at $d_{\rm g} \;=\; 200\ \mu$m. The thickness of the mirrors changes from $d \;=\; 50\ \mu$m in panel (a) to $d \;=\; 100\ \mu$m in panel (d), respectively. The right panels display parts of the same spectra with enhanced resolution around the resonance at $E - E_{_0} \;\simeq\; -5$ meV. The smallest resonance width is obtained for the thickest crystals. Indeed, for a crystal thickness $d \;=\; 50\ \mu$m , the resonance width is $\Delta E \;=\; 250\ \mu$eV – panel (a); for $d \;=\; 75\ \mu$m is $\Delta E \;=\; 115\ \mu$eV – panel (b); for $d \;=\; 85\ \mu$m is $\Delta E \;=\; 88\ \mu$eV – panel (c); and for $d \;=\; 100\ \mu$m is $\Delta E \;=\; 72\ \mu$eV – panel (d). However, the energy resolution improves at a cost of decreasing peak transmissivity. The energy resolution can be reduced further, e.g., to $\Delta E \;=\; 48\ \mu$eV at $d \;=\; 125\ \mu$m with a maximum transmissivity of 5%.

Notably, different Fabry-Pérot resonances do not behave in the same way. With increasing crystal thickness some resonances disappear. Those resonances

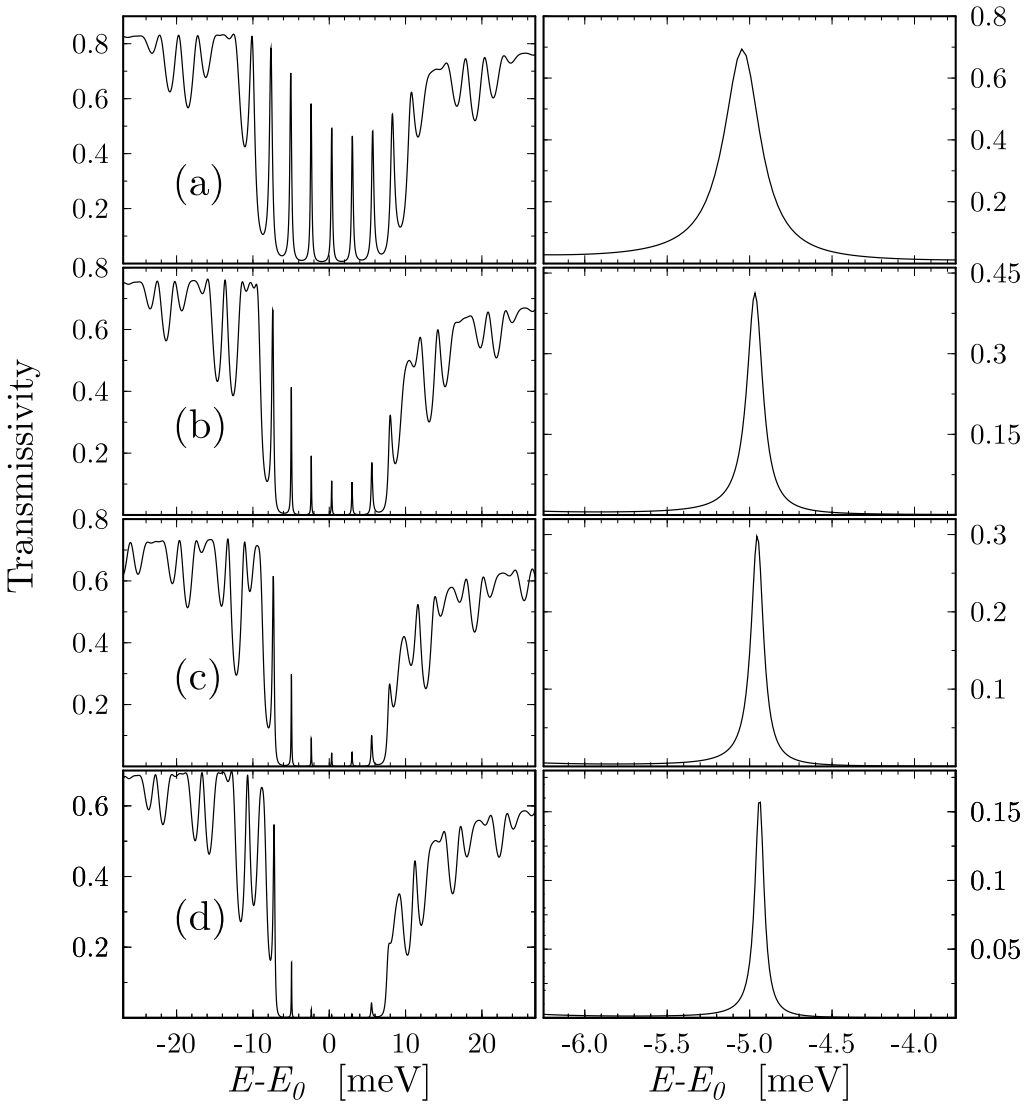

Figure 5.8: Energy dependence of transmission for an x-ray Fabry-Pérot resonator made of two α-Al_2O_3 single crystal plates of thickness (a) $d = 50$ μm, (b) $d = 75$ μm, (c) $d = 85$ μm, and (d) $d = 100$ μm. $E_0 = 14.3148$ keV. The vacuum gap between the plates is $d_g = 200$ μm. The incident radiation is a plane monochromatic wave at normal incidence ($\delta\theta = 0$) to the reflecting $(0\ 0\ 0\ 30)$ atomic planes. The reflecting atomic planes in both crystal plates are in perfect registry relative to each other. The right panels display fragments of the same spectra with enhanced resolution.

which reside in the vicinity of the highest Bragg reflectivity tend to survive. In the example of Fig. 5.8 this is the region around $E - E_0 \simeq -5$ meV. In the

dynamical theory of x-ray diffraction it is known that the highest reflectivity within the Bragg peak is at the point where the photo-absorption of the electromagnetic field inside the crystal reaches its minimum. This anomalously low photo-absorption is achieved when the field is in the form of a standing wave with nodes at the atomic planes, see, e.g., (Pinsker 1978).

Even though such behavior is very special, one can also find here similarities between the x-ray and optical resonator: The higher the reflectivity and the lower the absorption, the sharper are the Fabry-Pérot resonances. From this point of view, Be single crystals would be the best material for the x-ray resonator. Unfortunately, the crystal lattice perfection of current Be crystals is not sufficient. The next best choice is diamond. For example, Fig. 5.15 (p. 174) shows the calculated transmission spectrum of a diamond x-ray resonator. Due to low photo-absorption and very high Bragg reflectivity strong and narrow Fabry-Pérot resonances can be expected. Because of the cubic lattice, and therefore problems with multiple-beam diffraction, diamond resonators can be used only under near-normal incidence condition.

Thus, the capabilities of x-ray Fabry-Pérot resonators as high energy resolution filters surpass by far the capabilities of single Bragg reflections. Indeed, as mentioned previously in sec. 2.2.3, eq. (2.86), the relative energy resolution of a single Bragg reflection is inversely proportional to the number of reflecting planes N^* along the extinction length. The relative energy resolution of Bragg reflections for x-rays of $\simeq 15$ keV is therefore $\simeq 10^{-7}$ at best. In contrast, the performance of the x-ray Fabry-Pérot resonator as an interference filter is characterized by two enhancement factors; see eq. (5.51). First, the magnitude of the gap can be chosen much larger than the extinction length and thus $N_{\mathrm{g}} \gg N^*$. Second, due to multiple Bragg reflections within the gap, the finesse $\mathcal{F} \gg 1$.

One more interesting feature should be pointed out. The position of the resonances shift slightly in the direction of increasing energy with increasing thickness of the mirrors; see the right panels in Fig. 5.8. This can be attributed to the fact that the phase jump $\phi_{\mathcal{R}}$ on the Bragg reflection, which enters the Airy phase, depends on the thickness of the reflecting mirrors.

Additionally, a comparison of the spectra in Fig. 5.6 may remind one of the idea of a compound interference filter composed of many serial resonators with different gaps. By placing such filters successively one after another, one can hope to obtain a single transmission maximum as for the single interference filter with the smallest gap – Fig. 5.6(b). However, the energy width of this compound filter will be as small as the energy width of the single interference filter with the largest gap – Fig. 5.6(d). The idea of the compound resonator

in visible-light optics was introduced and realized by Houston (1927). Such devices are called multiple or multi-pass resonators (Vaughan 1989).

5.3.6 Time dependence

Time and energy are complementary. Therefore, the sharp energy resonances of the Fabry-Pérot resonator should be observable in the time response. This is in complete analogy with nowadays established technique: the very sharp nuclear resonances are observed either by measuring nuclear resonant energy or time spectra, see e.g., sec. 4.8. For more details see also review papers (Gerdau and de Waard 1999/2000).

According to the previous considerations, the transmission spectrum of the x-ray resonators can be approximated by a set of Lorentzians of an energy width Γ, separated by the free spectral range E_{f}. By analogy to nuclear resonance spectroscopy in the time domain, one could then expect that the time response of the x-ray Fabry-Pérot resonator to the excitation with a δ-function-like radiation pulse should be a decaying exponential function with superimposed oscillations. The decay constant is evidently $\tau = \hbar/\Gamma$, or by using $\Gamma = E_{\mathrm{f}}/\mathcal{F}$ one obtains

$$\tau = \frac{\hbar}{E_{\mathrm{f}}}\,\mathcal{F}. \tag{5.52}$$

The oscillations are a kind of quantum beating, generally known to be due to interference of the path amplitudes of scattering via neighboring resonances. In applications to nuclear resonance scattering they were first discussed by Trammell and Hannon (1978). The quantum beat period is

$$t_{\mathrm{f}} = \frac{2\pi\hbar}{E_{\mathrm{f}}}. \tag{5.53}$$

By using (5.48) one obtains

$$t_{\mathrm{f}} = \frac{2L_{\mathrm{g}}}{c}\left(1 + \frac{2d_e(0)}{d_{\mathrm{g}}}\right). \tag{5.54}$$

Thus the quantum beat period t_{f} is equal to the time lag between successive multiply-scattered beams. One should note here that the time lag is determined not only by the optical path in the gap L_{g} but also includes the part related to the extinction length $d_e(0)$ in both mirrors; see eq. (5.48).

These results can be obtained in a more rigorous fashion. The time response $T_{\mathrm{FP}}(t)$ of an x-ray Fabry-Pérot resonator in the forward direction to the excitation with a radiation pulse is given by $T_{\mathrm{FP}}(t) = |t_{\mathrm{FP}}(t)|^2$. Here $t_{\mathrm{FP}}(t)$ is the

amplitude of the time response. The time dependence of the amplitude is calculated as a Fourier transform of the product of the energy dependence of the transmission amplitude $t_{\rm FP}(E)$ and the spectral amplitude of the incident radiation pulse $a_{\rm inc}(E)$:

$$t_{\rm FP}(t) \;=\; \int_{-\infty}^{\infty} \frac{{\rm d}E}{2\pi\hbar}\, {\rm e}^{-{\rm i}Et/\hbar}\, t_{\rm FP}(E)\, a_{\rm inc}(E). \tag{5.55}$$

By putting $t_{\rm FP}(E) = 1$ one obtains from (5.55) the amplitude of the time dependence $a_{\rm inc}(t)$ of the incident radiation pulse, as a particular case.

The transmission spectrum amplitude of the x-ray Fabry-Pérot resonator, given by (5.28), can be written as a power series of $\mathcal{R}{\rm e}^{{\rm i}\varphi(E)}$:

$$t_{\rm FP}(E) \;=\; \mathcal{T}{\rm e}^{{\rm i}\phi_{\mathcal{T}}} \sum_{n=0}^{\infty} \mathcal{R}^n {\rm e}^{{\rm i}\varphi(E)\, n}. \tag{5.56}$$

To obtain an analytical expression for $t_{\rm FP}(t)$, we assume for simplicity that $\mathcal{R}$, $\mathcal{T}$, and $\phi_{\mathcal{T}}$ are energy independent in the region of the Bragg peak $E_{\rm c} - \Delta E/2 \leq E \leq E_{\rm c} + \Delta E/2$, where ΔE is given by (2.84) and (2.83). Outside the region $\mathcal{R} = 0$. By using eqs. (5.47) and (5.53) the Airy phase can be written: $\varphi(E) = (E - E_0)t_{\rm f}/\hbar$. We assume further that many Fabry-Pérot resonances enter into ΔE, i.e., $\Delta E \gg E_{\rm f}$. Furthermore, $a_{\rm inc}(E) \simeq {\rm const}$ within the region of total reflection. The latter means that the spectrum of the incident radiation pulse is assumed to be much broader than ΔE. Alternatively, the duration of the incident pulse is much shorter than the Bragg diffraction from an individual crystal mirror, cf. sec. 2.2.5. As a result with good accuracy, one obtains for the response amplitude

$$t_{\rm FP}(t) \;=\; \mathcal{T}{\rm e}^{{\rm i}\phi_{\mathcal{T}}} \sum_{n=0}^{\infty} \mathcal{R}^n\, {\rm e}^{-{\rm i}nE_0 t_{\rm f}/\hbar}\, \delta(t \,-\, n\, t_{\rm f}). \tag{5.57}$$

Thus the time response amplitude is a sequence of very sharp pulses reappearing every time interval $t_{\rm f}$ with the next one attenuated by $\mathcal{R}$. This structure is clearly due to multiple reflections between the mirrors of the resonator.

Since the time response amplitude is only significant at $t = nt_{\rm f}$ one can substitute $t/t_{\rm f}$ for n. As a result one arrives at

$$t_{\rm FP}(t) \;\simeq\; \mathcal{T}{\rm e}^{{\rm i}\phi_{\mathcal{T}}}\, \exp\left(-{\rm i}\frac{E_0 t}{\hbar} - \frac{t}{2\tau^*}\right) \sum_{n=0}^{\infty} \delta(t \,-\, n\, t_{\rm f}), \tag{5.58}$$

with

$$\tau^* = \frac{t_{\rm f}}{2\ln(1/\mathcal{R})}. \tag{5.59}$$

One obtains finally by using (5.30) for the time response of the resonator

$$T_{\rm FP}(t) \simeq |\mathcal{T}|^2 \exp(-t/\tau^*) \sum_{n=0}^{\infty} \delta(t - n\, t_{\rm f}). \tag{5.60}$$

The characteristic response time of the x-ray Fabry-Pérot resonator is τ^*. If $\mathcal{R} \simeq 1$ then $\ln(1/\mathcal{R}) \simeq 1 - \mathcal{R} \simeq \pi/\mathcal{F}$. As a result $\tau^* \simeq t_{\rm f}\mathcal{F}/2\pi$, or $\tau^* = \tau$. Thus τ^* is equivalent to τ obtained in eq. (5.52) from the energy width of the Fabry-Pérot resonances.

The separation between the successive pulses $t_{\rm f}$ is equivalent to the "period of quantum beats", derived in (5.53) from the distance between the Fabry-Pérot resonances. The width of the periodic δ-pulses in (5.58) and (5.60) is zero, as a very large number of the Fabry-Pérot resonances is assumed to fall into the Bragg peak ($\Delta E/E_{\rm f} \gg 1$). In reality the pulses are about $\hbar/\Delta E$ wide and described by $\sin^2(\Delta E t/2)/t^2$ instead of the δ-function for the terms with $n > 0$.

By using the above derived formulae, one can estimate that for an x-ray Fabry-Pérot resonator with a gap of 5 cm the time lag between successive multiply-scattered beams is $t_{\rm f} = 333$ ps. Thus, in this case, an extinction length of $\simeq 15$ μm gives only a 0.06% correction to $t_{\rm f}$. If the finesse $\mathcal{F} = 15$, then the characteristic response time of the resonator is $\tau^* \simeq 0.8$ ns, which corresponds to an energy width of the Fabry-Pérot resonances $\Gamma \simeq 0.8$ μeV.

One can use eq. (5.55) to perform non-approximated numerical calculations. Figure 5.9 shows an example of such calculations for an x-ray Fabry-Pérot resonator with the same parameters as used for the evaluation of the energy spectra in Fig. 5.6. The time dependence labeled with (b) correspond to a gap $d_{\rm g} = 27.2$ μm, (c) $d_{\rm g} = 81.6$ μm, and (d) $d_{\rm g} = 462.4$ μm. They represent time responses to the excitation with 0.32 ps radiation pulses (5 meV spectral width). The corresponding energy transmission spectra of the x-ray Fabry-Pérot resonator are shown in the right panels (the same as in Fig. 5.6). The dotted lines show the spectrum of the incident radiation pulse.

As is clearly seen, in all three cases the decay is given by an exponential function. This is attributed to a Lorentzian form of the Fabry-Pérot resonances on the energy scale. The decay time increases with the gap (with decreasing free spectral range $E_{\rm f}$), in agreement with eq. (5.52). This is also in agreement with the corresponding behavior of the width of the resonances, cf. sec. 5.3.5. In the case presented in panel (d), where the incident radiation pulse excites many resonances simultaneously, the decay is modulated by quantum beats. The period of quantum beats is a reciprocal value of the energy difference between the resonances $E_{\rm f}$ - eq. (5.53), or equivalently it scales with $\tilde{L}_{\rm g} = L_{\rm g}\,(1 + 2d_e(0)/d_{\rm g})$. With the extinction length $d_e(0) = 15$ μm for the Bragg

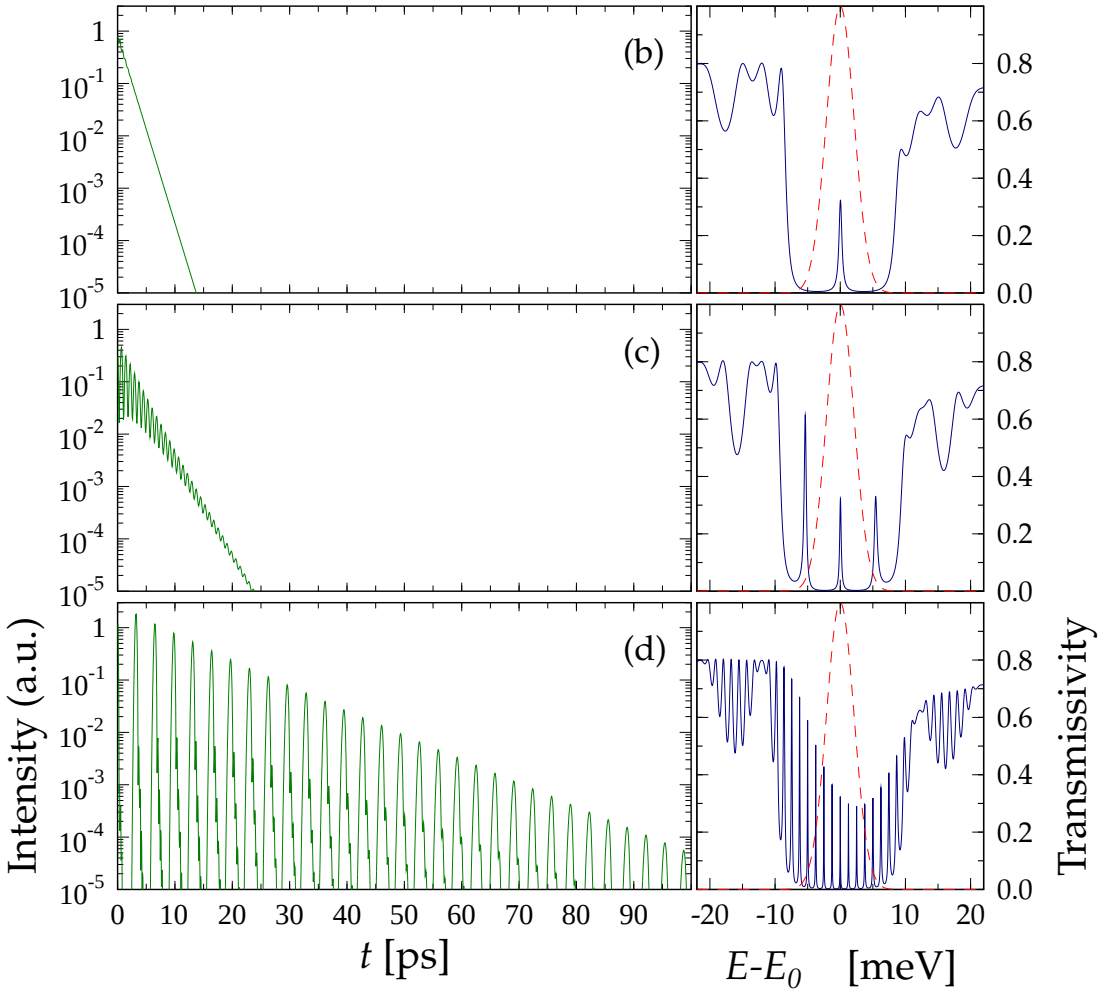

Figure 5.9: Left: the time dependence of transmission of a short radiation pulse through an x-ray Fabry-Pérot resonator. Right: the energy spectrum of transmission through the resonator (the same as in Fig. 5.6). The dotted lines show the spectrum of the incident radiation pulse, 5 meV spectral width, corresponding to a 0.32 ps pulse duration. The x-ray Fabry-Pérot resonator is made of two α-Al_2O_3 single crystal plates: $d = \tilde{d} = 50$ μm at $T = 300$ K, with a gap (b) $d_g = 27.2$ μm, (c) $d_g = 81.6$ μm, and (d) $d_g = 462.4$ μm. The incident radiation is a plane wave at normal incidence ($\delta\theta = 0$) to the reflecting $(0\ 0\ 0\ 30)$ atomic planes . $E_0 = 14.3148$ keV.

reflection in question, the quantum beat period is 6.7% longer than the time of flight between the mirrors. This agrees perfectly with the calculated time dependence in Fig. 5.9(d).

5.3.7 Angular dependence

The preceeding discussion was general, in the sense that it was not restricted to any specific glancing angle θ. By changing the glancing angle θ the Fabry-Pérot resonances are shifted on the energy scale. The divergent incident beam thus can blur the resonances. In practice it is important to know the admissible angular divergence of the primary beam which does not yet smear out the resonances. In other words, knowledge of the angular widths of the Fabry-Pérot resonances is of practical importance.

For a fixed x-ray energy E (wavelength λ), the center of the angular region of total reflection is given by θ_c (2.78). The Airy phase φ (5.41) as a function of θ then reads

$$\varphi \;=\; 2\pi N_g \,(\,\sin\theta \;-\; \sin\theta_c\,) \;+\; \boldsymbol{H}\boldsymbol{u} \;+\; \phi_{_H} \;+\; \phi_{\mathcal{R}}. \tag{5.61}$$

The angular width of a Fabry-Pérot resonance can be calculated from the phase width $\Delta\varphi = 2\pi/\mathcal{F}$ (5.35) of the Fabry-Pérot resonance.

Let us first assume that θ_c is far enough from $\pi/2$ so that the approximation $\sin\theta \;-\; \sin\theta_c \simeq (\theta - \theta_c)\,\cos\theta_c$ can be applied. Then the angular width is

$$\Delta\theta \;=\; \frac{1}{N_g \mathcal{F} \cos\theta_c}. \tag{5.62}$$

By using this relation, one can estimate that for $\cos\theta_c > 0.1$, i.e., for $\theta_c < 85°$, the angular width of the Fabry-Pérot resonances is very small. Indeed, for a Fabry-Pérot resonator with a gap of $d_g = 1$ cm, $d_{_H} = 0.5$ Å, and $\mathcal{F} = 30$, the angular width of the Fabry-Pérot resonances is typically $\Delta\theta \approx 10^{-9}/\cos\theta_c$. For a gap of $d_g = 0.1$ mm, the width $\Delta\theta \approx 10^{-7}/\cos\theta_c$ is still very small. In any event it is much smaller than the angular divergences of available or planned x-ray sources. Thus, it is practically impossible to excite selectively separate Fabry-Pérot resonances at glancing angles far from $\pi/2$ ($\cos\theta_c > 0.1$).

From (5.62) the angular width of the resonances can be enhanced drastically by choosing θ_c close to $\pi/2$. For example, for $\cos\theta_c \approx 10^{-4}$ (the angular deviation from normal incidence is $\delta\theta = \pi/2 - \theta_c \approx 1.4 \times 10^{-2}$) the corresponding widths are $\approx 10^3$ larger. It is therefore favorable to operate the x-ray resonator at glancing angles close to $\pi/2$.

The effect is most pronounced when $\theta_c = \pi/2$. Under this condition the approximation $\sin\theta \;-\; \sin\theta_c \simeq -\delta\theta^2/2$ can be applied. According to eq.(5.61) the phase φ is proportional to the square of the angular deviation from normal incidence:

$$\varphi \;=\; -\pi N_g\,\delta\theta^2 \;+\; \boldsymbol{H}\boldsymbol{u} \;+\; \phi_{_H} \;+\; \phi_{\mathcal{R}}. \tag{5.63}$$

As a result the angular positions of the resonances are not equidistant and their widths are not equal.

By using eq. (5.35) and the definition of $N_{\rm g}$ one obtains for the width of the transmission peak at near-normal incidence

$$\Delta\theta \;=\; 2\sqrt{\frac{d_{_H}\,|\gamma_{_H}|}{d_{\rm g}\,\mathcal{F}}}. \tag{5.64}$$

By using this equation and eq. 5.51, one can obtain a very simple relation between the angular acceptance and the relative spectral width $\epsilon_{_{\rm FP}}$ of the Fabry-Pérot resonances

$$\Delta\theta \;=\; 2\sqrt{\epsilon_{_{\rm FP}}}. \tag{5.65}$$

The relation is valid at near-normal incidence to the reflecting planes. It demonstrates one of the most striking features of these devices. The angular acceptance scales with the *square root* of the spectral resolution! Thus, resonances with a relative spectral width as small as $\epsilon_{_{\rm FP}} \;=\; 10^{-10}$ could still be selectively excited by an x-ray beam of a 20 μrad divergence. Such beams are routinely available at modern synchrotron radiation facilities.

This square root dependence is due to the backscattering geometry. A similar situation is also observed for single Bragg reflections, see eq. (2.89). The crucial difference is in the enhanced spectral resolution of the resonators owing to multiple-beam interference effects.

Figure 5.10 shows an example of numerical calculations. The angular dependence of transmission (left panels) and reflection (right panels) are calculated with the same parameters for the x-ray Fabry-Pérot resonator used in the calculations of the energy dependence in Fig. 5.6. The difference is that the x-ray energy is now fixed at $E = E_{_0}$, i.e., at the energy at which maximum reflectivity occurs at normal incidence. The curves labeled with (a) correspond to a zero gap ($d_{\rm g} = 0$), i.e., a single crystal plate of a thickness $d+\tilde{d}$. The angular dependence show a typical for Bragg back-diffraction broad ≈ 2 mrad region of high reflectivity and very low transmissivity, respectively, as discussed, e.g., in sec. 2.2.2.

The angular dependence of transmission calculated for non-zero gaps are marked by (b),(c), or (d) in Fig. 5.10. They show maxima in the region of initially low transmissivity. The reflection curves show sharp minima at the same positions. The angular widths of the transmission maxima are not constant. The largest width is observed at near-normal incidence. It decreases rapidly with increasing incidence angle $\delta\theta$.

The angular width of the region of high transmissivity at near-normal incidence decreases with increasing gap width. For a gap of $d_{\rm g} \;=\; 27.2$ μm the

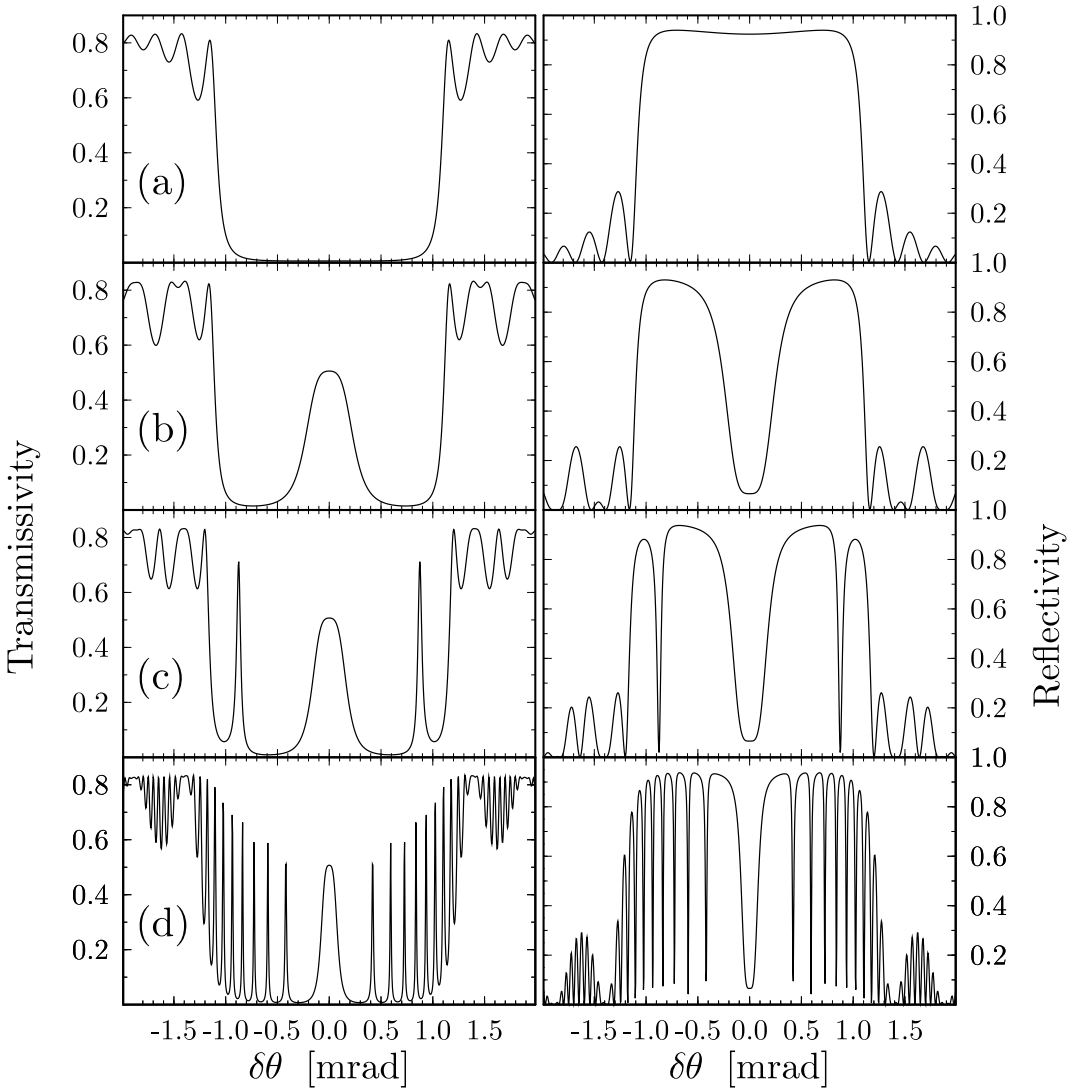

Figure 5.10: Angular dependence of transmission (left panels) and reflection (right panels) for an x-ray Fabry-Pérot resonator made of two single crystal plates of α-Al_2O_3. The radiation is a plane monochromatic wave ($E = E_0 = 14.3148$ keV) at near-normal incidence to the reflecting $(0\ 0\ 0\ 30)$ atomic planes. The reflecting $(0\ 0\ 0\ 30)$ atomic planes in both crystal plates are in perfect registry relative to each other, i.e., $\boldsymbol{H}\boldsymbol{u} = 2\pi n$. The thicknesses of the crystal plates $d = \tilde{d} = 50$ μm, and their temperature $T = 300$ K. The vacuum gap between the plates is taken to be (a) $d_{\rm g} = 0$, (b) $d_{\rm g} = 27.2$ μm, (c) $d_{\rm g} = 81.6$ μm, (d) $d_{\rm g} = 462.4$ μm.

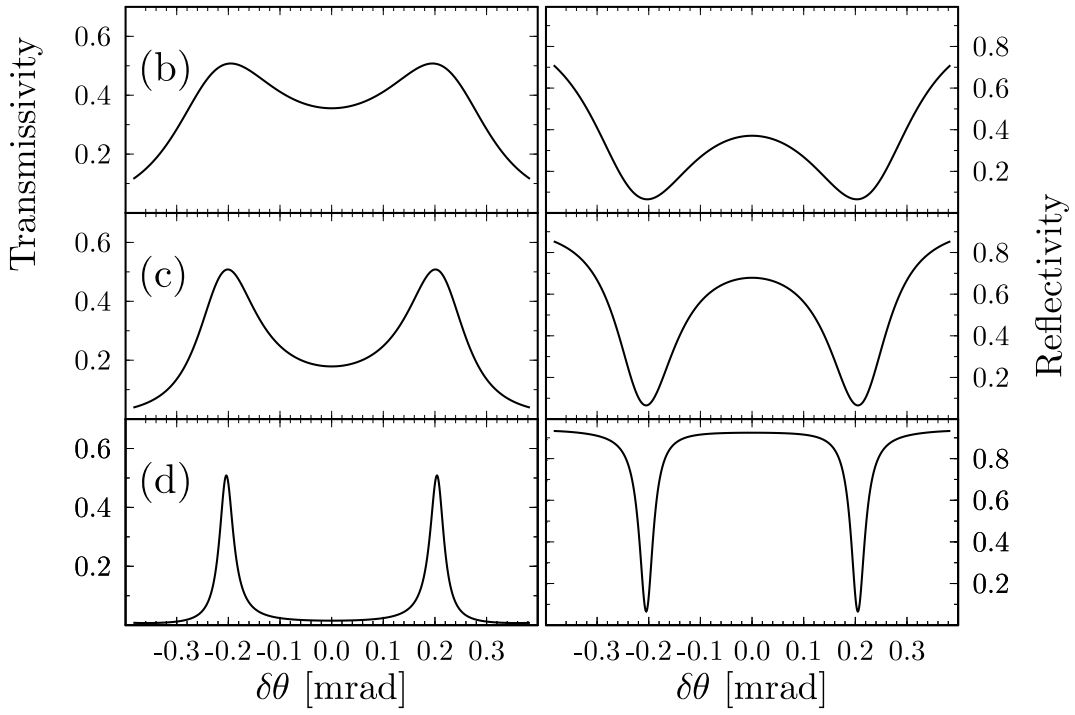

Figure 5.11: Angular dependence of transmission (left panels) and reflection (right panels) for the x-ray Fabry-Pérot resonator made of two single crystal plates of α-Al_2O_3. The vacuum gap between the plates is taken to be (b) $d_g = 27.2$ μm, (c) $d_g = 81.6$ μm, (d) $d_g = 462.4$ μm. In contrast to Fig. 5.10, the x-ray energy is changed by $\delta E = 0.3$ meV ($E = E_0 + \delta E$).

angular width is 500 μrad - Fig. 5.10(b), while for a gap of $d_g = 462.4$ μm the angular width is 160 μrad - Fig. 5.10(d). However, it is still much larger than the typical angular divergence of $\simeq 20$ μrad for synchrotron radiation at third generation facilities. This fact demonstrates that it is favorable to operate the x-ray resonator as a high energy resolution filter at near-normal incidence, where the high transmissivity is preserved over a large angular range.

The unfavorable influence of multiple beam diffraction in crystals with the diamond structure (Si, Ge, diamond, etc) on the performance of the x-ray resonator was already discussed. To avoid this problem, Steyerl and Steinhauser (1979) have proposed operating the resonator *slightly off* normal incidence. The recent studies of Shvyd'ko and Gerdau (1999) and Sutter et al. (2001) (see also sec. 2.4.3) have shown that in some cases one has to deviate the incident beam as far as 200 μrad from normal incidence to avoid completely the multiple beam diffraction effects. It is therefore of interest to know how broad is the

angular region of high transmissivity of the x-ray Fabry-Pérot resonator in this case.

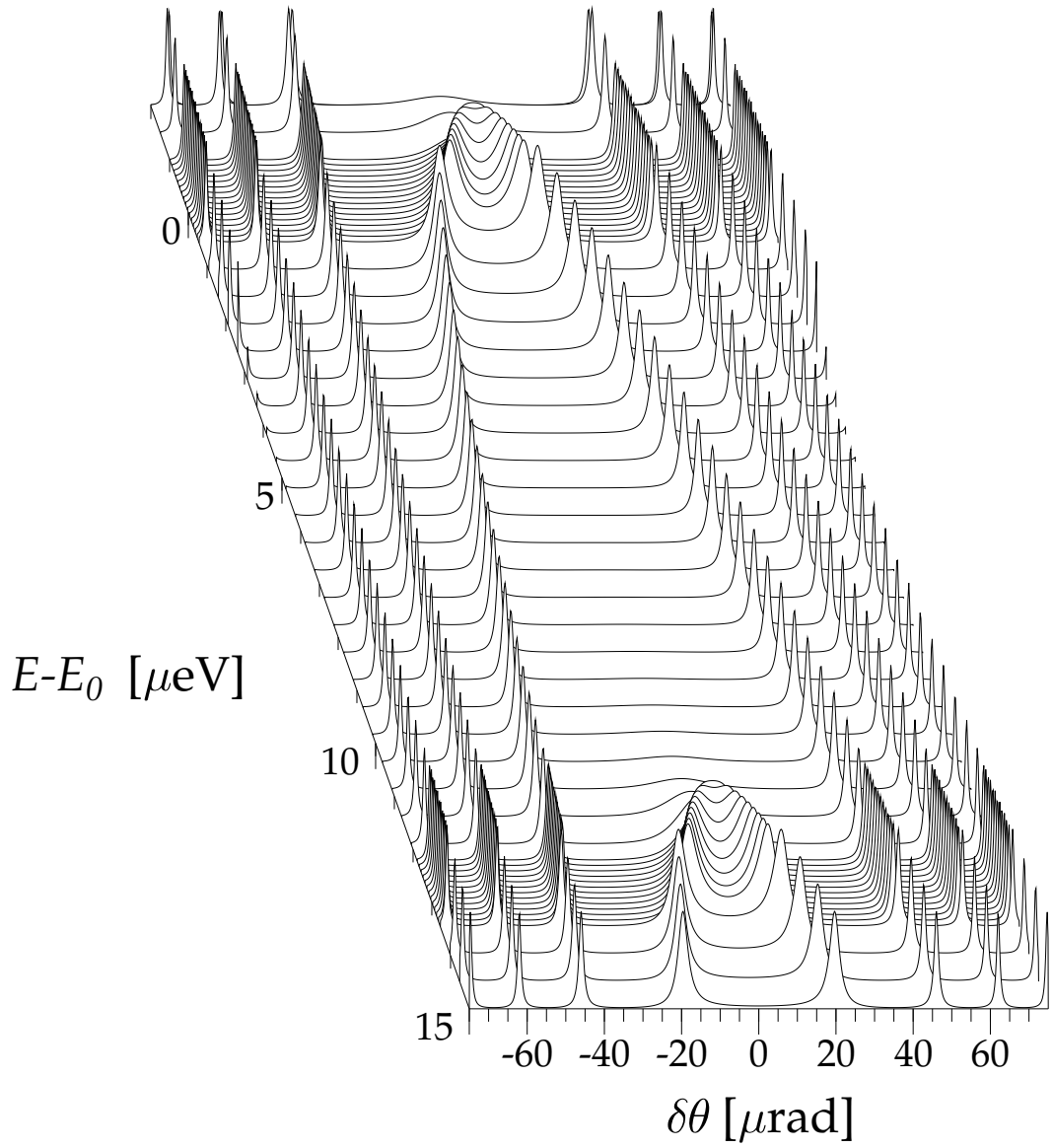

Figure 5.12: Two-dimensional $(E, \delta\theta)$ plot of transmissivity of x-rays through a system of two ideally parallel single crystal plates of α-Al_2O_3 spaced a distance of 5 cm apart. Crystal plates are 50 μm thick. Crystal surfaces are parallel to the (0001) atomic planes. X-rays with an energy E in the vicinity of $E_0 = 14.3148$ keV incident upon the crystal plates almost normal to the atomic planes. The angle of deviation from normal incidence is $\delta\theta$. The Bragg reflection (0 0 0 30) is used.

By way of example, the same sapphire resonator is used. The energy of x-rays has now to be slightly changed by $\delta E = 0.3$ meV to $E = E_0 + \delta E$, so that the maximum transmissivity is observed at $\delta\theta = \pm 200$ μrad. With this exception the curves shown in Fig. 5.11 were calculated using the same set of parameters as for Fig. 5.10. For convenience, the angular dependence in Fig. 5.11 are shown for a smaller angular range. The results of the calculation are given only for non-zero gaps, which are labeled as before by (b), (c) and (d), respectively.

As in the previous case, the width of the angular range of high transmissivity decreases with gap width. The absolute values of the angular widths are smaller. For example, for a gap of $d_g = 462.4$ μm - panel (d) - the angular width is 30 μrad which is already comparable with a typical angular divergence of x-rays available at third generation synchrotron radiation facilities.

This example shows in particular, cases where one can operate the x-ray Fabry-Pérot resonator off exact normal incidence without deteriorating its performance too much. In practice a decision, whether it is possible or not, depends mostly on the interplay of the angular divergence of the incident beam and the angular width of high transmissivity which is eventually defined by the required energy width of the Fabry-Pérot resonances.

Two-dimensional picture

To gain more insight into the performance of the x-ray Fabry-Pérot resonator a two-dimensional (E, θ) plot of transmissivity is presented in Fig. 5.12. The same model of the sapphire x-ray resonator is used. It is a system of two ideally parallel 50 μm thick single crystal plates in perfect registry. The gap between the plates is chosen to be 5 cm.

Because of the rather large gap, the widths of the Fabry-Pérot resonances are significantly smaller than in the previous cases. The energy width of the resonances is about 1 μeV. Despite this fact these very sharp resonances can be selectively excited by a beam of $10 - 20$ μrad angular divergence. For this however, the center of the radiation cone should be directed exactly perpendicular to the reflecting planes ($\delta\theta = 0$). If this condition is not fulfilled, say $\delta\theta \geq 20$ μrad, a broad distribution of the Fabry-Pérot resonances with different resonance energies will be excited. This example clearly demonstrates the advantages of the normal-incidence geometry for selective excitation of the resonances in x-ray Fabry-Pérot resonators.

5.3.8 Temperature dependence

Another physical parameter, which influences the performance of x-ray Fabry-Pérot resonators is the temperature T. Its influence is brought to bear in two different ways. First, it changes the interplanar distance $d_{_H}(T)$ of the reflecting atomic planes in the crystal mirrors and thus shifts the Bragg peak position. Second, it changes the relative position of the mirrors, which also changes the gap width $d_{\rm g}$. This happens because of thermal expansion (contraction) of the material holding the crystal mirrors in space. The thermal expansion coefficient of the crystals $\beta_{_H} = d_{_H}^{-1}(\mathrm{d}d_{_H}/\mathrm{d}T)$ in the direction of the diffraction vector $\boldsymbol{H}$, and the expansion coefficient of the supporting material $\beta_{\rm g} = d_{\rm g}^{-1}(\mathrm{d}d_{\rm g}/\mathrm{d}T)$ are used in the subsequent considerations.

The change of the interplanar distance $d_{_H}(T)$ with temperature shifts the region of total reflection, i.e. the window of observation. The shift on the energy scale is $\delta E = -E_{_H}\,\beta_{_H}\,\delta T/\sin\theta$, as derived from Bragg's law. Let us assume, that the energy E (or the glancing angle θ) of x-rays follows the change of the temperature in such a way, that the "observation" point is always kept at the center of the region of total reflection. In such a "reference system" α_c and $\phi_{\mathcal{R}}$ do not change with changing temperature. One can use then eq. (5.37) or (5.38) for the subsequent analysis of the variation of the Airy phase with temperature. As a result one obtains

$$\frac{\mathrm{d}\varphi}{\mathrm{d}T} = 2\pi\frac{d_{\rm g}}{d_{_H}}\left[(\beta_{\rm g}-\beta_{_H}) - \beta_{\rm g}\left(\chi_0' - \chi_{\rm g}'\right)\right]. \tag{5.66}$$

It was assumed for simplicity of the analysis that $\boldsymbol{H} \parallel \hat{\boldsymbol{z}}$.

The first term in the square brackets is due to the variation of the diffractive and the second - of the refractive phase, respectively. Because of the smallness of χ_0' and $\chi_{\rm g}'$ the second term in eq. (5.66) is, generally speaking, about 10^5 times smaller than the first one. In most cases it can be neglected, except for the case, where the first term is zero.

This happens if the thermal expansion coefficient of the material that holds the crystals and that of the crystals are equal, i.e., $\beta_{\rm g} = \beta_{_H}$. Under this condition the diffractive phase does not change at all - the first term in the square brackets is zero. This situation is automatically realized if the two crystal mirrors are monolithically cut from a single crystal block such that the spatial lattice coherence between the two slabs is preserved. Independent of the temperature the reflecting atomic planes in both crystals are in perfect registry, i.e., $\boldsymbol{H}\boldsymbol{u} = 2\pi n$, and the diffractive phase is insensitive to the temperature. In this case only the refractive phase changes, however very slowly.

Thus if the thermal expansion coefficients of the material that holds the crystal mirrors and that of the crystals themselves are equal, the Fabry-Pérot resonances within the region of total reflection do not move. A small correction, given by the second term in eq. (5.66) be can neglected. The resonances move together with the region of total reflection as a whole. This property is very important for the design of tunable high energy resolution filters based on the x-ray Fabry-Pérot resonator, see sec. 5.5.

5.3.9 Finite number of multiple reflections

In the foregoing discussion an infinite train of successively reflected waves was used in all calculations of the transmissivity and reflectivity of the resonator - eqs. (5.19)-(5.21). It is of interest to figure out how many reflections $m_{\min}$ are actually sufficient to obtain a perfect interference pattern.

To simulate a finite number of interfering rays the summation in eq. (5.19) and in eq. (5.20) is truncated at the term $m = m_{\min}$. Figure 5.13 shows results of calculations of the energy spectra for different values of $m_{\min}$. As can be seen, the interference pattern in Fig. 5.13(b), calculated with 15 reflected rays, is practically indistinguishable from the interference pattern in Fig. 5.13(a), calculated with infinite number of reflected rays[3].

$m_{\min} = 15$ is not a universal number. It is specific for the given resonator. Numerical simulations show that the minimum number of required reflections is larger the higher is the reflectivity (or the thickness) of the mirrors, or equivalently, the higher the finesse of the device.

The effective number of reflected beams contributing to the practically complete response of the x-ray Fabry-Pérot resonator can be ascertained analytically by using the time dependence derived in sec. 5.3.6. We shall require so many reflections, that the remainder do not contribute to the signal by more than $\approx 1\%$. From eq. (5.60) this criterion is fulfilled after a time interval of $t^* \simeq 2\pi\tau$. The number of reflected rays is then $\mathcal{N}_r = t^*/t_{\mathrm{f}}$ or by using $\tau = t_{\mathrm{f}}\mathcal{F}/2\pi$ one obtains

$$\mathcal{N}_r \simeq \mathcal{F}. \tag{5.67}$$

The effective number of scattering events is obviously twice as much: $\mathcal{N}_s \simeq 2\mathcal{F}$. As follows from eq. (5.67), the finesse $\mathcal{F}$ is also a measure of the effective number of reflections in the x-ray Fabry-Pérot resonator.

This analytical result is in agreement with the numerical simulations presented in Fig. 5.13. In this particular case the peak Bragg reflectivity for each

[3]Intensities in the vicinity of the peaks differ by at most 1%.

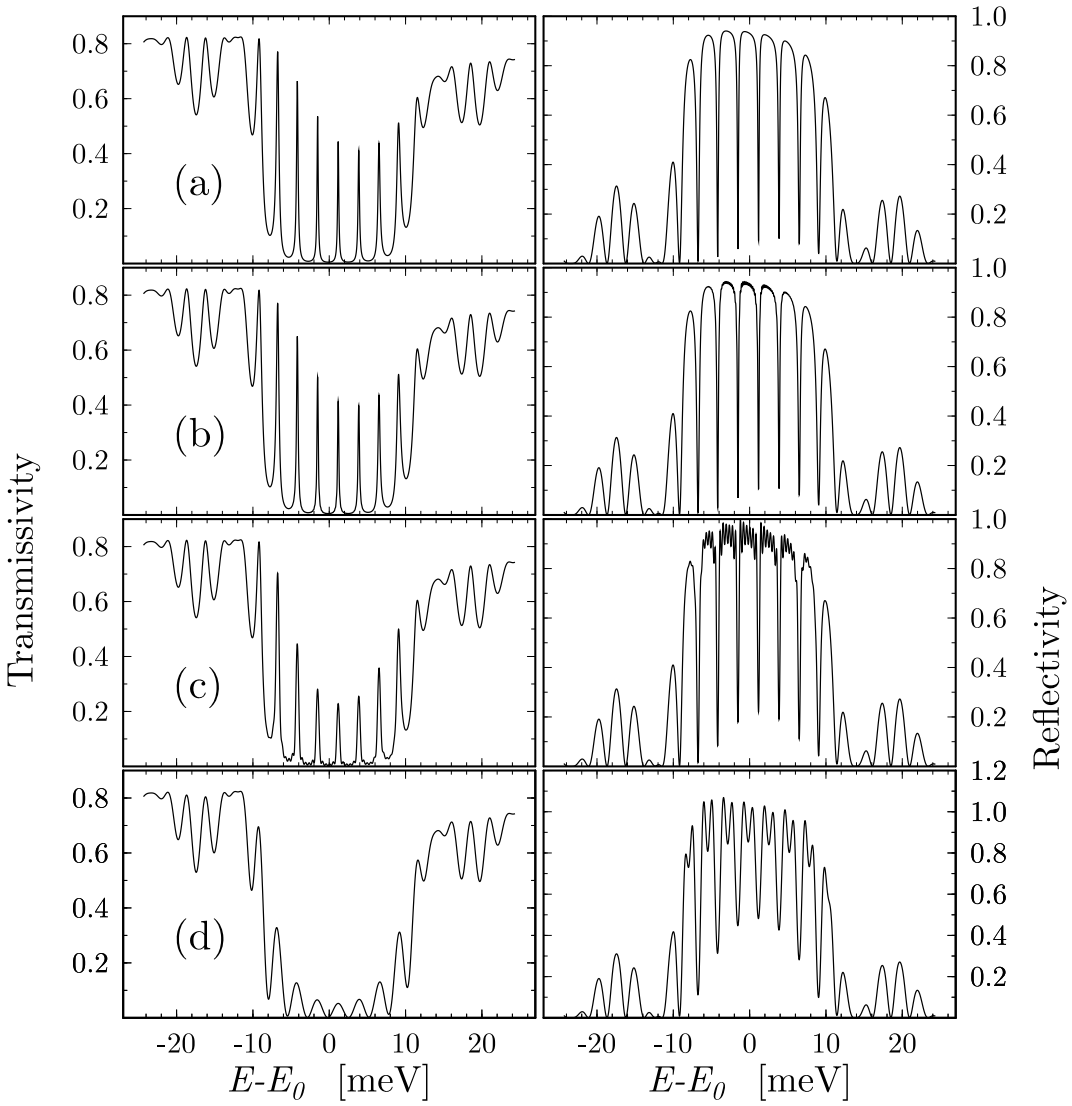

Figure 5.13: Energy dependence of transmission (left panels) and reflection (right panels) for an x-ray Fabry-Pérot resonator made of two single crystal plates of α-Al_2O_3. The number of successively reflected rays contributing to the net signal is (a) infinite, (b) artificially limited to $m_{\min} = 15$, (c) 5, (d) 1. The gap between the crystal plates is $d_g = 200$ μm. All other parameters are the same as used for calculation of the energy spectra in Fig. 5.7

mirror is $\simeq 0.8$. The finesse can be estimated as $\mathcal{F} \simeq 14$ and the effective number of rays contributing to the interference pattern is $\mathcal{N}_r \simeq 14$, according to eq. (5.67).

5.3.10 A practical expression for the Airy phase

As was ascertained in the present chapter, the Airy phase changes due to different terms: x-ray energy, incidence angle, temperature, gap width, etc. It is the variation of the Airy phase which eventually causes drastic changes in the transmissivity of an x-ray Fabry-Pérot resonator. As was also realized in the present chapter, x-ray Fabry-Pérot resonators operate favorably at near-normal incidence ($\delta\theta \ll 1$). Furthermore, the energy of x-rays should be tuned to the region of total Bragg reflection, where Fabry-Pérot resonances have the smallest width. It would be practical to obtain an approximate expression for the Airy phase under these conditions.

For this we shall use the general expression (5.41) and assume that at normal incidence to the reflecting atomic planes of the crystal mirrors the center of the region of total reflection is at an x-ray wavelength $\lambda_{\mathrm{c}} = 2d_{_H}/(1 + w_{_H})$ or at an x-ray energy $E_{\mathrm{c}} = hc/\lambda_{\mathrm{c}}$, respectively. If we define relatively small deviations of x-ray energy from E_{c} as $\epsilon = (E - E_{\mathrm{c}})/E_{\mathrm{c}}$, and remember that at small deviations from normal incidence $\sin\theta \simeq= -\delta\theta^2/2$, then we arrive at the desired expression for the Airy phase:

$$\varphi = \boldsymbol{H}\boldsymbol{u} + 2\pi N_{\mathrm{g}} \left(\epsilon - \frac{(\delta\theta)^2}{2} + w_{_H} \right) + \phi_{\mathcal{R}}, \tag{5.68}$$

with $w_{_H}$ and $\phi_{\mathcal{R}}$ as previously defined.

5.4 Imperfect x-ray Fabry-Pérot resonator

The performance of the perfect x-ray Fabry-Pérot resonator was discussed at length in the previous section. Here we consider the influence of possible imperfections, such as surface roughness of the crystal mirrors, the inhomogeneity of their thickness, errors in the parallelism of the atomic planes in the crystal mirrors, and last but not least, the difference in temperatures of the reflecting crystals.

To gain a better insight into the physical nature of the problem, it is advantageous to perform analytical calculations. The particular case of symmetric ($b = -1$) normal incidence ($\theta \simeq \pi/2$) Bragg diffraction is discussed.

5.4.1 Roughness of internal surfaces

The roughness of a surface may be characterized by the height h of the deviation of the surface from the mean value. Let us consider first the roughness of the internal surfaces of the x-ray Fabry-Pérot resonator. Due to the roughness of the internal surfaces, x rays hitting different points of the resonator sense different gap widths $d_{\rm g}$. As was pointed out in the previous section the Airy phase, and thus the positions and widths of the Fabry-Pérot resonances, are very sensitive to $d_{\rm g}$ - eq.(5.38). Thus the roughness of the internal surfaces, or more correctly, the inhomogeneous gap width, can blur the resonances. It is clear that the surface roughness does not affect the diffractive phase, as it does not change the coherence of the reflecting atomic planes. The roughness influences the refractive phase.

Two values of the gap width are considered: $d_{\rm g} - h$ and $d_{\rm g} + h$. The phase difference for these two values is estimated with eq.(5.38) as

$$\delta\varphi \;=\; 2Kh\,\left(\chi_0' \;-\; \chi_{\rm g}'\right). \tag{5.69}$$

The phase difference $\delta\varphi$ has to be less than $\Delta\varphi$, the width of the Fabry-Pérot resonances on the φ scale, i order not to blur them. From of eq.(5.35) $\Delta\varphi = 2\pi/\mathcal{F}$. This yields for the admissible roughness (inhomogeneity of the gap width $\delta d_{\rm g}$)

$$2h \;\equiv\; \delta d_{\rm g} \;\ll\; \frac{2d_H}{|\chi_0' \;-\; \chi_{\rm g}'|}\,\frac{1}{\mathcal{F}}. \tag{5.70}$$

A very interesting consequence of the derived expression is that the performance of the x-ray resonator may be not influenced by surface roughness at all, if the gap is filled with a material of the same electric susceptibility as that of the crystals, i.e., if $\chi_0' \;=\; \chi_{\rm g}'$. This feature of the x-ray resonator was already

pointed out by Steyerl and Steinhauser (1979), who have proposed filling the gap with liquids of sufficiently high electronic density but low x-ray absorption cross section. It should be noted that the low photo-absorption of the liquids is a very important issue. The photo-absorption in the gap, which is formally expressed via the imaginary part of the electric susceptibility $\chi_{\rm g}''$, decreases $\mathcal{R}$ and thus the finesse $\mathcal{F}$. This can be easily seen from eqs. (5.27) and (5.36).

The admissible surface roughness given by (5.70) could be relatively large, even for a vacuum gap $\chi_{\rm g}' = 0$. For example, for the $(0\ 0\ 0\ 30)$ Bragg reflection in Al_2O_3 $|\chi_0'| = 7.95 \times 10^{-6}$, $2d_{_H} = 0.87$ Å, and by taking the finesse $\mathcal{F} = 30$, one obtains $2h \ll 0.36$ μm. This estimate agrees with the computer simulations performed by Kohn et al. (2000).

A roughness of $\simeq 0.1$ μm is routine for modern micro-technology. However, this concerns freely accessible surfaces. If the x-ray Fabry-Pérot resonator is monolithically cut out of a single crystal block, it could be a problem to manufacture internal surfaces with such a small roughness. It should be noted that the surface roughness required by eq. (5.70) has to be preserved over the area of the crystal surfaces illuminated by the incident x-rays.

The x-ray Fabry-Pérot resonator is less sensitive to the roughness of the external surfaces. What is actually important, is not the roughness itself, but the inhomogeneous mirror thickness due to the roughness of the internal and external surfaces.

5.4.2 Inhomogeneous mirror thickness

Alternating mirror thicknesses change the effective reflection coefficient $\mathcal{R}$ of the mirrors and the phase jump $\phi_{\mathcal{R}}$. The variation of the phase jump $\phi_{\mathcal{R}}$ changes the Airy phase and shifts the Fabry-Pérot resonances; see right panels in Fig. 5.8. This effect clearly imposes some constraints on the admissible inhomogeneity of a mirror's thickness. The limits are determined first of all by the sharpness of the Fabry-Pérot resonances. The requirement on the thickness homogeneity is not very stringent. For example, for the case of the $\Delta E = 72$ μeV broad resonance in Fig. 5.8(d) an error of $\simeq 10\mu$m in the homogeneity of the mirror's thickness would be admissible.

5.4.3 Non-parallel mirrors

When the x-ray resonator is built of two separate single crystal plates, a major problem is to keep the reflecting planes in different mirrors parallel to each

other. As will be shown the angle Φ which describes admissible deviations from parallel alignment, is very small despite the fact that Bragg back diffraction of a single crystal plate has a large angular width.

Following Kohn et al. (2000), the error in parallelism of the reflecting planes in the two crystals can be considered as a crystal lattice defect which leads to a displacement $\mathbf{u}(x,z)$ of the atoms from their ideal positions. Here we assume, as before, that the z-axis is normal while the x-axis and y-axis are parallel to the surface of the crystal plate. A rotation of the crystal plate around the y-axis at the position (x_0, z_0) by a small angle Φ results in the displacement field

$$\delta u_x = -(z - z_0)\Phi, \qquad \delta u_z = (x - x_0)\Phi \tag{5.71}$$

Such a displacement leads to a broken coherence of the atomic planes in both crystals, which results in an additional shift of the Airy phase (in fact of the diffractive phase):

$$\delta\varphi(x) = \boldsymbol{H}\delta\boldsymbol{u}(x) = 2\pi s(x), \qquad s(x) = \gamma_0 \frac{(x - x_0)}{d_{_H}}\Phi. \tag{5.72}$$

The existence of a phase shift varying in space along the surface of the x-ray resonator leads to a variation of the transmissivity. The admissible angular error in parallelism which does not destroy the peaks of transmissivity is determined by the condition $\delta\varphi < \Delta\varphi$, where

$$\delta\varphi = 2\pi \frac{X}{d_{_H}}\Phi, \quad \Delta\varphi = \frac{2\pi}{\mathcal{F}}. \tag{5.73}$$

Here X is the linear dimension of the resonator surface illuminated with the incident x-rays. Alternatively, X could be also interpreted as the width of the x-ray detector.

In terms of the angle between the mirrors this means

$$\Phi \; < \; \frac{d_{_H}}{X}\,\frac{1}{\mathcal{F}}. \tag{5.74}$$

For $\mathcal{F} = 15$, $d_{_H} = 0.43$ Å, and $X = 1$ mm one obtains $\Phi < 3 \cdot 10^{-9}$ rad. This is a very stringent condition. Eq. (5.74) implies that it is favorable to work with beams of small cross section. For example, by reducing X to 10 μm the admissible angle increases to 0.3 μrad.

5.4.4 Temperature gradients

It may happen that the crystal plates of the x-ray resonator have a slightly different temperature. Let the difference be δT. There are at least two negative effects of such a temperature gradient on the performance of the resonator.

First, the interplanar distance $d_{_H}$ changes with crystal temperature. This shifts the location of the region of total reflection. From eq. (2.75) the shift is $\delta\alpha = -4\beta_{_H}(T)\delta T$. In the limiting case, if the temperature difference is too large, the regions in both crystal do not overlap and no multiple scattering and thus no interference effects take place. The width of the region of total reflection in weakly-absorbing and thick crystals is $\Delta\alpha = 4|C\chi_{_H}|/\sqrt{|b|}$ (2.75). By using the condition $\Delta\alpha \gg |\delta\alpha|$ one obtain the following estimate for the tolerable temperature difference between the crystals:

$$\delta T \ll \frac{|\chi_{_H}|}{\beta_{_H}}. \tag{5.75}$$

Here we used $b = -1$ and $|C| = 1$. Let us consider the example of the sapphire x-ray resonator with the $(0\ 0\ 0\ 30)$ Bragg reflection for which $|\chi_{_H}| = 8.63 \times 10^{-7}$. At $T \approx 295$ K the thermal expansion coefficient is $\beta_{_H} = 5.92 \times 10^{-6}$. Thus, the admissible temperature difference is $\delta T \ll 0.15$ K.

The second effect arises if the diffraction vector $\boldsymbol{H}$ is not parallel to the surface normal $\hat{\boldsymbol{z}}$. We will assume that the angle between the vectors is η - Fig. 2.1. As was discussed in sec. 2.2.1 - eqs. (2.23) and (2.24) - the virtual reflecting planes are at an angle $\Psi = K|\alpha|\sin\eta/2H|\gamma_{_H}|$ to the relevant atomic planes. If the temperature of the crystals is different, then the parameter α is different as well. As a result, the virtual reflecting planes in the crystals are not parallel. The angle between the planes is

$$\delta\Psi = \sin\eta\frac{K|\delta\alpha|}{2H|\gamma_{_H}|} = \beta_{_H}\ \tan\eta\ \delta T. \tag{5.76}$$

The last transformation in eq. (5.76) was performed by using the relation $\delta\alpha = -4\beta_{_H}\delta T$ of eq. (2.75), and by $\theta \approx \pi/2$, $K \simeq 2H$, $|\gamma_{_H}| \simeq \cos\eta$.

Now one can use the result of the previous section, in which the admissible error in parallelism of the reflecting planes was estimated. Combining inequality (5.74) with eq. (5.76) and taking $\Phi = \delta\Psi$ one arrives at the following admissible temperature difference in the crystals of the resonator:

$$\delta T < \frac{d_{_H}}{X\,\mathcal{F}}\,\frac{1}{\beta_{_H}\tan\eta}. \tag{5.77}$$

By using the numerical examples of the present and the previous section one obtains $\delta T < 0.3\ \text{mK}/\tan\eta$. If $\tan\eta \approx 1$ ($\eta \approx 45^\circ$), then one obtains a very demanding requirement: $\delta T < 0.3$ mK. The requirement becomes less stringent for small angles η. E.g., if $\eta \leq 0.5^\circ$ ($\tan\eta \leq 0.01$) then $\delta T < 30$ mK. Still, the admissible temperature difference is small and requires precise temperature control of the resonator crystals.

5.5 Exemplary applications

In conclusion to this chapter, we would like to propose some applications of x-ray Fabry-Pérot resonators. Not all possibilities are discussed. Applications such as Fourier spectroscopy and some others will be discussed elsewhere. We concentrate primarily on the three following types of applications.

The first type of application deals with direct measurements of radiation wavelengths in the x-ray spectral region in terms of visible light wavelengths. In particular, direct measurements of the wavelengths of Mössbauer photons in terms of the wavelength of an iodine stabilized He-Ne laser are considered. The problem of the Mössbauer wavelength standard for atomic scales was discussed in sec. 4.2. In sec. 5.5.1 we propose an instrument, which will allow implementation of this program.

The second type of application deals with monochromatic x rays. X rays with a 100 μeV bandpass have a coherence length of about 2 mm and could be used for instance in x-ray holography, as will be discussed in sec. 5.5.2 in connection with diamond interference filters.

Studies of dynamics of biological macromolecules, and phonon spectra in condensed matter, employ inelastic neutron and inelastic x-ray scattering techniques. These techniques use monochromatic radiation. The spectrum of incident photons is transformed by the samples due to inelastic scattering. The energy analysis of the scattered radiation provides information on the dynamics of atoms; see, e.g., recent review articles of Sette et al. (1998) and Burkel (2000) for more details. Instruments for inelastic x-ray scattering with $\simeq$ 1 meV-resolution are currently available. Concrete designs of instruments for inelastic x-ray scattering with $\simeq 100$ μeV resolution are proposed in sec. 5.5.3.

The third type of application deals with phase contrast imaging and is discussed in sec. 5.5.4.

5.5.1 X-ray to visible light wavelength ratios

Since their introduction Fabry-Pérot resonators have been used in metrology to link radiation wavelengths of visible light with the standard meter; see e.g., (Vaughan 1989). Nowadays the length standard is defined via the speed of light in vacuum c. Using high-precision frequency measurements it is possible to determine the wavelength $\lambda_{\rm s} = c/f_{\rm s}$ of an iodine stabilized He-Ne laser with a relative uncertainty of $\simeq 10^{-11}$. Length measurements are then performed in terms of $\lambda_{\rm s}$. We have discussed in detail in sec. 4.2 the problem of the secondary length standard for atomic scales and of the advantages of us-

ing the wavelength of Mössbauer radiation of ^{57}Fe nuclei for this purpose. Its value was measured with a relative uncertainty of 0.19 ppm by using the lattice constant of silicon as a transfer standard, see sec. 4.4. However, the direct measurement of the wavelength of Mössbauer radiation in terms of λ_s would be most appropriate.

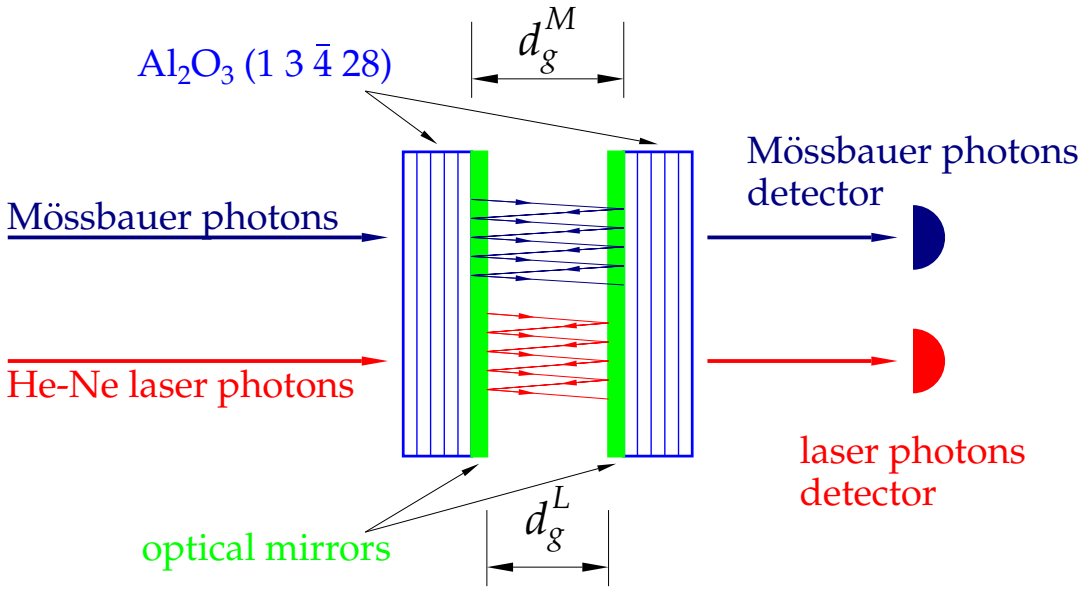

Figure 5.14: Scheme for measurement of the wavelength of the ^{57}Fe Mössbauer radiation in terms of the wavelength of the iodine stabilized He-Ne laser.

The problem could be solved by building a specially designed Fabry-Pérot interferometer for both Mössbauer and visible light photons. The idea could be implemented in the following way. A Fabry-Pérot interferometer for Mössbauer photons is built by using sapphire crystal mirrors of normal incidence with the $(1\ 3\ \overline{4}\ 28)$ Bragg back reflection at 371.6 K, see tab. 3.1. Sapphire is transparent for visible light photons. Therefore, the crystals could be used simultaneously as substrates for reference mirrors for the laser photons. As a result, one could have Fabry-Pérot interferometers for both the Mössbauer and He-Ne laser photons in one device, see Fig. 5.14. The gap widths d_g^M for the Mössbauer and laser photons d_g^L are slightly different, but an arbitrary absolute change of the gap width δd_g is the same.

According to eqs. (5.40) and (5.11), the Fabry-Pérot transmission resonances appear every time when the spacing between the mirrors is changed by $\delta d_g = m\,\lambda/2\cos\delta\theta$ ($m = 0, \pm1, \pm2, ...$). Here λ stands either for the wavelength of Mössbauer photons λ_M or for visible light photons λ_s. By varying the gap and

counting Fabry-Pérot transmission resonances with both Mössbauer and laser photon detectors, one can measure directly the wavelength of the Mössbauer photons $\lambda_{\rm M}$ in terms of the wavelength $\lambda_{\rm s}$ of the He-Ne laser photons. One should take care, that the angles of incidence $\delta\theta$ for both types of photons do not differ too much from each other.

5.5.2 μeV energy resolution interference filters

The higher the reflectivity of the mirrors the larger is the finesse of the resonator and thus the sharper are the Fabry-Pérot resonances. This rule applies to Fabry-Pérot resonators in any spectral range. Bragg reflection optics allows one to achieve very high reflectivities. As was discussed in sec. 2.2.3, the reflectivity of a non-absorbing crystal with thickness larger than the extinction length approaches 100%. Unfortunately, one can never avoid photo-absorption. A reflectivity of 100% exists only in theory. The larger the ratio $d_e(0)/d_{\rm ph}$ of the extinction length to the photo-absorption length the closer one approaches the 100% limit. The best values are achieved for diamond (C) and beryllium (Be) crystals. Be crystals of a good crystal quality are not available. Good diamond single crystals are already available and their quality is steadily improving (Ishikawa et al. 2000, Sellschop et al. 2000). Bragg back reflections in diamond crystals clearly suffer from multiple-beam diffraction at the exact normal incidence, as in silicon crystals. One has to employ Bragg reflections slightly off the exact normal incidence, see Fig. 5.11.

Figure 5.15 shows the performance for 12 keV x-rays of the Fabry-Pérot interference filters built from diamond single crystals. The most impressive feature of the diamond filters demonstrated by this graph is the possibility of obtaining resonances with a finesse of $\simeq 100$ [4]. The resonance widths are less than 100 μeV. The peak transmissivity is $\simeq 50\%$ for the resonance with an energy width of 42 μeV, see Fig. 5.15(b). It is a technical challenge to realize such a microstructure. The difficult problem is to manufacture a gap of a few tens of microns with 10 nm precision. The latter is necessary to prevent blurring the very sharp resonances. Obviously, such μeV filters should be used in combination with meV monochromators, which have first to select one of the Fabry-Pérot resonances.

Diamond crystals used in backscattering Bragg reflection optics have the same drawbacks as silicon crystals. We have mentioned the problem of multiple-beam Bragg diffraction. The problem of tunability of backscattering en-

[4] The finesse values achievable with sapphire backscattering mirrors are about $15-25$. For silicon crystals they are typically about a factor of two less.

ergies is even more severe in this case, since the lattice constant of diamond and the thermal expansion coefficient are about two times smaller than those of silicon crystals. Interference filters using diamond single crystals could be applied only in those cases where no specific x-ray energies are required. If this is required, sapphire single crystals are the better choice.

One of the possible applications of such μeV filters could be x-ray holography requiring not only transverse but also longitudinal coherence. Future linac

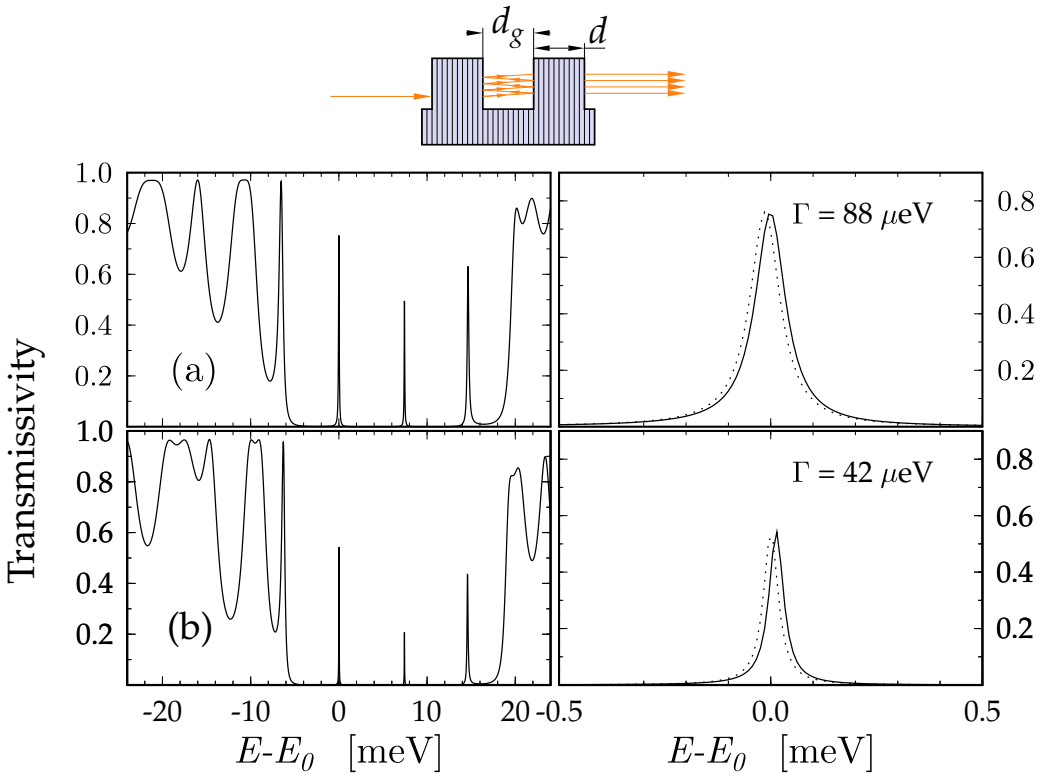

Figure 5.15: Energy dependence of transmission though a Fabry-Pérot interference filter made of two single crystal plates of diamond - left panels. The right panels show the parts of the same spectra in a narrower energy range. The vacuum gap between the plates is taken to be $d_g = 64.0$ μm. The dotted line shows the sensitivity of the resonances to the variation of the gap by 0.02 μm. The reflecting atomic planes in both crystal plates are in perfect registry relative to each other, i.e., $\boldsymbol{Hu} = 2\pi n$. The thicknesses of the crystal plates are (a) $d = \tilde{d} = 50$ μm, (b) $d = \tilde{d} = 60$ μm, and their temperatures are $T = 300$ K. The incident radiation is a plane monochromatic wave at normal incidence ($\delta\theta = 0$) to the (444) reflecting atomic planes. $E_0 = 12.040$ keV.

based synchrotron radiation sources will provide radiation with full transverse coherence, and about 1 mm^2 in cross-section (LCLS 1998, Materlik and Tschentscher 2001). The above described interference filters could be used to obtain photons with a coherence length of about 1 mm, and thus completely coherent in a volume of 1 mm^3.

5.5.3 Instruments for inelastic x-ray scattering

The monochromator and the analyzer are the main components of instruments employed to study the dynamics of matter by inelastic x-ray scattering. Bragg back-scattering is used both for monochromatization and analysis, see e.g., (Burkel 1991, Sinn 2001) and references therein. The backscattering crystal analyzers should be curved to increase the solid angle of acceptance. It is a major problem to manufacture such curved analyzers without deteriorating the intrinsic energy resolution of the Bragg back reflection used. To push the energy resolution of such instruments into the sub-meV range is very difficult, see e.g. (Masciovecchio et al. 1996, Alp et al. 2000b, 2001a, Baron et al. 2001b).

Alternatively, the energy analysis of x rays could be performed by using nuclear resonance absorption. For example, the nuclear resonances listed in table 3.1 can be employed for this purpose. If one of these isotopes is present in the sample under study, it can be used as a built-in analyzer. This technique pioneered by Seto et al. (1995) and Sturhahn et al. (1995) is being intensively developed; see the review papers of Chumakov and Sturhahn (1999), Sturhahn and Kohn (1999) and Alp et al. (2001b). One can use the nuclei also as external analyzers. In application to x-ray inelastic scattering, this possibility was demonstrated by Chumakov et al. (1996a). The energy resolution of such analyzers is extremely sharp – in the sub-μeV range – as determined by the energy width of the nuclear resonances. In this case the energy resolution of x-ray monochromators has to match the resolution of the analyzers. Röhlsberger et al. (1997) have demonstrated a μeV-monochromator tunable about 14.4 keV in the meV range, by using nuclear resonant scattering from a rotating medium. Yabashi et al. (2001) have recently demonstrated a 130 μeV silicon crystal monochromator for 14.4 keV. These monochromators require x-rays of very small divergence and cross-section.

We propose here an alternative solution employing Fabry-Pérot interference filters. Perhaps the most remarkable feature of these devices is their relatively large angular acceptance. Furthermore, they can be operated at a nuclear resonance energy. This enables one to use nuclear resonant analyzers. Examples of concrete designs are presented below for the 14.4 keV nuclear

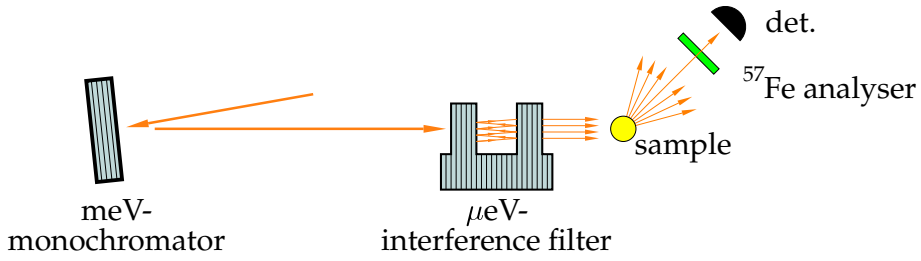

Figure 5.16: Schematic of an experimental arrangement for measuring spectra of inelastic x-ray scattering with μeV resolution.

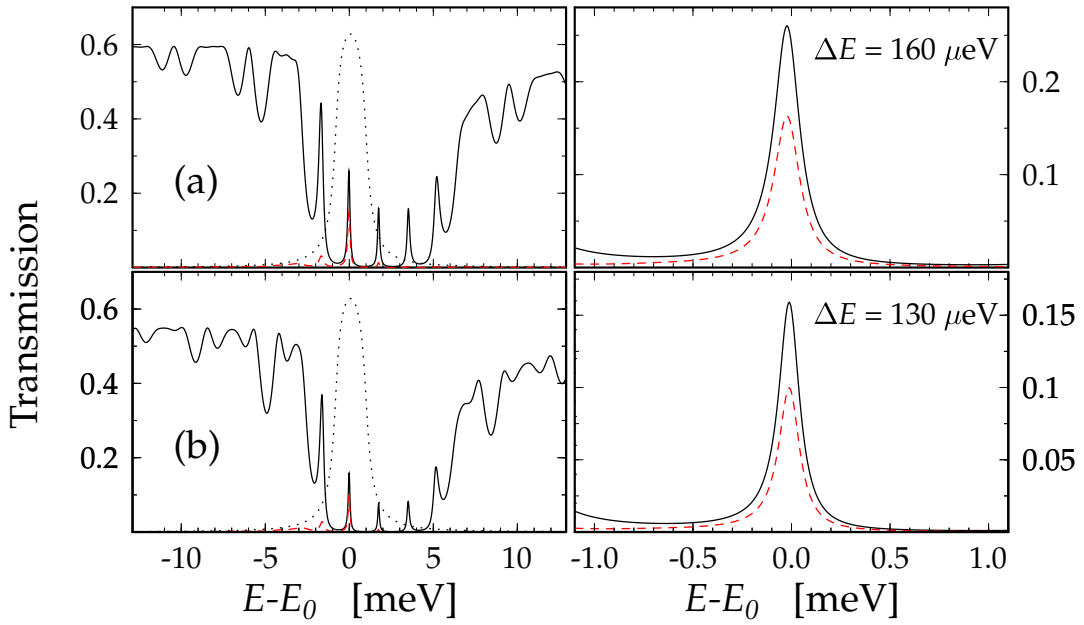

Figure 5.17: Left: Energy dependence of transmission through a sapphire Fabry-Pérot interference filter (solid line) with the $(1\ 3\ \overline{4}\ 28)$ Bragg reflection; gap width $d_g = 280$ μm; crystal thickness (a) $d = 130$ μm, (b) $d = 150$ μm; $T = 372.8$ K; and $E_0 = 14.4125$ keV. The dotted line shows the reflectivity of the backscattering meV-monochromator with the Bragg reflection α-$Al_2O_3(1\ 6\ \bar{7}\ 22)$ at $T = 150$ K. Right: the central region on an expanded scale. The dashed line is a product of the transmissivity of the interference filter and the reflectivity of the meV-monochromator, i.e., the instrumental function.

resonance in ^{57}Fe and for the 23.8 keV nuclear resonance in ^{119}Sn.

Employing the 14.4 keV ^{57}Fe nuclear resonance

Monochromatization with a Fabry-Pérot interference filter is achieved in two stages, as shown in Fig. 5.16. At first, a meV-monochromator is used to monochromatize the radiation to a bandpass of the free spectral range of the interference filter. At the second stage the interference filter is employed, see Fig. 5.17, to achieve the highest monochromatization.

Figure 5.16 shows a possible experimental arrangement with a single-bounce backscattering meV-monochromator. The single-bounce type is advantageous because of smaller losses and a larger angular acceptance. The (1 6 $\bar{7}$ 22) reflection in α-Al_2O_3 at $T = 150$ K with an energy width of 1.9 meV can be used to match the energy of the ^{57}Fe nuclear resonance; see table 3.1. The energy width of the reflection determines the minimum value of the free spectral range and therefore the maximum gap width of the interference filter. To make the Fabry-Pérot resonances sharper, the Bragg reflection with the highest reflectivity should be used for the mirrors of the interference filter. For the given x-ray energy, the best choice is the $(1\ 3\ \overline{4}\ 28)$ reflection in α-Al_2O_3. The sharpness of the resonances can be also tailored by changing the thickness of the mirrors. Details of the design of the Fabry-Pérot interference filter are given in Fig. 5.17 and its caption.

The energy of the radiation selected in this way are changed by scanning synchronously the temperatures of the α-Al_2O_3 crystals in the meV-monochromator and in the interference filter. The temperatures are scanned with the rates $\mathrm{d}T/\mathrm{d}E$ given in Tab. 3.1.

To avoid mechanical adjustment of the mirrors of the interference filter, it is most practical to cut them out of a single crystal block. The main technical challenge is to manufacture the gap width with high precision. In order not to blur the resonances by more than 10%, the gap width may not vary by more than $\delta d_{\mathrm{g}} \pm 80$ nm, see eq. (5.70). Fortunately, the specified tolerance should be adhered to over a rather small area - the area illuminated by the incident beam. The thickness of the mirrors should be uniform with a tolerance of $\simeq \pm 5\ \mu$m.

The relative spectral resolution obtainable with such a monochromator system is $\epsilon_{_{\mathrm{FP}}} \simeq 10^{-8}$, see Fig. 5.17(b). Despite the smallness of this value, the angular acceptance of the monochromator system which is defined by the angular width of the Fabry-Pérot resonances is still relatively large. It equals $2\sqrt{\epsilon_{_{\mathrm{FP}}}} = 100\ \mu$rad, see eq. (5.65). Beams of even smaller divergence are routinely available at modern synchrotron radiation facilities.

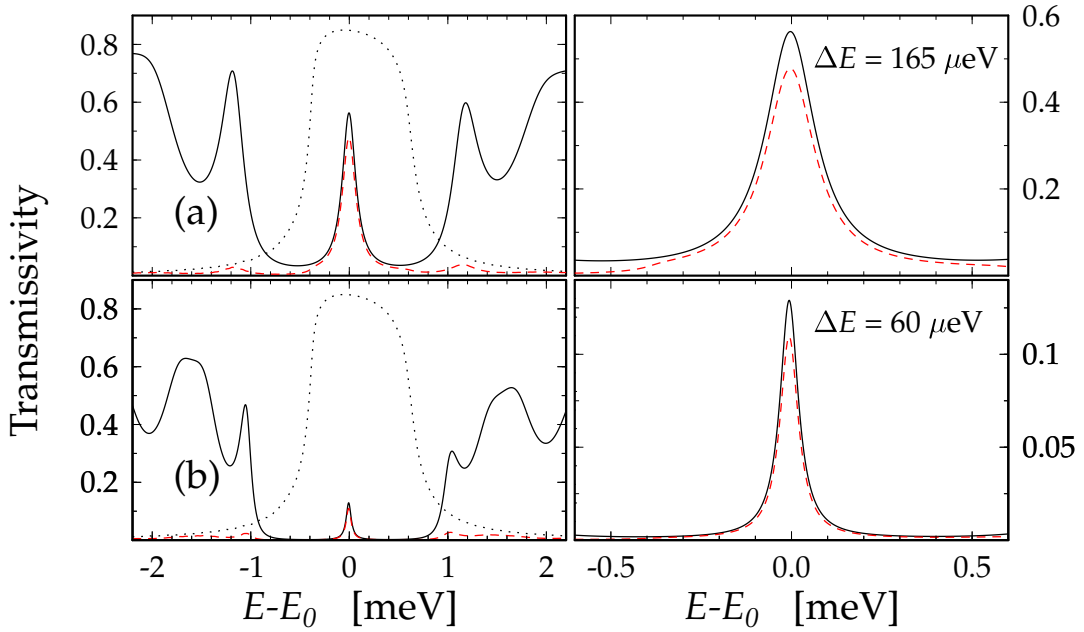

Figure 5.18: Left: energy dependence of transmission through a sapphire Fabry-Pérot interference filter (solid line) with the $(1\ 9\ \overline{10}\ 40)$ Bragg reflection; gap width $d_g = 300\ \mu$m; crystal thickness (a) $d = 300\ \mu$m, (b) $d = 500\ \mu$m; $T = 268.9$ K; and $E_0 = 23.879$ keV. The dotted line (left) shows the reflectivity of the backscattering meV-monochromator with the Bragg reflection α-$Al_2O_3(6\ 5\ \overline{10}\ 40)$ at $T = 268.9$ K. Right: the central region on an expanded scale. The dashed line is a product of the transmissivity of the interference filter and the reflectivity of the meV-monochromator, i.e. the instrumental function.

Employing the 23.8 keV ^{119}Sn nuclear resonance

Figure 5.18 shows the results of calculations, which demonstrate the performance of a monochromator system matched to the 23.8 keV nuclear resonance in ^{119}Sn. Details of the Fabry-Pérot interference filter and of the single-bounce meV-monochromator are given in the caption for Fig. 5.18.

The relative spectral resolution obtainable with such a filter is $\epsilon_{\rm FP} \simeq 2.5 \times 10^{-9}$, see Fig. 5.18(b). Despite the smallness of this value, the angular acceptance of the system defined by the angular width of the Fabry-Pérot resonances is relatively large: $2\sqrt{\epsilon_{\rm FP}} = 50\ \mu$rad.

5.5.4 Phase contrast imaging

Fabry-Pérot-type interferometers possess enhanced phase sensitivity due to multiple-beam interference, as described in sec. 5.3.3. The phase width of the Fabry-Pérot transmission resonances is a factor $\mathcal{F}$ smaller than the width of the two-beam interference fringes. This enhanced sensitivity opens up new possibilities for phase-contrast imaging. The higher the finesse of the resonator the higher is its phase sensitivity. One achieves very high finesse values by using diamond single crystals as Bragg reflection mirrors (at slightly off-normal incidence).

The finesse of the diamond resonator with the parameters given in Fig. 5.15 is $\mathcal{F} \simeq 100$. Even a very small change of the gap width of $\simeq 20$ nm results in a distinct change in the resonance positions. An equivalent effect is caused by a $\simeq 20$ nm layer of carbon inserted into the resonator gap. This is a pure phase shift effect. Any other material will cause a similar effect however with the magnitude dependent on the atomic number Z of the atoms of the material[5]. Such behavior can be used for phase contrast imaging. At this point one should mention that nowadays phase contrast imaging is successfully performed using Bonse-Hart x-ray interferometers. For more details see (Bonse and Hart 1965a,b, Hart 1975, Bonse 1997). Being a two-beam interference device, it does not possess however the enhanced phase sensitivity of the Fabry-Pérot resonator.

One needs monochromatic x-rays to record phase contrast images using x-ray resonators. The spectral width of the x-rays should be less than the resonance width.

Alternatively, phase contrast imaging can be performed by employing a compound Fabry-Pérot interference filter, as shown in Fig. 5.19. The spectrum of the incident x-rays should be initially narrowed only to a bandpass of the Bragg reflection of the interference filter. For this one can use the same Bragg reflection at normal or near-normal incidence from the same kind of crystal. The gap widths in the compound interference filter should be equal, so that the positions of the transmission resonances of each part are the same. The insertion of a phase shifter (a sample) into any of its parts will cause a shift of the the transmission resonances. As a result, the transmissivity of the combined system will change. Such device may provide phase contrast-enhanced images of very small objects.

[5]Also the effect of absorption should be enhanced due to multiple passage through the sample.

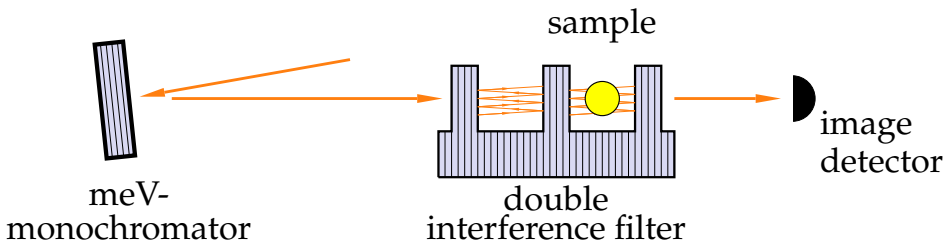

Figure 5.19: Phase contrast imaging with a compound x-ray Fabry-Pérot interference filter. The mV-monochromator is used to select x-rays falling into the spectral range of the Bragg reflection of the resonator mirrors.

Chapter 6

Towards achieving x-ray resonators

The physics underlying the x-ray Fabry-Pérot resonators have been addressed in the preceeding chapter. We have understood the technical challenges of the implementation of such devices. Earlier, we have ascertained that sapphire is a proper material for the construction of Bragg back-reflection mirrors. The desired performance of the sapphire mirrors has been successfully demonstrated. Everything is in principle ready to launch a first attack on the experimental realization of x-ray Fabry-Pérot resonators. In the current chapter results of the development of a test device and of first experiments with this device are presented.

The concept of the test device is presented in sec. 6.1. In sec. 6.2 we describe the procedure of manufacturing thin sapphire resonator mirrors, the design of a two-axis nanoradian goniometer for angular adjustment of the mirrors, the temperature control of the mirrors, $\simeq 150$ ps fast detectors, and the layout of the experimental setup. In sec. 6.3 the results of the first experiments with the test x-ray resonators are presented.

6.1 Concept of the test device

What device we are actually going to test? There are many options.

For instance, one is confronted with the alternative: should the mirrors be monolithically cut out of a single crystal piece, or should they be independently adjustable? Both alternatives are of interest for future applications discussed in sec. 5.5. Both alternatives also have their own difficulties in realization.

We have decided to built our test device with independently adjustable mirrors. First, this allows a better quality control of the sapphire mirrors. Secondly, it allows one to study the sensitivity to angular misalignment of the

mirrors – a very important issue for future applications.

Another alternative with which one is confronted: how to observe the Fabry-Pérot resonances? One option would be to use monochromatic x rays. However, an x-ray monochromator with a bandpass smaller than the width of the Fabry-Pérot resonances is problematic. One could certainly think of Mössbauer photons which have neV spectral width. Instead of this, one can use very short radiation pulses to measure the time response of the resonator. As we have discussed in sec. 5.3.6, the time response provides information on the width of the resonances and on the magnitude of the free spectral range. Furthermore, detection of the time response offers a possibility of direct observation of the multiple reflections. The longest time response (the largest number of multiple reflections) should be observed for perfectly aligned mirrors. Therefore, one can perform angular adjustment of the mirrors by maximizing the duration of the time response. We have chosen this option, as it also allows one to be more generic and not to be bound to the specific energies of Mössbauer transitions.

The duration of x-ray radiation pulses at modern synchrotron radiation facilities is typically 50 to 150 ps. The time resolution of the available x-ray detectors is in the same range[1]. To resolve the multiple reflections on the time scale, the back and forth time-of-flight between the mirrors should be larger than the pulse width and the detector time resolution. This dictates that the gap width d_{g} should be a few centimeters. We have chosen for our test device a gap of $d_{\mathrm{g}} = 5$ cm. The time delay between two successively reflected beams is $t_{\mathrm{f}} = 2d_{\mathrm{g}}/c = 334$ ps. The free spectral range under these conditions is $E_{\mathrm{f}} = 12.39$ μeV.

For the Bragg reflection, we have selected the $(0\ 0\ 0\ 30)$ reflection. It has a high peak reflectivity of 95% (for infinitely thick crystal) and a Bragg energy of $E_{_H} = 14.3148$ keV. For a crystal with a thickness of 55 μm the peak reflectivity $R = 0.83$ (Fig. 2.13). The resonator with mirrors of such reflectivity has a finesse of $\mathcal{F} \simeq 16.8$. The expected resonance width $\Gamma = E_{\mathrm{f}}/\mathcal{F}$ is $\simeq 0.73$ μeV and the response time $\tau = \hbar/\Gamma$ is $\simeq 0.89$ ns. The relative spectral resolution of the resonances $\epsilon_{_{\mathrm{FP}}} = \Gamma/E_{_H}$ is $\simeq 5.5 \times 10^{-11}$. The angular acceptance of the Fabry-Pérot resonances at exact normal incidence $\Delta\theta = 2\sqrt{\epsilon_{_{\mathrm{FP}}}}$ is $\simeq 15$ μrad [eq. (5.65)].

The parameters given above agree with those obtained from numerical model calculations with the computer code FPET. Model calculations for x-ray Fabry-Pérot resonators with the $(0\ 0\ 0\ 30)$ Bragg reflection have been presented

[1]We do not consider here streak cameras which possess in fact better time resolution but very low efficiency.

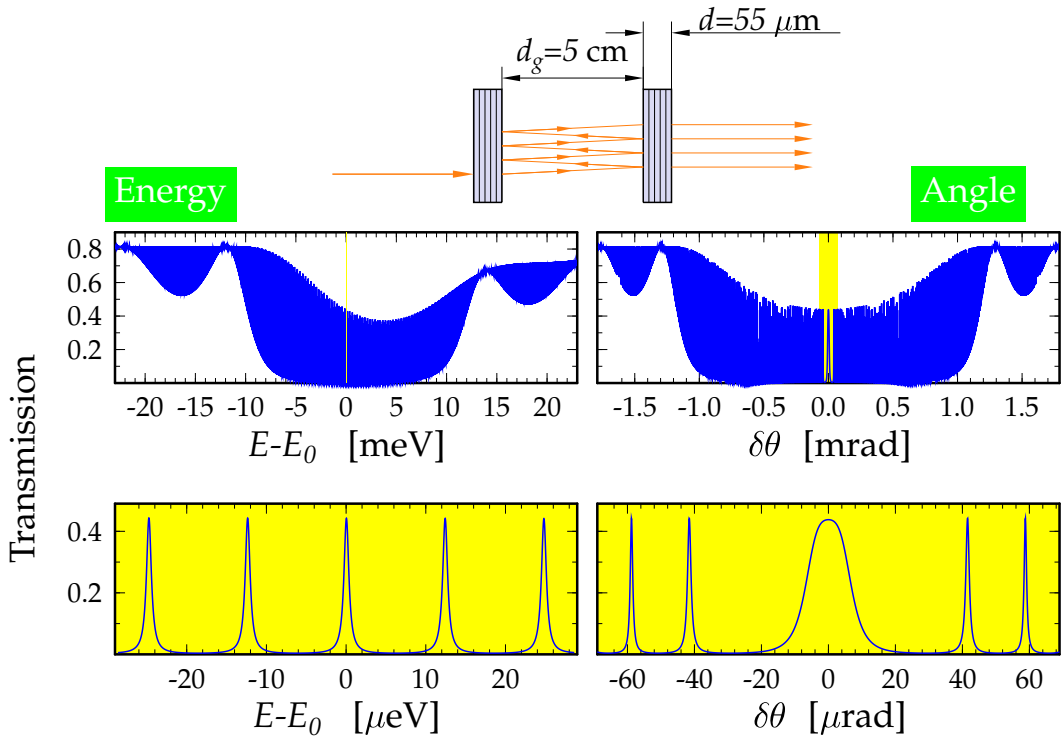

Figure 6.1: Top: schematic of a test x-ray resonator with α-$Al_2O_3(0\ 0\ 0\ 30)$ mirrors. Center and bottom: the appearance of the Fabry-Pérot resonances on the x-ray energy (left), and incidence angle (right) scales. The bottom graphs are the central parts marked in grey in the upper graphs on an expanded scale.

in sec. 5.3. In particular, a two-dimensional $(E, \delta\theta)$ plot of transmissivity of x-rays through a resonator with two ideally parallel $50\ \mu$m thick sapphire crystal mirrors spaced a distance $d_g = 5$ cm apart, is shown in Fig. 5.12.

Figure 6.1 shows a schematic view of the test resonator and the appearance of the Fabry-Pérot resonances on the x-ray energy and incidence angle scales.

6.2 Instrumentation

To implement the test resonator one "merely" needs thin wafers of perfect sapphire aligned in parallel and kept at the same temperature. To observe the time response of the test device one needs x-ray detectors with a time resolution of better than 200 ps. We present here technical details of the required instrumentation.

6.2.1 Manufacturing sapphire mirrors

Concept

For the given Bragg $(0\ 0\ 0\ 30)$ back reflection, the optimal thickness of the sapphire mirrors is $\simeq\ 40\ -\ 70\ \mu$m, as shown in Fig. 5.8. Such thin crystals are not easy to produce and to handle. Luckily, the mirrors have to have only a small area – about 10 mm^2 – a little bit more than the cross-section of the incident x-ray beam.

Instead of manufacturing thin wafers, a technique of thinning down a large sapphire disk is employed. In this way, the thin mirror is framed by a thick ring and is safe to handle.

What should be also respected in the production, is the angle between the reflecting $(0\ 0\ 0\ 30)$ atomic planes and the mirror surface η. It should be as small as possible to simplify the adjustment of the parallelism of the atomic planes of the resonator crystal mirrors. Since the angular range of the nanoradian stage used for this adjustment is 0.7 mrad ($0.04°$) – see next section for more details – the mismatch η should be less than this value. This is a serious technological problem.

To mitigate this problem, the following procedure is applied. Each pair of resonator mirrors is produced monolithically from the same sapphire disk. Then disk is cut into two independent mirrors. We shall term such mirrors as "twin-mirrors". Each pair of twin-mirrors has the same angular mismatch η. Due to this property, in the reversed position of the second mirror (i.e., the direction of the surface normal is reversed) there exists an angle of rotation about its surface normal at which the atomic planes in both mirrors are exactly parallel.

To prove this statement, let us consider the following geometrical problem. Assume, a pair of twin-mirrors is mounted as one crystal block (not yet cut into parts) on a surface of an imaginary parallel-sided plate. The surface normal of the plate is $\hat{\boldsymbol{z}} = \{0, 0, 1\}$ which is simultaneously the normal to the crystal surface. The direction of the diffraction vector of the crystal is

$\hat{\boldsymbol{H}} = \{\sin\eta\cos\psi, \sin\eta\sin\psi, \cos\eta\}$. The vectors $\hat{\boldsymbol{z}}$ and $\hat{\boldsymbol{H}}$ are not parallel. There is a small angle η between them - the aforementioned mismatch. In the following we assume that $\eta \ll 1$ and ψ takes arbitrary values. Now, imagine that the mirrors are separated and one of them is mounted on the opposite surface of the parallel-sided plate. The diffraction vector of this crystal is $\hat{\boldsymbol{H}}'$. The question now is: Is it possible by rotating of the second crystal around $\hat{\boldsymbol{z}}$ by, say, an angle Υ to make $\hat{\boldsymbol{H}}$ and $-\hat{\boldsymbol{H}}'$ parallel? Mathematically the transformation of $\hat{\boldsymbol{H}}$ into $\hat{\boldsymbol{H}}'$ is described by $\hat{\boldsymbol{H}}' = \hat{R}\hat{\boldsymbol{H}}$, where $\hat{R}$ is the rotation matrix

$$\hat{R} = \begin{pmatrix} \cos\Upsilon & \sin\Upsilon & 0 \\ \sin\Upsilon & -\cos\Upsilon & 0 \\ 0 & 0 & -1 \end{pmatrix}$$

The result is $\hat{\boldsymbol{H}}' = \{\sin\eta\cos(\Upsilon-\psi), \sin\eta\sin(\Upsilon-\psi), -\cos\eta\}$. It can be readily shown that the angle between $-\hat{\boldsymbol{H}}$ and $\hat{\boldsymbol{H}}'$ or, what is the same, between the atomic planes of the mirrors is

$$\Theta = 2\eta\cos(\psi - \Upsilon/2). \tag{6.1}$$

If $\Upsilon = 2\psi - \pi$ then the atomic planes in the both crystals are parallel.

The following important inferences can by extracted from the simple mathematically formulated model. The atomic planes of the twin-mirrors mounted on the opposite surfaces of a parallel-sided plate can be adjusted to be parallel despite the non-zero mismatch η by a rotation of one of the mirrors about its surface normal. Still, as follows from eq. (6.1), the smaller the mismatch η the easier it is to find the angular range of Υ where the atomic planes are parallel to a certain degree.

Production steps

HEMEX sapphire disks of 27 mm diameter and $\simeq 3$ mm thick are cut parallel to the $(0\ 0\ 0\ 30)$ atomic planes with an accuracy $\eta \simeq 0.5^\circ$. Four cylindrical blind holes ($\simeq 2.5$ mm deep and 5 mm in diameter) are made from one side. Circular cuts 8 mm in diameter and 1.5 mm deep are made from the other side (around the blind holes) whose purpose is to release strain in the thin parts. Cross-sections of the ready-to-use mirrors are shown in Figs. 6.2 and 6.3, where they are termed as M_1 and M_2.) The defective layers which have been introduced by the machining are removed with the help of chemical polishing in a 1:1 H_2SO_4:H_3PO_4 solution at 560 K (Reisman et al. 1971). Typically $\simeq 100$ μm of the surface layers are removed from both sides.

The crystal surface from the other side of the blind hole is regarded as the inner surface of the resonator. It was mechanically polished to achieve the required roughness of $\simeq 0.1$ μm (as described in sec. 5.4) and the required thickness of $\simeq 50$ μm. After mechanical polishing the sapphire disks were once more chemically polished for a short time of $\simeq 30$ min. This procedure drastically improves the Bragg reflectivity of the mechanically polished side.

The thickness variation of the mirrors due to non-uniform flatness of the opposite surface is $\simeq 5$ μm. However, such a thickness variation is admissible, as described in sec. 5.4.

The crystal perfection of the thinned down parts was checked with the help of x-ray white beam topography. If there are a minimum of two dislocation-free parts, the disk is selected and cut into four independent pieces each containing the thin part. The dislocation free pair, as shown for instance in Fig. 3.6, is used for the twin mirrors of the test x-ray resonator.

6.2.2 Two-axis monolithic nanoradian stage

The reflecting atomic planes of the crystal mirrors should be adjusted to be parallel with sub-μrad or even nanoradian accuracy, as was discussed in sec. 5.4. The higher the finesse the more stringent is the requirement. However, they should be not only adjusted; the atomic planes should also be kept parallel with this accuracy.

An important additional issue is the angular range over which the crystals should be tilted. The required range is defined in our case by the angular mismatch η between the reflecting atomic planes and the surface of the sapphire crystal mirrors, which inevitably exists. We have proceeded from the assumption that the crystal mirrors with a mismatch of not more than 1 mrad could be manufactured.

Therefore, the task was to build a two-dimensional rotation stage with $\simeq 1$ nrad resolution and $\simeq 1$ mrad range (dynamic range 10^6). Commercially such devices are not available.

The atomic planes of the mirrors M_1 and M_2 of the x-ray Fabry-Pérot interferometer are adjusted parallel to each other using a specially designed monolithic nanoradian angular rotation stage. A cross section of the stage is shown in Fig. 6.2; a perspective view with a cross section is shown in Fig. 6.3. As the name suggests, the smallest angular step of the stage is about 1 nrad. Flexural pivots instead of ball bearings are used to provide sub-nanometer repeatability. A flexured pivot is a frictionless linkage based on elastic deformation, also known as a weak-link. A general discussion of the monolithic rotation

and translation mechanisms can be found, e.g., in the publications of Tanaka (1983) and Nakayama and Tanaka (1986).

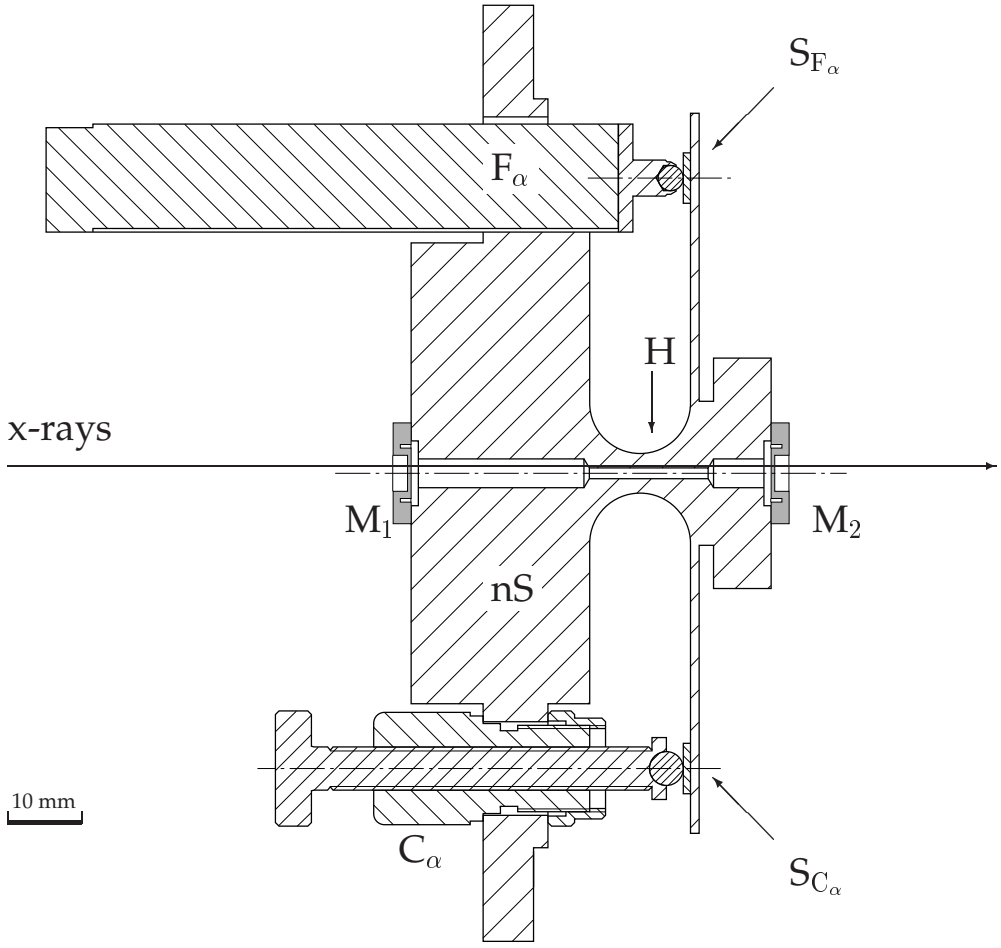

Figure 6.2: Cross section of the monolithic nanoradian stage (nS) for parallel adjustment of the sapphire mirrors M_1 and M_2. Details see in text.

The nanoradian stage is machined out of a single block of Pernifer36^{TM} invar alloy[2]. Invar is used to minimise instabilities due to temperature gradients and temperature fluctuations. Two-dimensional rotation of the mirror M_2 relative to M_1 is performed with the help of a two-dimensional circular notched flexure hinge – H. The rotation is activated by bending or releasing the leaf springs S_{F_α} and S_{C_α} cut out of the monolith. This is carried out by the linear drives C_α and F_α. The index α takes values A or B representing one of two mu-

[2]Pernifer36^{TM}is the trademark of Krupp VDM GmbH, Kleffstraße, D-58762 Altena, Germany.

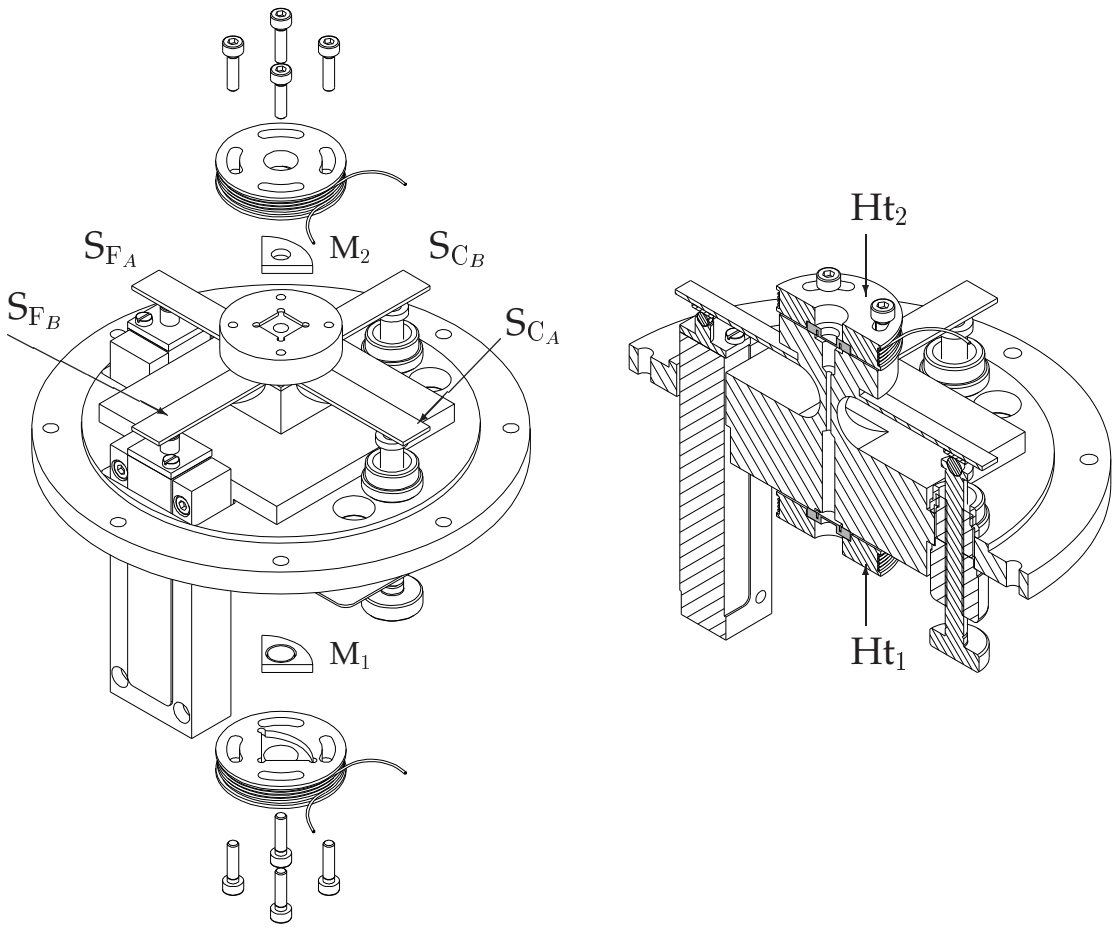

Figure 6.3: Monolithic nanoradian stage for parallel adjustment of the sapphire mirrors M_1 and M_2. Left: perspective view. Right: perspective view with cross section.

tually perpendicular axis of the flexure hinge. Two pairs of springs are used. One pair – for each axis. One of the two leaf springs in each pair is used for fine (F) and another for coarse (C) motion to reach the required angular resolution and angular range, respectively. In the initial position the leaf springs are preloaded, so that the driving points are shifted by 0.5 mm from their free state. We have limited the total range of the linear motion to $\simeq 1$ mm not so as to go over the elastic deformation boundary in invar. Four linear drivers (two for each axis) are mounted on the stage to drive the springs.

A Picomotor$^{\mathrm{TM}}$ – a piezo-driven micrometer screw (C_α) – with a 20 nm

to 40 nm step [3] – is used for the coarse motion over the whole 1 mm range. The Picomotor^{TM} requires no holding power to keep the attained position. Therefore, it is noiseless, which is very important.

The fine motion is performed by a closed-loop controlled piezo linear stage actuator (F_α) – LISA^{TM} [4]. The LISA^{TM} stage allows translations of up to 38 μm reproducible with an accuracy of better than 1 nm. The smallest nominal step size of the LISA stages is 0.1 nm. The displacements are measured with an accuracy of 0.1 nm with the help of built-in capacitive sensors.

By choosing the dimensions of the pivot of the flexure hinge and the dimensions of leaf springs (length, thickness, width) the specified parameters of angular rotation could be reached. The simulation of the circular flexure hinge are performed by using the results of Smith et al. (1997). The dimensions have been chosen to obtain a transmission factor of the linear to angular motion of 1 mrad/mm.

The performance of the nanoradian stage is demonstrated in Fig.6.4, where the dependence of the tilt angle $\delta\Phi$ of the head of the nanoradian stage is measured as a function of the linear translation δx of the driving point of one of the leaf springs. The linear translation was done with the Picomotor^{TM} and measured using the Heidenhain incremental sensor CT-2501 with 50 nm resolution. The corresponding angular inclination of the head of the nanoradian stage was measured with an optical autocollimator and an optical mirror mounted at the position of the crystal mirror M_2. The linear dependence of the tilt angle vs translation was observed for both axes. Both axes show an approximately equal transmission factor of 700 ± 30 μrad/mm, a value very close to the designed value [5]. Thus the angular resolution of the nanoradian stage is 0.7 nrad. The maximal angular range is $\simeq 700$ μrad.

Both flat surfaces of the nanoradian stage to which the mirrors are attached have been polished. In the unloaded state (the leaf springs are not loaded), the surfaces are parallel to each other with an accuracy of $\simeq 50$ μrad.

---

[3] Picomotor^{TM} is the trademark of New Focus, Inc. Santa Clara, CA 95051-0905. Rotating shaft, model MRA8321. The range of linear motion is $\simeq 10$ mm, the step size is not reproducible.

[4] LISA NanoAutomation Stage Actuators, Model P-753.31C. LISA^{TM} is the trademark of Physik Instrumente (PI) GmbH, Auf der Römerstraße, 76228 Karlsruhe, Germany. `www.physikinstrumente.com`

[5] The distance from the center of the stage to the driving point of the leaf spring is 41 mm. A rigid 41 mm long lever would produce a rotation of 24.39 mrad for every 1 mm. The "gear ratio" of the nanoradian stage is $\simeq 35$.

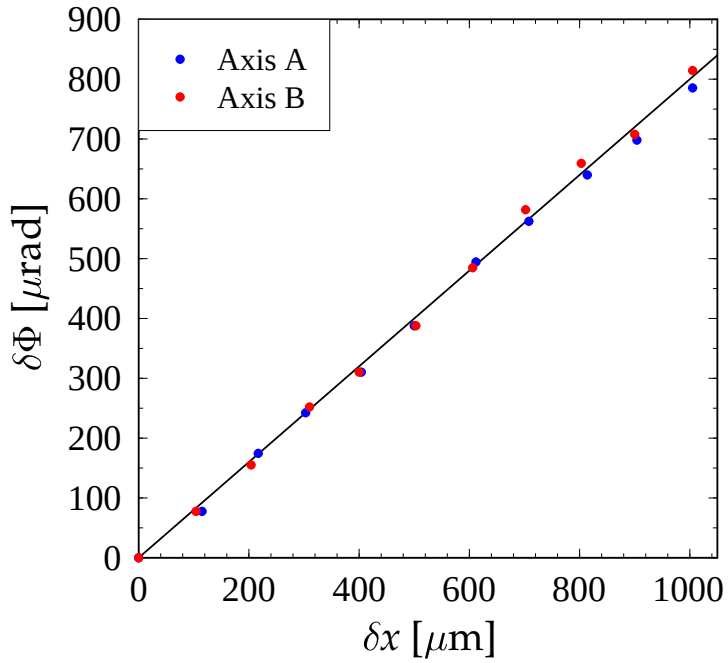

Figure 6.4: Calibration of the nanoradian stage by using an optical autocollimator.

6.2.3 Temperature control

The Bragg energy changes with temperature at a rate of -0.083 meV/mK for the $(0\ 0\ 0\ 30)$ reflection. The energy width of the reflection is $\simeq 13$ meV. Therefore, the temperature of both crystal mirrors should be equal and stable within $\simeq 10$ mK so as not to shift their reflectivity peaks apart by more than 1 meV.

We have used a combination of passive and active temperature controls.

The nanoradian stage with the sapphire mirrors (the resonator) was thermally isolated from the environment. For this the resonator was mounted inside two concentric stainless steel sealed tanks. The internal one that houses the resonator was filled with air, and the external one was evacuated. The walls of the internal tank were heated with surface heaters to a temperature slightly higher than the ambient temperature. The temperature was measured at one position with a PT100 thermo-resistor. At this point the temperature was maintained constant with 1 mK accuracy by using computer control (Lucht 1998).

The sapphire mirrors were attached to the flat surfaces of the nanoradian stage with the help of copper holders which also incorporated wire heaters

Ht_1 and Ht_2, see Fig. 6.3. The PT100 sensors were mounted on each copper holder. Its sensitive part was about 1 mm away from the sapphire mirror. The temperature of each copper holder in the immediate vicinity of the sensor was stabilized to an accuracy of 1 mK by using the heaters and computer control. The temperature equality was checked directly by measuring the energy dependence of Bragg reflectivity independently for each mirror, as shown, in Fig. 2.13.

6.2.4 Fast detectors

To observe exact Bragg backscattering semitransparent EG&G C30703F APDs with 0.7 ns time resolution were used, as described in sec. 2.3.

This time resolution however was not sufficient to observe the multiple reflections in the test device. For this purpose we have used faster silicon APDs from Hamamatsu Photonics[6]. The active thickness of the Hamamatsu devices is smaller. As a result they are faster although less efficient. The Hamamatsu APD S5343 with a 10 μm active layer ($\varnothing 1$ mm) provides the best time resolution close to 100 ps (Kishimoto 1991, 1992). Recently the Hamamatsu low-capacitance APD S5344SPL with a thicker $\simeq$ 25 μm active layer and larger area ($\varnothing 3$ mm) has been tested by Baron (2000). It showed better efficiency and nearly the same time resolution as the S5343 devices.

By using $\simeq$ 150 ps synchrotron radiation pulses at HASYLAB, we have measured an overall duration of the time response of 200-220 ps (FWHM) for both S5343 and S5344SPL APDs. The intrinsic time resolution of both Hamamatsu APDs could be estimated to be $\lesssim 150$ ps.

6.2.5 Experimental setup

Figure 6.5 shows the schematic view of experiments on x-ray resonators. They were performed at the wiggler beamline BW4 at HASYLAB (DESY, Hamburg). X rays from the BW4 wiggler were monochromatized to a 2 eV band with a Si(111) monochromator (both the wiggler and the monochromator are not shown in Fig. 6.5). By using the nested meV-monochromator the bandpass of the x-ray spectrum was further narrowed down to $\simeq 7$ meV, see sec. 2.3. The bandpass was narrower than the energy width of the reflectivity curve for the $(0\ 0\ 0\ 30)$ Bragg reflection, see Fig. 2.13, which then allowed one to select a certain region of the reflectivity curve by tuning the meV-monochromator.

[6]Hamamatsu Photonics K.K., Solid State Division, 1126-1, Ichinio-cho, Hamamatsu City, 435-91 Japan. `www.hamamatsu.com`

The vertical divergence of the beam (in the plane of Fig. 6.5) was $\sigma_v \simeq 20\ \mu$rad. It was defined by the angular acceptance of the Bragg reflections in the eV- and meV-monochromators. The horizontal divergence of the beam was narrowed down to the same $\sigma_h \simeq 20\ \mu$rad by installing a Si(111) channel-cut crystal (with horizontal scattering plane) before the meV-monochromator. The size of the beam could be changed by using a system of slits (S).

Monochromatized and collimated x rays impinge upon the x-ray resonator (XR). The x-ray resonator comprised first of all the sapphire $(0\ 0\ 0\ 30)$ twin-mirrors attached to the nanoradian stage. The stage together with the linear actuators, temperature sensors, heaters, etc., was placed inside two concentric sealed tanks. The external tank was evacuated. An absorber could be automatically inserted between the resonator mirrors. This was helpful to distinguish between the back-reflection signals originating from the different mirrors. The x-ray resonator was installed on a two-circle goniometer (χ, θ), allowing a variation of the incidence angle of the x rays.

The semitransparent EG&G C30703F APD (D_1) with a time resolution of 0.7 ns was used to monitor the incident and reflected beams. The Hamamatsu

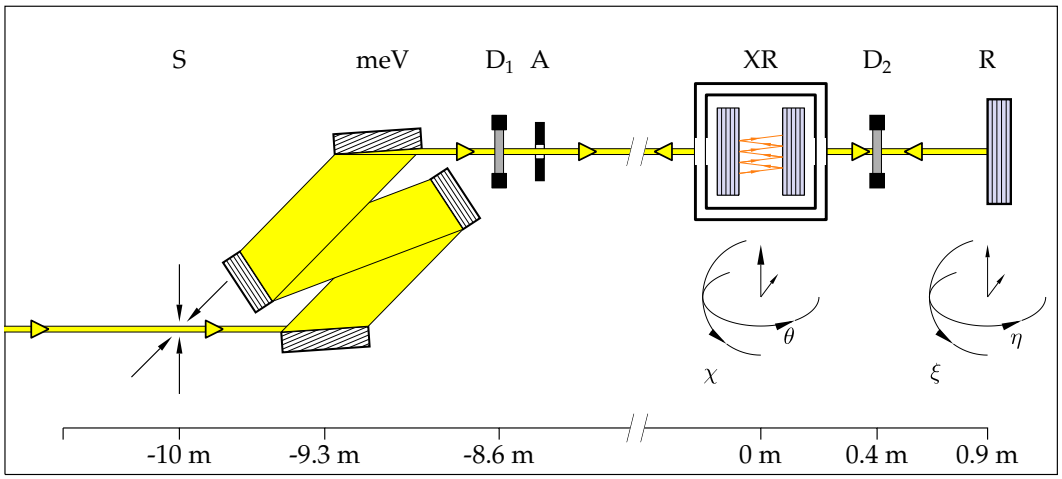

Figure 6.5: Schematic view of experiments on x-ray resonators. X rays monochromatized to a bandwidth of 7 meV with a nested monochromator (meV) impinge upon an x-ray resonator (XR). Detectors D_1 and D_2 monitor the reflected and transmitted x rays. An aperture (A) is used as autocollimator to adjust exact back-scattering from the resonator mirrors. A reflector (R) is used to redirect x rays back into the resonator. The resonator and reflector are installed on two-circle goniometers.

S5344SPL APD (D_2) with a time resolution of $\lesssim 0.15$ ns was used to monitor the radiation transmitted through the resonator.

An apertures (A) of proper diameter could be installed downstream from D_1. The aperture was used as an autocollimator to adjust exact back reflection from the resonator mirrors. The distance from the aperture to the resonator was about 8 m. With an aperture of $\varnothing 0.5$ mm it was possible to adjust the reflecting atomic planes of the sapphire mirrors perpendicular to the incident beam with an accuracy of $\simeq 15$ μrad. The following procedure was used. At first, by using the (χ, θ) two-circle goniometer the $(0\,0\,0\,30)$ atomic planes of the mirror M_2, as shown in Fig. 6.2, were set perpendicular to the incident beam by observing backscattering through the aperture. The same procedure was repeated with the mirror M_1 [7]. If the difference in the angular positions for exact Bragg back-scattering from the the mirrors M_1 and M_2 was larger than the 0.7 mrad range of the nanoradian stage, the mirror M_1 was manually rotated about its surface normal until the difference became smaller. The difference was reduced further to $\simeq 15$ μrad by tilting the mirror M_2 with the help of the nanoradian stage. A finer parallel adjustment was performed by observation of the time dependence of transmission, as described in the next section.

The possibility of redirecting the x rays back into the resonator by using a reflector (R) was also implemented. The idea behind this was to analyse the radiation filtered by the resonator with the help of the resonator itself. The reflector was a thick α-Al_2O_3 crystal. The same $(0\ 0\ 0\ 30)$ Bragg reflection was employed. The crystal was placed in the oven, as described in sec. 2.3. Its temperature was controlled in the same way as the temperature of the sapphire mirrors of the resonator. The angular position for exact back reflection was adjusted with the 0.5 mm aperture (A).

The temperatures of both resonator mirrors and of the reflector were adjusted in such a way, that the peak reflectivity of the three crystals occurred at the same x-ray energy.

[7] To distinguish between the signals originating from different mirrors, their temperatures and thus the peak reflectivities were detuned. Also, the absorber could be automatically inserted between the resonator mirrors.

6.3 Experiments on x-ray resonators

6.3.1 Time response

Two x-ray cavities with pairs of mirrors of different thicknesses were tested.

X-ray cavity with 55 μm thick mirrors

The measured peak reflectivity of these mirrors is $R = 0.83$, as shown in Fig. 2.13(b). The finesse of a resonator with mirrors of such reflectivity is $\mathcal{F} = 16.8$ – see eq. (5.36). The gap width between the mirrors is $d_{\rm g} = 50.5 \pm 0.1$ mm. One expects a quantum beat period of $t_{\rm f} = 0.337$ ns, response time $\tau = 0.89$ ns, and the resonance width $\Gamma = 0.73$ μeV, respectively.

The cavity is excited by 150 ps radiation pulses. The left panels in Fig. 6.6 show the measured time response of the cavity in transmission (circles). The right panels in Fig. 6.6 show the energy dependence of the mirror reflectivity (circles) and the spectral distribution of the incident x-ray photons (solid line normalized to the maximum of the reflectivity curve). In Fig. 6.6(a), the center E of the spectral distribution of the incident radiation pulses is tuned to the peak reflectivity of the sapphire mirrors: $E - E_0 = 0$. In Fig. 6.6(b), it is detuned $E - E_0 = 4$ meV off, in (c) $E - E_0 = 9$ meV off, and in (d) $E - E_0 = 100$ meV off the reflectivity peak, respectively.

The Bragg reflectivity of the mirrors changes with the energy of the incident radiation. Far from the Bragg reflection region the reflectivity is very low and the incident radiation pulses traversed the cavity without reflections and any delay - see Fig. 6.6(d). This graph represents in fact the time dependence of the incident radiation.

The closer the energy of x rays is to the reflectivity maximum the more significant changes occur. Satellite pulses reappearing every 338 ± 1 ps with descending strength are observed. The time period agrees with the estimated value of the back-and-forth time-of-flight in the gap of the x-ray cavity. The observed periodic signals are the x-ray pulses due to multiple reflections, which contribute to the formation of sharp interference resonances, provided the pulses are mutually coherent.

More than 30 successively reflected beams are observed when the x-ray energy coincides with the reflectivity maximum, see Fig. 6.6(a). The time response attenuates nearly exponentially. It deviates from the exponential law at the beginning. The finite spectral width of the incident photons accounts for that, as discussed later. The number 30 is limited only by the intensity of the x-ray source used. The decay time is $\tau \simeq 0.9 \pm 0.01$ ns. The long response time

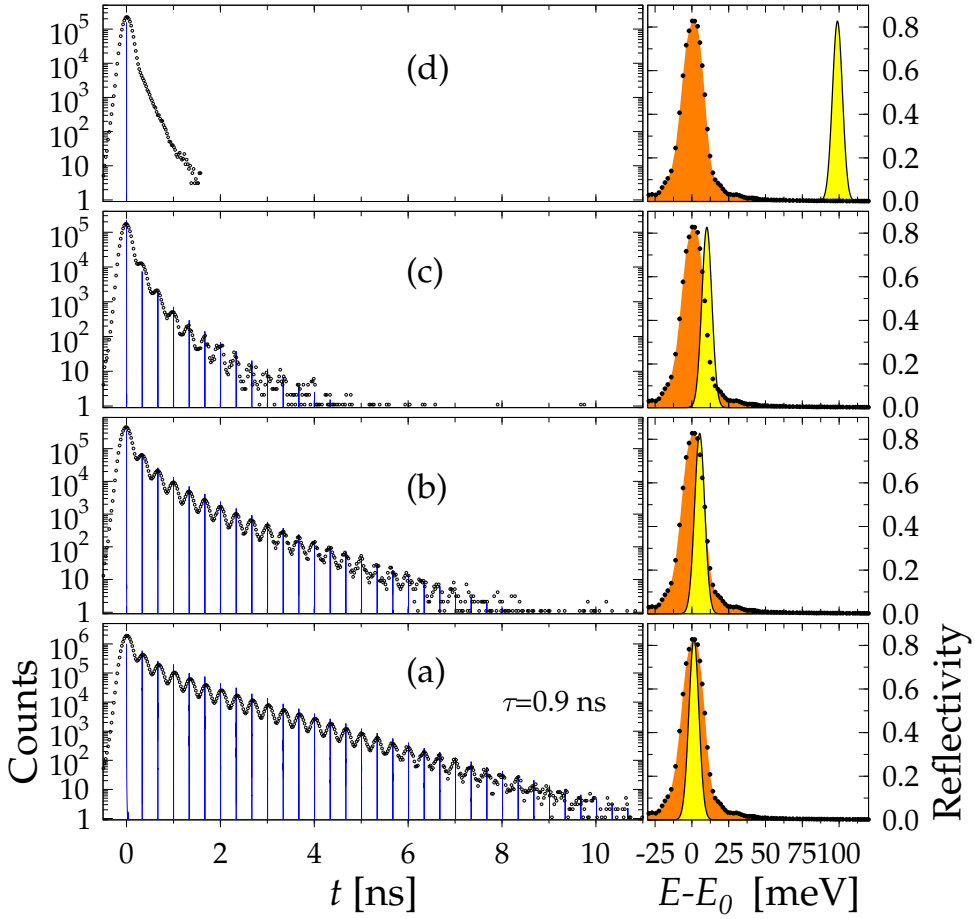

Figure 6.6: Left: time response of an x-ray cavity with 55 μm thick sapphire mirrors (circles). The solid lines (sharp peaks) are the theoretical fits, without convolution with the time instrumental function. Right: energy dependence of the reflectivity of the cavity mirrors (dots) and the spectrum of incident x-ray photons (solid line normalized to the maximum of the reflectivity curve). The center of the spectral distribution E of the incident radiation pulses is tuned (a) to the peak reflectivity of the mirrors: $E - E_0 = 0$, (b) detuned $E - E_0 = 4$ meV off, (c) $E - E_0 = 9$ meV off, and (d) $E - E_0 = 100$ meV off the peak reflectivity, respectively. Spectral width of the incident radiation pulses is 7 meV, pulse duration is 150 ps.

or alternatively the large number of observed multiply reflected beams is the necessary condition for the formation of sharp interference resonances. Such a decay time corresponds to an energy width of $\Gamma \simeq 0.73$ μeV for the transmission resonances. It is noteworthy that, the observed decay time agrees very well with the above estimates.

The solid lines in the left panels of Fig. 6.6 (seen as a set of very sharp peaks) show the numerically calculated theoretical time spectrum. Each calculated time spectrum looks like a set of equidistantly distributed peaks with descending amplitudes. In fact these are very sharp $\simeq 0.7$ ps pulses. Their narrowness is due to the interference of a very large number ($\simeq 500$) of Fabry-Pérot resonances simultaneously excited by the 7 meV broad incident radiation spectrum. The calculation procedure was described in sec. 5.3.6. The incident pulse duration is taken to be 0.22 ps, deduced from the 7 meV spectral width. No convolution with the instrumental function (real pulse width and detector resolution) is made. The parameters of the test sapphire x-ray resonator are used in the calculations. The amplitudes of the calculated time spectra agree very well with the measured ones. The best fit of the decay rate is achieved by assuming 58 μm thick mirrors. This differs slightly from the value of 55 μm obtained from the fit of the reflectivity curve in Fig. 2.13(b).

The deviation from the exponential form at the beginning of the time dependence is due to the fact that the Bragg reflectivity varies significantly in the vicinity of its peak value over the 7 meV region corresponding to the spectral width of the incident photons. The decay becomes purely exponential for photons with narrower bandwidths. Alternatively, the decay becomes purely exponential if the region of the Bragg reflectivity gets broader. This happens, if the mirrors are thinned down, as described below.

X-ray cavity with 39 μm thick mirrors

The measured peak reflectivity of the mirrors with a thickness of 39 ± 1 μm is $R = 0.69$, as shown in Fig. 2.13(a). The finesse of the resonator with mirrors of such reflectivity is $\mathcal{F} = 8.4$. The gap between the mirrors is $d_{\rm g} = 52.5$ mm. One expects a quantum beat period of $t_{\rm f} = 0.350$ ns, response time $\tau = 0.47$ ns, and resonance width $\Gamma = 1.4$ μeV, respectively.

Figure 6.7 shows the measured time response of the x-ray cavity with 39 μm thick mirrors. The center of the spectral distribution of the incident x-ray photons is tuned to the peak reflectivity of the mirrors. The time response is purely exponential. A slightly increased period of of $\simeq 0.35 \pm 0.02$ ns between the successive peaks is observed, compared to the previous case. This agrees with the aforementioned estimate, since the gap between the mirrors is increased by 2 mm.

More significantly, the application of thinner mirrors results in a shorter decay time of $\tau \simeq 0.44 \pm 0.02$ ns. This is consistent with the fact that thinner mirrors have a lower Bragg reflectivity, and as a result a shorter decay time.

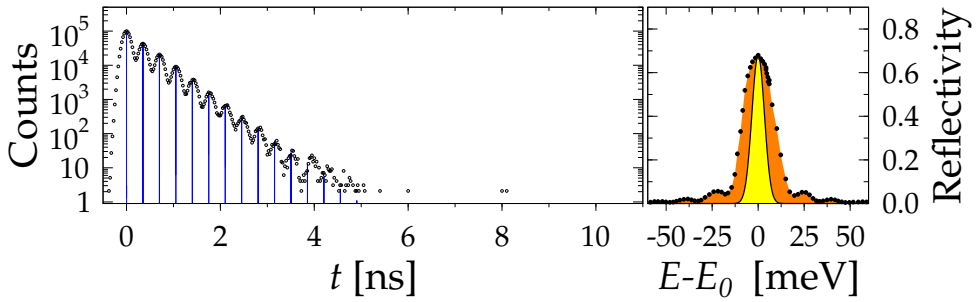

Figure 6.7: Left: time response of an x-ray cavity with 39 μm thick sapphire mirrors (circles). The solid lines is the theoretical fit, without convolution with the time instrumental function. The peak at 4 ns is due to a spurious electron bunch in the storage ring. Right: energy dependence of the reflectivity of the cavity mirrors (dots) and the spectrum of incident x-ray photons (solid line). The center E of the spectral distribution of the incident radiation pulses is tuned to the peak reflectivity of the mirrors: $E - E_0 = 0$. Spectral width of the incident radiation pulses is 7 meV, pulse duration is 150 ps.

One should note that the opposite behavior has been observed in the attempt to build an x-ray resonator consisting of silicon mirrors (Liss et al. 2000). In our experiment, the observed decay time agrees very well with the estimated one. A decay time of $\tau \simeq 0.44 \pm 0.02$ ns corresponds to an energy width of $\Gamma \simeq 1.4$ μeV for the transmission resonances.

The solid lines in Fig. 6.7(left) represent the theoretical time spectrum. It is a set of very short $\simeq 0.7$ ps periodic pulses with descending amplitudes. The amplitude values agree very well with the experiment. The best fit requires 41 μm thick mirrors. Again, it is slightly larger than the value obtained from the fit of the reflectivity curve in 2.13(a). This small discrepancy could be attributed to a slightly too high value of the Debye-Waller factor used in the theoretical calculations.

6.3.2 Effects of angular and temperature mismatch

A priori, it is obvious that the time response with the longest decay time will be observed if both mirrors of the x-ray cavity operate with the highest reflectivity. For this not only the energy of x rays should be tuned to the reflectivity maximum, but also the reflecting atomic planes should be parallel and the reflectivity maxima of both mirrors should coincide.

In the discussion of the experimental results in the preceeding section it

was implicit that the reflecting atomic planes in the sapphire mirrors have been adjusted parallel to each other and the temperature of the mirrors were equal. In fact the presented data were taken under such mirror settings which yielded the longest decay times, as depicted in Fig. 6.6(a) and Fig. 6.7.

How is such state is reached? For this, a time window $t_1 \rightarrow t_1 + \Delta t$ is selected in which the count rate is much lower than in the vicinity of $t = 0$. Only x-ray photons appearing in this time interval are counted. The angular position of the mirror M_2, see Figs. 6.2 and 6.3, is varied by using the nanoradian stage to maximize the count rate in the selected time window. Then the window is shifted to even later time $t_2 > t_1$ and the procedure is repeated. The procedure is repeated until the count rate is still sufficient to draw a more precise conclusion. In this way, it was possible to adjust the mirrors with an accuracy of $\delta\Phi \simeq 1$ μrad. This accuracy was limited by the brilliance of the x-ray source. The accuracy can be increased by a factor of $10^2 - 10^3$ by using much more brilliant third generation synchrotron radiation facilities.

Figure 6.8 shows examples of what happens to the time response if the mirrors are misaligned. The data were recorded when no perfect alignment and consequently the maximum decay time of 0.9 ns was not yet reached.

By using a similar procedure, the temperature of the mirrors can be equalized. Figure 6.9 shows examples of the time response if the mirrors temperatures are mismatched.

The theoretical fit of the time spectrum in Fig. 6.6(a) demonstrates that the attained accuracy of $\delta\Phi \simeq 1$ μrad in the angular alignment of the mirrors is sufficient to observe at least 30 successively reflected beams with intensities in agreement with the theory. In sec. 5.3.9, it was shown that the interference of $\mathcal{N}_r \simeq \mathcal{F}$ successively reflected beams is sufficient for the formation of the perfect Fabry-Pérot resonances. The finesse of the test cavity with 55 μm thick mirrors is $\mathcal{F} = 16.8$. Therefore, the observed number of beams is more than enough to produce the expected 0.74 μeV sharp Fabry-Pérot resonances. A similar conclusion applies also for the test cavity with 39 μm thick mirrors. Thus, all necessary the attributes of x-ray resonators which can be observed in the time responses have been observed in the preceeding experiments. It is still a question, whether these attributes are sufficient.

6.3.3 Transmission spectrum in different time windows

The measured time responses demonstrate that the incident x-ray photons with energies closest to the reflectivity peak are captured in the cavities for the longest time. This implies, that the energy spectrum of the transmitted

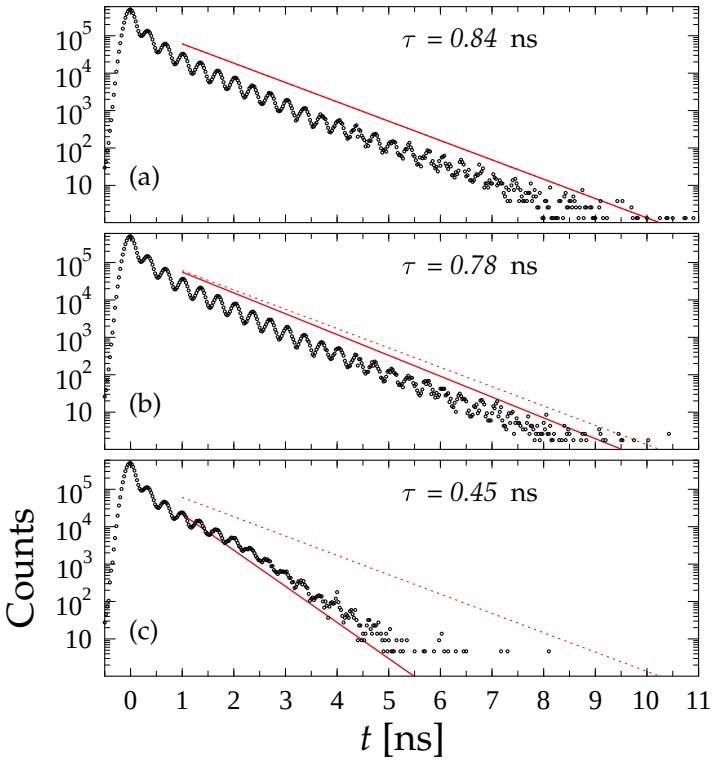

Figure 6.8: Time response of an x-ray cavity with 55 μm thick sapphire mirrors for different relative angular settings of the interferometer mirrors: (a) providing the longest response time, (b) $\delta\Phi = 1.4$ μrad off, and (c) $\delta\Phi = 15.4$ μrad off. The x-ray energy is tuned to the transmission minimum. The dotted lines indicate the decay rate with the largest time constant $\tau = 0.84$ ns. The solid lines and the time constants τ indicate the actual values.

photons should depend on the time delay at which it is observed – the larger the time delay the sharper should be the spectrum.

Figure 6.10 shows the transmissivity of the x-ray cavity with 55 μm thick sapphire mirrors (circles) as a function of the energy of incident x-ray photons. In fact, the center E of the spectral distribution of the incident x-ray photons was varied. The incident photons have a spectral bandwidth of $\simeq$ 7 meV, which is almost three orders of magnitude larger than the width of the resonances expected in such a cavity. Therefore, discrete Fabry-Pérot resonances could not be observed. The transmissivity was measured by counting the photons in different time windows. Figure 6.10(a) presents the energy dependence when all the photons are counted, independent of time. The energy dependence reveals a minimum at the same position where the reflectivity shows a maximum.

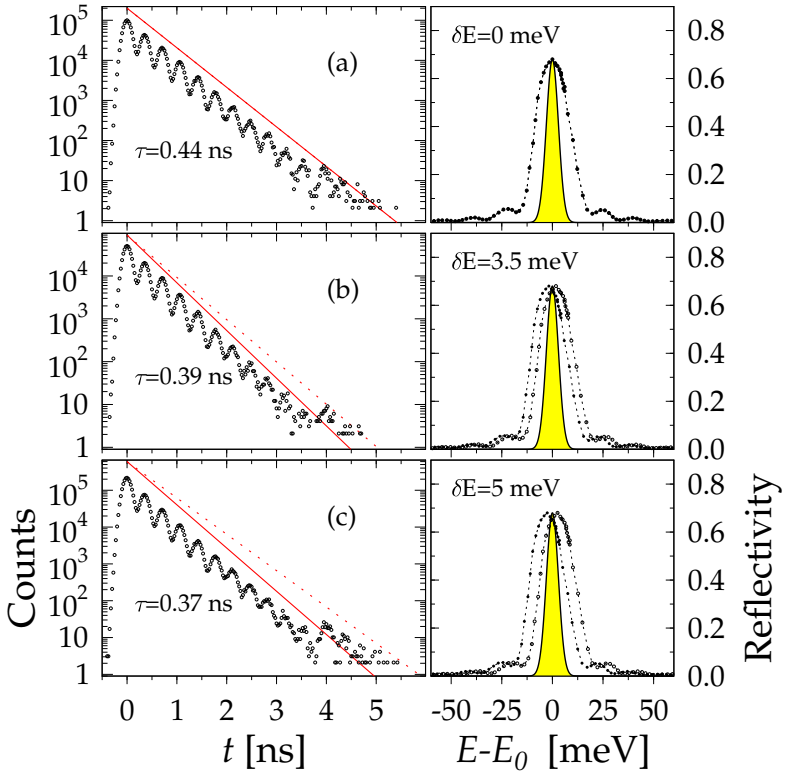

Figure 6.9: Left: time response of an x-ray cavity with 39 μm thick sapphire mirrors. The temperature of the mirrors is (a) equal (with 10 mK accuracy), or differs by (b) 40 mK , and (c) 60 mK. The dotted lines indicate the decay rate with the largest time constant $\tau = 0.44$ ns. The solid lines and the time constants τ indicate the actual values. Pronounced peak at $t = 4$ ns is a due to a spurious electron bunch. Right: energy dependence of the reflectivity of both cavity mirrors (dots) and the spectrum of incident x-ray photons (solid line). δE is the mismatch of the peak reflectivities resulting from the temperature mismatch.

Figures 6.10(b) and 6.10(c) show the energy dependence of transmission of the photons which have escaped from the cavity with a time delay larger than 0.55 ns after excitation at $t = 0$ and larger than 3.4 ns, respectively. In place of the minimum a maximum is observed. The width of this maximum decreases with the delay. Interestingly, no further reduction of the energy width is observed by further increasing the delay. Such behavior is reasonable, since the spectrum can not be sharper than the spectrum of the incident photons. The measured width of 6.7 meV in Fig. 6.10(c) agrees with the width of the incident radiation spectrum. The intrinsic width of the spectrum of transmission

through the x-ray cavity is much less than this value.

This technique can be used for monochromatization of x rays. However, one should distinguish it from the Fabry-Pérot mechanism, since it does not require coherence between the reflected beams. Due to this fact, it is less efficient.

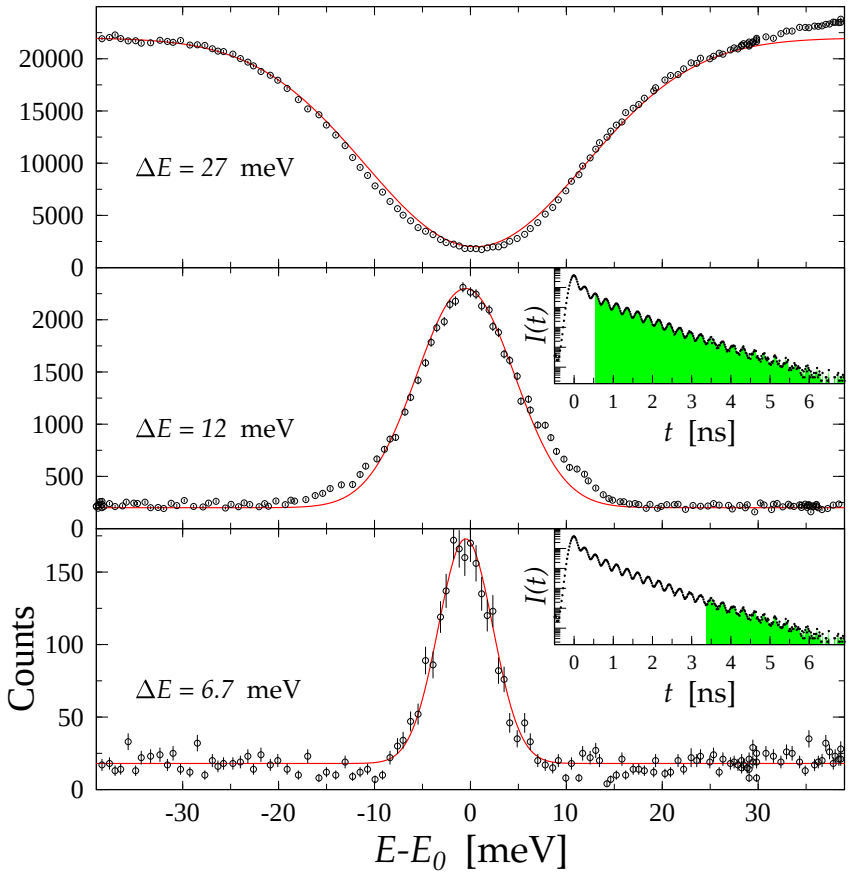

Figure 6.10: Transmission through the x-ray cavity with $55\ \mu$m thick sapphire mirrors (circles) vs energy of incident x-ray photons. The transmitted photons are counted (a) in the whole time range, (b) with a 0.55 ns delay, and (c) with a 3.4 ns delay after excitation. The insets show the time dependence of the time response at $E = E_0$ and the corresponding time range where the photons are counted. Solid lines are fits with Lorentzians with a width of ΔE. The background is due to spurious bunches.

6.3.4 Repeated transmission through x-ray cavity

The observed time responses indicate the perfect performance of the x-ray cavity. The time responses agree very well with the theoretical predictions. The almost nanosecond decay times observed indicate that $\simeq 1$ μeV sharp Fabry-Pérot resonances could have been excited. Direct evidence of this, however, is important. Unfortunately, x-ray monochromators with μeV resolution required for this purpose are not available. As a way out of this problem, we propose using the resonator as an auto-analyzer, i.e., to analyze the radiation created by the resonator with the resonator itself. Furthermore, instead of observing the resonances on the energy scale, we need to observe them on the equivalent angular scale.

To do so, the photons passed through the x-ray cavity are re-directed back and observed with the detector D_1 from the other side, as shown in Fig. 6.5. The resonators are transparent to the photons re-directed exactly on the same way back, i.e., exactly at the same incidence angle. However, if the incidence angle is changed the transparency should change as well. A picture of emerging and submerging Fabry-Pérot transmission resonances with changing incidence angle should be observed, as shown in Fig. 6.1(bottom right) (see also Fig. 5.12). The picture applies for an incident plane wave. In the experiment, one should observe a convolution with the divergence of the incident beam.

A back-reflection crystal (R) is used to reverse the direction of the x rays passed through the x-ray cavity. The angle at which the photons re-enter the device can be varied by rotation about the ξ- or ϕ-axis of the two-circle goniometer. Both, the horizontal and vertical divergence of the x rays is 20 μrad. This is sufficient to observe the central Fabry-Pérot resonance at $\delta\theta = 0$ - see Fig. 6.1(bottom right). The other resonances with intrinsic widths of $\lesssim 2$ μrad could hardly be resolved.

Figure 6.11 shows the distribution of events on the time scale as seen by detector D_1. The signal corresponding to the primary beam is not shown. The first peak at $t = 0$ corresponds to those photons directly reflected from the x-ray cavity. The second peak at $t = 6.0$ ns (grey area) is due to the photons reflected from the reflector, and which have thus passed twice through the x-ray cavity. This additional 6.0 ns delay is due to the back-and-forth time-of-flight of the photons between the x-ray cavity and the reflector. The multiple reflections between the mirrors of the x-ray cavity are not seen, because of the insufficient for this time resolution (0.7 ns) of the detector D_1. All other peaks in Fig. 6.11 appear due to multiple reflections between the reflector and x-ray cavity. Thus, by counting the events belonging only to the first peak at

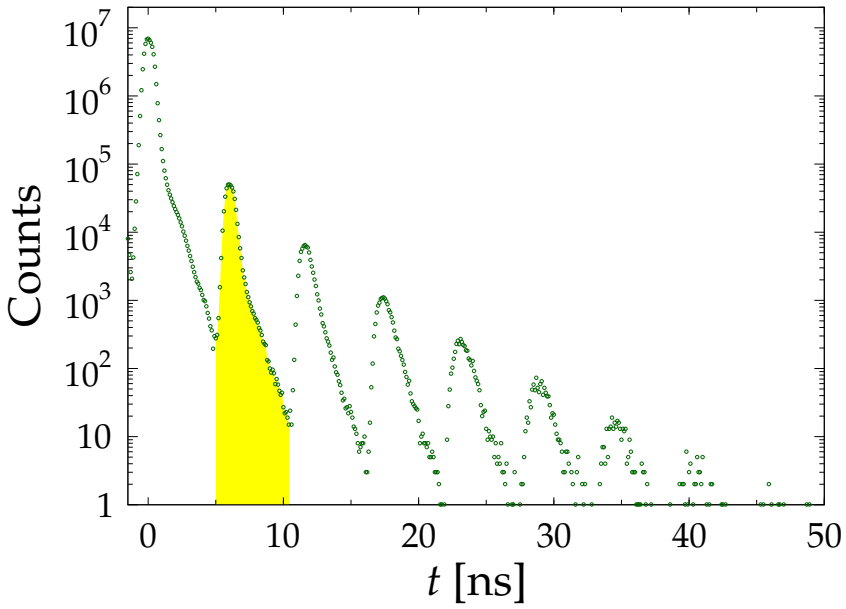

Figure 6.11: Events in the detector D_1 as a function of time.

$t = 0$, one measures the reflectivity of the x-ray cavity. By counting the events belonging to the second peak at $t = 6.0$ ns, one measures the back-and-forth transmission through the x-ray cavity.

With the help of the autocollimator (A), the mirrors of the x-ray cavity and the reflector are set normal to the direction of the incident beam. It is then removed and the photons twice transmitted through the x-ray cavity are counted as a function of the reflection angle ξ of the reflector.

Figure 6.12 shows the effect of the repeated transmission through the x-ray cavity with 55 μm thick sapphire mirrors vs reflection angle ξ of the reflector. The reflection angle ξ and the incidence angle $\delta\theta$ of x rays re-entering the x-ray cavity are related by $\delta\theta = 2\xi$. The transmission curve shows a maximum at normal incidence when the mirrors are adjusted nominally parallel to each other. Qualitatively, this agrees with our expectations. However, the width of the curve is $\Delta(\delta\theta) = 220 \pm 10$ μrad. This is more than an order of magnitude larger than the expected $\simeq 15$ μrad intrinsic width of the central Fabry-Pérot resonance, cf. Fig. 6.1(bottom, right), and the $\simeq 20$ μrad divergence of the beam.

No other mechanism other than the Fabry-Pérot mechanism is known which would provide enhanced transparency of a system of highly reflecting mirrors. Therefore, the cumulation of transmissivity observed while approaching

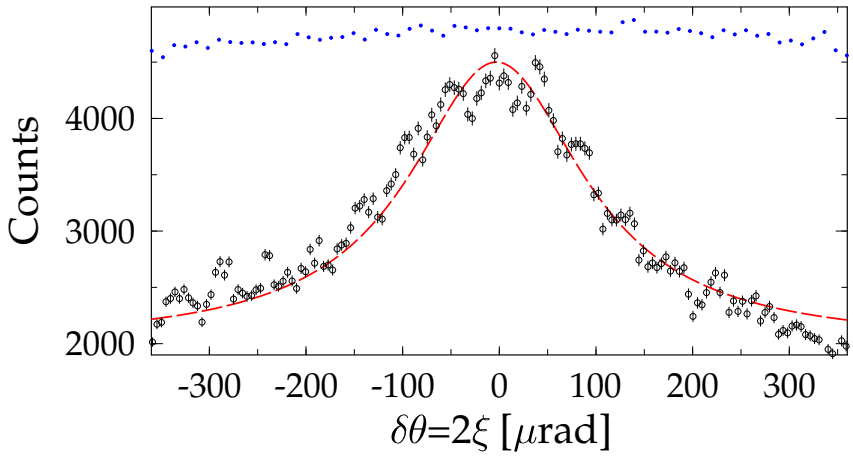

Figure 6.12: Repeated transmission through the x-ray cavity vs reflection angle ξ of the reflector ($\delta\theta = 2\xi$ is the incidence angle for x rays re-entering the x-ray cavity): (a) the mirrors of the x-ray cavity are adjusted nominally parallel to each other (b) one sapphire mirror is tilted by 0.14 μrad. The solid line is a fit with a Gaussian (210 μrad FWHM). The horizontal dotted line shows the count-rate in the detector when the cavity is removed from the beam.

the maximum reflectivity of individual mirrors is very strong evidence of the proper performance of the x-ray cavity. However, the much larger width than expected of the transmission curve suggests, that the selective excitation of the Fabry-Pérot resonances has not yet been achieved.

Most probable, to obtain the selected excitation the resonator mirrors should be adjusted parallel with better than $\delta\Phi \simeq 1$ μrad accuracy. To achieve this, use of much more brilliant third generation synchrotron radiation facilities is required. These experiments are in progress.

Concluding remarks

In this report, we have reviewed important advances on the route towards achieving x-ray resonators. X-ray resonators are highly desirable for high-resolution spectroscopy and interferometry. In the hard x-ray range μeV energy resolution can be obtained by employing such devices. This will enable studies of the dynamics of biological macromolecules, and the phonon spectra in condensed matter with much higher energy resolution than before. This will allow one to measure with very high precision wavelengths in the x-ray spectral region in terms of visible light wavelengths, which is an important task in nano-metrology. Phase-contrast imaging with enhanced sensitivity and x-ray holography using x-rays fully coherent in $\simeq 1$ mm^3 volume will be possible.

The main elements of an x-ray resonator are normal incidence x-ray mirrors of *high reflectivity* arranged parallel and separated by a gap. Back reflection geometry is essential to minimize the effect of the finite beam divergence on the spectral resolution of x-ray resonators. To realize x-ray resonators it was necessary: i) to study *exact* Bragg backscattering of x rays and to devise techniques for its observation; ii) to find and to test a single crystal material that could be used for construction of high reflectivity x-ray backscattering mirrors in a wide spectral range, iii) to develop further the theory of x-ray Fabry-Pérot resonators, to extend it to practical cases, and to understand all the technical challenges of realization of x-ray resonators; iv) to design, built and study a test device.

The first major task was to achieve normal incidence x-ray mirrors of high reflectivity. The project was initiated at a time when Bragg backscattering of x rays was already well developed both in theory and experiment. Application of backscattering, primarily in high energy-resolution optics, was also an established technique. However, the main experimental work has been done under *near-normal* incidence conditions. Surprisingly *exact* Bragg backscattering regime has been neglected. We have developed an experimental method for studying exact Bragg backscattering, which uses semitransparent detectors and time-of-flight techniques. Our studies demonstrated that while approach-

ing normal incidence to the reflecting atomic planes in silicon crystals the peak reflectivity drops because of the increasing role of multiple-beam Bragg diffraction, and also the energy spectrum undergoes undesirable changes. This has a dramatic impact on the practical use of exact Bragg backscattering. Silicon crystals that are widely used in x-ray crystal optics are unsuitable for use in the *exact* backscattering geometry.

Silicon crystals suffer from other drawbacks. It is difficult to find a matching Bragg back reflections for the required x-ray energy, and the reflectivity of silicon crystals in the backscattering geometry drops rapidly with increasing x-ray energy, and falls to below 10% at 40 keV.

To overcome these problems, we proposed using crystals with lower (non-cubic) crystal symmetry, higher Debye temperature, and small photo-absorption. Sapphire (α-Al_2O_3) is the best choice among the commercially available crystals. α-Al_2O_3 crystals permit Bragg backscattering for a wide variety of energies above $\gtrsim 10$ keV. Furthermore, the problem with multiple-beam diffraction is not as severe as with silicon crystals. Most importantly, the reflectivity of sapphire crystals is high even for hard x-rays. At 40 keV Bragg reflectivity is still $\simeq 80\%$. Sapphire crystals have great potential for high energy resolution x-ray optics in the 10-70 keV spectral range. For this, however, i) crystals of good quality and ii) precise data on the crystal lattice constants are required.

Quality assessment of the commercially available sapphire crystals was performed using white beam x-ray topography and reflectivity measurements. It was shown that sapphire crystals with less than one dislocation per 1 mm^2 are available. Such crystals reveal practically theoretical reflectivity at normal incidence for x ray photons with energies $\lesssim 15$ keV. Reflectivity of a minimum of 86% was measured. Thus, normal incidence mirrors of high reflectivity was achieved for x rays with energies $\lesssim 15$ keV.

The next task was to measure precisely values of the sapphire lattice constants and their temperature dependence. These are required since in many applications specific photon energies are used, and it is necessary to predict Miller indices of the back reflections and the relevant crystal temperatures for this x-ray energies. A relative uncertainty in absolute measurements of the lattice constants to better than 1 ppm was required.

At this point, we realized that precision length measurements at atomic scales are not easy to implement. First, the existing silicon length standard is not so easy to reproduce, even with a moderate relative uncertainty of 1 ppm. Secondly, to gauge interatomic distances, one needs *radiation* with a well-defined wavelength rather than an etalon of a well-defined material. Thus, it is desirable to have access to an *easy reproducible wavelength standard* for atomic scales.

The wavelength of the 14.4 keV ^{57}Fe Mössbauer radiation would be ideal. An important first step leading to its practical use was the precise measurement of the absolute value of the wavelength. We have used silicon as a transfer standard and have measured the Mössbauer wavelength with respect to the silicon lattice constant. For this, a Bragg backscattering technique was devised which enables the comparison of lattice constants with the radiation wavelength to better than 0.2 ppm relative uncertainty. By using this technique the wavelength of the Mössbauer radiation was measured with a relative uncertainty of 0.19 ppm. Its value was determined as $\lambda_{\mathrm{M}} = 0.86025474(16) \times 10^{-10}$ m.

By using the Mössbauer wavelength standard and the backscattering technique, we have measured with up to 0.2 ppm relative uncertainty the lattice constants of sapphire over a broad temperature range. Thus, the problem concerning the precise crystal data of sapphire was solved.

By using these data precise predictions of the Miller indices of the back reflections and the relevant crystal temperatures were made for specific energies of Mössbauer transitions over the 6 to 50 keV range. This is of importance for nuclear resonant scattering techniques that require high energy resolution monochromators at these specific energies.

As an example of such applications, the sapphire backscattering monochromator was employed to observe for the first time nuclear resonant forward scattering of synchrotron radiation from the 25.6 keV level of ^{161}Dy. Electron spin dynamics in Dy-metal in the slow-relaxation regime was observed and studied using this technique.

A precise knowledge of the lattice constants of sapphire as well as the ability of sapphire crystals to back-reflect x-rays of any energy was used also to determine the wavelength of Mössbauer radiation from other isotopes. By using the new wavelength standard, the wavelengths of the Mössbauer radiation of ^{151}Eu: 57.556185(27) pm, ^{119}Sn: 51.920811(39) pm, and ^{161}Dy: 48.334336(19) pm were measured. The relative uncertainty achieved is in a range of 0.4-0.7 ppm. Together with the wavelength of the ^{57}Fe Mössbauer photons they provide a set of reference wavelengths in the hard x-ray range of the electromagnetic radiation spectrum with a uniquely small uncertainty and easy reproducibility.

Now returning to our main goal – x-ray resonators. The next task was to understand the technical challenges of the implementation of such devices. For this, the physics underlying x-ray Fabry-Pérot resonators was addressed. Although theories of x-ray Fabry-Pérot resonators were in existence, they were not complete and in some points erroneous. We have derived expressions for the transmissivity and reflectivity of the perfect x-ray resonator using a geometrical approach based on the summation of the probability amplitudes of

multiple reflections. The introduction of a new very important phase factor was found to be necessary. A detailed analytical analysis was performed. In particular, the position and width of the Fabry-Pérot transmission resonances were calculated analytically as a function of gap between the mirrors, x-ray energy, angle of incidence, and temperature.

A very new aspect of the theory presented in this report is the analysis of the time response of x-ray resonators. It was shown that by measuring the time response it is possible to characterize the performance of x-ray resonators. Observation of the time response plays an important role in the experiments on x-ray Fabry-Pérot resonators presented in the report. A comprehensive set of numerical simulations with the computer code FPET of the energy, time and angular dependence has been carried out to characterize the performance of x-ray Fabry-Pérot resonators.

The theory was completed by considering the influence of possible imperfections, such as the roughness of the crystal surfaces, errors in the parallelism of the atomic planes, and unequal mirror temperatures.

The concept of a test device was worked out. To implement the test resonator one "merely" needs $\simeq 50\mu$m thin wafers of perfect sapphire aligned in parallel with nano-radian accuracy and kept within a few mK at the same temperature. To observe the time response of the test device one needs x-ray detectors with a time resolution of better than 200 ps. A procedure for manufacturing the thin sapphire resonator mirrors was devised and implemented. A two-axis goniometer allowing angular adjustment of the resonator mirrors with nano-radian precision was designed and built. The mK temperature control of the mirrors, and $\simeq 150$ ps fast detectors were tested.

We have succeeded in designing and building a test x-ray resonator for hard x-rays ($\simeq 14.3$ keV) with independently adjustable crystal mirrors. The key element of the x-ray resonator is normal incidence mirrors of high reflectivity. Sapphire (α-Al_2O_3) single crystals are used in this role. Bragg backscattering from sapphire crystals provides high reflectivity. The time response of the resonator to the excitation with short synchrotron radiation pulses was studied. The time response of the resonator with a decay time as long as 0.9 ns was observed. The time behavior of the test device is well described by the theory of the perfect x-ray Fabry-Pérot resonator and indicates that x-ray resonances with a resonance width of $\simeq 0.73$ μeV were excited.

There is still some way to go before we will be able to leave the realm of demonstration experiments. The physical principles are clear, however, many technological problems still have to be solved before x-ray resonators can be used as instruments for high-resolution spectroscopy and interferometry.

Hamburg, Rissen, 2001. *Yuri Shvyd'ko*

Bibliography

Abragam, A.: 1961, *The Principles of Nuclear Magnetism*, Oxford University Press. London.

Afanas'ev, A. M. and Kagan, Y.: 1967, The role of lattice vibrations in dynamical theory of x-rays, *Acta Cryst.* **A24**, 163.

Aldebert, P. and Traverse, J. P.: 1982, Neutron diffraction studies of structural characteristics and ionic mobility of α- Al_2O_3 at high temperatures, *J. Am. Ceram. Soc.* **65**, 460.

Alp, E. E., Sinn, H., Alatas, A. and Shvyd'ko, Y. V.: 2000a, Bragg reflectivity studies of Al_2O_3 at 21.6 kev., *unpublished*.

Alp, E. E., Sinn, H., Alatas, A., Sturhahn, W., Toellner, T., Zhao, J., Sutter, J., Hu, M., Shu, D. and Shvyd'ko, Y. V.: 2001a, Source and optics considerations for new generation high-resolution inelastic x-ray spectrometers, *Nucl. Instrum. Methods Phys. Res. A* **467-468**, 617–622.

Alp, E. E., Sturhahn, W. and Toellner, T. S.: 2001b, Lattice dynamics and inelastic nuclear resonant x-ray scattering, *J. Phys.: Condens. Matter* **13**(34), 7645–7659.

Alp, E. E., Sturhahn, W., Sinn, H., Toellner, T., Hu, M., Sutter, J. and Alatas, A.: 2000b, Inelastic scattering of synchrotron radiation from electrons and nuclei for lattice dynamics studies, *AIP Conf. Proc.* **506**, 479.

Ambacher, O.: 1998, Growth and applications of group III-nitrides, *J. Phys. D: Appl. Phys.* **31**, 2653.

Andrianov, A. V., Vasil'ev, A. N. and Gaidukov, Y. P.: 1991, Low temperature magnetic phase diagrams of dysprosium and gadolinium, *Physica B* **169**, 469.

Azaroff, L. V., Kaplow, R., Kato, N., Weiss, R. J., Wilson, A. J. C. and Yung, R. A.: 1974, *X-Ray Diffraction*, McGraw-Hill, Inc.

Barbee, T. W. and Underwood, J. H.: 1983, Solid Fabry-Pérot étalons for x-rays, *Opt. Commun.* **48**, 161–166.

Baron, A. Q. R.: 2000, Detectors for nuclear resonant scattering experiments, *Hyp. Interact.* **125**, 29.

Baron, A. Q. R., Tanaka, Y., Ishikawa, D., Miwa, D., Yabashi, M. and Ishikawa, T.: 2001a, A compact optical design for Bragg reflections near backscattering, *J. Synchrotron Rad.* **8**, 1127–1130.

Baron, A. Q. R., Tanaka, Y., Miwa, D., Ishikawa, D., Mochizuki, T., Takeshita, K., Goto, S., Matsushita, T., Kimura, H., Yamamoto, F. and Ishikawa, T.: 2001b, Early commissioning of the SPring-8 beamline for high resolution inelastic x-ray scatterin, *Nucl. Instrum. Methods Phys. Res. A* **467-468**, 627–630.

Basile, G., Bergamin, A., Cavagnero, G., Mana, G., Vittone, E. and Zosi, G.: 1994, Measurement of the Silicon (220) lattice spacing, *Phys. Rev. Lett.* **72**, 3133.

Batterman, B. W. and Cole, H.: 1964, Dynamical diffraction of x rays by perfect crystals, *Rev. Mod. Phys.* **36**, 681–717.

Batterman, B. W. and Hilderbrandt, G.: 1967, Observation of x-ray Pendellösung fringes in Darwin reflection, *Phys. Stat. Solidi* **23K**, 147–149.

Batterman, B. W. and Hilderbrandt, G.: 1968, X-ray Pendellösung fringes in Darwin reflection, *Acta Cryst.* **A24**, 150–157.

Bearden, J. A.: 1965, Selection of W K_{α_1} as the x-ray wavelength standard, *Phys. Rev.* **137**, B455–461.

Bearden, J. A.: 1967, X-ray wavelengths, *Rev. Mod. Phys.* **39**, 78–84.

Bearden, J. A. and Blurr, A. F.: 1967, Reevaluation of the atomic energy levels, *Rev. Mod. Phys.* **39**, 125.

Becker, P., Dorenwendt, K., Ebeling, G., Lauer, R., Lucas, W., Probst, R., Radermacher, H.-J., Reim, G., Seyfried, P. and Siegert, H.: 1981, Absolute measurements of the (220) lattice plane spacing in a silicon crystal, *Phys. Rev. Lett.* **46**, 1540.

Bonse, U.: 1997, Interferometry, *in* A. Haase, G. Landwehr and E. Umbach (eds), *Röntgen Centennial*, World Scientific Publishing, pp. 521–537. Singapore.

Bonse, U. and Hart, M.: 1965a, Principles and design of the Laue case x-ray diffractometer, *Z. Physik* **188**, 154.

Bonse, U. and Hart, M.: 1965b, An x-ray interferometer, *Appl. Phys. Lett.* **6**, 155.

Born, M. and Wolf, E.: 1980, *Principles of Optics*, Pergamon Press.

Bowden, G. J., Bunbury, D. S. P. and Williams, J. M.: 1967, A Mössbauer study of hyperfine interactions in dysprosium metal, *Proc. Phys. Soc.* **91**, 612–619.

Bowen, D. K. and Tanner, B. K. (eds): 1998, *High Resolution X-ray Diffraction and Topography*, Taylor and Francis, London.

Brossel, J.: 1947a, Multiple-beam localised fringes: part I - Intensity distribution and localisation, *Proc. Phys. Soc.* **59**, 224–234.

Brossel, J.: 1947b, Multiple-beam localised fringes: part II - Conditions of observation and formation of ghosts, *Proc. Phys. Soc.* **59**, 235–242.

Brown, A. S., Spackman, M. A. and Hill, R. J.: 1992, The electron distribution in corundum. study of the utility of merging single crystal and powder diffraction data, *Acta Cryst.* **A49**, 513.

Brümmer, O., Höche, H. R. and Nieber, J.: 1979, X-ray diffraction in the Bragg case at Bragg angles of about $\pi/2$, *Phys. Stat. Solidi (a)* **53**, 565.

Burgess, D. S.: 2000, Measuring the ultrasmall, *Photonics spectra* p. 29.

Burkel, E.: 1991, *Inelastic Scattering of X rays with Very High Energy Resolution*, Vol. 125 of *Springer Tracts in Modern Physics*, Springer, Berlin.

Burkel, E.: 2000, Phonon spectroscopy by inelastic x-ray scattering, *Rep. Prog. Phys.* **63**, 171–232.

Burns, G. and Glazer, A. M.: 1978, *Space Groups for Solid State Scientists*, Academic Press.

Caticha, A., Aliberty, K. and Caticha-Ellis, S.: 1996, A Fabry-Perot interferometer for sub-mev x-ray energy resolution, *Rev. Sci. Instrum.* **67**, 3380.

Caticha, A. and Caticha-Ellis, S.: 1982, Dynamical theory of x-ray diffraction at angles near $\pi/2$, *Phys. Rev. B* **25**, 971.

Caticha, A. and Caticha-Ellis, S.: 1990a, Dynamical theory of x-ray diffraction by thin crystals at angles near $\pi/2$, *Phys. Stat. Solidi (a)* **119**, 47.

Caticha, A. and Caticha-Ellis, S.: 1990b, A Fabry-Perot interferometer for hard x-rays, *Phys. Stat. Solidi (a)* **119**, 643.

Caticha, A. and Caticha-Ellis, S.: 1996, A thermal neutron interferometer of the Fabry-Perot type, *Phys. Stat. Solidi (a)* **153**, 29–46.

Caticha-Ellis, S., Boyce, R. and Winick, H.: 1990, Conceptual design of instrumentation to measure diffraction profile of a single crystal at Bragg angle near $\pi/2$ by using synchrotron radiation, *Nucl. Instrum. Methods Phys. Res. A* **291**, 132.

Chen, W. M., McNally, P. J., Shvyd'ko, Y. V., Tuomi, T., Danilewsky, A. N., Kanatharana, J., Lowney, D., Lerche, M., Knuuttila, L. and Riikonen, J.: 2001a, Dislocation analysis for heat-exchanger method grown sapphire with white beam synchrotron x-ray topography., *J. Cryst. Growth*. in press.

Chen, W. M., McNally, P. J., Shvyd'ko, Y. V., Tuomi, T., Lerche, M., Danilewsky, A. N., Kanatharana, J., Lowney, D., O'Hare, M., Knuuttila, L., Riikonen, J. and Rantamäki, R.: 2001b, Quality assessment of sapphire wafers for x-ray crystal optics using white beam synchrotron x-ray topography, *Phys. Stat. Solidi (a)* **186**, 365–371.

Chin, G.: 2000, Atomic scale length standard, *Science* **289**, 833.

Chukhovskii, F. N. and Förster, E.: 1995, Time-dependent x-ray Bragg diffraction, *Acta Cryst.* **A51**, 668–72.

Chumakov, A. I. and Sturhahn, W.: 1999, Experimental aspects of the inelastic nuclear resonance scattering, *Hyp. Interact.* **123/124**, 781.

Chumakov, A. I., Baron, A. Q. R., Rüffer, R., Grünsteudel, H., Grünsteudel, H. F. and Meyer, A.: 1996a, Nuclear resonance energy analysis of inelastic x-ray scattering, *Phys. Rev. Lett.* **76**, 4258.

Chumakov, A. I., Metge, J., Baron, A. Q. R., Grünsteudel, H., Rüffer, R. and Ishikawa, T.: 1996b, An x-ray monochromator with 1.65 mev energy resolution, *Nucl. Instrum. Methods Phys. Res. A* **383**, 642.

Chumakov, A. I., Rüffer, R., Leupold, O., Barla, A., Thiess, H., Gil, J. M., Alberto, H. V., Vilão, R. C., de Campos, N. A., Kohn, V. G., Gerken, M. and Lucht, M.: 2001, Nuclear inelastic scattering with ^{161}Dy, *Phys. Rev. B* **63**, 172301.

Cusatis, C., Udron, D., Mazzaro, I., Giles, C. and Tolentino, H.: 1996, X-ray back-diffraction profiles with a Si (111) plate, *Acta Cryst.* **A52**, 614–620.

Deslattes, R. D. and Henins, A.: 1973, X-ray to visible wavelength ratios, *Phys. Rev. Lett.* **31**, 972.

Deutsch, M. and Hart, M.: 1984, X-ray refractive-index measurements in silicon and lithium fluoride, *Phys. Rev. B* **30**, 640.

Deutsch, M. and Hart, M.: 1985, Electronic charge distribution in silicon, *Phys. Rev. B* **31**, 3846.

Deutsch, M. and Hart, M.: 1988, High-energy x-ray anomalous dispersion correction for silicon, *Phys. Rev. B* **37**, 2701.

Dobrovinskaya, L., Lytvynov, L. and Pishchuk, V.: 2002, *Sapphire and other corundum crystals*, Institute for Single Crystals, Ukraine-Charkiv.

Fabry, C. and Pérot, A.: 1899, Theorie et applications d'une nouvelle methode de spectroscopie interferentielle, *Ann. Chim. Phys.* **7**, 115–144.

Faigel, G., Siddons, D. P., Hastings, J. B., Haustein, P. E., Grover, J. R., Remeika, J. P. and Cooper, A. S.: 1987, New approach to the study of the nuclear Bragg scattering of synchrotron radiation, *Phys. Rev. Lett.* **58**, 2699.

Firestone, R. B., Shirley, V. S., Chu, S. Y. F., Baglin, C. M. and Zipkin, J.: 1996, *Table of Isotopes*, John Wiley & Sons, Inc., New York.

Franz, H., Hukelmann, B. and Schneider, J.: 2000, The nuclear-resonance-scattering station at the PETRA II undulator beamline, *Hyp. Interact.* **126**, 397.

Gerdau, E. and de Waard, H. (eds): 1999/2000, *Nuclear Resonant Scattering of Synchrotron Radiation*, Baltzer. Special issues of the *Hyperfine Interact.*, Vol. 123-125.

Gerdau, E., Rüffer, R., Hollatz, R. and Hannon, J. P.: 1986, Quantum beats from nuclei excited by synchrotron radiation, *Phys. Rev. Lett.* **57**, 1141.

Gerdau, E., Rüffer, R., Winkler, H., Tolksdorf, W., Klages, C. P. and Hannon, J. P.: 1985, Nuclear Bragg diffraction of synchrotron radiation in yttrium iron garnet, *Phys. Rev. Lett.* **54**, 583.

Graeff, W. and Materlik, G.: 1982, Millielectron volt energy resolution in Bragg backscattering, *Nucl. Instrum. Methods Phys. Res.* **195**, 97.

Gschneider, K. A., Pecharsky, V. K. and Fort, D.: 1997, Novel thermal effects at the first order magnetic phase transition in erbium, and a comparison with dysprosium, *Phys. Rev. Lett.* **78**, 4281.

Guichet, C. and Rasigni, G.: 1997, Considerations of the finesse and resolving power of Fabry-Pérot étalons for soft x rays, *Opt. Eng.* **36**, 2107.

Hart, M.: 1975, Ten years of x-ray interferometry, *Proc. R. Soc. Lond. A* **346**, 1.

Hashizume, H., Nakayama, K., Matsushita, T. and Kohra, K.: 1970, Variation of Bragg-case diffraction curves of x-rays from a thin silicon crystal with crystal thickness, *J. Phys. Soc. Japan* **29**, 806.

Hastings, J. B., Siddons, D. P., van Bürck, U., Hollatz, R. and Bergmann, U.: 1991, Mössbauer spectroscopy using synchrotron radiation, *Phys. Rev. Lett.* **66**, 770.

Hecht, E. and Zajac, A.: 1974, *Optics*, Addison-Wesley Publishing Company, Inc.

Houston, W. V.: 1927, A compound interferometer for fine structure work, *Phys. Rev.* **29**, 478–84.

Irion, R.: 2000, An Angström-long meter stick, *Physical Review Focus*. http://focus.aps.org/v6/st2.html.

Ishikawa, T., Tamasaku, K., Yabashi, M., Gotob, S., Tanaka, Y., Yamazaki, H., Takeshita, K., Kimura, H., Ohashi, H., Matsushita, T. and Ohata, T.: 2000, 1-km beamline at SPring-8, *Proc. SPIE - Int. Soc. Opt. Eng.* **4145**, 1.

Ishikawa, T., Yoda, Y., Izumi, K., Suzuki, C. K., Zhang, X. W., Ando, M. and Kikuta, S.: 1992, Construction of a precision diffractometer for nuclear Bragg scattering at the photon factory, *Rev. Sci. Instrum.* **63**, 1015.

James, R. W.: 1950, *The Optical Principles of the Diffraction of X-Rays in Crystals*, G. Bell & Sons, Ltd.

Kagan, Y., Afanas'ev, A. M. and Kohn, V. G.: 1979, On excitation of isomeric nuclear states in a crystal by synchrotron radiation, *J. Phys. C: Solid St. Phys.* **12**, 615–631.

Khattak, C. P. and Schmid, F.: 2001, Growth of the world's largest sapphire crystals, *J. Cryst. Growth* **225**, 572.

Khurgin, B., Nowik, I., Rakavy, M. and Ofer, S.: 1970, Spin relaxation phenomena in Mössbauer spectra of magnetically ordered dysprosium intermetallic compounds, *J. Phys. Chem. Solids* **31**, 49–54.

Kikuta, S.: 1994, Studies of nuclear resonant scattering at TRISTAN-AR, *Hyp. Interact.* **90**, 335.

Kikuta, S., Imai, Y., Iizuka, T., Yoda, Y., Zhang, X.-W. and Hirano, K.: 1998, X-ray diffraction with a Bragg angle near to $\pi/2$ and its applications, *J. Synchrotron Rad.* **5**, 670.

Kinosita, K.: 1953, Numerical evaluation of the intensity curve of a multiple-beam fizeau fringe, *J. Phys. Soc. Japan* **8**, 219.

Kirfel, A. and Eichhorn, K.: 1990, Accurate structure analysis with synchrotron radiation. the electron density in Al_2O_3 and Cu_2O, *Acta Cryst.* **A46**, 271.

Kishimoto, S.: 1991, An avalanche photodiode detector for x-ray timing measurements, *Nucl. Instrum. Methods Phys. Res. A* **309**, 603.

Kishimoto, S.: 1992, High time resolution x-ray measurements with an avalanche photodiode detector, *Rev. Sci. Instrum.* **63**, 824.

Kissel, L. and Pratt, R.: 1990, Corrections to tabulated anomalous scattering factors, *Acta Cryst.* **A46**, 170–175. www-phys.llnl.gov/Research/scattering.

Kissel, L., Zhou, B., Roy, S., Gupta, S. K. S. and Pratt, R. H.: 1995, Validity of form-factor, modified-form-factor and anomalous-scattering-factor approximations in elastic scattering calculations, *Acta Cryst.* **A51**, 271–288.

Kohn, V. G., Kohn, I. V. and Manykin, E. A.: 1999, Diffraction of x-rays at a Bragg angle of $\pi/2$ (back reflection) with consideration of multi-wave effects, *JETP* **89**, 500.

Kohn, V. G., Shvyd'ko, Y. V. and Gerdau, E.: 2000, On the theory of an x-ray Fabry-Perot interferometer, *Phys. Stat. Solidi (b)* **221**, 579.

Kohra, K. and Matsushita, T.: 1972, Some characteristics of dynamical diffraction at a Bragg angle of about $\pi/2$., *Z. Naturforsch. A* **27**, 484.

Koyama, I., Yoda, Y., Zhang, X. W., Ando, M. and Kikuta, S.: 1996, Nuclear resonant scattering of ^{161}Dy and ^{151}Eu by synchrotron radiation, *Japn. J. Appl. Phys.* **35**, 6297.

Kushnir, V. I. and Suvorov, E. V.: 1986, Experimental observation of the half-degree angular interval of x-ray reflection in backscattering ($\theta \simeq \pi/2$) from a high-quality crystal, *JETP Lett.* **44**, 262.

Kushnir, V. I. and Suvorov, E. V.: 1990, X-ray backscattering on perfect crystals ($2\theta \simeq \pi$), *Phys. Stat. Solidi (a)* **122**, 391.

LCLS: 1998, Linac coherent light source, design study report, *Technical Report SLAC-R-521, UC-414*, Stanford Linear Accelerator Center, CA 94025 USA.

Lederer, C. M. and Shirley, V. S.: 1976, *Table of Isotopes*, John Wiley & Sons, Inc., New York.

Lepetre, Y., Rivoira, R., Philip, R. and Rasigni, G.: 1984, Fabry-Pérot étalons for x-rays: construction and characterization., *Opt. Commun.* **51**, 127–130.

Lerche, M.: 2000, Investigations of sapphire single crystals: application for monochromatization and for exact Bragg backscattering of synchrotron radiation, Diploma thesis, University of Hamburg.

Leupold, O., Pollmann, J., Gerdau, E., Rüter, H. D., Faigel, G., Tegze, M., Rüffer, G. B. R., Chumakov, A. I. and Baron, A. Q. R.: 1996, Nuclear resonance scattering of synchrotron radiation at the 21.5 kev resonance of ^{151}Eu, *Europhys. Lett.* **35**, 671.

Lewis, J., Schwarzenbach, D. and Flack, H. D.: 1982, Electric field gradients and charge density in corundum, α- Al_2O_3, *Acta Cryst.* **A38**, 733.

Libbert, J., Pitney, J. and Robinson, I.: 1997, Asymmetric fraunhofer diffraction from roller-blade slits, *J. Synchrotron Rad.* **7**, 125.

Liss, K.-D., Hock, R., Gomm, M., Waibel, B., Magerl, A., Krisch, M. and Tucoulou, R.: 2000, Storage of x-ray photons in a crystal resonator, *Nature* **404**, 371.

Loh, E., Chien, C. L. and Walker, J. C.: 1974, Sublattice magnetization of dysprosium near the Neel point, *Phys. Lett.* **49A**, 357.

Lucht, M.: 1998, High-precision temperature control: application for monochromatization and for exact Bragg backs cattering of synchrotron radiation, Diploma thesis, University of Hamburg.

Lucht, M., Lerche, M., Wille, H.-C., Gerdau, E., Franz, H., Rüter, H. D. and Shvyd'ko, Y. V.: 2001, Precise measurements of the lattice constants of Al_2O_3 in the 4-400 k temperature range. (to be published).

Masciovecchio, C., Bergmann, U., Krisch, M., Ruocco, G., Sette, F. and Verbeni, R.: 1996, A perfect crystal x-ray analyser with mev energy resolution, *Nucl. Instrum. Methods Phys. Res. B* **111**, 181–186.

Materlik, G. and Tschentscher, T. (eds): 2001, *TESLA. The superconducting Electron-Positron Linear Collider with an Integrated X-ray Laser Laboratory. Part V, The X-Ray Free Electron Laser*, DESY, Hamburg.

Missalla, T., Uschmann, I., Förster, E., Jenke, G. and von der Linde, D.: 1999, Monochromatic focusing of subpicosecond x-ray pulses in the kev range, *Rev. Sci. Instrum.* **70**, 1288–99.

Mohr, P. J. and Taylor, B. N.: 2000, CODATA recommended values of the fundamental physical constants: 1998, *Rev. Mod. Phys.* **72**, 351–495.

Moncton, D. E.: 1996, *Rev. Sci. Instr.* **67**, 3380.

Mooney, T. M., Toellner, T. S., Sturhahn, W., Alp, E. E. and Shastri, S. D.: 1994, High-resolution, large-angular-acceptance monochromator for hard x-rays, *Nucl. Instrum. Methods Phys. Res. A* **347**, 348.

Moos, H. W., Imbusch, G. F., Mollenauer, L. F. and Schawlow, A. L.: 1963, Tilted-plated interferometry with large plate separations, *Appl. Opt.* **2**, 817.

Nakayama, K. and Tanaka, M.: 1986, Monolithic rotation mechanism with nanoradian resolution, *in* S. Hosoya, Y. Ittaka and H. Hashizume (eds), *X-Ray Instrumentation for the Photon Factory: Dynamic Analyses of Micro-Structures in Matter*, KTK Scientific Publishers, pp. 277–282. Tokyo.

NID: 2000-2001, Normal incidence x-ray diffraction beamline at APS, *unpublished*.

Nowik, I.: 1967, The rate equation method applied to relaxation effects in Mössbauer spectra, *Phys. Lett.* **24A**, 487.

Nowik, I. and Wickman, H. H.: 1966, Relaxation phenomena in Mössbauer spectra of magnetically ordered erbium, *Phys. Rev. Lett.* **17**, 949.

Ofer, S., Rakavy, M., Segal, E. and Khurgin, B.: 1965, Mössbauer effect in ^{161}Dy in metallic dysprosium, $DyFe_2$, and $DyAl_2$, *Phys. Rev.* **138**, A 241.

Okada, Y. and Tokumaru, Y.: 1984, Precise determination of lattice parameter and thermal expansion coefficient of silicon between 300 and 1500 k., *J. Appl. Phys.* **56**, 314.

Pinsker, Z. G.: 1978, *Dynamical Scattering of X rays in Crystals*, Springer.

Polster, H. D.: 1969, Multiple beam interferometry, *Appl. Opt.* **8**, 522.

Reisman, A., Berkenblit, M., Cuomo, J. and Chan, S. A.: 1971, The chemical polishing of sapphire and MgAl spinel, *J. Electrochem. Soc.* **118**, 1653.

Rogers, J. R.: 1982, Fringe shifts in multiple-beam fizeau interferometry, *J. Opt. Soc. Am.* **72**, 638.

Röhlsberger, R., Gerdau, E., Rüffer, R., Sturhahn, W., Toellner, T. S., Chumakov, A. and Alp, E. E.: 1997, X-ray optics for μev-resolved spectroscopy, *Nucl. Instrum. Methods Phys. Res. A* **394**, 251.

Rüffer, R., Gerdau, E., Hollatz, R. and Hannon, J. P.: 1987, Nuclear Bragg scattering of synchrotron radiation pulses in a single-reflection geometry, *Phys. Rev. Lett.* **58**, 2359.

Schmid, F., Khattak, C. P. and Felt, D. M.: 1994, Producing large sapphire for optical applications, *Am. Ceram. Soc. Bull.* **73**(2), 39.

Sellschop, J. P. F., Connell, S. H., Nilen, R. W. N., Detlefs, C., Freund, A. K., Hoszowska, J., Hustache, R., Burns, R. C., Rebak, M., Hansen, J. O., Welch, D. L., and Hall, C.: 2000, Synchrotron x-ray applications of synthetic diamonds, *New Diamond and Frontier Carbon Technology* **10**, 253.

Seto, M., Yoda, Y., Kikuta, S., Zhang, X. W. and Ando, M.: 1995, Observation of nuclear resonant scattering accompanied by phonon excitation using synchrotron radiation, *Phys. Rev. Lett.* **74**, 3828.

Sette, F., Krisch, M. H., Masciovecchio, C., Ruocco, G. and Monaco, G.: 1998, Dynamics of glasses and glass-forming liquids studied by inelastic x-ray scattering, *Science* **280**, 1550–1555.

Shastri, S. D., Zambianchi, P. and Mills, D. M.: 2001a, Dynamical diffraction of ultrashort x-ray free-electron laser pulses, *J. Synchrotron Rad.* **8**, 1131–1135.

Shastri, S. D., Zambianchi, P. and Mills, D. M.: 2001b, Femtosecond x-ray dynamical diffraction by perfect crystals, *Proc. SPIE - Int. Soc. Opt. Eng.* **4143**, 69–77.

Shvyd'ko, Y. V.: 1998, BASS. The program calculates energy Bragg backscattering spectra of x rays in kinematical approximation and provides fits to experimental ones.

Shvyd'ko, Y. V.: 1999, Nuclear resonant forward scattering of x-rays: Time and space picture., *Phys. Rev. B* **59**, 9132.

Shvyd'ko, Y. V.: 2000, Motif: Evaluation of time spectra for nuclear forward scattering, *Hyp. Interact.* **125**, 173–188.

Shvyd'ko, Y. V. and Gerdau, E.: 1999, Backscattering mirrors for x-rays and Mössbauer radiation, *Hyp. Interact.* **123/124**, 741–776.

Shvyd'ko, Y. V. and Smirnov, G. V.: 1990, Experimental study of time and frequency properties of collective nuclear excitations in a single crystal, *J. Phys.: Condens. Matter* **1**, 10563–10584.

Shvyd'ko, Y. V., Gerdau, E., Jäschke, J., Leupold, O., Lucht, M. and Rüter, H. D.: 1998, Exact Bragg backscattering of x-rays, *Phys. Rev. B* **57**, 4968.

Shvyd'ko, Y. V., Gerken, M., Franz, H., Lucht, M. and Gerdau, E.: 2001, Nuclear resonant scattering of synchrotron radiation from ^{161}Dy at 25.61 kev, *Europhys. Lett.* **56**, 39.

Shvyd'ko, Y. V., Lerche, M., Jäschke, J., Gerdau, M. L. E., Gerken, M., Rüter, H. D., Wille, H.-C., Becker, P., Alp, E. E., Sturhahn, W., Sutter, J. and Toellner, T. S.: 2000a, γ-ray wavelength standard for atomic scales, *Phys. Rev. Lett.* **85**, 495.

Shvyd'ko, Y. V., Lucht, M., Gerdau, E., Alp, E. E. and Sutter, J.: 2000b, Powder Bragg backscattering spectroscopy, *Advanced Photon Source User Activity Report* **1**, 467. www.aps.anl.gov/xfd/communicator/user2000/shvydkoy2.pdf.

Shvyd'ko, Y. V., Lucht, M., Gerdau, E., Lerche, M., Alp, E. E., Sturhahn, W., Sutter, J. and Toellner, T. S.: 2002, Measuring wavelengths and lattice constants with the Mössbauer wavelength standard, *J. Synchrotron Rad.* **9**, 17–23.

Shvyd'ko, Y. V., Smirnov, G. V., Popov, S. L. and Hertrich, T.: 1991, Observation of the enhanced forward γ-emission in spontaneous nuclear decay, *Pis'ma. Zh. Eksp. Teor. Fiz.* **53**, 69. [(1991) *JETP Lett.* **53**, 69].

Siddons, D. P., Hastings, J. B. and Faigel, G.: 1988, A new apparatus for the study of nuclear Bragg scattering, *Nucl. Instrum. Methods Phys. Res. A* **266**, 329.

Sinn, H.: 2001, Spectroscopy with mev energy resolution, *J. Phys.: Condens. Matter* **13**(34), 7525–7537.

Smirnov, G. V. and Shvyd'ko, Y. V.: 1986, Experimental study of the time evolution of the decay of Bragg modes of the collective nuclear excitations in a crystal, *Pis'ma. Zh. Eksp. Teor. Fiz.* **44**, 431–435. [(1986) *Sov. Phys. JETP* **44**, 431-435].

Smirnov, G. V. and Shvyd'ko, Y. V.: 1989, Measurements of the lifetime of a nucleus excited near a resonance, *Zh. Eksp. Teor. Fiz.* **95**, 777–789. [(1989) *Sov. Phys. JETP* **68**, 444-450].

Smith, S. T., Badami, V. G., Dale, J. S. and Xu, Y.: 1997, Elliptical flexure hinge, *Rev. Sci. Instrum.* **68**, 1474.

Steyerl, A. and Steinhauser, K.-A.: 1979, Proposal of a Fabry-Perot-type interferometer for x-rays, *Z. Phys. B* **34**, 221–227.

Sturhahn, W. and Kohn, V. G.: 1999, Theoretical aspects of incoherent nuclear resonant scattering, *Hyp. Interact.* **123/124**, 367.

Sturhahn, W., Toellner, T. S., Alp, E. E., Zhang, X., Ando, M., Yoda, Y., Kikuta, S., Seto, M., Kimball, C. W. and Dabrowski, B.: 1995, Phonon density of states measured by inelastic nuclear resonant scattering, *Phys. Rev. Lett.* **74**, 3832.

Sutter, J. P.: 2000, *Applications of special x-ray diffraction cases in silicon crystals*, PhD thesis, Purdue University.

Sutter, J. P., Alp, E. E., Hu, M. Y., Lee, P. L., Sinn, H., Sturhahn, W., and Toellner, T. S.: 2001, Multiple-beam x-ray diffraction near exact backscattering in silicon, *Phys. Rev. B* **63**, 094111.

Tanaka, M.: 1983, The dynamical properties of a monolithic mechanism with notch flexure hinges for precision control of orientation and position, *Japn. J. Appl. Phys.* **22**, 193–200.

Tappert, J., Keune, W., Brand, R. A., Vulliet, P., Sanchez, J.-P. and Shinjo, T.: 1996, Magnetism and structure of Dy/Fe multilayers studied by ^{57}Fe and ^{161}Dy Mössbauer spectroscopy, *J. Appl. Phys.* **80**, 4503.

Teworte, R. and Bonse, U.: 1983, High-precision determination of structure factors f_h of silicon, *Phys. Rev. B* **29**, 2102.

Toellner, T. S.: 2000, Monochromatization of synchrotron radiation for nuclear resonant scattering experiments, *Hyp. Interact.* **125**, 3.

Toellner, T. S., Hu, M., Sturhahn, W., Bortel, G., Alp, E. E. and Zhao, J.: 2001, Crystal monochromator with a resolution beyond 10^8, *J. Synchrotron Rad.* **8**, 1082–1086.

Toellner, T. S., Hu, M., Sturhahn, W., Quast, K. and Alp, E. E.: 1997, Inelastic nuclear resonant scattering with sub-mev energy resolution, *Appl. Phys. Lett.* **71**, 2112.

Toellner, T. S., Shu, D., Bortel, G. and Hu, M.: 2000, In-line high-resolution monochromator for 21.6 kev x-rays, *Advanced Photon Source User Activity Report* **1**, 284. www.aps.anl.gov/xfd/communicator/user2000/toellnert2.pdf.

Tolansky, S.: 1960, *Surface Microtopography*, Interscience.

Trammell, G. T. and Hannon, J. P.: 1978, Quantum beats from nuclei excited by synchrotron pulses, *Phys. Rev. B* **18**, 165–172. Erratum: *Phys. Rev. B* **19**, 3835 (1979).

Tuomi, T., Naukkarinen, K. and Rabe, P.: 1974, Use of synchrotron radiation in x-ray diffraction topography, *Phys. Stat. Solidi (a)* **25**, 93.

van Bürck, U., Mössbauer, R. L., Gerdau, E., Rüffer, R., Hollatz, R., Smirnov, G. V. and Hannon, J. P.: 1987, Nuclear Bragg scattering of synchrotron radiation with strong speedup of coherent decay, measured on antiferromagnetic $^{57}FeBO_3$, *Phys. Rev. Lett.* **59**, 355.

Vaughan, J. M.: 1989, *The Fabry-Perot interferometer*, Hilger.

Verbeni, R., Sette, F., Krisch, M., Bergmann, U., Gorges, B., Halcoussis, C., Martel, K., Masciovecchio, C., Ribois, J. F., Ruocco, G. and Sinn, H.: 1996, X-ray monochromator with 2×10^{-8} energy resolution, *J. Synchrotron Rad.* **3**, 62–64.

von Laue, M.: 1931, Die dynamische Theorie der Röntgenstrahlinterferenzen in neuer Form, *Ergeb. Exakt. Naturwiss.* **10**, 133–158.

Wickman, H. H.: 1966, Mössbauer paramagnetic hyperfine structure, *in* I. J. Gruverman (ed.), *Mössbauer Effect Methodology*, Vol. 2, Plenum Press, pp. 39–65. New York.

Wickman, H. H., Klein, M. P. and Shirley, D. A.: 1966, Paramagnetic hyperfine structure and relaxation effects in Mössbauer spectra: ^{57}Fe in ferrichrome a, *Phys. Rev.* **152**, 345.

Wilkins, S. W.: 1978, Bragg-case x-ray thin-crystal rocking curves for Si - a direct comparison between theory and experiment, *Phys. Lett.* **66A**, 134–6.

Wilkinson, M. K., Koeller, W. C., Wollan, E. O. and Cable, J. W.: 1961, Neutron diffraction investigations of magnetic ordering in dysprosium, *J. Appl. Phys.* **32**, 485.

Xiaowei, Z., Yoda, Y. and Imai, Y.: 2000, Precision wavelength measurement of the 14.4 kev Mössbauer photon, *J. Synchrotron Rad.* **7**, 189.

Yabashi, M., Tamasaku, K., Kikuta, S. and Ishikawa, T.: 2001, An x-ray monochromator with an energy resolution of 8×10^{-9} at 14.4 kev, *Rev. Sci. Instrum.* **72**, 4080.

Yim, W. M. and Paff, R. J.: 1973, Thermal expansion of aln, sapphire, and silicon, *J. Appl. Phys.* **45**, 1456.

Zachariasen, W. H.: 1945, *Theory of X-Ray Diffraction in Crystals*, John Wiley & Sons, Inc.

Ziman, J. M.: 1969, *Principles of the theory of solids*, Cambridge University Press.